AGH UNIVERSITY OF SCIENCE AND TECHNOLOGY

FIELD OF SCIENCE Natural Sciences

SCIENTIFIC DISCIPLINE Physical Sciences

DOCTORAL THESIS

The development of NMR imaging applications for nano- and micrometric porous systems in the presence of non-uniform magnetic field gradients

Author: mgr inż. Weronika Mazur

First PhD Advisor: dr hab. Artur T. Krzyżak, prof. AGH
Second PhD Advisor: prof. dr hab. Czesław Kapusta

Completed in: Faculty of Physics and Applied Computer Science and Faculty of Geology, Geophysics and Environmental Protection of the AGH University of Science and Technology

Kraków, 2023

Statement by the author of the thesis:

I declare, aware of the criminal responsibility for certifying untruth, that I have completed this thesis by myself and independently and that I have not used sources other than those mentioned in the thesis.

.....
date, Author's signature

Statement by the PhD Advisors:

This dissertation is ready to be reviewed.

.....
date, signature of the first PhD Advisor of the thesis

.....
date, signature of the second PhD Advisor of the thesis

Research described within this thesis has been completed in the framework of the Program POWER, project No. POWR.03.02.00-00-I004/16, co-financed by the European Union within the Interdisciplinary PhD Studies "Physical, Chemical and Biophysical Foundations of Modern Technologies and Materials Engineering" (FCB)

Badania opisane w rozprawie były finansowane ze środków Programu POWER (POWR.03.02.00-00-I004/16) współfinansowanego przez Unię Europejską w ramach Interdyscyplinarnych Środowiskowych Studiów Doktoranckich „Fizyczne, Chemiczne i Biofizyczne Podstawy Nowoczesnych Technologii i Inżynierii Materiałowej" (FCB);

by the National Centre for Research and Development from the Strategic Program STRATEGMED2 Funds within the project "Cardiovascular ischemic injury regeneration using Wharton Jelly as unlimited therapeutic stem cells source" (STRATEGMED2/265761/10/NCBR/2015);

ze środków Programu Badań Stategicznych STRATEGMED2 Narodowego Centrum Badań i Rozwoju w ramach projektu „Regeneracja uszkodzeń niedokrwiennych układu sercowo-naczyniowego z wykorzystaniem Galarety Whartona jako nieograniczonego źródła terapeutycznego komórek macierzystych (STRATEGMED2/265761/10/NCBR/2015);

and by the Medical Research Agency within the project "Evaluation of the clinical effectiveness of BSD (B-matrix Spatial Distribution) technology and algorithms based on artificial intelligence for the analysis of MRI images in the course of multiple sclerosis (MS)" the field of non-commercial clinical trials (2020/ABM/01/00006-00).

oraz przez Agencję Badań Medycznych w ramach projektu „Ocena efektywności klinicznej technologii BSD (B-matrix Spatial Distribution) oraz algorytmów opartych na sztucznej inteligencji do analizy obrazów MRI w przebiegu stwardnienia rozsianego (SM)" w zakresie niekomercyjnych badań klinicznych.

Acknowledgement

I would like to thank my PhD Advisors, Professors Artur T. Krzyżak and Czesław Kapusta, for giving me the opportunity for this doctoral thesis, creating the path for my research and for supporting me during these past five years. I am thankful for a very pleasant working atmosphere and friendly relations.

I would like to express my special thanks to my leading Supervisor, Artur T. Krzyżak, who enabled me to work on many very interesting projects that he has administered, for all the knowledge he imparted to me and the insightful discussions we had about the research, science and life in general. I am very grateful for the freedom at work, homeyness, support and encouragements. He taught me to believe in myself and always aim for the sky. I always did my utmost and I am the scientist who I am today mainly thanks to him.

I will forever be thankful of my colleagues that I worked with and who helped me at the beginning. Dr Krzysztof Kłodowski, who taught me how to use the tomographic system, the basics of BSD calibration and who supervised my work more than once. Krzysztof was my physics lab teacher in my first year of engineering studies and he got me into the habit of correctly reporting data. Our paths crossed during my studies and I am pleased that he agreed to give a short lecture about his research work during my master's degree. Thanks to him, I ended up in the NMR tomography and spectroscopy laboratory under the supervision of Professor Krzyżak and I had a chance to continue my research work with NMR. Dr Iwona Habina-Skrzyniarz, who introduced to me the basics of low-field relaxometry, taught me how to perform measurements and helped me when I needed it. I don't know a more systematic, helpful and warm person and I am very happy that we could work together. Dr Adam Fheed for fruitful discussions, conduction of common research in the field of geoscience and support. I thank to Dr Krzysztof Janc for many insightful discussions, scientific advices, suggestions and help in the simulations regarding diffusion tensor imaging and BSD calibration. He was my primary resource for getting my science questions answered and always helped me gain perspective. Many thanks are due to other colleagues from the laboratory and studies for creating a friendly atmosphere in the workplace, talking and laughing together over lunch or coffee, for scientific trips and support.

Last but not least, I am incredibly thankful for Tomek, my partner, for all the support, consideration and help in everyday duties, when deadlines approached and when science was consuming me. All my achievements are our achievements, thank you for everything. I also want to thank my family, especially my Parents and Sisters for hearing me out, supporting me and always repeating me that I can do anything.

Dedication

I dedicate this doctoral thesis to my late grandmothers and grandfather, for whom I was always one of the greatest source of pride. You looked forward to watching it happen…

Table of content

STRESZCZENIE

Rozprawa dotyczy zastosowania magnetycznego rezonansu jądrowego (MRJ) do badań nano- i mikrometrycznych układów porowatych w polu magnetycznym, którego gradient jest niejednorodny z powodu niedoskonałości sprzętu i/lub niejednorodnych właściwości magnetycznych próbki. Nadrzędnym celem tych badań jest polepszenie istniejących oraz znalezienie nowych aplikacji MRJ w badaniach mikrostrukturalnych układów porowatych spotykanych w biologii, medycynie, geologii i inżynierii materiałowej. Do tego celu użyto technik MRJ do pomiarów relaksacji i dyfuzji, a także zaimplementowano metody korekcji, takie jak „B-matrix Spatial Distribution" (BSD) w obrazowaniu tensora dyfuzji (ang. *diffusion tensor imaging,* DTI).

Prowadzone prace badawcze skupiały się na pokonaniu barier napotykanych w charakterystyce mikrostruktury: i) skala, ii) ilość materiału badawczego, iii) skład chemiczny próbki, iv) artefakty obrazowe, v) błędy pomiarowe (systematyczne i stochastyczne). W ramach rozprawy, do dokładniejszego opisu mikrogeometrii układów biologicznych *in vitro* zaproponowano w pierwszej kolejności zastosowanie metody pomiaru współczynnika dyfuzji zależnego od czasu dyfuzji na jednostronnym skanerze NMR MoUSE, operującym w stałym, bardzo silnym gradiencie pola magnetycznego. Opracowana na komórkach modelowych drożdży piekarskich metodologia została przeniesiona do układów mezenchymalnych komórek macierzystych i umożliwiła charakterystykę ich własności biofizycznych oraz mikrostruktury, w tym głównie wykrycie składowej w sygnale pochodzącej od jądra komórkowego. Dzięki temu wskazano możliwość rozróżnienia dwóch mechanizmów śmierci komórek (nekroza i apoptoza). W tych pracach badawczych pokonano barierę skali oraz ilości materiału badawczego.

Rozprawa prezentuje również podejścia i zalety kliniczne dokładniejszego opisu mikrostruktury układów biologicznych *in vivo*- tkanek. Skupiono się na mięśniach szkieletowych podudzi w chorobie niedokrwiennej. Zbadano wpływ leczenia mezenchymalnymi komórkami macierzystymi w podwójnie zaślepionej próbie klinicznej, analizując zmiany mikrostruktury mięśni. Prawidłowa analiza i diagnostyka wymaga eliminacji błędów systematycznych, w tym przypadku z użyciem metody BSD.

Ostatni obszar badań mikrostruktury stanowiły naturalne układy porowate- próbki rdzeni skalnych. Zaproponowano pomiary MRJ procesów relaksacji w niskim polu magnetycznym jako metodę do rozróżnienia czertów typu „bedded" i „nodular" tylko na podstawie cech mikrostruktury porowej w całym zakresie skali (od nano- do makro-), w tym efektów powierzchniowych. Jako metodę pomocniczą zaproponowano analizę składowych głównych. Dokładna analiza danych MRJ była możliwa dzięki dużej korelacji próbek z naturalnymi układami krzemionkowymi (zeolitami) oraz korekcji ze względu na skład chemiczny. Krokiem naprzód w charakterystyce mikrostruktury skał było zastosowanie techniki obrazowania tensora dyfuzji, co było możliwe dla próbek węglanowych. Pokazano sposób interpretacji wyników DTI, a na ich podstawie wyznaczono szereg parametrów geofizycznych, w tym jedną nową metrykę mogącą odzwierciedlać przepuszczalność.

ABSTRACT

The dissertation concerns the application of nuclear magnetic resonance (NMR) for nano- and micrometric studies of porous systems in a magnetic field whose gradient is non-uniform due to hardware imperfections and/or inhomogeneous magnetic properties of the sample. The major goal of this research is to improve existing and find new NMR imaging applications in microstructural studies of porous systems found in biology, medicine, geology and material engineering. For this purpose, NMR techniques were used to measure relaxation and diffusion, and correction methods such as "B-matrix Spatial Distribution" (BSD) were implemented in diffusion tensor imaging (DTI).

The research work focused on overcoming the barriers encountered in the characterization of the microstructure: i) scale, ii) amount of research material, iii) chemical composition of the sample, iv) image artifacts, v) measurement errors (systematic and random). As part of the dissertation, for a more accurate description of the microgeometry of biological systems *in vitro*, it was first proposed to use the method of measuring the time-dependent diffusion coefficient on a single-sided NMR MoUSE scanner, operating in a constant, very strong magnetic field gradient. The methodology developed on model cells of baker's yeast was transferred to the mesenchymal stem cells and enabled the characterization of their biophysical properties and microstructure, including mainly the detection of a component in the signal coming from the cell nucleus. This indicated the possibility of distinguishing two mechanisms of cell death (necrosis and apoptosis). In these research works, the scale and amount of research material barriers were overcome.

The dissertation also presents approaches and clinical advantages of a more accurate description of the microstructure of biological systems *in vivo*-tissues. The focus was on the skeletal muscles of the lower leg in ischemic disease. The effect of mesenchymal stem cell treatment was investigated in a double-blind randomized clinical trial, through the analysis of changes in muscles microstructure. Proper analysis and diagnosis require the elimination of systematic errors, in this case using the BSD method.

The last area of microstructure research were natural porous systems- samples of rock cores. NMR measurements of relaxation processes in a low magnetic field have been proposed as a method to distinguish between "bedded" and "nodular" cherts only on the basis of the features of the pore microstructure in the entire scale range (from nano- to macro-), including surface effects. Principal component analysis was proposed as an auxiliary method. Accurate analysis of NMR data was possible due to the high correlation of samples with natural silica systems (zeolites) and correction for chemical composition. A step forward in rock microstructure characterization was the use of diffusion tensor imaging (DTI), which was possible with carbonate samples. The method of interpreting the DTI results was shown, and on their basis a number of geophysical parameters were determined, including one new metric that could reflect the permeability.

THESIS ARRANGEMENT

The doctoral dissertation consists of a collection of six articles describing the new applications of NMR imaging for the accurate quantitative characterization of microstructure of biological, medical and geological nano- and microporous systems, in which non-uniform magnetic field gradients are present.

A1 **Weronika Mazur**, Artur T. Krzyżak, *Attempts at the Characterization of In-Cell Biophysical Processes Non-Invasively-Quantitative NMR Diffusometry of a Model Cellular System*, Cells 9, 2124. https://doi.org/10.3390/cells9092124 (2020)

A2 Artur T. Krzyżak, Iwona Habina-Skrzyniarz, Weronika Mazur, Maciej Sułkowski, Marta Kot, Marcin Majka, *Nuclear magnetic resonance footprint of Wharton Jelly mesenchymal stem cells death mechanisms and distinctive in-cell biophysical properties in vitro*. J. Cell. Mol. Med. 26, 1501–1514. https://doi.org/10.1111/jcmm.17178 (2022)

A3 **Weronika Mazur**, Małgorzata Urbańczyk-Zawadzka, Robert Banyś, Rafał Obuchowicz, Mariusz Trystuła, Artur T. Krzyżak, *Diffusion as a Natural Contrast in MR Imaging of Peripheral Artery Disease (PAD) Tissue Changes. A Case Study of the Clinical Application of DTI for a Patient with Chronic Calf Muscles Ischemia*. Diagnostics 11, 92. https://doi.org/10.3390/diagnostics11010092 (2021)

A4 **Weronika Mazur**, Małgorzata Urbańczyk-Zawadzka, Robert Banyś, Rafał Obuchowicz, Mariusz Trystuła, Artur T. Krzyżak, *Diffusion tensor imaging as a tool to assess the structure of lower limb muscles invisible on T1- and T2-weighted images in the course of the chronic phase of peripheral artery disease*. Adv. Interv. Cardiol. w Kardiol. Interwencyjnej 18, 1–4. https://doi.org//10.5114/aic.2022.121343 (2022)

A5 Artur T. Krzyżak, **Weronika Mazur**, Jacek Matyszkiewicz, Alicja Kochman, *Identification of Proton Populations in Cherts as Natural Analogues of Pure Silica Materials by Means of Low Field NMR*. J. Phys. Chem. C 124, 5225–5240. https://doi.org/10.1021/acs.jpcc.9b11790 (2020)

A6 Artur. T Krzyżak, **Weronika Mazur**, Adam Fheed, Władysław P. Węglarz, *Prospects and Challenges for the Spatial Quantification of the Diffusion of Fluids Containing 1H in the Pore System of Rock Cores*. J. Geophys. Res. Solid Earth 127, 1–20. https://doi.org/10.1029/2021jb023299

The dissertation starts with the list of acronyms, which are followed by 4 chapters. The first chapter presents the motivation and main goals of this thesis. The second chapter presents the introduction consisting of theoretical background of nuclear magnetic resonance phenomenon, signal detection,

three main processes occurring after resonant excitation of magnetization in isotropic and confining media, imaging principles, diffusion tensor imaging technique and B-matrix spatial distribution method. Third chapter includes reviews of papers A1-A6. In the last, fourth chapter, a summary of the entire dissertation and conclusions gathered during the research are included. In the following parts of the dissertation supplements and articles are attached.

LIST OF ACRONYMS

2D	Two-dimensional
3D	Three-dimensional
BSD	B-matrix spatial distribution
CPMG	Carr-Purcell-Meiboom-Gill
DL	Longitudinal diffusivity
DT	Transverse diffusivity
DTI	Diffusion tensor imaging
DWI	Diffusion-weighted imaging/images
EPI	Echo-planar imaging
FA	Fractional anisotropy
FEM	Force equilibrium model
GM	Gastrocnemius medialis muscle
GPA	Gaussian phase approximation
KCU	Kraków-Częstochowa Upland
LF-NMR	Low-field NMR
MD	Mean diffusivity
MICP	Mercury incjection capillary pressure
MoUSE	Mobile Universal Surface Explorer
MRI	Magnetic resonance imaging
NMR	Nuclear magnetic resonance
PAD	Peripheral artery disease
PCA	Principal component analysis
PDT	Principal diffusion tracts
PGSE	Pulsed-gradient spin echo
PSD	Pore size distribution
r.m.s.	Root-mean-square
RCT	Randomized clinical trial
RF	Radiofrequency
SD	Standard deviation
SE	Spin echo
SGP	Short gradient pulse

SNR	Signal-to-noise ratio
SOL	Soleus muscle
SPI	Single-point imaging
SPRITE	Single-point ramped imaging with T1-enhancement
ST	Slice thickness
T1WI	T1-weighted image
T2WI	T2-weighted image
TA	Tibialis anterior muscle
TDDC	Time-dependent diffusion coefficient
TE	Echo time
TR	Repetition time
uCT	Micro-computed tomography
WJMSC	Wharton Jelly mesenchymal stem cells
ZTE	Zero echo time

I. MOTIVATION AND AIM

"[…] the range of [NMR] microscopic applications

is potentially enormous and, as yet, largely unexplored."

Paul T. Callaghan
"Principles of Nuclear Magnetic Resonance Microscopy", 1991

The history of nuclear magnetic resonance (NMR) development is inextricably linked to the Nobel Prize-to-Nobel Prize path. It has all started in 1921 when Isidor Isaac Rabi, originally from Rymanów, currently Poland, presented a new method of measuring a nuclear magnetic moment. He passed a molecular beam of his sample through oscillating magnetic fields, for which he was awarded the Nobel Prize in 1944 (Boesch, 2004; Giunta and Mainz, 2020). Rabi's work inspired and was transferred to the bulk solutions and solids by two independent researchers- Felix Bloch (Stanford University) and Edward Purcell (experiments in Harvard University, although originally connected to Massachusetts Institute of Technology). After successful experiments, they published their papers on NMR in 1946, although it was not immediately clear that they dealt with the same phenomenon. In 1952 they were awarded the Nobel Prize, and four years later the nomenclature was made consistent and to this day has been called **nuclear magnetic resonance phenomenon**. In the meantime, Nicolaas Bloembergen (Purcell's postgraduate student), Purcell and Robert Pound published (in 1948) a theoretical and experimental considerations on the energy transfer between nuclear spins and their environment- spin-lattice relaxation, which was later called a "BPP theory" and become very important in the characterization of condensed matter. Two years after Bloch's and Purcell's discoveries, NMR gained a large attention in the research of a condensed matter and was applied in many fields of studies (science and technology) (Hennel, 1966), mainly to the analysis of a chemical and physical structure of molecules.

About 40 years after the Bloch's and Purcell's Nobel Prizes, Richard R. Ernst won his Nobel Prize in 1991 in the field of chemistry for introducing a multidimensional spectroscopy using Fourier Transform. He gave, then, a very important Nobel Lecture in which he acknowledged many researchers, Nobel Laureates, who greatly contributed to the development of NMR, but never received a Nobel Prize- among others Bloembergen (for BPP theory) or Norman F. Ramsey (for introducing the concept of the chemical shift and J coupling). In 2002 Kurt Wuthrich received the Nobel Prize "for his development of nuclear magnetic resonance spectroscopy for determining the three-dimensional structure of biological macromolecules in solution" (proteins) (Boesch, 2004) and one year later the history looped the loop when in 2003 Paul C. Lauterbur and Sir Peter Mansfield shared the Nobel Prize for their impact on the medical magnetic resonance imaging (MRI). In 1973, they reported the first NMR image- proton spin density maps, and the relationship

between the spin density and the NMR signal, respectively (Callaghan, 1991). However, transfer to the practical medicine was not until 1986, when the first NMR micrographs were produced (Callaghan, 1991). Last but not least, the great appreciation should be given to the polish scientists. Andrzej Hrynkiewicz, Jacek Hennel and Olgierd Korybut-Daszkiewicz were the first, who obtained the NMR signal in Poland in 1953, here in Cracow. Thus, making the city the cradle of polish NMR research. The first NMR image was obtained by Andrzej Jasiński, who completed a scientific internship under the supervision of the Nobel laureate prof. Peter Mansfield. A. Jasiński group worked on the development of MRI equipment for the tomographic microscopy. They succeeded in 1993 and started research on the bee anatomy. The NMR tomographic microscope allowed them to study water diffusion in tissues, such as the spinal cord, for which they implemented diffusion tensor imaging (DTI) for the first time in Poland and almost along with the first DTI technique introduction reported by Peter J. Basser, James Mattiello and Denis Le Bihan in 1994.

It has been nearly 80 years since the first NMR developments. The history shows that NMR research area is a Nobel Prize worthy, while between subsequent discoveries, numerous applications were found. The chapter opening quote was derived from the Paul T. Callaghan's book pressed in 1991 (Callaghan, 1991), and after 30 years it seems still valid. Technical, electronical, material and computer science progress supports constantly emerging NMR techniques and new equipment. The possibilities they offer are enormous, in the laboratory as well as in the clinical research. The rapid pace of progress in the last 20 years has led to the point where by using NMR it is possible to study single molecules, in-cell processes, to image at very high spatial and temporal resolutions, moving objects such as heart, and use NMR metrics as disease biomarkers in clinical practice. This is due to the fact that although initially found exotic, NMR and MRI equipment have quickly become essential in modern laboratories and hospitals. Widespread access to the equipment has resulted in an increase in the number of applications in different fields of study besides chemistry and physics, such as geology, medicine and material science, but there is still more to explore.

The motivation of this dissertation was mainly the NMR history briefly presented above. It can be seen how NMR- originally a physical tool, evolved into Nobel Prize worthy applications in chemistry and medicine. The growing interest and ubiquitous statements about the potential of NMR, as well as the experience and ideas of the Advisors of this work, were the motivation to contribute to bridging the gap between the possibilities and undiscovered applications of NMR. The development of the NMR hardware creates predispositions for applying MRI (mainly diffusion contrast) to describe biophysical processes and biochemical, time-related changes inside the cell on a smaller and smaller scale, as well as for a deeper insight into the microstructure of the examined system in a non-invasive way. It is worth noting that diffusion MRI, as a non-invasive technique, has found a number of applications in many fields of science, mainly in medicine. According to

PubMed, there is an exponential increase of publications for the keywords "diffusion" and "MRI" in the title or abstract. Moreover, according to SciVal, in the years 2011-2020, as many as 45 548 articles were published in the thematic cluster "Magnetic Resonance Imaging; brain; Diffusion", of which 3 984 under the theme "Diffusion Weighted Imaging". In addition, according to PubMed, the number of articles with the keywords "microstructure" and "MRI" in the title or abstract doubles every 2.7 years (2 047 publications), and "cells" and "biophysical" doubles every 7 years for a total of 10 065 publications (Fig. 1). However, despite the huge development of the diffusion MRI technique, it is not fully explored in practice. For example, it can be seen that despite the increasing number of articles on diffusion MRI, their citation decreases each year (-10% for "Diffusion Weighted Imaging" in the years 2011-2020 according to SciVal). On the other hand, numerous national grants of the National Center for Research and Development can be cited, e.g.: "Regeneration of ischemic damage to the cardiovascular system using Wharton jelly as an unlimited source of therapeutic stem cells", and European ERC and Horizon 2020, e.g.: "Magnetic resonance imaging platform for probing fat microstructure", "Frontier research in arterial fiber remodeling for vascular disease diagnosis and tissue engineering", "MRI based mapping of microscopic brain composition in a mouse model of Alzheimer's disease", which were awarded in recent years for research using diffusion MRI. Therefore, the conclusion is that the applications of the method are constantly developing, more and more publications related to it are being published, but there is still a barrier to routine applications. To overcome the existing barriers, the development of new, more advanced models and methods, as well as additional experimental work are required.

The aim of this doctoral thesis is the development of new applications of NMR in various porous systems encountered in geology, biology, medicine, as well as in synthetic porous materials. Special focus was put on the improvement of quantitative characterization of nano- and micrometric scale porous systems, where the main challenge is inhomogeneous magnetic field and non-uniform magnetic field gradients. The overall goal of the conducted research was to somehow overcome the existing barriers and at the same time to deliver tools or open the research paths for Scientists from other fields of study.

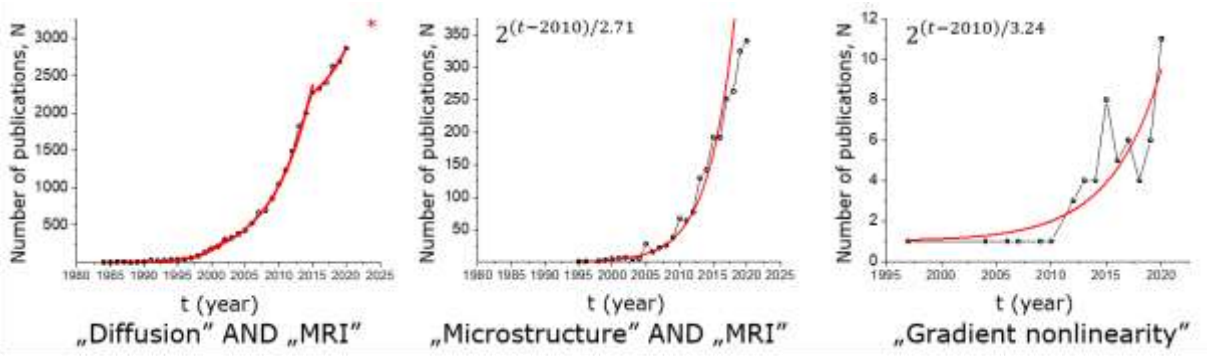

Fig. 1. Number of publications (according to PubMed) per year containing keywords (title and abstract) given in quotation marks. Power functions shown in the panels were fitted to the data, while "*" in the first panel indicates interval fitting of exponential functions.

II. INTRODUCTION

1. NUCLEAR MAGNETIC RESONANCE THEORY

1.1. Nuclear magnetization

Atomic nucleus can have its own angular momentum called spin. From this spin arises the magnetic dipole moment, $\boldsymbol{\mu}$:

$$\boldsymbol{\mu} = \gamma\hbar\boldsymbol{I}, \tag{1.1}$$

where γ is gyromagnetic ratio, $\hbar$ is Planck's constant, h, divided by 2π and $\boldsymbol{I}$ is quantum operator of a spin. For atomic nucleus with magnetic moment, $\boldsymbol{\mu}$, spin-up and spin-down states can be separated when it is placed in the static magnetic field, $\boldsymbol{B_0}$, due to the splitting of the atomic energy levels, which is called Zeeman effect. The interaction energy of $\boldsymbol{\mu}$ in the external magnetic field, $\boldsymbol{B_0}$, (Zeeman interaction) is equal to $-\boldsymbol{\mu} \cdot \boldsymbol{B_0}$. In B_0 that is magnetic field oriented along the laboratory z axis, i.e. $\boldsymbol{B_0} = (0, 0, B_0)$, the Hamiltonian- the energy operator, can be determined using classical potential energy formula ($E = -\boldsymbol{\mu} \cdot \boldsymbol{B_0}$), which gives

$$\mathcal{H} = -\gamma\hbar B_0 I_z, \tag{1.2}$$

where I_z is z-th coordinate of $\boldsymbol{I}$ and the eigenvalues, m, of I_z can be equal to $-I$ to I. The eigenvalues of the Hamiltonian in (1.2) are defined as

$$E(m) = -\gamma\hbar B_0 m, \tag{1.3}$$

which is called the energy level of a nuclear spin in a magnetic field and m is magnetic spin quantum number. For nucleus with spin quantum number I, there is $2I$+1 energy levels. The distance between two adjacent energy levels ($\Delta m = \pm 1$) is equal to

$$\Delta E = E(m+1) - E(m) = -\gamma\hbar B_0. \tag{1.4}$$

This thesis focused on the hydrogen nucleus (proton) resonance, for which $I = \frac{1}{2}$ and γ=267519000 $\frac{1}{T \cdot s}$.

A macroscopic hydrogen-rich sample (e.g. 1 ml of water, which will have $6.68 \cdot 10^{22}$ hydrogen nuclei) in a magnetic field will contain two proton populations in two different eigenstates. According to the Boltzmann distribution, there will be a surplus of protons on the higher energy level. This results in the resultant magnetic moment per sample's volume, which is called magnetization, $\boldsymbol{M}$. Magnetization can be defined in terms of the magnetic field induction as

$$\boldsymbol{M} = \chi\boldsymbol{B_0}, \tag{1.5}$$

where $\chi = \frac{\chi_\infty}{\mu_0}$ is magnetic susceptibility, while χ_∞ is magnetic susceptibility in equilibrium and $\mu_0 \approx 4\pi \cdot 10^{-8} \frac{H}{m}$ is permeability of free space.

1.2. Larmor precession

Magnetic moment of a non-zero spin nucleus placed in the external magnetic field will experience a torque tending to align it. However, due to already existing angular momentum, this torque induces precessional motion instead. The phenomenon is called *Larmor precession*. Based on the quantum mechanics rules, magnetic moment's eigenstate function can be presented as the product of time independent and time dependent factors. The latter describes the rotational motion of xy component of a magnetic moment in time with the angular velocity given by

$$\boldsymbol{\omega_0} = \gamma \boldsymbol{B_0}, \tag{1.6}$$

called Larmor frequency, while the motion phase is equal to $\gamma \boldsymbol{B_0} t$, where t is the time spent by the nucleus in a magnetic field.

1.3. Nuclear magnetic resonance (resonant excitation)

Let us consider a disturbance of a spin's motion caused by the additional, oscillating magnetic field $\boldsymbol{B_1}$ applied transversely to the main magnetic field, B_0. The operator of the spin's energy in a laboratory frame of reference is then dependent on the two magnetic fields interacting with this spin:

$$\mathcal{H}_{lab} = -\gamma \hbar B_0 I_z - 2\gamma B_1 \cos(\omega t)\, I_x, \tag{1.7}$$

where I_x is x-th coordinate of $\boldsymbol{I}$. The Hamiltonian can be made time-independent if presented in the rotating frame of reference as given by

$$\mathcal{H}_{rot} = -\gamma \left(B_0 - \frac{\omega}{\gamma}\right) I_z - \gamma B_1 I_x. \tag{1.8}$$

The magnetic resonance occurs when $\omega = \omega_0$. According to the bracket in (7) such value of ω causes B_0 vanishing, so that at resonance spins precess around the $\boldsymbol{B_1}$.

Macroscopically, the NMR signal in the receiver coil is built from the magnetization vector, $\boldsymbol{M}$, disturbed by $\boldsymbol{B_1}$ transverse to $\boldsymbol{B_0}$ and returning to the equilibrium. The time evolution of $\boldsymbol{M}$ is described by

$$\frac{\mathrm{d}\boldsymbol{M}}{\mathrm{d}t} = \gamma \boldsymbol{M} \times \boldsymbol{B}, \tag{1.9}$$

where $\boldsymbol{B}$ is the effective magnetic field coming from $\boldsymbol{B_0}$ and $\boldsymbol{B_1}$. At the resonance:

$$\boldsymbol{B_1}(t) = B_1 \cos(\omega_0 t)\,\mathbf{i} - B_1 \sin(\omega_0 t)\,\mathbf{j}, \tag{1.10}$$

where **i, j** and **k** are versors of the laboratory x, y and z axes, respectively, and by using (8), the evolution of the individual components of $\boldsymbol{M}$ are given by the following equations:

$$\frac{\mathrm{d}M_x}{\mathrm{d}t} = \gamma\left[M_y B_0 + M_z B_1 \sin(\omega_0 t)\right], \tag{1.11a}$$

$$\frac{\mathrm{d}M_y}{\mathrm{d}t} = \gamma[M_z B_1 \cos(\omega_0 t) - M_x B_0], \tag{1.11b}$$

$$\frac{\mathrm{d}M_z}{\mathrm{d}t} = \gamma\left[-M_x B_1 \sin(\omega_0 t) - M_y B_1 \cos(\omega_0 t)\right]. \tag{1.11c}$$

Assuming that in the time $t = 0$ $\boldsymbol{M} = M_0\mathbf{k}$, the solution of equations (11) is

$$M_x = M_0 \sin(\omega_1 t) \sin(\omega_0 t), \tag{1.12a}$$

$$M_y = M_0 \sin(\omega_1 t) \cos(\omega_0 t), \tag{1.12b}$$

$$M_z = M_0 \cos(\omega_1 t), \tag{1.12c}$$

where $\omega_1 = \gamma B_1$. The manipulation of the magnetization vector via the radiofrequency (RF) pulses is the foundation of every NMR experiment. There is much experimental capacity in manipulating both ω_1 and RF duration. The latter determines the angle $\phi = \omega_1 t$, by which $\boldsymbol{M}$ can be tipped. The most popular is to tip the magnetization by the angle of 90º in order to obtain the maximal signal in the receiver coil, however, lower angles can be useful for fast imaging sequences.

Nuclear magnetic resonance can thought as a quantum radiation absorption. If ΔE between two spin's energy levels is given by (4), then resonant absorption of RF pulse energy will occur for RF quants with frequency of $\nu = \frac{\Delta E}{\hbar}$. It can also be proved, that by using RF coils only $\Delta m = \pm 1$ quantum leaps are possible.

1.4. Relaxation

Magnetization disturbed by the oscillating field, right after the RF pulse starts to release gained energy in order to come back to the thermal equilibrium given by the state $M_0\mathbf{k}$. The equilibrium can be restored through the exchange of energy of magnetization and its environment, called "lattice". The process of the restoration is therefore called spin-lattice relaxation and is described by the equation

$$\frac{\mathrm{d}M_z}{\mathrm{d}t} = -\frac{M_z - M_0}{T_1} \tag{1.13}$$

with solution

$$M_z(t) = M_z(0)\exp\left(-\frac{t}{T_1}\right) + M_0\left(1 - \exp\left(-\frac{t}{T_1}\right)\right), \tag{1.14}$$

where T_1 is the time constant of the process called spin-lattice or longitudinal relaxation time (restoration of the longitudinal to B_0 component).

The growth of the longitudinal magnetization is inherently connected with the disappearance of the transverse component. However, phase coherence of spin states in the transverse plane is lost faster than spin-lattice relaxation due to the dipole-dipole interactions between nuclear and electronic magnetic moments, as well as among nuclear moments. Hence, transverse relaxation is a process of returning to equilibrium among spins, and therefore is called spin-spin relaxation and is described as

$$\frac{\mathrm{d}M_{xy}}{\mathrm{d}t} = -\frac{M_{xy}}{T_2} \tag{1.15}$$

with solution

$$M_{xy}(t) = M_{xy}(0)\exp\left(-\frac{t}{T_2}\right), \tag{1.16}$$

where T_2 is spin-spin or transverse relaxation time, M_{xy} is the transverse component of magnetization and $M_{xy}(0)$ is the initial transverse component, i.e. the M_{xy} length right after turning off the RF pulse. This exponential behavior applies when the spin-spin interactions are weak, for example in liquid samples. Macromolecules or solids can exhibit more complicated transverse signal decay.

1.5. Diffusion

Self-diffusion is a random translational motion of molecules having thermal energy, therefore occurs always in temperature higher than 0 K. According to Stokes-Einstein equation, macroscopically it is strictly dependent on the size of molecules:

$$D = \frac{kT}{6\pi\eta r_S}, \tag{1.17}$$

where D is self-diffusion coefficient, k is the Boltzmann constant, T is temperature, η is viscosity of a solution and r_S is Stokes (hydrodynamic) radius.

As mentioned in the previous section, the existence of transverse magnetization is directly related to the spins phase coherence. Thus, the influence of diffusional motion on the spins phase will be presented. Diffusion NMR relies on the intended disturbance of magnetic field, i.e. on the magnetic field gradients. In the experiment, only diffusion along the magnetic field gradient, $\boldsymbol{G}$, is measured and

$$\boldsymbol{G} = \boldsymbol{\nabla B_0} = \frac{\partial B_0}{\partial x}\mathbf{i} + \frac{\partial B_0}{\partial y}\mathbf{j} + \frac{\partial B_0}{\partial z}\mathbf{k}. \tag{1.18}$$

The gradient reassures the spatially dependent spin precession frequency, $\omega(\boldsymbol{r})$, given by

$$\omega(\boldsymbol{r}) = \omega_0 + \gamma(\boldsymbol{G} \cdot \boldsymbol{r}). \tag{1.19}$$

Microscopically, molecular self-diffusion can be pictured as the displacement composed of discrete hops separated by the time step τ_s, so that in the time $t = n\tau_s$ molecule does n jumps. If we denote ξ for the root mean square (r.m.s.) displacement in one dimension and a_i for a random number equal to ±1, then the displacement along an arbitrary axis is

$$L(n\tau_s) = \sum_{i=1}^{n} \xi a_i \tag{1.20}$$

and r.m.s. displacement along this axis is

$$< L^2(n\tau_s) >= n\xi^2. \tag{1.21}$$

Defining self-diffusion coefficient as

$$D = \frac{\xi^2}{2\tau_s} \tag{1.22}$$

ones obtain the formula on r.m.s. displacement, which is known as Einstein-Smoluchowski equation:

$$\langle Z^2(t) \rangle = 2dDt, \tag{1.23}$$

where $\langle Z^2(t) \rangle$ is the r.m.s. displacement of molecules after the time t and d is number of diffusion dimensions.

Next, local Larmor frequency in (19) can be presented as

$$\omega(n\tau_s) = \gamma B_0 + \gamma G \sum_{i=1}^{n} \xi a_i \tag{1.24}$$

and the cumulative phase angle change after time t is

$$\Delta\phi(t) = \gamma G \xi \tau_s \sum_{i=1}^{n} (n + 1 - i) a_i. \tag{1.25}$$

Phase modulation of transverse magnetization due to diffusional motion can be evaluated by the determination of the coefficient $\overline{\exp(\mathrm{i}\Delta\phi)}$ assuming Gaussian phase distribution, $P(\Delta\phi)$, from:

$$\overline{\exp(\mathrm{i}\Delta\phi)} = \int_{-\infty}^{\infty} P(\Delta\phi) \exp(\mathrm{i}\Delta\phi)\, \mathrm{d}(\Delta\phi), \tag{1.26}$$

which yields

$$\overline{\exp(\mathrm{i}\Delta\phi)} = \exp\left(-\frac{\overline{\Delta\phi^2}}{2}\right), \tag{1.27}$$

and assuming large number of steps, n, and by using (25) we get

$$\overline{\Delta\phi^2} = \frac{1}{3}\gamma^2 G^2 \tau_s^2 \xi^2 n^3. \tag{1.28}$$

Substituting (22) and using (23) for one dimension case ($d = 1$), we obtain the signal attenuation due to the self-diffusion in the presence of steady gradient

$$\overline{\exp(\mathrm{i}\Delta\phi)} = \exp\left(-\frac{1}{3}\gamma^2 G^2 D t^3\right). \tag{1.29}$$

For the spin-echo pulse sequence in steady gradient (π-pulse in the middle of the distance between $t = 0$ and t) the net phase shift is equal to

$$\overline{\Delta\phi^2} = \frac{1}{12}\gamma^2 G^2 D (TE)^3, \tag{1.30}$$

where TE is echo time, while for pulsed-gradient spin echo sequence (PGSE) (gradient pulses with duration δ on the both sides of the π-pulse and separated by the time interval of Δ instead of steady gradient)

$$\overline{\Delta\phi^2} = 2\gamma^2 G^2 \delta^2 D \left(\Delta - \frac{\delta}{3}\right). \tag{1.31}$$

Using (31) and (27) we obtain the attenuation due to self-diffusion in PGSE, which can be denoted as signal attenuated, S, to signal not attenuated by diffusion, S_0, ratio

$$\frac{S}{S_0} = \exp(-\gamma^2 G^2 \delta^2 D \left(\Delta - \frac{\delta}{3}\right) = \exp(-bD), \tag{1.32}$$

which is known as the Stejskal-Tanner equation, where b coefficient is called b-value and determines the strength of the diffusion-weighting in the NMR signal. This equation was derived under the assumption that the magnetic field gradient is time-dependent and independent on the position in space, meaning that the gradient is homogeneous. However, numerous works showed, that magnetic field time-dependent gradients are non-uniform (Bammer et al., 2003; Doran et al., 2005; Du and Parker, 1996; Janke et al., 2004; Krzyżak and Olejniczak, 2015). The theoretical description for non-uniform magnetic field gradients was proposed and called the generalized Stejskal-Tanner equation (Borkowski and Krzyżak, 2018), for which Stejskal-Tanner equation is a special case for homogeneous gradient.

1.6. Magnetization motion description: Bloch and Bloch-Torrey equations

In 1946 Felix Bloch for the first time formulated the problem of the magnetization motion in the effective field coming from the static and oscillating fields. This was made under the assumptions that the magnetization motion is a superposition of a precession in an effective field and relaxation according to (13)-(16). The obtainment of the equations describing magnetization

motion can be commenced from the analysis of the velocity of the magnetization vector tip. In a rotating frame of reference, effective magnetic field is given by

$$\boldsymbol{B} = \left(B_0 + \frac{\omega_1}{\gamma}\right)\mathbf{k} + B_1\mathbf{i}. \tag{1.33}$$

Velocity coordinates in the precession motion can be determined using (9) and (33), which gives

$$\left[M_y(\gamma B_0 + \omega_1), M_z\gamma B_1 - M_x(\gamma B_0 + \omega_1), -M_y\gamma B_1\right], \tag{1.34}$$

while in relaxation motion using (14) and (16), which gives

$$\left[-\frac{M_x}{T_2}, -\frac{M_y}{T_2}, -\frac{M_z - M_0}{T_1}\right]. \tag{1.35}$$

Vector sum yields

$$\frac{d}{dt}M_x = M_y(\gamma B_0 + \omega_1) - \frac{M_x}{T_2}, \tag{1.32a}$$

$$\frac{d}{dt}M_y = -M_x(\gamma B_0 + \omega_1) + \gamma B_1 M_z - \frac{M_y}{T_2}, \tag{1.36b}$$

$$\frac{d}{dt}M_z = -M_y\gamma B_1 - \frac{(M_z - M_0)}{T_1}, \tag{1.36c}$$

which are known as Bloch equations (Bloch, 1946).

In 1956 Henry C. Torrey generalized Bloch equations (36) by adding the contribution of the self-diffusion of magnetization. He introduced diffusion current density of magnetization concept. First, in arbitrarily chosen x axis of the laboratory frame general formula for diffusion current density was shown, which contained the drift velocity $\boldsymbol{V}$. Applying formulas on the force acting on spins (derivative of potential energy of magnetic moments in external magnetic field $\boldsymbol{B_0}$) and Einstein's conductivity, $K = \frac{kT}{D}$, the diffusion currents parallel (+) and anti-parallel (-) to x axis were given as

$$\boldsymbol{j}_{\pm} = \pm\left(\frac{D}{kT}\right) n_{\pm}\nabla B_x - D\nabla n_{\pm}, \tag{1.37}$$

where $n_{\pm}$ denotes for parallel (+) and anti-parallel (-) to x axis spins, k is the Boltzmann's constant and T is temperature, and then, the diffusion current of the M_x were given by

$$\mu(\boldsymbol{j}_+ - \boldsymbol{j}_-) = -D\nabla(M_x - M_{0x}), \tag{1.38}$$

where M_{0x} is the x component of magnetization in thermal equilibrium.

Then, the rate of increase of the x component of magnetic moment in the volume element Δv were calculated as

$$\int \left(\frac{\partial M_x}{\partial t}\right)_D dv = \nabla \cdot D\nabla(M_x - M_{0x})\Delta v. \tag{1.39}$$

Dividing by the volume element and repeating the analysis for the two remaining axes yielded

$$\frac{\partial M_x}{\partial t} = M_y(\gamma B_0 + \omega_1) - \frac{M_x}{T_2} + \nabla \cdot D\nabla\big(M_x - M_{0y}\big), \tag{1.40a}$$

$$\frac{\partial M_y}{\partial t} = -M_x(\gamma B_0 + \omega_1) + \gamma B_1 M_z - \frac{M_y}{T_2} + \nabla \cdot D\nabla\big(M_y - M_{0y}\big), \tag{1.40b}$$

$$\frac{\partial M_z}{\partial t} = -M_y \gamma B_1 - \frac{(M_z - M_0)}{T_1} + \nabla \cdot D\nabla(M_z - M_{0z}), \tag{1.40c}$$

which are called Bloch-Torrey equations. It can be seen, that besides the new, self-diffusion term added to each equation, the time derivatives of the magnetization components are partial. This means that they refer to a particular point in space (Torrey, 1956).

1.7. NMR signal

Bloch-Torrey equations can be presented in a vector form as

$$\frac{\partial \boldsymbol{M}(\boldsymbol{r},t)}{\partial t} = \gamma \boldsymbol{M} \times \boldsymbol{B}_0 - \frac{M_x \mathbf{i} + M_y \mathbf{j}}{T_2} - \frac{(M_z - M_0)\mathbf{k}}{T_1} + D\nabla^2 \boldsymbol{M}. \tag{1.41}$$

Transverse magnetization can be defined as a complex number, which in a rotating frame gives

$$M_{xy} = M_x + iM_y \tag{1.42}$$

and using $\boldsymbol{B_0} = \boldsymbol{G} \cdot \boldsymbol{r}$, (38) yields

$$\frac{\partial M_{xy}}{\partial t} = -i\omega_0 M_{xy} - i\gamma(\boldsymbol{G} \cdot \boldsymbol{r})M_{xy} - \frac{M_{xy}}{T_2} + D\nabla^2 M_{xy}. \tag{1.43}$$

In the absence of diffusion, M_{xy} is damped by the T_2 relaxation according to the formula

$$M_{xy} = \phi \exp\left(-i\omega_0 t - \frac{t}{T_2}\right), \tag{1.44}$$

where ϕ represents the magnetization amplitude unattenuated by relaxation. Then, by using (43) and after dropping irrelevant term, one gets

$$\frac{\partial \phi}{\partial t} = -i\gamma(\boldsymbol{G} \cdot \boldsymbol{r})\phi + D\nabla^2 \phi. \tag{1.45}$$

The first component reflects the attenuation due to inhomogeneity, while the second due to translational self-diffusion. The solution is

$$\phi = M_0 A(t) \exp(-i\gamma(\boldsymbol{G} \cdot \boldsymbol{r})t), \tag{1.46}$$

where $A(t)$ is given by (48) (Torrey, 1956). The NMR signal received in a coil is produced by the motion of transverse magnetization, which is a function of position, r, and time, t, described by the general formula containing all kinds of attenuation shown above according to

$$\boldsymbol{M_{xy}}(\boldsymbol{r},t) = A(t)\exp\left[-i\gamma\boldsymbol{r}\cdot\int_0^t \boldsymbol{G}(t')dt'\right]\exp\left(-\frac{t}{T_2}\right), \tag{1.47}$$

where

$$A(t) = \exp\left[-D\gamma^2\int_0^t\left(\int_0^{t'}\boldsymbol{G}(t")dt"\right)^2\ dt'\right]. \tag{1.48}$$

In experimental practice, signal averaging is intended to enhance signal-to-noise ratio (SNR). As a result SNR is increased by $N^{\frac{1}{2}}$, where N is a number of experiments. However, there is a limitation of how often can the experiment be repeated. This is due to the fact, that excitation (the first, magnetization tipping rf pulse) should be performed on a fully-recovered, equilibrium magnetization. If inter-experimental delay (repetition time, TR) is too short, then the effect of partial saturation can be observed. In such case, longitudinal equilibrium magnetization is different than the thermal equilibrium magnetization, and is equal to

$$M_z = M_0\frac{1-\exp\left(-\frac{TR}{T_1}\right)}{1-cos\theta\exp\left(-\frac{TR}{T_1}\right)}, \tag{1.49}$$

where θ is the angle by which the magnetization is tipped by the exciting rf pulse.

2. MAGNETIC RESONANCE IMAGING (MRI)

Magnetic resonance imaging (MRI) relies on the application of additional imaging gradients. At the heart of MRI lies the dependence of Larmor frequency on the location in space of imaged nuclei given by (2.20). Neglecting chemical shifting and velocities of moving spins, NMR signal coming from the small volume element of the sample, dV, where the local spin density is $\rho(\boldsymbol{r})$, is

$$\mathrm{d}S(\boldsymbol{G},t) = \rho(\boldsymbol{r})dVexp(i(\gamma B_0 + \gamma \boldsymbol{G}\cdot\boldsymbol{r})t). \tag{2.1}$$

Given that in phase-sensitive detection rf signal is mixed with the reference oscillation at γB_0 frequency and the signal is detected at the differential frequency, $\gamma \boldsymbol{G}\cdot\boldsymbol{r}$ (heterodyne mixing), signal amplitude can be written as

$$S(\boldsymbol{G},t) = \iiint \rho(\boldsymbol{r})exp(i(\gamma \boldsymbol{G}\cdot\boldsymbol{r})t)\,\mathrm{d}\boldsymbol{r}, \tag{2.2}$$

where d$\boldsymbol{r}$ represents a volume integration. Such integration has a Fourier transformation form, which was more obvious after the introduction of the reciprocal space, described by the vector $\boldsymbol{k}$

$$\boldsymbol{k} = \frac{\gamma \boldsymbol{G}t}{2\pi}, \tag{2.3}$$

which has the unit of m^{-1}. The signal and spin density are conjugate variables, and in the formalism of k-space they can be described as

$$S(\boldsymbol{k}) = \iiint \rho(\boldsymbol{r})exp(i2\pi\boldsymbol{k}\cdot\boldsymbol{r})\,\mathrm{d}\boldsymbol{r}, \tag{2.4}$$

and

$$\rho(\boldsymbol{r}) = \iiint S(\boldsymbol{k})\exp(-i2\pi\boldsymbol{k}\cdot\boldsymbol{r})\,\mathrm{d}\boldsymbol{k}. \tag{2.5}$$

2.1. Selective excitation

Suppose that gradient is longitudinal to the z-axis of the laboratory frame and equal to G_z. The Bloch equations are now

$$\frac{dM_x}{dt} = \gamma M_y G_z z, \tag{2.6a}$$

$$\frac{dM_y}{dt} = \gamma(M_z B_1(t) - M_x G_z z), \tag{2.6b}$$

$$\frac{dM_z}{dt} = -\gamma M_y B_1(t), \tag{2.6c}$$

the solution of which yields the complex signal (2.39), M_{xy} equal to

$$M_{xy} = -\gamma M_0 \exp(-i\gamma G_z z T)\int_{-T}^{T} B_1(t)\exp(-i\gamma G_z z t)\,\mathrm{d}t, \tag{2.7}$$

where the integral is a Fourier transform (spectrum) of an excitation RF pulse with a duration from $-T$ to T. Equation (2.7) tells us that i) the NMR signal is proportional to the amplitude of the RF spectrum at plane z, ii) spins at z have the net phase shift of $\gamma G_z z T$. Due to its result on the NMR signal, G_z is called slice-selective gradient.

In reality, selected slice will have a certain thickness of Δz, which will impose the usage of bandwidth term instead of a single frequency value. The bandwidth can be defined as

$$\Delta\omega = \gamma \Delta z G_z, \tag{2.8}$$

and if it is the same in case of an RF pulse, then the slice of thickness Δz can be excited.

2.2. Slice image reconstruction

After the slice excitation, two-dimensional (2D) image reconstruction can be done by the $\boldsymbol{k}$-space sampling. Fourier transform of the $\boldsymbol{k}$ -space gives the image. $\boldsymbol{k}$-space sampling requires two additional gradients in the slice plane, G_x and G_y, and is performed for finite number of points, which determines the image matrix. Matrix can be distributed based on the Cartesian or polar coordinates. In terms of the theory, Cartesian raster is simpler and known as Fourier imaging. In Fourier imaging x and y coordinates are the directions of signal readout and phase encoding, respectively. Therefore, G_x and G_y are called "read" (or frequency encoding) and phase encoding gradients. Those gradients encode the position of a group of spins by imparting the frequency and phase modulation to the NMR signal. Using (2.4), signal is

$$S(k_x, k_y) = \int_{-ST/2}^{ST/2} \int_{-\infty}^{\infty} \int_{-\infty}^{\infty} \rho(x, y, z) \exp\left(i2\pi\left(k_x x + k_y y\right)\right) \mathrm{d}x\, \mathrm{d}y\, \mathrm{d}z, \tag{2.9}$$

where ST is slice thickness. The image is reconstructed via inverse Fourier transformation of (2.9)

$$\rho(x, y) = \int_{-\infty}^{\infty} \int_{-\infty}^{\infty} S(k_x, k_y) \exp\left(-i2\pi\left(k_x x + k_y y\right)\right) \mathrm{d}k_x\, \mathrm{d}k_y, \tag{2.10}$$

where the one integral was omitted and $\rho(x, y)$ is the volume spin density averaged normal to the slice.

In (2.9) and (2.10) x and y components of the k-space vector are defined as

$$k_x = \frac{\gamma G_x t_x}{2\pi}, \tag{2.10}$$

$$k_y = \frac{\gamma G_y t_y}{2\pi}, \tag{2.10}$$

where t_x and t_y denote for the two different time periods and association with gradients in x and y direction, respectively, and should not be understood as time coordinates. $\boldsymbol{k}$–space vector's

components determine spatial resolution of an image. It may be user-adjusted by setting number of points in readout direction and phase lines, together with the area ones want to image- field of view (FOV). For k_x and k_y from the range of $-k_{x,max}$ to $k_{x,max}$ and $-k_{y,max}$ to $-k_{y,max}$, respectively,

$$\Delta k_x = \frac{1}{FOV_x}, \tag{2.11}$$

$$\Delta k_y = \frac{1}{FOV_y}, \tag{2.12}$$

where FOV_x and FOV_y are image spatial dimension along x and y axis, respectively. The volume element (voxel) size is $\Delta x \times \Delta y \times \Delta z = ST$, where ST is slice thickness and pixel's width and height can be defined using reciprocal space as

$$\Delta x = \frac{1}{k_{x,max} - (-k_{x,max})} = \frac{1}{k_{FOV,x}}, \tag{2.11}$$

$$\Delta y = \frac{1}{k_{y,max} - (-k_{y,max})} = \frac{1}{k_{FOV,y}}. \tag{2.12}$$

There are numerous ***k***-space sampling schemes (Cartesian, radial, spiral, "zig-zag") and acquisition techniques. The most popular is echo-planar imaging (EPI), which is a fast imaging technique and therefore, it is routinely used in clinical practice. It relies on multiple ***k***-space lines (phases) sampling within a single shot. If the whole ***k*** -space is sampled within a single shot, then the imaging sequence is called "single-shot EPI", otherwise, if several pulses are used to sample the ***k***-space, then the sequence is called "multi-shot EPI".

3. EFFECTS OF RESTRICTIONS

3.1. T_2 Relaxation

The most common pulse sequence for measuring transverse relaxation is Carr-Purcell-Meiboom-Gill's one (CPMG), which relies on the RF pulse tipping the magnetization by 90° ($\frac{\pi}{2}$-pulse) and a series of n π-pulses at times $\tau, 3\tau, 5\tau$, etc., following the $\frac{\pi}{2}$-pulse, up to the time $t = n\tau$. For such pulse sequence, a natural consequence of equation (2.44) is the echo amplitude exponential decay with the effective (experimental) T_2 relaxation time constant, given by

$$\frac{1}{T_2} = \frac{1}{T_{2bulk}} + \frac{1}{3} D\gamma^2 G^2 \tau^2. \tag{3.1}$$

When researchers noticed discrepancies between T_2s of bulk liquids and in confided geometries, such as biological cells, a new theories were developed to correct for them. Initially, they relied on the necessity to change water properties in biological media in order to fit the experimental to theoretical values of transverse relaxation times. In 1979 Browstein and Tarr (Brownstein and Tarr, 1979) presented a theory used to this day, which relied on two relaxation sink mechanisms, that encompassed diffusion (bulk volume sink) and bounding surface interactions (surfacelike sink). Their theoretical considerations resulted in the introduction of the transverse surface relaxivity, ρ_2, concept used nowadays, that they originally called the mean sink strength density over the whole active surface. The theory greatly explained multimodal relaxation in restricted geometries in slow diffusion regime (meaning that the time window of the measurement is adequate for observing the effects of diffusion, otherwise the higher modes amplitude coming from diffusion and surface are too small in comparison to the ground mode associated with the transverse relaxation in the bulk volume). Hence, in restricting geometries spin echoes amplitude decays with the time constant T_2 given by

$$\frac{1}{T_2} = \frac{1}{T_{2bulk}} + \frac{1}{T_{2surface}} + \frac{1}{T_{2diffusion}}, \tag{3.2}$$

where T_{2bulk} is T_2 relaxation unaffected by sink mechanisms and for water (Coates et al., 1999)

$$T_{2bulk} \cong 3\left(\frac{T_K}{298\eta}\right), \tag{3.3}$$

where T_K is temperature and η is viscosity,

$$\frac{1}{T_{2surface}} = \frac{\rho_2 S}{V}, \tag{3.4}$$

where ρ_2 is T_2 surface relaxivity (the strength of the surface to cause additional spins dephasing and echo amplitude decrease) and $\frac{S}{V}$ is surface-area to volume ratio of a confining geometry, and for CPMG the last component is equal to

$$\frac{1}{T_{2diffusion}} = \frac{1}{3} D\gamma^2 G^2 \tau^2 = \frac{D\gamma^2 G^2 (TE)^2}{12}, \quad (3.5)$$

where echo time $TE = 2\tau$.

3.2. T_1 Relaxation

M_{xy} and M_z magnetization components are mutually independent, since i) their initial values can be discretionary settled by the disturbance (such as RF pulse) and ii) their motion is governed by different rules (Hennel, 1966). Moreover, since M_{xy} visibility is governed by the spins coherence maintenance, its lifetime in the presence of disturbances was considered. In case of M_z, diffusion, convection and magnetic field inhomogeneity do not influence its decay and growth. The growth of M_z depends on the surrounding (lattice) of the group of spins, and its ability to disperse kinetic energy through thermal motion (although in room temperatures the influence of longitudinal relaxation on the sample's temperature has not been detected). Therefore, in confined geometries signal decays due to T_1 relaxation occurs according to

$$\frac{1}{T_1} = \frac{1}{T_{1bulk}} + \frac{1}{T_{1surface}}, \quad (3.6)$$

where T_{1bulk} is T_1 relaxation unaffected by sink mechanisms and for water (Coates et al., 1999)

$$T_{1bulk} \approx T_{2bulk}, \quad (3.7)$$

and

$$\frac{1}{T_{1surface}} = \frac{\rho_1 S}{V}, \quad (3.8)$$

where ρ_1 is T_1 surface relaxivity (the strength of the surface to speed up M_z growth and echo amplitude decrease).

3.3. Diffusion

3.3.1. Spin echo free diffusion signal in reciprocal space

The restrictions encountered by the diffusing molecule cause the changes in the displacement probability function ($P(\boldsymbol{r}|\boldsymbol{r}', \Delta)$ may no longer be Gaussian, meaning that Gaussian phase approximation (GPA) is not fulfilled), but also impose time-dependence of diffusion coefficient and characteristic length scales. The total probability of finding a particle at location $\boldsymbol{r}'$ at the time t is given by

$$\Psi(\boldsymbol{r}', t) = \int \Psi(\boldsymbol{r}, 0) P(\boldsymbol{r}|\boldsymbol{r}', t) \mathrm{d}\boldsymbol{r}, \quad (3.9)$$

where $\Psi(\boldsymbol{r},0)$ is the particle density, $\rho(\boldsymbol{r})$. Using $\Psi(\boldsymbol{r}',t)$ approach for the description of self-diffusion seems a good alternative for Fick's law, which describes the diffusion due to particle concentration differences, whereas Fick's law description is possible using (9). If the Fick's spatial derivatives are presented in terms of the displacement probability

$$P(\boldsymbol{r}|\boldsymbol{r}',0) = \delta(\boldsymbol{r}-\boldsymbol{r}'), \tag{3.10}$$

where δ is Dirac's function, then the Fick's first law of diffusion is given by

$$\boldsymbol{J} = -D\nabla P, \tag{3.11}$$

where $\boldsymbol{J}$ is the "conditional probability flux" and D is self-diffusion coefficient, whereas the Fick's second law of diffusion:

$$\frac{\partial P}{\partial t} = -D\nabla^2 P. \tag{3.12}$$

The solution of (3.12) for the free (or unrestricted) diffusion gives

$$P(\boldsymbol{r}|\boldsymbol{r}',t) = (4\pi Dt)^{-\frac{3}{2}} \exp\left[-\frac{(\boldsymbol{r}\prime-\boldsymbol{r})^2}{4Dt}\right]. \tag{3.13}$$

Equation (3.13) can be used to determine the "average propagator" function based on the concept of the dynamic displacement, which delivers the average probability for any particle to have a dynamic displacement $\boldsymbol{R}$ over a time t according to

$$\overline{P(\boldsymbol{R},t)} = \int P(\boldsymbol{r}|\boldsymbol{r}+\boldsymbol{R},t)\rho(\boldsymbol{r})\mathrm{d}\boldsymbol{r} = (4\pi Dt)^{-\frac{3}{2}} \exp\left[-\frac{\boldsymbol{R}^2}{4Dt}\right], \tag{3.14}$$

where $\rho(\boldsymbol{r})$ is particle density function. Introducing reciprocal $\boldsymbol{q}$-space, so that

$$\boldsymbol{q} = \frac{\gamma\delta\boldsymbol{G}}{2\pi}, \tag{3.15}$$

where γ is gyromagnetic ratio, δ is diffusion gradient pulse duration and $\boldsymbol{G}$ is diffusion gradient vector, and assuming "short gradient pulse" (SGP) approximation (the assumption that during the diffusion gradient applied for a time δ, the magnitude of diffusion is nonsignificant compared to the magnitude during Δ- diffusion gradients separation time, which can be denoted as $\Delta \gg \delta$) the echo amplitude in PGSE sequence for *unrestricted diffusion* is given by

$$S(\boldsymbol{q}) = \int \overline{P(\boldsymbol{R},\Delta)} \exp(i2\pi\boldsymbol{q}\cdot\boldsymbol{R})\mathrm{d}\boldsymbol{R}, \tag{3.16}$$

where Δ is magnetic field diffusion gradient separation time, which in SGP can be assumed diffusion time. Solving (3.16) for PGSE of freely diffusing particles, one obtains the analogous formula for r.m.s. displacement, as that in 2.23. Thus, the statistical description of a motion of a spins ensemble is the second method for the derivation of the Einstein-Smoluchowski equation.

This Fourier relation in $\boldsymbol{q}$-space is in resemblance with imaging of spin density, $\rho(\boldsymbol{r})$, in $\boldsymbol{k}$-space (section 3). In this manner it was shown that molecular displacement due to self-diffusion can be an image contrast similarly to spin density. It can be seen that for unrestricted diffusion PGSE signal is sensitive to the averaged propagator, which is independent of the particle's initial position, but the net displacement $\boldsymbol{R}$ during t. This is obviously not true for confining media, where the influence of boundaries on the PGSE signal is expected and hence, $P(\boldsymbol{r}|\boldsymbol{r}', t)$ should be analyzed.

3.3.2. Spin echo attenuation functions for restricted diffusion

As shown by Tanner and Stejskal (Tanner and Stejskal, 1968), that adapting heat diffusional transport model and assuming boundary condition $P(\boldsymbol{r}|\boldsymbol{r}', t) = 0$ at the edge of restriction, the diffusion propagator inside the laminar system (diffusion between two parallel, infinite barriers separated by the distance a):

$$P(\boldsymbol{r}|\boldsymbol{r}', t) = (4\pi a D t)^{-\frac{3}{2}} \exp\left[-\frac{(\boldsymbol{r}'-\boldsymbol{r})_{||}^2}{4Dt}\right] \times \left[1 + 2\sum_{n=1}^{\infty} \exp\left(-\frac{n^2\pi^2 D t}{a^2}\right) \cos\left(\frac{n\pi \boldsymbol{r}'_{\perp}}{a}\right) \cos\left(\frac{n\pi \boldsymbol{r}_{\perp}}{a}\right)\right], \tag{3.17}$$

where subscripts $||$ and $\perp$ denote for position vector in the direction parallel and perpendicular to the barriers. The attenuation of spin echo resulting from the diffusion in laminar system is

$$S(\boldsymbol{q}) = \exp\left(-4\pi^2 \boldsymbol{q}_{||}^2 D\Delta\right) \left\{\frac{2[1-\cos(2\pi \boldsymbol{q}_{\perp} a)]}{(2\pi \boldsymbol{q}_{\perp} a)^2} + 4(2\pi \boldsymbol{q}_{\perp} a)^2 \sum_{n=1}^{\infty} \exp\left(-\frac{n^2\pi^2 D\Delta}{a^2}\right) \frac{1-(-1)^n \cos(2\pi \boldsymbol{q}_{\perp} a)}{[(2\pi \boldsymbol{q}_{\perp} a)^2 - (n\pi)^2]^2}\right\}, \tag{3.18}$$

which is an exact solution for a given geometry. However, it is easier to analyze the problem of restricted diffusion using two diffusion limiting signal behavior: short-time $\left(\Delta \ll \frac{a^2}{2D}\right)$ and long-time $\left(\Delta \gg \frac{a^2}{2D}\right)$ limits. The solution for different geometries are shown in table 1.

Table 1. Spin echo attenuation functions in short- and long-time diffusion limits in different geometries of size a, for diffusion sensitizing gradient perpendicularly to the boundary and assuming SGP (laminar, rectangular) or GPA (spherical).

Confining geometry	**Short-time limit** $\left(\boldsymbol{\Delta} \ll \frac{\boldsymbol{a^2}}{\boldsymbol{2D}}\right)$	**Long-time limit** $\left(\boldsymbol{\Delta} \gg \frac{\boldsymbol{a^2}}{\boldsymbol{2D}}\right)$
Laminar	$S(q) = \exp(-4\pi^2 q^2 D\Delta)$	$S(q) = \frac{2[1-\cos(2\pi qa)]}{(2\pi qa)^2}$
Rectangular	$S(q) = \exp(-4\pi^2 q^2 D\Delta)$	$S(q) = \frac{2[1-\cos(2\pi qa)]}{(2\pi qa)^2}$
Spherical	$S(q) = \exp(-4\pi^2 q^2 D\Delta)$	$S(q) = \exp\left(-4\pi^2 q^2 \left(\frac{1}{5}a^2\right)\right)$

Long-time limit can be also investigated for small $2\pi \boldsymbol{q} a \ll 1$ or $G \ll \frac{1}{\gamma \delta a}$ (table 2).

Table 2. Long-time limit for the further limit imposed on $\boldsymbol{q}a$, so that $2\pi \boldsymbol{q} a \ll 1$ in different confining geometries having size a.

Confining geometry	**Long-time limit for** $2\pi \boldsymbol{q} a \ll 1$ **limit**
Laminar	$S(q) \approx 1 - \frac{1}{12}(2\pi qa)^2 \approx \exp\left(-\gamma^2\delta^2 G^2 D_{eff}\Delta\right), D_{eff} = a^2/12\Delta$
Rectangular	$S(q) \approx 1 - \frac{1}{12}(2\pi qa)^2 \approx \exp\left(-\gamma^2\delta^2 G^2 D_{eff}\Delta\right), D_{eff} = a^2/12\Delta$
Spherical	$S(q) = \frac{9[2\pi qa\cos(2\pi qa) - \sin(2\pi qa)\,]^2}{(2\pi qa)^6}$

Spin echo attenuation formula for all geometries can be summarized as (Åslund and Topgaard, 2009)

$$\ln(S) = -2\gamma^2 G^2 \sum_{m=1}^{\infty} \frac{1}{\alpha_m^2\left(\alpha_m^2 R^2 + 1 - d\right)} \times \frac{2\alpha_m^2 D_0 \delta - 2 + 2L(\delta) + 2L(\Delta) - L(\Delta-\delta) - L(\Delta+\delta)}{\left(\alpha_m^2 D_0\right)^2}, \quad (3.19)$$

where $L(t) = \exp(\alpha_m^2 D_0 t)$, d is the number of geometry dimensions (d=1, 2 and 3 for planes, cylinder and sphere, respectively), R is the half of the distance between restriction boundaries and α_m is m-th root of the n-th order Bessel function of the first kind given by

$$J_{\frac{d}{2}}(\alpha_m R) - \alpha_m R J_{1+\frac{d}{2}}(\alpha_m R) = 0. \tag{3.20}$$

The restriction size can be obtained from the r.m.s. displacement $< Z(\delta, t_d)^2 >$ at weak gradients, where t_d is diffusion time, obtained after inserting (3.19) to

$$< Z(\delta, t_d)^2 >= -\frac{2}{\gamma^2 \delta^2} \lim_{G \to 0} \frac{\partial \ln(E)}{\partial G^2}, \tag{3.21}$$

whereas some limits allowed the simplification of the exact solution:

1) $\delta \ll \frac{R^2}{D_0} \Rightarrow \langle Z(\delta, t_d)^2 \rangle = \sum_{m=1}^{\infty} \frac{1 - L(t_d)}{\propto_m^2 (\propto_m^2 R^2 + 1 - d)}$ (3.22)

2) $t_d \ll \frac{R^2}{D_0} \Rightarrow \langle Z(\delta, t_d)^2 \rangle = 2 D_0 t_d$ (3.23)

3) $t_d \gg \frac{R^2}{D_0} \Rightarrow \langle Z(\delta, t_d)^2 \rangle = 8 \sum_{m=1}^{\infty} \frac{1}{\propto_m^2 (\propto_m^2 R^2 + 1 - d)} \times \frac{\propto_m^2 D_0 \delta - 1 + L(\delta)}{(\propto_m^2 D_0 \delta)^2}$ (3.24)

4) $\delta \gg \frac{R^2}{D_0}, t_d \gg \frac{R^2}{D_0} \Rightarrow \langle Z(\delta, t_d)^2 \rangle = C \frac{R^4}{D_0 \delta}$ (3.25)

5) $\delta \ll \frac{R^2}{D_0}, t_d \gg \frac{R^2}{D_0} \Rightarrow \langle Z(\delta, t_d)^2 \rangle = \frac{2}{2 + d} R^2,$ (3.26)

where in 4) C is a constant dependent on the geometry, and $C = \frac{8}{15}, \frac{7}{24}$ and $\frac{32}{175}$ for planar, cylindrical and spherical geometry, respectively.

3.4. Time-dependent diffusion coefficient (TDDC) in porous systems

3.4.1. Short-time diffusion behavior

As shown by the Einstein-Smoluchowski equation diffusion coefficient is dependent on the observation time. The above formulas showed, that spin echo signal attenuation due to self-diffusion is therefore also dependent on time. Preservation of SGP approximation allows the signal to be dependent on the diffusion time, which can be assumed to be $t_d = \Delta$. Finite pulse duration is possible, but then the echo amplitude attenuation is governed by the more complicated formulas with simplified long-time limits. Therefore, in this section the time-dependence of spin echo signal in diffusion-sensitive measurements will be analyzed in terms of general diffusion time, t_d, which also accounts for the finite magnetic field diffusion-sensitizing gradient pulse.

Reflecting boundaries

Preserving $\boldsymbol{q}$-space terminology, PGSE signal amplitude in a pore volume V is

$$S(\boldsymbol{q},t) = \frac{1}{V}\int \mathrm{d}\boldsymbol{r}\mathrm{d}\boldsymbol{r}' \exp\left(i\boldsymbol{q}\cdot(\boldsymbol{r}-\boldsymbol{r}')\right) P(\boldsymbol{r}-\boldsymbol{r}',t), \tag{3.27}$$

where diffusion propagator satisfies equation (3.12), but for the sake of time-dependence analysis self-diffusion coefficient of a free liquid will be denoted as D_0 and perfectly reflecting pore boundary will be assumed. The analysis of the spectrum and eigenfunctions of (3.12) delivers the information about the influence of restricting barriers. In short-time limit, $\sqrt{D_0 t_d} \ll a$, where a is a pore size, only particles originating at $\boldsymbol{r}$ close to the pore wall with surface area of S will experience the contact with the wall (Fig. 2). Thus, the fraction of random walkers experiencing restricted diffusion instead of the free diffusion is

$$\frac{\sqrt{D_0 t_d}S}{V}. \tag{3.28}$$

Due to this fraction, the observed TDDC, $D_{app}(t_d)$ slightly decreases according to (Mitra et al., 1993)

$$\frac{D_{app}(t_d)}{D_0} = 1 - \frac{4}{3d\sqrt{\pi}}\frac{\sqrt{D_0 t_d}S}{V} - \left(\frac{1}{4d}\frac{S}{V}H\right) D_0 t_d + O\left((D_0 t_d)^{\frac{3}{2}}\right), \tag{3.29}$$

where d is again spatial dimension of confining geometry, i.e. pore, and

$$H = \frac{1}{S}\int \mathrm{d}\sigma \left[\frac{1}{R_1} + \frac{1}{R_2}\right] \tag{3.30}$$

is the mean curvature averaged over the smooth parts of the surface, R_1 and R_2 are the principal radii of the curvature at each point on the solid-pore space interface.

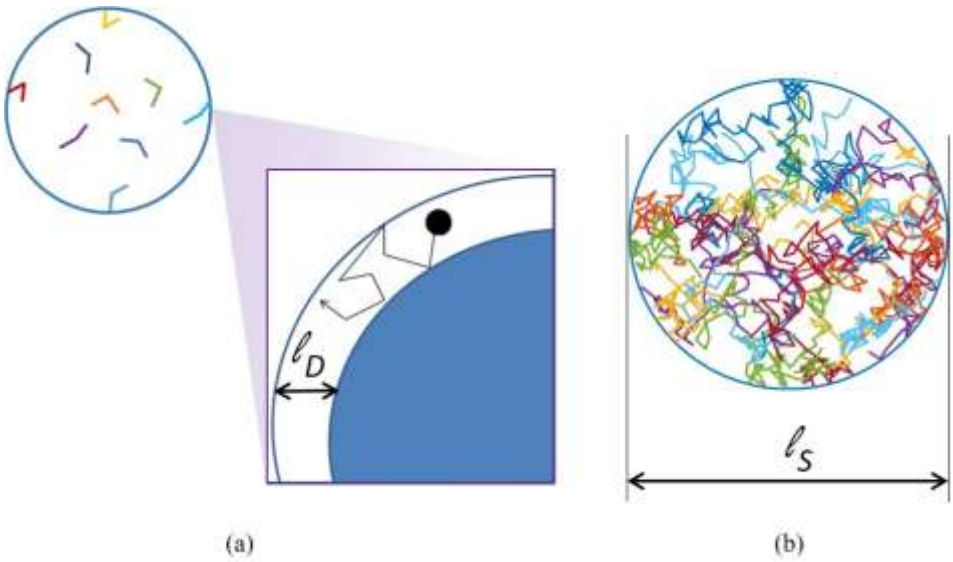

Fig. 2. Schematic representation of diffusion in a short- (a) and long-time limit (b). Random walkers paths are presented within a single circular pore. Based on the r.m.s. displacement of particles, diffusion (ℓ_D) and structural (ℓ_S) characteristic length scales are depicted.

Partially absorbing boundaries

Partially absorbing pore walls can be depicted as boundaries with a certain surface relaxivity, ρ, due to which the number of random walkers is not preserved. The analysis of the surviving particles (those who did not experienced surface absorption) has to consider magnetization sinks. In this case, the short-time behavior is described as (Mitra et al., 1993)

$$\frac{D_{app}(t_d)}{D_0} = 1 - \frac{4}{3d\sqrt{\pi}}\frac{\sqrt{D_0 t_d}S}{V} - \left(\frac{1}{4d}\frac{S}{V}H + \frac{1}{2d}\frac{\rho S}{V}\right)D_0 t_d + O\left((D_0 t_d)^{\frac{3}{2}}\right), \tag{3.31}$$

where ρ is surface relaxivity.

3.4.2. Long-time diffusion behavior

Long-time regime is more complicated, since in a pore particles cannot diffuse freely. However, porous diffusion propagator can be thought as a Gaussian modulated by the presence of excluded regions (solid phase, for example rock matrix, grains, etc.), for which the ansatz was proposed (Mitra et al., 1992)

$$P(\boldsymbol{r}-\boldsymbol{r}', t_d) = \frac{C(t_d)}{(4\pi D_1(t_d)t_d)^{\frac{d}{2}}}\exp\left(-\frac{(\boldsymbol{r}-\boldsymbol{r}')^2}{4D_1(t_d)t_d}\right)S(\boldsymbol{r}-\boldsymbol{r}'), \tag{3.32}$$

where $C(t_d)$ is a normalization constant, $D_1(t_d)$ is an effective width of the Gaussian propagator and $S(\boldsymbol{r}-\boldsymbol{r}')$ is the connected pore-space structure function defined as

$$S(\boldsymbol{r}-\boldsymbol{r}') = \frac{1}{V}\int \mathrm{d}\boldsymbol{R}\chi(\boldsymbol{r}+\boldsymbol{R})\chi(\boldsymbol{r}'+\boldsymbol{R}), \tag{3.33}$$

where $\chi(\boldsymbol{r})$ is characteristic function equal to 1 and 0 for the pore and solid space, respectively. The ansatz was verified and proved to model the diffusion propagator in porous media for the whole range of diffusion time and all wavelength scales.

In long-time regime, $D_{app}(t_d)$ approaches the asymptotic value D_{eff}. In disordered porous systems, the long-time behavior was found to be (Latour et al., 1993)

$$\frac{D_{app}(t_d)}{D_0} = \alpha + \frac{\beta_1}{t_d} + \frac{\beta_2}{t_d^{3/2}}, \tag{3.34}$$

where $\alpha = \frac{1}{\tau}$, where τ is tortuosity and coefficients β_1 and β_2 depend on the microgeometry detail and cannot be predicted. In geological systems, porous structure can be understood as a pore space in a rock matrix (or as a solution of fluid and reflecting grains). For such media, long-time diffusion coefficient $D_{eff} \cong D_0\alpha$, and $\alpha = \left(1 - \left(\frac{f}{2}\right)\right), \beta_1 = \frac{(fa^2)}{4D_0}$ and $\beta_2 = \frac{f}{4\sqrt{\pi}}\left(\frac{a^2}{D_0}\right)^{\frac{3}{2}}$, where f is the volume fraction of the spherical grains having a size of a (De Swiet and Sen, 1996).

Other relations for D_{eff} have been proposed for biological cells systems, for example

$$\frac{1}{D_{eff}} = \frac{1}{D_0} + \frac{1}{Pa}, \tag{3.35}$$

where P is permeability of a periodic array of parallel barriers with spacing equal to a. However, the inaccuracy of the model results from the fact, that $D_{eff} \to 0$, when $P \to 0$. Therefore, the permeability of biological cells were rather determined by using alternative methods, such as Kärger model of diffusion (Kärger, 1985) or methods applying effective medium theory (Latour et al., 1994) or the analysis of time-dependent molar fractions.

3.4.3. Intermediate-time diffusion behavior

Intermediate-time diffusion limit is connected to the localization regime (see descriptions below), which was revisited relatively recently. It turned out that localization regime is tricky, mainly it does not exhibit Gaussian phase behavior (Grebenkov, 2007). Since the short- and long-time limits were easier to describe mathematically, the Padé approximant was used to cover the data in the intermediate-time limit (Latour et al., 1993)

$$\frac{D_{app}(t_d)}{D_0} = 1 - \left(1 - \frac{1}{\alpha}\right) \times \frac{c\sqrt{t_d} + \left(1 - \frac{1}{\alpha}\right)\frac{t_d}{\theta}}{\left(1 - \frac{1}{\alpha}\right) + c\sqrt{t_d} + \left(1 - \frac{1}{\alpha}\right)\frac{t_d}{\theta}}, \tag{3.36}$$

where $c = \left(\frac{4}{9\sqrt{\pi}}\frac{S}{V}\right)\sqrt{D_0}$ and θ has dimensions of time.

3.5. Diffusion in systems with multiple regions

It is very common that porous systems contain multiple regions, that have different size and/or diffusion properties. Mostly, such systems exchange spins after a certain lifetime of spins in a region. After adequately long time, spins from all compartments are mixed and in consequence, one effective, averaged self-diffusion coefficient, $\overline{D_{eff}}$, is obtained for the whole system from the single-exponential echo attenuation dependence in SGP

$$S(\Delta, G) = \exp\left(-\gamma^2\delta^2G^2\overline{D_{eff}}\Delta\right). \tag{3.37}$$

This limit in multi-regional systems is also called motional averaging regime.

In a short-time limit, echo attenuation is a linear superposition of a compartment molar fraction-weighted attenuations

$$S(\Delta, G) = \sum_{i=1}^{n} p_i \exp(-\gamma^2\delta^2G^2D_i\Delta), \tag{3.38}$$

where n is a number of compartments, while p_i and D_i are molar fraction and self-diffusion coefficient of the i-th compartment. Gaussian dependence is true, when for a certain value of Δ all compartments are in a so-called free diffusion regime.

Intermediate time behavior is more complex due to spin exchange between compartments occurring during diffusion time or due to magnetization localization effects (Moutal and Grebenkov, 2020). For a two-phase exchanging system Kärger model (Kärger, 1985) can be applied, which is given by

$$\frac{\partial M_1}{\partial t} = -\gamma^2\delta^2G^2D_1M_1 - k_1M_1 + k_2M_2, \tag{3.39a}$$

$$\frac{\partial M_2}{\partial t} = -\gamma^2\delta^2G^2D_2M_2 - k_2M_2 + k_1M_1, \tag{3.39b}$$

where "–" sign denotes for spins escaping from a given compartment, while "+" those entering this compartment, and k_i is the exchange rate for i-th compartment, which is defined as

$$k_i = \frac{1}{\tau_i}, \tag{3.40}$$

where τ_i is a mean lifetime of spins in i-th compartment. The solution of equations (3.39) gives

$$S(\Delta) = p_1' \exp(-\gamma^2\delta^2G^2D_1'\Delta) + p_2' \exp(-\gamma^2\delta^2G^2D_2'\Delta), \tag{3.41}$$

where

$$D_1' = \frac{1}{2}\left\{D_1 + D_2 + \frac{1}{\gamma^2\delta^2G^2}\left(\frac{1}{\tau_1} + \frac{1}{\tau_2}\right) - \left[\left[D_2 - D_1 + \frac{1}{\gamma^2\delta^2G^2}\left(\frac{1}{\tau_1} - \frac{1}{\tau_2}\right)\right]^2 + \frac{4}{\gamma^4\delta^4G^4\tau_1\tau_2}\right]^{\frac{1}{2}}\right\}, \tag{3.42a}$$

$$D_2' = \frac{1}{2}\left\{D_1 + D_2 + \frac{1}{\gamma^2\delta^2G^2}\left(\frac{1}{\tau_1} + \frac{1}{\tau_2}\right) + \left[\left[D_2 - D_1 + \frac{1}{\gamma^2\delta^2G^2}\left(\frac{1}{\tau_1} - \frac{1}{\tau_2}\right)\right]^2 + \frac{4}{\gamma^4\delta^4G^4\tau_1\tau_2}\right]^{\frac{1}{2}}\right\}, \tag{3.42b}$$

$$p_2' = \frac{1}{D_2' - D_1'}(p_1D_1 + p_2D_2 - D_1'), \tag{3.42c}$$

$$p_1' = 1 - p_2'. \tag{3.42d}$$

3.5.1. Identification of a diffusion regime

It can be seen that depending on a diffusion time, NMR diffusion-sensitive signal attenuation is described by different models. The choice of the appropriate model can be made based on the values of three characteristic scales:

- diffusion length, $l_D = \sqrt{D_0 t_d}$, (3.43)

- dephasing length, $l_G = \left(\frac{D_0}{\gamma G}\right)^{\frac{1}{3}}$, (3.44)
- restriction length, l_S. (3.45)

The shortest of the lengths indicates that the system is in the associated regime. Free diffusion, localization and motional averaging regimes occur, when the shortest is the diffusion, dephasing and restriction length, respectively. In the presence of boundaries, one more characteristic length can be defined as

$$l_R = \frac{D_0}{\rho}, \tag{3.46}$$

where ρ is surface relaxivity. l_R is called relaxation length and may be used instead of l_S, since it is a distance that the spin has to travel near the boundary to experience surface relaxivity, which results in a magnetization reduction.

4. DIFFUSION TENSOR IMAGING

Self-diffusion coefficient, D, in the equations shown in the previous chapters carries different kind of information depending on the system for which it was determined. In isotropic media, single value of D fully describes the diffusion of molecules in a fluid. Moreover, self-diffusion is independent on the diffusion-sensitizing gradient, $\boldsymbol{G_d}$, direction, since there is equal probability of molecules travelling in each direction and the r.m.s. displacement for diffusion time $t_d \to \infty$ is equal for each direction (Einstein-Smoluchowski equation). This is in opposition to anisotropic systems, in which the r.m.s. displacement for diffusion time $t_d \to \infty$ is dependent on a chosen direction. Therefore, a complete description of a diffusion in anisotropic media requires the introduction of a diffusion tensor, $\boldsymbol{D}$, defined as

$$\boldsymbol{D} = \begin{pmatrix} D_{xx} & D_{xy} & D_{xz} \\ D_{xy} & D_{yy} & D_{yz} \\ D_{xz} & D_{yz} & D_{zz} \end{pmatrix}, \tag{4.1}$$

where D_{ij} are diffusion tensor components and x, y, z are laboratory frame axes. It is symmetric 3x3 matrix and therefore, it requires at least six diffusion-weighted images (DWIs) along non-collinear $\boldsymbol{G_d}$ directions. The diffusion tensor eigenfunction

$$\boldsymbol{D}\varepsilon_i = \lambda_i \varepsilon_i = \lambda_i \mathbf{I} \varepsilon_i, \tag{4.2}$$

where i={1, 2, 3}, ε_i is i-th eigenvector and λ_i is i-th eigenvalue, can be presented in a matrix form

$$\begin{pmatrix} D_{xx} & D_{xy} & D_{xz} \\ D_{xy} & D_{yy} & D_{yz} \\ D_{xz} & D_{yz} & D_{zz} \end{pmatrix} \begin{pmatrix} \varepsilon_{1x} & \varepsilon_{2x} & \varepsilon_{3x} \\ \varepsilon_{1y} & \varepsilon_{2y} & \varepsilon_{3y} \\ \varepsilon_{1z} & \varepsilon_{2z} & \varepsilon_{3z} \end{pmatrix} = \begin{pmatrix} \varepsilon_{1x} & \varepsilon_{2x} & \varepsilon_{3x} \\ \varepsilon_{1y} & \varepsilon_{2y} & \varepsilon_{3y} \\ \varepsilon_{1z} & \varepsilon_{2z} & \varepsilon_{3z} \end{pmatrix} \times \begin{pmatrix} \lambda_1 & 0 & 0 \\ 0 & \lambda_2 & 0 \\ 0 & 0 & \lambda_3 \end{pmatrix} \tag{4.3a}$$

$$\boldsymbol{DE} = \boldsymbol{E\Lambda}, \tag{4.3b}$$

where $\boldsymbol{E}$ and $\boldsymbol{\Lambda}$ are eigenvectors and eigenvalues matrices, respectively. Because three eigenvectors are orthonormal, then $\boldsymbol{E}$ can be treated as rotation matrix, meaning that

$$(\boldsymbol{E^{-1}} = \boldsymbol{E^T}). \tag{4.4}$$

This allows the determination of a diagonal tensor, $\boldsymbol{\Lambda}$, using

$$\boldsymbol{E^T E\Lambda} = \boldsymbol{\Lambda} = \boldsymbol{E^T DE}, \tag{4.5}$$

which is diffusion tensor in a geometry-based frame of reference. The most popular diffusion tensor visualization is diffusion ellipsoid, which is constructed by encompassing the whole trajectory of moving molecules. The dimensions of the ellipsoid are given by the three eigenvalues, while its orientation with respect to the laboratory frame of reference by the eigenvectors. Eigenvalues are sorted in the way that the first eigenvalue, λ_1, describes the largest dimension and is sometimes

called longitudinal diffusivity (DL). The second and the third eigenvalue, λ_2 and λ_3, respectively, describe diffusion in a plane transverse to λ_1 and their mean is sometimes called transverse diffusivity (DT).

Assuming GPA, Stejskal-Tanner equation can be formulated for diffusion tensor

$$S = S_0 \exp(-\boldsymbol{b}:\boldsymbol{D}), \tag{4.6}$$

where $\boldsymbol{b}$ is b-matrix

$$\boldsymbol{b} = \begin{pmatrix} b_{xx} & b_{xy} & b_{xz} \\ b_{xy} & b_{yy} & b_{yz} \\ b_{xz} & b_{yz} & b_{zz} \end{pmatrix}, \tag{4.7}$$

and S is a vector of diffusion-weighted signals (at least six). Recalling PGSE pulse sequence: $\frac{\pi}{2}$-pulse, $\boldsymbol{G_{d,n}}$, π-pulse, $\boldsymbol{G_{d,n}}$, readout, where $\boldsymbol{G_{d,n}}$ is diffusion-sensitizing magnetic field gradient in n-th direction; three time intervals, t_1, t_1^-, t_1^+ and t can be defined, which denote for the π-pulse moment, period before π-pulse, period after π-pulse and echo readout moment, respectively. Given that $\boldsymbol{k}$-space vector in each moment of time, t'

$$\boldsymbol{k}(t')=[k_x(t'), k_y(t'),\ k_z(t')]^T \tag{4.8}$$

and

$$\boldsymbol{k}(t_1^-) = \gamma \int_0^{t'} \boldsymbol{G}(t")\mathrm{d}t" \ - \ 2H(t' - t_1)\boldsymbol{k}(t_1^-), \tag{4.9}$$

where

$$\boldsymbol{k}(t_1^-) = \gamma \int_0^{t_1} \boldsymbol{G}(t")\mathrm{d}t", \tag{4.10}$$

$H(t)$ is unit step, Heavyside function and $\boldsymbol{G}(t")$ is the total gradient occurring in a given period. Then, the b-matrix can be calculated from

$$\boldsymbol{b}(t) = \int_0^t \boldsymbol{k}(t')\boldsymbol{k}^T(t')\mathrm{d}t', \tag{4.11}$$

which after substituting (4.9) gives

$$\boldsymbol{b}(t) = \gamma^2 \int_0^t \left[\int_0^{t'} \boldsymbol{G}(t")\mathrm{d}t" \ - \ 2H(t' - t_1)\boldsymbol{k}(t_1^-)\right] \times \left[\int_0^{t'} \boldsymbol{G}(t")\mathrm{d}t" \ - \ 2H(t' - t_1)\boldsymbol{k}(t_1^-)\right]^T \mathrm{d}t'. \tag{4.12}$$

Neglecting magnetic field gradients other than diffusion-sensitizing ones, we can write:

$$\boldsymbol{G_{d,n}} = \left(g_x, g_y, g_z\right)^T, \tag{4.13}$$

where

$$g_x^2 + g_y^2 + g_z^2 = 1 \tag{4.14}$$

and relative b_{ij} amplitudes can be calculated from the dot product of normalized amplitudes of gradients, $g_i g_j$, where $i, j = x, y, z$. Thus,

$$\boldsymbol{g} = \boldsymbol{G_{d,n} G_{d,n}^T} = \begin{pmatrix} g_x \\ g_y \\ g_z \end{pmatrix} (g_x \quad g_y \quad g_z) = \begin{pmatrix} g_x^2 & g_x g_y & g_x g_z \\ g_y g_x & g_y^2 & g_y g_z \\ g_z g_x & g_z g_y & g_z^2 \end{pmatrix}, \tag{4.15}$$

$$\boldsymbol{b} = b\boldsymbol{g}, \tag{4.16}$$

$$\boldsymbol{b}:\boldsymbol{D} = b\boldsymbol{g}:\boldsymbol{D}. \tag{4.17}$$

4.1. Systematic errors

A true diffusion tensor is determined from a $\boldsymbol{b}$-matrix given by (4.16) only when the total time-dependent magnetic field gradient from excitation ($t = 0$) to readout ($t = TE$) is equal to $\boldsymbol{G_d}$, which is usually taken to calculations. In diffusion tensor imaging (DTI), in this period there are also slice-selective, frequency and phase encoding gradients, the so-called imaging gradients, $\boldsymbol{G_i}$. Moreover, some other types of unwanted gradient contributions may occur, such as background gradients ($\boldsymbol{G_b}$), eddy currents-driven gradients, non-linear parts of $\boldsymbol{G_d}$ and $\boldsymbol{G_i}$, etc. (which can be denoted as $\boldsymbol{G_n}$). From the definition of $\boldsymbol{b}$-matrix (4.11-4.12), all those components should be integrated and contribute to the $\boldsymbol{b}$-matrices. If not accounted, diffusion tensor is erroneously estimated.

Due to multiple magnetic field gradient components, the total $\boldsymbol{b}$-matrix is also composed of components associated with those gradients, as well as their cross-terms, which directly result from (4.11). Hence, the total $\boldsymbol{b}$-matrix can be written as

$$\boldsymbol{b} = \boldsymbol{b_d} + \boldsymbol{b_i} + \boldsymbol{b_b} + \boldsymbol{b_n} + \boldsymbol{b_{di}} + \boldsymbol{b_{db}} + \boldsymbol{b_{dn}} + \boldsymbol{b_{ib}} + \boldsymbol{b_{in}} + \boldsymbol{b_{bn}}. \tag{4.18}$$

Determination of $\boldsymbol{D}$ from (4.6) is connected to the division of S and S_0 data, that were obtained with and without $\boldsymbol{G_d}$, respectively while all the other components of the total gradient were present in both experiments. Therefore, the division should provide the elimination of $\boldsymbol{b_i}, \boldsymbol{b_b}, \boldsymbol{b_n}, \boldsymbol{b_{ib}}, \boldsymbol{b_{in}}$ and $\boldsymbol{b_{bn}}$. Cross-term $\boldsymbol{b_{di}}$ can be removed by the application of one of the methods: i) applying the refocusing gradients before and after each diffusion and imaging gradient; ii) conducting additional experiments with diffusion gradients having reversed polarity (denoted as S^+ and S^-) and calculating geometrical mean from the two signals ($(S^+S^-)^{1/2}$) before calculating the diffusion tensor. The second method requires two times more of the experimental time.

Another aspect is that the abovementioned correction methods are not always implemented or not applied due to time restrictions. By default, the experimenter is provided the single $\boldsymbol{b}$-matrix by the vendor for the whole imaged volume. Unwanted gradient contributions cause a spatially distributed $\boldsymbol{b}$-matrices. Within this thesis the alternative methodology of reducing systematic errors was used based on the $\boldsymbol{B}$-matrix spatial distribution DTI (BSD-DTI).

4.2. $\boldsymbol{B}$-matrix spatial distribution diffusion tensor imaging

BSD-DTI is a proprietary (Polish, American, European, Japan patents) calibration method used for the elimination of systematic errors in DTI (Krzyżak, 2008). It relies on the DTI of the anisotropic phantom with well-known diffusion properties using exactly the same protocol as for the target object. As described in the patent, in order to determine a single (for one diffusion gradient direction) $\boldsymbol{b}$-matrix, at least six phantom orientations are needed ($\boldsymbol{b}$-matrix is also symmetric and thus, six components has to be estimated, for which six DWIs are required). The procedure begins with placing the phantom in such a way that the phantom's principal axes coincide with the axes of the laboratory frame of reference (diffusion tensor, D_E). A DTI is then performed for N diffusion gradients. Next, the phantom is rotated by known Euler angles so that the tensor of the phantom in the laboratory frame is well known ($D_L = R^{-1}(\Omega_L) D_E R(\Omega_L)$, where D_L is phantom's diffusion tensor in laboratory axes system, $R(\Omega_L)$ is a rotation matrix and $\Omega_\mathrm{L} = (\alpha_L, \beta_L, \gamma_L)$ are Euler angles that define orientations of the principal axes system with respect to the laboratory system) and DTI is repeated for the same N diffusion gradient directions. The "rotation, DTI" procedure is repeated $M - 1$ times delivering $M * N$ equations, where M is the number of phantom orientations and N is a number of diffusion gradient directions (Fig. 3). $\boldsymbol{b}$-matrices, $\boldsymbol{b_n}$, for each direction, n, can be determined by solving a system of equations

$$\begin{aligned} \boldsymbol{\alpha_n} &= -\boldsymbol{b_n D} \\ &\vdots \\ \boldsymbol{\alpha_N} &= -\boldsymbol{b_N D}, \end{aligned} \tag{4.19}$$

where

$$\boldsymbol{\alpha_n} = \begin{bmatrix} \ln\left(\frac{S_{1,n}}{S_{01}}\right) \\ \vdots \\ \ln\left(\frac{S_{M,n}}{S_{0M}}\right) \end{bmatrix}^T, \tag{4.20}$$

$$\boldsymbol{b_n} = \left[b_{nxx}, b_{n,yy}, b_{n,zz}, b_{n,xy}, b_{n,xz}, b_{n,yz}\right], \tag{4.20}$$

$$\boldsymbol{D} = \begin{bmatrix} D_{1xx} & D_{1yy} & D_{1zz} & D_{1xy} & D_{1xz} & D_{1yz} \\ \vdots & \vdots & \vdots & \vdots & \vdots & \vdots \\ D_{Mxx} & D_{Myy} & D_{Mzz} & D_{Mxy} & D_{Mxz} & D_{Myz} \end{bmatrix} \tag{4.20}$$

and n denotes for a given direction and $n = 1, \ldots, N$, where minimum N=6, and $m = 1, \ldots, M$, where minimum M=6.

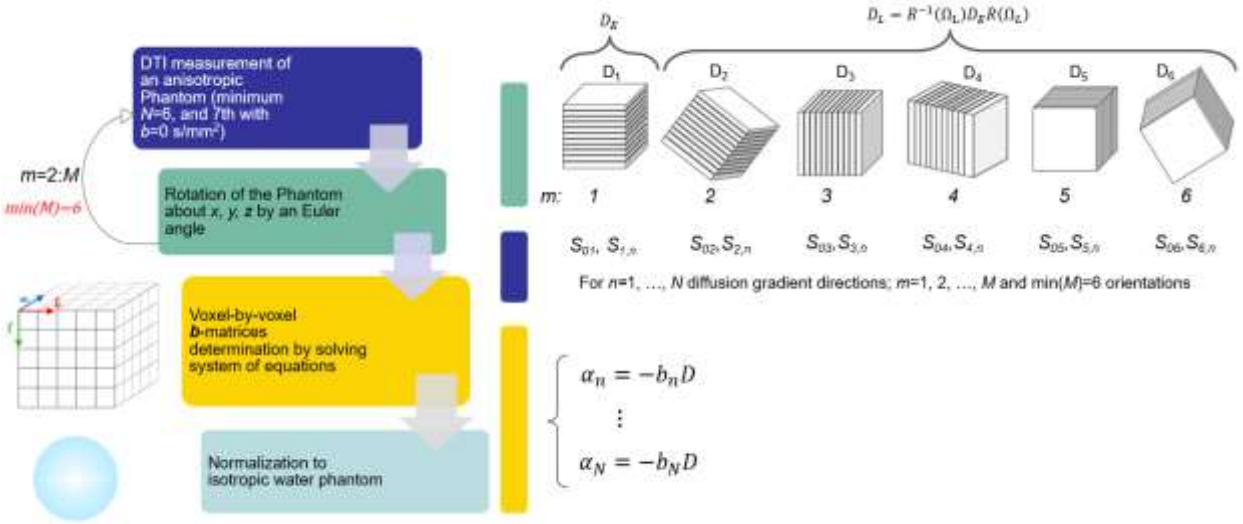

Fig. 3. Schematic representation of a B-matrix spatial distribution diffusion tensor imaging (BSD-DTI) calibration method. Steps in the process chart on the left side correspond to their description or depiction marked by coloristically matching panels on the right side. The description of the symbols can be found in the text.

III. ACHIEVEMENTS OF THE THESIS

The full characterization of porous media encompasses many aspects, such as fluid and compartment characterization, fluid transport, biophysical, biochemical and surface processes. They can be evaluated non-invasively by NMR methods with a proper adjustment of experimental protocol and analysis approach. However, the accuracy of the quantitative microgeometry characterization is diminished in the presence of unwanted effects resulting from the experimental issues, such as magnetic field and magnetic field gradients inhomogeneity or internal gradients resulting from the differences in magnetic susceptibility. They cause significant systematic errors and are intensified for decreasing resolution of geometry being described. Hence, nanoscale structures are more difficult to describe quantitatively than for example microscale ones.

In vitro biological systems are a good research material for testing NMR methods for microstructure characterization, because they are heterogeneous (in terms of size and physicochemical properties), biophysical and biochemical processes take place in them and there are no ethical limits for experiments on them (such as magnetic field strength, test time, etc.). On the other hand, all tissues are also biological porous systems, but their *in vivo* characterization additionally includes physiological processes and also differs due to hardware capabilities. In addition, the properties of the *in vivo* microstructure may change in the event of a disease. More and more modern methods of disease treatment are based on scaffolds or cell therapies. Therefore, an inseparable element of modern medicine is the development of research on both of these paths, i.e. *in vivo* and *in vitro*, in parallel, so that they can meet at some point, for example as a matter of translational medicine. Especially important is the improvement of quantitative analysis, which is an inherent element for the precise tracking, identification and evaluation of the cells *in vivo*, as well as for the accurate monitoring of the effects of tissue treatment.

Another type of natural porous systems are rocks, which are great research material for microstructure study by NMR. Their microgeometry is rather stochastically composed, which distinguishes them from tissues. In addition, rock matrix (the solid material that makes up the bulk of a rock) is composed of the minerals and other components, such as cements, micas, clay minerals, etc., which may introduce complex surface interactions with the pore-filling fluid and the induction of internal gradients caused by the magnetic susceptibility differences. This makes rocks very challenging NMR research material. However, with the proper methodology, many geoscience NMR applications can be found as an alternative research method for rocks, since:

- it is non-destructive, meaning that the rocks can be studied without altering or damaging them,
- it is fast, allowing scientists to acquire data quickly and efficiently,

- it can provide a wide range of information about the internal structure and composition of the rocks, including pore size and shape, total porosity, and saturation,
- it is safe, because it does not involve any hazardous materials or radiation.

Moreover, they can help with a general understanding of fundamental physical processes, as well as develop new mathematical formulas for earth science applications.

Within this thesis, research was focused on developing NMR-based methodologies for a more accurate quantitative characterization of the microstructure, including abovementioned aspects. With the aid of those methodologies, new practical applications of NMR were proposed in the fields of medicine, biophysics, geosciences and image analysis.

1. PROGRESS IN NMR IMAGING OF BIOLOGICAL POROUS SYSTEMS

[A1]: Attempts at the Characterization of In-Cell Biophysical Processes Non-Invasively-Quantitative NMR Diffusometry of a Model Cellular System

The aim of the [A1] work was the investigation of in-cell watery pools in a model cellular system of baker's yeast (*Saccharomyces Cerevisiae*) applying time-dependent diffusion coefficient (TDDC) method and using Mobile Universal Surface Explorer (MoUSE; Magritek, Aachen, Germany) operating in a stray field produced by the permanent magnets in a Halbach configuration.

The motivation for this work was to explore the possibilities of MoUSE in the study of cellular systems. MoUSE works in a high magnetic field gradient (24 T/m) and at the same time allows short gradient "pulses" encoding/decoding diffusion. This allows to obtain very large *b*-values and shorten the diffusion time, while maintaining SGP conditions. This, in turn, makes it possible to study the dynamics of water in nanometric (sub-micrometric) structures and in compartments filled with more viscous/dense fluid or macromolecules solutions (slow diffusion) in all diffusion regimes. Hence, it was expected that cellular organelles may separately contribute to the diffusion signal, which would cause the state-of-the-art upgrade. It should be emphasized, that hitherto, cellular systems were characterized by the two compartments- extra- and intracellular ones.

Diffusion was measured in a 200 μm slice using stimulated spin echo (SSE) pulse sequence, allowing for storing the magnetization along the B_0 magnetic field during the diffusion time (or mixing time), for b=0–597 000 s/mm^2. Then, the applicability of a more parameterized diffusion model than bi-exponential was tested quantitatively and qualitatively (as statistical tests work in favor of a model with more fitting parameters). Both of them were in favor of the three-compartmental model. Next, based on the literature values of organelles sizes and bulk self-

diffusion coefficients in *Saccharomyces Cerevisiae*, TDDCs were simulated for the diffusion times used in experiment. In short-time limit Mitra's relation was used. In the intermediate-time limit TDDCs were calculated from Einstein-Smoluchowski equation, where r.m.s. displacements inside the structures were simulated by Random Walking of 5000 particles assuming perfectly reflecting boundaries in Matlab (The MathWorks Inc., Natick, MA, USA). Step length was chosen to be dependent on the bulk self-diffusion coefficient found in the literature and it determined number of steps. Compartments identification was made by comparing the experimental and simulation data. In the last step, by using simulated TDDCs diffusion signal intensities in structures were simulated for all diffusion times and *b*-values in order to verify which water pool will not be visible in the total signal due to too low intensity or will not contribute to the signal attenuation. This allowed for the final modelling of the signal, in which either two exponents or two exponents with intercept were used in a certain *b*-value range depending on the diffusion time.

Adjustment of the signal attenuation due to diffusion model with the aid of Random Walk simulations helped to improve the characterization of the model cellular system. Very good agreement between literature (diffusion-based, but also biochemical reports) and experimental values was obtained for compartments sizes, self-diffusion coefficients, molar fractions, permeabilities and water lifetime. This study showed that diffusion-weighted spin echo signal obtained with MoUSE can be sensitive to extracellular space, cytoplasm, vacuoles, but also cell walls, nuclei and mitochondria, having sizes down to 0.0792 μm, non-invasively. The proposed methodology can be helpful in the identification and characterization of those structures, but requires more experimental and analytical effort, than the "extracellular/intracellular compartments" analysis. Mainly, in case when cellular organelles are seen experimentally, TDDCs for a given signal component cannot be associated with the same structures for the whole range of diffusion times.

[A2]: Nuclear magnetic resonance footprint of Wharton Jelly mesenchymal stem cells death mechanisms and distinctive in-cell biophysical properties in vitro

The aim of this work was the characterization of Wharton Jelly mesenchymal stem cells (WJMSC) *in vitro* for the purpose of translational medicine concerning regeneration of ischemic damage. Cells characterization is essential for *in vivo* identification and analysis, as well as for monitoring of the effect of cell-based therapies in tissues.

WJMSC were collected from the umbilical cords, cultured, evaluated and measured by NMR method in two low-field systems- with a bore aperture (longitudinal, T_1, and transverse, T_2, relaxation, diffusion-relaxation, $D-T_2$, and T_1-T_2 relaxation correlation measurements) and single-sided one (MoUSE; diffusion measurements of the culture in the Petri dish and cell

suspension in a cylindrical container). This complex approach allowed for in-depth insight into cellular compartments.

The results delivered a set of NMR parameters describing WJMSC. Based on the results from $D - T_2$ experiments on variable cell concentration it was possible to evaluate cells size. Based on the diffusometry of cell suspensions in a cylindrical container, two diffusion signal components were identified. The first one was a mean diffusivity in the extracellular space and in the cytoplasm. Concerning the second component, a good agreement was found between apparent diffusion coefficient for diffusion time equal to 20 ms obtained in the experiment and the one calculated using literature value of WJMSC nucleus radius and bulk self-diffusion coefficient obtained for nuclei in [A1]. This confirmed that the second component came from WJMCS nuclei having radius of 2 μm. This setting also enabled the identification of differences in the diffusional properties of WJMSC depending on the pressing forces proportional to the number of contacting 50 μm-thick layers of cells. In this way, it was shown that by using MoUSE it is possible to study biophysical processes in WJMSC.

WJMSC in cylindrical container after the diffusion measurements were incubated for six days at the room temperature without any culture medium supply. After that time, diffusion measurements were repeated. Self-diffusion for the first component decreased by 1.5-3 times, while for the second one it remained unchanged. When it came to molar fractions, for the first component a visible decrease was again observed, while for the other almost 3 times increased was obtained. This simple analysis exhibited substantial time-related in-cell transitions, reflecting viscoelastic changes due to cell death. It was shown that self-diffusion coefficient can reflect the degree of necrosis and apoptosis, which indicated that diffusion can be proposed as a natural biomarker of cells viability. Apoptosis was reflected in the increase of nuclear component molar fraction, since in the process cells evacuate apoptotic bodies containing nuclear content (DNA). Necrosis was associated with the decrease of the first self-diffusion coefficient connected to extracellular fluid and cytoplasm (increase of density and viscosity of those fluids due to nuclear content evacuation resulting from nuclear envelope damage).

Next, by using simulations of TDDC developed in [A1] it was possible to determine bulk intracellular and cytoplasm self-diffusion coefficients. This was achieved by comparing the simulated data with the experimental ones from the culture setting. Interestingly, cultured WJMSC are characterized by a visibly smaller intracellular self-diffusion coefficient in comparison to cells that WJMSC can differentiate to. The same concerned cytoplasm, suggesting that it is composed of the higher content of dry weight, ions or lipids compared to other cells. This can be a potentially important information and support their identification *in vivo* and exploring their functions, such as tracking the differentiation process.

2. NEW APPLICATIONS FOR MEDICAL NMR IMAGING

[A3]: Diffusion as a Natural Contrast in MR Imaging of Peripheral Artery Disease (PAD) Tissue Changes. A Case Study of the Clinical Application of DTI for a Patient with Chronic Calf Muscles Ischemia

Peripheral artery disease (PAD) is a widespread condition causing impaired muscle function and pain due to ischemia. The disease results from the obstructed arteries, which restricts the oxygenation and nutrition of the muscles. Ischemic muscle tissue evinces muscle cells degradation, protein denaturation, cytoplasm swelling, muscle cell membrane disintegration and hence, evacuation of fluids to the extracellular matrix and in the end gradual necrosis of the muscle. Regeneration of ischemic damages encompasses revascularization through surgical procedure or cell therapies. Within STRATEGMED 2 project, Wharton's Jelly mesenchymal stem cells (WJMSCs) were proposed for the muscles regeneration. They have the ability to directly repair muscle tissue or to act indirectly on it by stimulating the collateral circulation.

Skeletal muscles are composed of elongated muscle fibers surrounded by endomysium and arranged into fiber bundles wrapped by the perimysium. Such composition is a muscle unit-fascicle, while the whole muscle is built from several tightly arranged units surrounded by epimysium. In this way, muscle is a multicompartmental, anisotropic system. Diseased muscles, through the abovementioned effects, disorder the anisotropic structure, for example by the changed fiber density, increased endomysium space (edema) and impaired architecture caused by collateral circulation or fatty infiltration. Hence, in this article DTI was proposed as a technique for the evaluation of the calf muscles status in a patient with PAD in comparison to the healthy control. Muscles were reevaluated in the follow-up examination after the WJMSCs therapy in a double-blind randomized controlled trial (RCT).

76-year-old was offered an experimental method of treatment of the critical ischemia of the right lower limb using WJMSCs after endovascular and surgical methods of revascularization failure. Before medical intervention, T_1-weighted (repetition time, TR =440 ms, echo time, TE=10.8 ms) and T_2-weighted (TR/TE=3800/70 ms) MRI with fat suppression by using a Fast Spin Echo (FSE) sequence, as well as DTI (b-value = $350 \cdot 10^3$ s/mm^2, TR/TE= 5200/64 ms, field of view, FOV=59 × 39 cm^2, Number of Scans, NoS=1, 384 × 300 pixels matrix; slice thickness, ST=8 mm) using spin-echo echo-planar imaging (SE EPI) were conducted (the first patient's examination, E1). Next, the intraarterial and intramuscular injections of CardioCell based on WJMSCs were administered and after 83 days later T_1-weighted and T_2-weighted MRI and DTI were repeated with the same protocol (the second examination, E2). T_1-weighted and T_2-weighted

images were the reference for identifying anatomical structures and gaining complementary physiological information. DTI was calibrated from systematic errors by using B-matrix spatial distribution method (BSD-DTI). BSD-DTI metrics (fractional anisotropy, FA, mean diffusivity, MD and three eigenvalues, λ_1, λ_2, λ_3) were analyzed in three muscles: Gastrocnemius Medialis (GM), Soleus (SOL) and Tibialis Anterior (TA). BSD-DTI conducted in SOL and GM was analyzed qualitatively and quantitatively using also fiber tracts density (FTD) parameter defined as a number of tracts per voxel and averaged through the all voxels within the constant volume in the shape of cylinder.

Results showed that BSD-DTI had an impact on the values of DTI metrics, the greatest one observed for FA, λ_1 and MD in healthy control where standard approach (sDTI, i.e. without calibration) delivered highly underestimated results. Based on the results, the application of BSD-DTI seemed legitimate. For example, the analysis of sDTI would wrongly suggest that healthy control had lower muscles anisotropy than the patient. It was shown that in E1 patient had different course of disease in posterior (SOL, GM) and anterior (TA) compartments. Elevated values of MD, λ_3 and λ_2 in SOL and GM suggested cytoplasm swelling and muscle fibers disintegration increasing endomysium space, respectively. Decreased MD, λ_3 and λ_2 in TA indicated muscle dehydration, loss, fatty infiltration or fibrosis confirmed by MRI. After the medical intervention (E2) BSD-DTI metrics changed- they approached the healthy control for TA and GM, while for SOL the difference is even higher than in E1. This again showed the difference in the course of PAD after treatment between deep and superficial muscles. Tractographic BSD-DTI visualization indicated improved GM and impaired SOL muscles architecture.

Concluding, this article showed the possibility of BSD-DTI as a tool for non-invasive evaluation of calf muscle status in patients with PAD and in healthy control. Those results were based on the case study, hence, the compartmental course of PAD and effects of a double-blind RCT treatment were not verified at the moment of publication. However, the agreement between BSD-DTI metrics with the other MRI techniques outcome, as well as with clinical analysis suggested that diffusion can potentially be proposed as natural marker of PAD and its severity and status.

[A4]: Diffusion tensor imaging as a tool to assess the structure of lower limb muscles invisible on T1- and T2-weighted images in the course of the chronic phase of peripheral artery disease

This article is a continuation of the study of the course of PAD based on BSD-DTI. The whole methodology is exactly the same as for the patient in [A3] (sequences, protocols and interventional procedure). The case study concerned a 76-year-old female patient that exhibited the

following physiological differences of the calf muscles on T_1-weighted (T1WI) and T_2-weighted images (T2WI): significantly smaller fatty infiltration and neoangiogenesis (not able to be seen with the naked eye), strongly hyperintense T_2-weighted signal in all muscles except for GM and a part of SOL; and other differences: sex, follow-up examination after a longer period of time (almost 5 times later than the patient in [A3]).

The main goal of this study was to connect the values of BSD-DTI metrics with the type of change of the muscle structure due to PAD that may be not recognized on T1WI and T2WI. In general, increased fat content in the muscles would be associated with decreased T_1 and increased T_2, while edema with elevated both T_1 and T_2 in comparison to the healthy muscles. DTI, in turn, can deliver more detailed information about the muscle structure and the course of disease. In muscles, it is convenient to analyze the eigenvalues separately and FA, since λ_1 reflects the diffusion along the muscle fibers (thus, called longitudinal diffusivity, DL), λ_2 across the myofiber, λ_3 across the endomysium and FA the overall muscle architecture (for example FA decrease would be associated with the increase of myofiber and endomysium cross-sectional area, but also structure disorder). Thus, DTI can potentially distinguish: intramyocellular (intramuscular) and intermuscular fatty accumulation, sarcoplasm swelling, development of collateral circulation, overall muscle dehydration and atrophy, myofiber necrosis (see Table 3).

Table 3. The potential change of DTI parameters (λ_1 - the first eigenvalue, λ_2 - the second eigenvalue, λ_3 - the third eigenvalue, FA- fractional anisotropy) in the particular courses of PAD with respect to the healthy muscles.

	λ_1	λ_2	λ_3	FA
Intramuscular fatty accumulation	↓/≈	≈	↓	↑
Intermuscular fatty accumulation	↓/≈	↓	≈	↑
Sarcoplasm swelling	≈	↑	↓/≈	↑/↓
Development of collateral circulation	↑	↑	↑	↑/≈
Overall muscle dehydration and atrophy	↓/≈	↓	↓	↑/↓/≈
Myofiber necrosis	≈	↑	≈	↓

In this article, DTI metrics were shown in comparison to the healthy control together with the values from the [A3] to show the differences in metrics that allowed the extraction of more sophisticated details on the disease. Using table 3 it could be seen, that in this case study the dominating effect of PAD during E1 was intramuscular fatty infiltration in SOL, development of collateral circulation in GM and myofiber necrosis and intramuscular fatty accumulation in TA.

Conventional MRI in the follow-up did not exposed visible muscle structure change except for the higher T_1 signal intensity and lower T_2 signal intensity (Figures 1 C and D, respectively in [A4]), which was associated with T_1 decreasing and T_2 increasing (for TA the T_2 change is negligible). Based on these results, edema relief, muscle dehydration and fatty deposit were concluded. More sophisticated details could be potentially inferred from DTI: the progression of intramuscular and development of intermuscular fatty accumulation and dehydration in SOL, the reduction of edema in GM and TA. Fiber tractography showed visibly improved fiber tracts density and direction for TA and GM, while reduced density in SOL. This was in accordance with the DTI metrics.

In conclusion, it was shown that different courses of PAD can be reflected by DTI parameters and confirmed by tractography that delivered information about the architecture integrity. This was possible by the profound analysis of different patients, while T1WI and T2WI did not provide too much details on the physiological mechanisms. Similarly to [A3], at the time of publication, the authors were not informed about the type of treatment used and the clinical assessment of the patient, and they cannot clearly indicate the cause of the improvement/worsening of DTI metrics and tractography in particular muscles.

3. NEW APPLICATIONS OF NMR IMAGING FOR GEOLOGICAL POROUS SYSTEMS

[A5]: Prospects and Challenges for the Spatial Quantification of the Diffusion of Fluids Containing 1H in the Pore System of Rock Cores

In this article, a comprehensive overview of the prospects and challenges of using NMR and MRI to study the diffusion of fluids in rock cores was provided. Obtaining accurate measurements of the diffusion of fluids in rock cores can be difficult due to the complex nature of the rock pore system, which is tortuous and chemically complex. Moreover, NMR measurements can be affected by temperature, pressure, and the presence of other fluids. Nonetheless, NMR is a major method that can provide spatially resolved information about the diffusion of fluids in rock cores, which can be used to better understand the flow of fluids through the rock pore system. The spatial quantification of the diffusion of fluids containing 1H in the pore system of rock cores is an important area of research in the field of geosciences. This topic has been studied extensively in the past two decades, with numerous studies covering a wide range of fluid types, pore systems and rock core geometries. This article aimed to provide an overview of the current state of the art in the field of spatial quantification of the diffusion of fluids containing 1H in the pore system of rock cores and introduce DTI technique and its metrics for the more accurate description of pore microgeometry and rock core sample physical properties.

DTI was performed on a 9.4 T Bruker BioSpec 94/20USR scanner on a carbonate rock core sample from the Upper Permian, Zechstein Limestone (Ca1) formation of West Poland, the Brońsko Reef. High resolution (250 x 250 x 500 μm), reasonably short TE=20 ms, long TR=13 s, 4 scans, 6 diffusion gradient directions and moderate b-value, b=800 s/mm^2, were chosen, which was possible thanks to high magnetic field ensuring reasonable SNR. Complementarily, mercury incjection capillary pressure (MICP), low-field NMR (LF-NMR) relaxometry and micro-computed tomography (μCT) were performed for DTI results verification. For comparison, two anisotropic phantoms with laminar and capillary pores (sizes of 20 and 30 μm, respectively) were examined (a resolution of 470 x 470 x 2000 μm, TE=20 ms, TR=2.5 s, 2 scans, 6 diffusion gradient directions and b=800 s/mm^2). DTI data were analyzed and visualized in the in-house software (BSD-DTI ver. 2.0, AGH, Kraków).

Based on the images with the null diffusion gradient, proton density alike images were obtained for 26 slices delivering three-dimensional (3D) porosity distribution- the first parameter from DTI characterizing rock core sample. Based on the very accurate LF-NMR T_2 relaxometry, the total porosity was equal to 13.9%. Slight underestimation of the total porosity equal to 13.353% was obtained from DTI, which resulted from the signal loss of the species with $T_2 \leq TE$. In the next step, DTI metrics were analyzed in 3D. The average mean diffusivity (MD), the first, second and third eigenvalue (λ_1, λ_2 and λ_3, respectively) and fractional anisotropy (FA) were equal to $1.16\pm0.25\cdot10^{-3}$ mm^2/s, $1.58\pm0.29\cdot10^{-3}$ mm^2/s, $1.14\pm0.27\cdot10^{-3}$ mm^2/s, $0.76\pm0.37\cdot10^{-3}$ mm^2/s and 0.36±0.20, respectively. Standard deviations (SDs) well depict the heterogeneity of the sample. For example, SD of FA was slightly higher than for the regular, laminar phantom, while almost 5 times higher than for capillary phantom. DTI metrics were associated to the effective pore size and pore geometry (three orthogonal dimensions and the degree of anisotropy), which have the following geological meaning: i) they can distinguish among dissolution vugs/large voids (large MD) determining the storage capacity of a reservoir and zones subjected to dolomitization generating intercrystalline porosity (low, unimodal MD); ii) FA together with eigenvalues can distinguish among spherical, elongated and oblate pores, reflecting in carbonates spherical voids, fractures and dissolution channels. The last two types can determine the rock's permeability. The last DTI metric was diffusion tensor tractography, which for rocks has slightly different meaning- tracts no longer reflect the connected pore network, but they rather depict the linkage of connected or unconnected pores along the direction of the most probable fluid escape path. Metric was called principal diffusion tracts (PDT) and is suspected to reflect the permeability tensor (mean FA for the voxels through which the tracts pass, was higher by around 20%, which may suggest the impact of fractures, that determine permeability). Thus, it adds the dynamic information to the proton density 3D distribution.

In the next step, geophysical characterization based on diffusion tensor data was made. Firstly, the pore size distribution (PSD) was determined by using the following workflow: i) the identification of the diffusion regime by estimating $\xi = \frac{D_0 t_d}{d^2}$, where D_0 is bulk diffusion coefficient of water, t_d is diffusion time and d is pore size. It can be seen that this process is dependent on the unknown value of a variable to be determined (pore size). ia) For the experimental parameters, ξ was simulated for the wide range of d; ib) time-dependent diffusion coefficient, $D(t_d)$, was calculated from the Mitra's, Einstein-Smoluchowski and long-time limit formulas when $\xi \ll 1$, $\xi \approx 1$ and $\xi \gg 1$, respectively; ic) $D(t_d)$ allowed the determination of diffusion regimes boundaries; id) Experimental $D(t_d)$ were compared with the simulated ranges of three diffusion regimes and assigned the appropriate one. ii) pore size for each experimental $D(t_d)$ was determined by using a proper formula describing the assigned diffusion limit; iii) PSD was determined as a histogram of d values, with interval width corresponding with LF-NMR T_2 relaxometry, with which a very good agreement was obtained. Secondly, the average diffusive tortuosity for the sample, τ_d, was calculated using the formula $\tau_d = \frac{D_0}{D_\infty}$, where D_∞ is long-time diffusion coefficient, with the following workflow: i) calculation of the mean pore size from PSD based on DTI; ii) estimation of an exemplary long-time limit diffusion time from $\xi = \frac{D_0 t_d}{d^2}$ assuming $\xi = 10$ (t_d was equal to 500 ms); iii) determination of D_∞ from the long-time limit formula; iv) verification of the calculated D_∞ with the experimental values coming from the independent diffusion measurement in LF-NMR for t_d=500 ms; v) calculation of tortuosity. A very good agreement was obtained between calculated and experimental D_∞ ($1.17 \cdot 10^{-3}$ mm^2/s and $1.13 \cdot 10^{-3}$ mm^2/s, respectively). The obtained τ_d=1.71, which was within the range of 1.46-2.33 obtained after the calculation by using different literature tortuosity models for the carbonates. Finally, electrical conductivity tensor was estimated assuming the correspondence of its eigenvectors with those for diffusion tensor. Then, the conductivity tensor, $C = \eta \cdot D$, where η is proportionality constant calculated from the force equilibrium model (FEM). The eigenvalues of the electrical conductivity tensor were equal to 0.152, 0.109 and 0.073 S/m, with a mean of 0.111 S/m and anisotropy of 0.36.

The most important value of DTI for rock core samples is that it can deliver diffusivities and geophysical parameters that are rotationally invariant. This is in contrary to the most common diffusion or diffusion-relaxation correlation experiments in one dimension. However, some limitations were indicated for DTI of rocks connected to the lack of appropriate hardware. MRI 9.4 T Bruker system is currently of choice due to the possibility of imaging with high resolution and reasonably high SNR and low TE. However, the applied TE is not short enough for tighter rocks, such as sandstones or shales, that have significantly shorter $T_2 s$. MRI of such rock types would require low magnetic fields (0.1-0.2 T) and other sequences, such as single-point imaging (SPI),

single-point ramped imaging with T_1-enhancement (SPRITE) or zero echo time (ZTE), which currently do not have diffusion-weighted imaging option. Moreover, high field cannot be successfully used for highly doped rocks, for which internal gradients induced by the differences in magnetic susceptibility would completely destroy magnetization in a short period of time and disturb a reliable diffusivity estimation. For carbonates like this used in the study, magnetic susceptibility of rock and saturating water were equal to -13 ppm and -9 ppm, respectively, which in conjunction to the complementary information about T_2 and PSD from LF-NMR, did not have a significant influence on the diffusion coefficients.

In conclusion, the article showed the possibility of the DTI technique to very accurately and widely characterize the rock core sample. It can deliver rotationally invariant diffusion parameters, from which many geophysical quantities can be determined. Moreover, 3D DTI metrics distributions can be successfully compared with the μCT, LF-NMR and MICP results, and deliver complementary information. Thus, DTI can enhance the insight into the interior of the sample and predictions according to the reservoir recovery. Tighter and more doped rock require the technological progress in the field of MRI.

[A6]: Identification of Proton Populations in Cherts as Natural Analogues of Pure Silica Materials by Means of Low Field NMR

This article was written based on the research conducted against the geological problem- the origin of silica in bedded and nodular cherts from the Kraków-Częstochowa Upland (KCU). The established theory about the siliceous Hexactinellida sponges as a sole source of silica has been questioned for this part of stratigraphic column. The new hypothesis about radiolarians as the second potential source of silica was proposed and it requires many additional data. Due to different oxidation levels of silica, solid-state NMR was extensively used for cherts along with other physical methods. However, commonly thought non-porous, to date cherts were not studied by ^{1}H LF-NMR. In the work, it was successfully used to characterize the proton populations in bedded and nodular cherts.

Three nodular and one bedded chert were characterized by using conventional methods- scanning electron microscope (SEM) and fusion-inductively coupled plasma (FUS-ICP). Next, LF-NMR T_1 (TR/scans/minimal $\pi - \frac{\pi}{2}$ pulses delay/maximal $\pi - \frac{\pi}{2}$ delay=5 s/24/0.05 ms/5000 ms), T_2 (TE/TR /scans/number of echoes=60 μs/1500 ms/512/10000) and $T_1 - T_2$ (TE/TR /scans/number of echoes/minimal $\frac{\pi}{2} - \pi$ pulses delay/maximal $\frac{\pi}{2} - \pi$ delay =60 μs/1500 ms/128/10000/0.1 ms/5000 ms) experiments were conducted for three sample states: native, dry (200 °C, 12 h, vacuum) and saturated (room temperature, vacuum). Moreover, the 1D and 2D

relaxation times distributions were also obtained for differential signal of saturated and dry samples. Parameters from 1D LF-NMR (relaxation times for modes, integral of modes' distributions, logarithmic mean T_1 and T_2 and porosities) were taken to the principal component analysis (PCA). PCA reduces many original variables to several secondary variables called principal components based on the correlation among the primary variables. In this way PCA can group samples into clusters based on the similar properties.

First of all, results from LF-NMR were very surprising. Despite very low porosities (maximum od ~2%), 1D and 2D distributions were very complex having up to five modes. Moreover, native and dry samples were characterized by very similar distributions- peaks virtually coincided, differences only in the modes amplitudes. Therefore, T_2 distributions were divided into regions encompassing individual modes: 0.05-0.2 ms (R1), 0.2−2 ms (R2), 2−12 ms (R3), 18−40 ms (R4), and 90−300 ms (R5). After saturation some differences were noticed, mainly in the region which was the most saturated (bedded chert significantly saturated in R3 and R4, which was not observed for nodular cherts). Using additional information about T_1/T_2 ratios from $T_1 - T_2$ maps, each region was identified as a certain proton population: R1- hydroxyl (OH) groups in silanol, R2-R5- water in pores (R2- water bonded to the surface of open mesopores characterized by roughness (after comparison with standards) between MCM-41 and SBA-15; R3- water strongly bound to the rough surface due to very high T_1/T_2 ratio; R4- water in pores with larger diameters, located between crystallites). Due to the fact, that relaxation times modes did not disappear after drying, the existence of the closed porosity was expected (the so-called inclusions). In turn, differential data describe open porosity.

Further analysis of porosity was made in comparison to the pure mesoporous silica systems (MCM-41, SBA-15 and pure silica simulated pores simulations encountered in the literature), which was possible because samples were composed in 98% from SiO_2. It was shown that those systems have different surface roughness reflected in different T_1/T_2 ratios. Comparing relaxation times obtained for cherts and for pure silica materials, it was hypothesized that inclusions contain the solution of mesoporous silica particles and water. Different T_1/T_2 ratios suggested different surface roughness of particles and/or paramagnetic content.

Next, pore size distributions (PSDs) were calculated for each saturation state using the relation on $1/T_2$ in pores, which after reformulation gave

$$d = \frac{4\rho_2 \pm \sqrt{(-4\rho_2)^2 - 4C(-FD)}}{2C}, \tag{A6.6}$$

where D is diffusion coefficient, ρ_2 is sample's surface relaxivity (a weighted sum of surface relaxivities obtained in the literature for pure silica materials and iron (III) oxide), $C = \frac{1}{T_2} - \frac{1}{T_{2\,bulk}}$

and $F = \frac{(\gamma \Delta \chi B_0 TE)^2}{12}$, where T_2 is experimental time, $T_{2\,bulk}$ =2.2 s, γ is gyromagnetic ratio, $\Delta\chi = \chi_{H_2O} - \chi_{Sample}$ is the difference between magnetic susceptibilities of water and solid phase of a sample (a sum of χ_{SiO_2}=-10.55 ppm and $\chi_{Fe_2O_3}$=500 ppm weighted by their fractions in a given sample), B_0=0.05 T and TE=60 μs. (A6.6) formula accounts for the signal attenuation due to diffusion in an internal magnetic field gradient resulting from the differences in magnetic susceptibility. In the second approach it was omitted and PSD was calculated using a well-known equation

$$d = 4 \cdot \rho_2 \cdot T_{2\,surface}, \tag{A6.7}$$

where $T_{2\,surface}$ is T_2 relaxation time obtained in the experiment assuming surface as the predominant source of relaxation. In the literature, taking into account the diffusion was connected with the application of the bulk diffusion coefficient, D_0. Besides this approach, we introduced a modified approach using simulation data from the literature, which suggested the decrease of diffusion coefficient in the nanopores (up to 10 nm pore size) from around $2.3 \cdot 10^{-3}$ mm^2/s (D_0) to $0.045 \cdot 10^{-3}$ mm^2/s (pore size of 0.6 nm and less). The power function-based $D(d)$ model was developed and used in the PSD calculation. In general, noticeable changes were visible in the pore size range of 1−10 nm. The effect of internal gradients outside this range is negligible. Based on PSDs of saturated samples, micro-, meso- and macroporosity (according to IUPAC) contributions to the total porosity were determined.

The last part of the study was PCA, which automatically distinguished bedded chert sample from the nodular ones in each saturation state. On the presented biplots, vectors associated with original variables were grouped and each group was marked by a different color. Such presentation, helped to better visualize the variables which distinguished bedded chert from nodular ones. Moreover, since each mode is associated with different proton populations, further gathering on the geological differences between bedded and nodular cherts can be made.

In the paper it was shown that cherts, commonly thought non-porous, evinced very high porosity diversity for the total porosity not exceeding 2%. Conducted analysis delivered a complete set of parameters describing different types of porosity (micro-, meso-, macro-, open, closed, surface bound water, slits in the microcrystalline quartz). Dry state enabled the characterization of inclusions using diverse T_1/T_2 ratio and T_2 time pairs in comparison to pure silica materials (suggesting various geological processes of formation). The outcome indicates the possibility of the LF-NMR method for the noninvasive distinction of cherts types and effective characterization of porosity, which can help in the geological studies.

IV. CONCLUSIONS

In the series of papers constituting the dissertation, new applications of NMR imaging in non-uniform magnetic field gradients were presented. The research materials were three types of nano- and micrometric porous systems- biological (Baker's yeast and mesenchymal stem cells), tissues (skeletal muscles of thighs) and geological (cherts and carbonates). The aim of the research was to overcome barriers to improve the quantitative characterization of these materials and describe their microgeometry more accurately. For this purpose, each of them required unique methodology and equipment. The barriers encountered in the characterization of the microstructure were: i) scale, ii) amount of research material, iii) chemical composition of the sample, iv) image artifacts, v) measurement errors (systematic and random).

The barrier of scale and the amount of the research material could be overcome by the application of the single-sided NMR MoUSE operating at high magnetic field constant gradient. It allows the obtainment of very strong diffusion weighting and thus, the examination of proton populations with the low diffusion coefficient. In the first two articles from the cycle, the application of NMR MoUSE was introduced for the biological systems *in vitro*. In the first one, with the application of time-dependent diffusion coefficient method, the evidence of nano- and submicrometric structures was shown and verified by using Monte Carlo simulations and characteristics coming from the literature. In the second article, the same methodology was applied to the interpretation of the diffusion-weighted data in the cultured mesenchymal stem cells. The main findings of this work were twofold. Firstly, the results showed that cultured MSCs are characterized by a visibly smaller intracellular self-diffusion coefficient in comparison to cells that MSCs can differentiate to. The other finding was supported by the successful identification of the nuclear component in the signal. Tracking the time-related changes of the molar fraction and diffusion coefficient of this component helped to distinguish two cell death mechanisms. Besides the full characterization of the mesenchymal stem cells microstructure and its time-related changes, NMR MoUSE proved the possibility to examine the biophysical properties of biological systems. The paper also presented the differences in the diffusional properties of MSCs depending on the pressing forces proportional to the number of contacting 50 μm-thick layers of cells. The studies of biological systems *in vitro* by applying NMR MoUSE opened the path for tracking cells' transitions due to mechanical forces and consequently, cells' differentiation process. Moreover, it evinced the possibility to support their identification *in vivo*, exploring their functions, localization and tracking in the human body without contrast agents, something that remains largely uncovered.

Image artifacts and systematic and random errors are the main problem in the clinical imaging. Articles [A3] and [A4] presented new application of DTI corrected for systematic errors by using BSD method for the diagnosis and monitoring of the course of the peripheral artery disease

in ischemic patients. The DTI metrics and tractography were associated with the clinical status of the muscles, but also delivered information about intra- and interfiber microstructure. Elimination of systematic errors showed to be essential for the proper interpretation of clinical data. After the BSD correction, DTI metrics can be potentially used as biomarkers for muscle tissue condition. Currently, there is no other non-invasive technique for the evaluation of the actual muscle status and structure before surgical procedure. The application of DTI can be therefore used for the monitoring of the muscle structure change due to treatment, hitherto by using mesenchymal stem cells therapy.

The problem of chemical composition of the sample appears mainly in geological materials. In the [A5] article, we firstly showed that ^{1}H Low Field NMR can help to characterize and differentiate nodular and bedded chert rock core samples with the total porosity equal to around 2% or less. 1D-T_2 distributions reflected physicochemical changes in the porosity structure due to saturation. T_1-T_2 maps were also incorporated, which delivered T_1/T_2 ratio reflecting the desorption energy of proton species, which helped to classify the peaks as resulting from different populations, including hydroxyl groups in silanols, water adsorbed on the surface of micropores or entrapped in the slits of microcrystalline quartz (probably creating hydrogen bonds with surface silanols) and water in micro-, meso- and macropores. Further quantitative analysis was possible after the association of the highly siliceous samples with pure silica materials (MCM-41 and SBA-15) examined in the previous work. The findings are relevant in that they show, that low field relaxometry can be used to investigate different physicochemical properties of low porosity rocks based on the following parameters: T_1/T_2 ratio, pore size distribution (corrected for the diffusion in the induced magnetic field gradients), relaxation times. Besides non-invasive probing of the porosity, adsorbed species and surface processes, this technique brings new light on the characterization of cherts as natural porous silica materials. It is expected that this work will contribute to the studies on silica sources in the bedded and nodular cherts.

The last work introduced a new approach for measuring fluid diffusion in rock cores. The proposed method, based on a DTI technique, offers a spatial determination of the diffusion coefficients and derivative parameters in a truly quantitative manner that is related to the examined pore microstructure (rotationally invariant). This is a significant innovation in relation to numerous studies where the measurements of the diffusion coefficient in NMR/MRI experiments were determined in an ambiguous manner, namely depending on the direction of the diffusion gradient vector. This study is also within the scientific focus on the optimal determination and use of energy resources. This is largely due to the fact that the detailed geophysical parameters of the rock material, such as the geometry of pores controlling the migration of reservoir fluids, are the subject of our study. In other words, understanding the geometry and distribution of pores resolved via diffusion measurements has a critical impact on fluid migration, mineral dissolution or precipitation

and the capability of a reservoir to store injected fluids such as CO_2. We therefore believe, that our approach will be vital for increasing the precision of the determination of the geochemical and geophysical parameters of rocks based on the measurement of diffusion coefficients using non-invasive DTI technique. It should be emphasized that the proposed DTI can deliver metrics used in determining geophysical and geochemical parameters such as: pore geometry, pore size distribution, permeability, wettability, fluid structure, conductivity tensor, tortuosity (some of them shown in the work). These parameters are crucial for the precise determination and use of energy resources of oil, gas or geothermal deposits.

Summing up, the dissertation consists of the six articles concerning the problem of the accurate quantitative characterization of the microstructure and biophysical properties of porous systems encountered in different fields of study. Workflow of each research consisted of the predefinition of the existing barriers based on the state-of-the-art, development of appropriate experimental protocol and analysis method, definition of the obstacles for the accurate quantitative analysis, correction for the unwanted effects and finding the possible applications of the proposed methodology. Thus, the dissertation presents different approaches for the solution of the same problem, but adapted for the research material.

REFERENCES

Åslund, I., Topgaard, D., 2009. Determination of the self-diffusion coefficient of intracellular water using PGSE NMR with variable gradient pulse length. J. Magn. Reson. 201, 250–254. https://doi.org/10.1016/j.jmr.2009.09.006

Bammer, R., Markl, M., Barnett, A., Acar, B., Alley, M.T., Pelc, N.J., Glover, G.H., Moseley, M.E., 2003. Analysis and generalized correction of the effect of spatial gradient field distortions in diffusion-weighted imaging. Magn. Reson. Med. 50, 560–569. https://doi.org/10.1002/mrm.10545

Bloch, F., 1946. Nuclear induction. Phys. Rev. 70, 460–474. https://doi.org/10.1016/0031-8914(51)90068-7

Boesch, C., 2004. Nobel prizes for nuclear magnetic resonance: 2003 and Historical perspectives. J. Magn. Reson. Imaging 20, 177–179. https://doi.org/10.1002/JMRI.20120

Borkowski, K., Krzyżak, A.T., 2018. The generalized Stejskal-Tanner equation for non-uniform magnetic field gradients. J. Magn. Reson. 296, 23–28. https://doi.org/10.1016/j.jmr.2018.08.010

Brownstein, K.R., Tarr, C.E., 1979. Importance of classical diffusion in NMR studies of water in biological cells. Phys. Rev. A 19, 2446. https://doi.org/10.1103/PhysRevA.19.2446

Callaghan, P.T., 1991. Principles of Nuclear Magnetic Resonance Microscopy, 1st ed. Oxford University Press, New York. https://doi.org/10.1524/zpch.1992.176.part_1.132

Coates, G.R., Xiao, L., Prammer, M.G., 1999. NMR logging: Principles and Applications. Halliburton Energy Services.

De Swiet, T.M., Sen, P.N., 1996. Time dependent diffusion coefficient in a disordered medium. J. Chem. Phys. 104, 206–209. https://doi.org/10.1063/1.470890

Doran, S.J., Charles-Edwards, L., Reinsberg, S.A., Leach, M.O., 2005. A complete distortion correction for MR images: I. Gradient warp correction. Phys. Med. Biol. 50, 1343. https://doi.org/10.1088/0031-9155/50/7/001

Du, Y.P., Parker, D.L., 1996. Evaluation of gradient inhomogeneity in the optimal design of gradient coils. Magn. Reson. Imaging 14, 201–207. https://doi.org/10.1016/0730-725X(95)02055-X

Giunta, C.J., Mainz, V. V, 2020. Discovery of Nuclear Magnetic Resonance: Rabi, Purcell, and Bloch, in: ACS Symposium Series. pp. 3–20. https://doi.org/10.1021/bk-2020-1349.ch001

Grebenkov, D.S., 2007. NMR survey of reflected Brownian motion. Rev. Mod. Phys. 79, 1077–1137. https://doi.org/10.1103/RevModPhys.79.1077

Hennel, J.W., 1966. Wstęp do teorii magnetycznego rezonansu jądrowego. Państwowe Wydawnictwo Naukowe, Warszawa.

Janke, A., Zhao, H., Cowin, G.J., Galloway, G.J., Doddrell, D.M., 2004. Use of spherical harmonic deconvolution methods to compensate for nonlinear gradient effects on MRI images. Magn. Reson. Med. 52, 115–122. https://doi.org/10.1002/MRM.20122

Kärger, J., 1985. NMR Self-Diffusion studies in heterogeneous systems. Adv. Colloid Interface Sci. 23, 129–148.

Krzyżak, A.T., 2008. Anisotropic diffusion phantom for calibration of any MR, DTI imaging sequence and method of calibration of any MR tomograph. PL 385276 A1; US 8643369 B2, 2014; JP 6270174 B2, 2018; EP 2286258 B1, 2018.

Krzyżak, A.T., Olejniczak, Z., 2015. Improving the accuracy of PGSE DTI experiments using the spatial distribution of b matrix. Magn. Reson. Imaging 33, 286–295. https://doi.org/10.1016/j.mri.2014.10.007

Latour, L.L., Mitra, P.P., Kleinberg, R.L., Sotak, C.H., 1993. Time-Dependent Diffusion Coefficient of Fluids in Porous Media as a Probe of Surface-to-Volume Ratio. J. Magn. Reson. - Ser. A 101, 342–346. https://doi.org/10.1006/jmra.1993.1056

Latour, L.L., Svoboda, K., Mitra, P.P., Sotak, C.H., 1994. Time-dependent diffusion of water in a biological model system. Proc. Natl. Acad. Sci. U. S. A. 91, 1229–1233. https://doi.org/10.1073/pnas.91.4.1229

Mitra, P.P., Sen, P.N., Schwartz, L.M., 1993. Short-time behavior of the diffusion coefficient as a geometrical probe of porous media. Phys. Rev. B 47, 8565–8574. https://doi.org/10.1103/PhysRevB.47.8565

Mitra, P.P., Sen, P.N., Schwartz, L.M., Le Doussal, P., 1992. Diffusion propagator as a probe of the structure of porous media. Phys. Rev. Lett. 68, 3555–3558. https://doi.org/10.1103/PhysRevLett.68.3555

Moutal, N., Grebenkov, D.S., 2020. The localization regime in a nutshell. J. Magn. Reson. 320, 106836. https://doi.org/10.1016/j.jmr.2020.106836

Tanner, J.E., Stejskal, E.O., 1968. Restricted Self-Diffusion of Protons in Colloidal Systems by the Pulsed-Gradient, Spin-Echo Method. J. Chem. Phys. 49, 1768–1777. https://doi.org/10.1063/1.1670306

Torrey, H.C., 1956. Bloch Equations with Diffusion Terms. Phys. Rev. 104, 563–565.

LIST OF CONFERENCES

1. **Weronika Mazur***, Julia Lasek, Artur T. Krzyżak, *The effect of elimination of systematic errors on the distributions of diffusion tensor imaging metrics in automatically segmented regions of white and grey matter of the left and right hemisphere*, 64th Experimental Nuclear Magnetic Resonance Conference (ENC2023), 19-20 April 2023, Pacific Grove, California, USA (**oral**)

2. **Weronika Mazur***, Ewa Stodolak-Zych, Marcin Kudzin, Aleksandra Wesełucha-Birczyńska, Maciej Boguń, Artur T. Krzyżak, *Carbon fibers surface with active metallic nanometric layer to support cartilage regeneration process*, 2022 IEEE 12th international conference ”Nanomaterials: Applications & Properties (IEEE NAP-2022)”, 11–16 September 2022, Kraków, Poland (**oral**)

3. **Weronika Mazur***, Anna Stefańska-Bernatowicz, Artur T. Krzyżak *The influence of systematic and statistical errors on the DTI metrics and tractography of rat's brain white matter*, 63rd Experimental Nuclear Magnetic Resonance Conference (ENC2022), 24-29 April 2022, Orlando, Floryda, USA (**oral**)

4. **Weronika Mazur***, Artur T. Krzyżak, *Application of anisotropic phantoms with laminar and cylindrical pores to determination of important parameters characterizing porous media*, ESMRMB 2019 congress: 36th Annual Scientific Meeting, 3-5 October 2019 Rotterdam, NL (**lightening talk, poster**)

5. **Weronika Mazur***, Artur T. Krzyżak, Zbigniew Raszewski, Rafał Obuchowicz, *New models of biological structures: testing novel anisotropic phantoms by MRI : a preliminary study for cardiovascular applications*, New frontiers in regeneration therapies: from advanced therapy medicinal products (ATMP) through imaging to clinical outcomes: international scientific conference : 14-15 September 2018, Kraków, Poland (**oral**)

6. **Weronika Mazur***, Artur T. Krzyżak, *Diffusion tensor imaging with three types of correction to reveal physiological and morphological differences in the liver*, 64th Experimental Nuclear Magnetic Resonance Conference (ENC2023), 19-20 April 2023, Pacific Grove, California, USA (**poster**)

7. **Weronika Mazur***, Tomasz Zalewski, Artur T. Krzyżak, *Spatial characterization of a carbonate rock core sample microstructure using diffusion tensor imaging and T1- and T2-mapping*, AMPERE NMR School,19–25 June 2022, Zakopane, Poland (**poster**)

8. **Weronika Mazur***, Anna Stefańska-Bernatowicz, Ewa Stodolak-Zych, Artur Tadeusz Krzyżak, *Investigation of sodium alginate and polyvinyl alcohol based anisotropic hydrogel phantoms for calibration applications by DWI at 0.6 T*, Joint annual meeting ISMRM-ESMRMB & ISMRT 31st annual meeting : 07-12 May 2022,London, England, UK (**poster**)

9. **Weronika Mazur***, Artur T. Krzyżak, *Time-dependent diffusion coefficient in Baker's Yeast studied by single-sided NMR: attempts to the exploration of structures with a sub-micrometer size*, ESMRMB 2019 congress: 36th Annual Scientific Meeting, 3-5 October 2019 Rotterdam, NL (**poster**)

10. **Weronika Mazur***, Artur T. Krzyżak, Zbigniew Raszewski *Towards the precise microstructural mapping : testing new anisotropic phantoms with layered and capillary geometries*, 41st annual international conference of the IEEE Engineering in Medicine and Biology Society (EMBC 2019), 23-27 July 2019, Berlin, Germany (**poster**)

11. Artur T. Krzyżak, **Weronika Mazur***, Jacek Matyszkiewicz, Alicja Kochman, *Chert porosity distribution obtained by 1H Low Field NMR*, 10th Kraków Workshop on Novel Applications of Imaging and Spectroscopy in Medicine, Biology and Material Sciences, 23-25 September 2019, Kraków, Poland. (**poster**)

12. Ewa Stodolak-Zych, Marcin Kudzin, Artur T. Krzyżak, M. Gubernat, **Weronika Mazur**, R. Kurpanik, Maciej Boguń, *Nonwoven carbon fibers with nanometric metallic layers as a tool to monitoring regenerative processes*,13th Polish-Japanese joint seminar on Micro and nano analysis : 25–28 September 2022, Ustroń, Poland

13. Anna Stefańska-Bernatowicz, Alicja Kochman, **Weronika Mazur**, Artur T. Krzyżak, *Analysis of geophysical parameters of silicate rock cores using LF-NMR relaxation methods*, AMPERE NMR School, 19–25 June 2022, Zakopane, Poland (**poster**)

*Presenting author

PROJECTS AND INTERNSHIPS

1. Research contract within the **STRATEGMED2** project "Cardiovascular ischemic injury regeneration using Wharton Jelly as unlimited therapeutic stem cells source" (STRATEGMED2/265761/10/NCBR/2015);

2. Research contract within the **ABM** project "Evaluation of the clinical effectiveness of BSD (B-matrix Spatial Distribution) technology and algorithms based on artificial intelligence for the analysis of MRI images in the course of multiple sclerosis (MS)" implemented under the competition number ABM/1/2020 (1st round) for research and development activities in the field of non-commercial clinical trials (2020/ABM/01/00006-00).

3. Research contract within the project "Implementation of the study of machine learning algorithms in the clinical imaging diagnostics of liver cancer based on magnetic resonance tomography and lung cancer based on computed tomography, as well as the development and implementation of an innovative method for clinical liver research with methods using the NMR phenomenon for the purpose of building an IT platform to support and automate the diagnostic process in imaging studies" financed by National Centre for Research and Development (**Fast Track grant**, contract No. POIR.01.01.01-00-1666/20).

4. **Scientific internship** in the NanoBioMedical Centre at the Adam Mickiewicz University in Poznań, Poland, 10-15.04.2022.

5. Attendance in the **Ampere NMR School** organized by the NanoBioMedical Center and the Faculty of Macromolecular Physics of the Adam Mickiewicz University Adam Mickiewicz in Poznań in cooperation with the Center for European Integration under the auspices of Groupement AMPERE, Zakopane, Poland. 19-26.06.2022

STIPENDS AND AWARDS

1. **1st Laureate** of the poster session at the 10th Kraków Workshop on Novel Applications of Imaging and Spectroscopy in Medicine, Biology and Material Sciences, 23-25 September 2019, Kraków, Poland.

2. Rising Star in Nanoscience & Nanotechnology **Best Presentation Award** for oral presentation at the 2022 IEEE International Conference "Nanomaterials: Applications & Properties", 11–16 September 2022, Kraków, Poland.

3. **Student Stipend** funded by Norell, Inc. at the Experimental Nuclear Magnetic Resonance Conference (ENC2022), 24-29 April 2022, Orlando, Floryda, USA.

4. **Student Stipend** funded by Norell, Inc. at the 64th Experimental Nuclear Magnetic Resonance Conference (ENC2023), 16-20 April 2023, Pacific Grove, California, USA.

LIST OF PUBLICATIONS FROM OUTSIDE THE THESIS

Mazur, W., Urbańczyk-Zawadzka, M., Czyż, Ł., Kwiecień, E., Banyś, R., Musiałek, P., Krzyżak, A. T. (2022). *Diffusion-tensor magnetic resonance imaging of the human heart in health and in acute myocardial infarction using diffusion-weighted echo-planar imaging technique with spin-echo signals.* Advances in Interventional Cardiology/Postępy w Kardiologii Interwencyjnej, 18(3 (69)), 1–7. https://doi.org/10.5114/aic.2022.121344

Mazur, W., Krzyżak, A. T., Hennel, F. (2022). *Diffusion-weighted imaging and diffusion tensor imaging of the heart in vivo: major developments*. Advances in Interventional Cardiology/Postępy w Kardiologii Interwencyjnej, 18(3 (69)), 1–10. https://doi.org/10.5114/aic.2022.121345

Mazur, W., Krzyżak, A. T., Raszewski, Z. (2019). *Towards the precise microstructural mapping. Testing new anisotropic phantoms with layered and capillary geometries.* In 41st Annual International Conference of the IEEE Engineering in Medicine and Biology Society, EMBS (pp. 2835–2839). https://doi.org/10.1109/EMBC.2019.8857065

Krzyżak, A. T., Habina-Skrzyniarz, I., Machowski, G., **Mazur, W.** (2020). *Overcoming the barriers to the exploration of nanoporous shales porosity.* Microporous and Mesoporous Materials, 298, 110003. https://doi.org/10.1016/j.micromeso.2020.110003

Strączek, T., Fiejdasz, S., Rybicki, D., Goc, K., Przewoźnik, J., **Mazur, W.**, Nowakowska M., Zapotoczny S., Rumian S., Kapusta C. (2019). *Dynamics of Superparamagnetic Iron Oxide Nanoparticles with Various Polymeric Coatings.* Materials, 12(11), 1793–1808.

cells

MDPI

Article

Attempts at the Characterization of In-Cell Biophysical Processes Non-Invasively—Quantitative NMR Diffusometry of a Model Cellular System

Weronika Mazur [1,2,*] and Artur T. Krzyżak [2]

[1] Faculty of Physics and Applied Computer Science, AGH University of Science and Technology, ul. Reymonta 19, 30-059 Cracow, Poland

[2] Faculty of Geology, Geophysics and Environmental Protection, AGH University of Science and Technology, al. Mickiewicza 30, 30-059 Cracow, Poland; akrzyzak@agh.edu.pl

* Correspondence: Weronika.Mazur@fis.agh.edu.pl; Tel.: +48-12-617-40-66

Received: 17 August 2020; Accepted: 18 September 2020; Published: 19 September 2020

Abstract: In the literature, diffusion studies of cell systems are usually limited to two water pools that are associated with the extracellular space and the entire interior of the cell. Therefore, the time-dependent diffusion coefficient contains information about the geometry of these two water regions and the water exchange through their boundary. This approach is due to the fact that most of these studies use pulse techniques and relatively low gradients, which prevents the achievement of high *b*-values. As a consequence, it is not possible to register the signal coming from proton populations with a very low bulk or apparent self-diffusion coefficient, such as cell organelles. The purpose of this work was to obtain information on the geometry and dynamics of water at a level lower than the cell size, i.e., in cellular structures, using the time-dependent diffusion coefficient method. The model of the cell system was made of baker's yeast (*Saccharomyces cerevisiae*) since that is commonly available and well-characterized. We measured characteristic fresh yeast properties with the application of a compact Nuclear Magnetic Resonance (NMR)-Magritek Mobile Universal Surface Explorer (MoUSE) device with a very high, constant gradient (−24 T/m), which enabled us to obtain a sufficient stimulated echo attenuation even for very short diffusion times (0.2–40 ms) and to apply very short diffusion encoding times. In this work, due to a very large diffusion weighting (*b*-values), splitting the signal into three components was possible, among which one was associated only with cellular structures. Time-dependent diffusion coefficient analysis allowed us to determine the self-diffusion coefficients of extracellular fluid, cytoplasm and cellular organelles, as well as compartment sizes. Cellular organelles contributing to each compartment were identified based on the random walk simulations and approximate volumes of water pools calculated using theoretical sizes or molar fractions. Information about different cell structures is contained in different compartments depending on the diffusion regime, which is inherent in studies applying extremely high gradients.

Keywords: constant gradient; time-dependent diffusion coefficient; in-cell diffusion

1. Introduction

Water in cells is very important for many processes, including cell division [1]. Water permeability is an important feature of biological cells that can be used as an indicator of a cell's condition and death [2,3]. Nuclear Magnetic Resonance (NMR) diffusion imaging is a useful tool in studies on membrane permeability because it is sensitive to molecular motion. It has been shown by Mitra et al. that the time-dependent diffusion coefficient in the slow regime, i.e., when $t \ll R^2 D_0^{-1}$, where t is a time of diffusion observation, R is a cell radius and D_0 is a self-diffusion coefficient, is independent

of microgeometry and membrane permeability [4] and can be applied to the determination of a self-diffusion coefficient of a liquid confined in a compartment with a specific Surface-area-to-Volume ratio, S/V.

Many works concern the application of a Pulsed Field Gradient (PFG) for studies on water dynamics in biological cells (e.g., [4–11] and references therein). However, in studies of porous systems with very small pores containing fluids whose transverse relaxation time is very short (<1 ms), the usage of the PFG technique may be problematic, mainly due to time limitations concerning the adjustment of sequence parameters. Fischer and Kimmich [12] discussed the problems associated with applying PFG and presented the method of a secondary stimulated echo for measuring the self-diffusion coefficients of polymers by using a constant gradient. The application of a constant gradient was also presented by Rata et al. [13] for the determination of self-diffusion coefficients in water-saturated sandstone cores.

A widely used model of diffusion in biological systems is the two compartmental model in which the exchange of water between the two pools occurs after a certain time, the so-called residence time or lifetime. An assumption about the two fractions making a contribution to the signal is sufficient for moderate gradient strengths and time parameters in pulsed techniques. This is due to the fact that intra- and extracellular space sizes are comparable to the diffusion length scales obtainable by systems with the mentioned features. This limitation may be overcome by the application of constant, very strong gradients. As we will show in this work, by using a constant gradient strength of 24 Tm^{-1} and Stimulated Spin Echo (SSE) sequence, it is possible to explore structures with length scales lower than 1 µm and self-diffusion coefficients significantly smaller than bulk water. In order to do so, a three-compartmental model was used to determine self-diffusion coefficients which were later analyzed in regard to their dependency on time. Admittedly, three compartments were applied earlier by Stanisz [14] to characterize diffusion in a bovine optic nerve, but one compartment was associated with extracellular space, while the other two with intracellular spaces with different geometries. On the other hand, Schoberth [8] studied small prokaryotic cells with sizes below 1 µm (*Corynebacterium glutamicum* bacteria having a diameter of 0.7 µm), but the PFG technique allowed him to measure intracellular water on the border between the localization and the motional averaging regime.

To the best of our knowledge, we applied the three-compartmental model of diffusion for the first time, where one of the compartments is significantly smaller than 1 µm and associated with cellular organelles. We will also show that, depending on the diffusion regime, the time-dependent diffusion coefficient will provide information on the biophysical properties of different structures. For this reason, when using an extremely strong diffusion gradient, three compartments cannot be rigidly assigned to specific spaces over the entire diffusion time range, as in the case of two-compartmental analysis.

2. Materials and Methods

2.1. Sample of a Model Cellular System

Fresh baker's yeast (*Saccharomyces cerevisiae*; Lesaffre Polska S.A., Wołczyn, Poland) was purchased from a local market. Water content in the sample was equal to 24% of the total weight. The yeast was placed in a petri dish in its original form and its temperature was successively controlled. The experiments were conducted after ~1 h, when the yeast's temperature was equal to the ambient temperature of 25 °C. The ambient temperature was maintained at a constant level. A referential measurement of a bulk water sample yielded a bulk water coefficient $D_{bulk} = (2.403 \pm 0.044) \times 10^{-9}$ m^2s^{-1}.

2.2. System

The ^1H NMR diffusion measurements were performed on a Magritek Mobile Universal Surface Explorer (MoUSE; Magritek, Aachen, Germany). This device is constructed with the application of permanent magnets and allows measurements in a stray field. The construction scheme is presented in Figure S1. The magnetic field gradient is constant, directed perpendicularly to the surface of the table (marked as T in the Figure S1) and has an amplitude of 24 T/m. A slice can be chosen by an adequate

movement of the high precision lift below the magnets. Due to the constant gradient, radio-frequency (RF) pulses can only excite a given slice of a sample at a chosen depth, compared to PFG techniques in which the whole sample is excited. All experiments were performed at 2.5 mm from the table, which was the depth in the lower half of the yeast. The slice thickness achieved for echo times (TEs) used in our study (from 0.04 ms to 1.2 ms) was equal to 200 µm.

2.3. Experiments

Diffusion was measured using the SSE pulse sequence (Figure S2). Time intervals τ and t_m are analogues of δ and Δ in the PFG techniques and denote for gradient duration and gradients separation time, respectively. To register an echo attenuation for a particular diffusion time in PFG, the gradient's amplitude is usually altered. Since our system operates at a constant gradient, attenuation was obtained via changing τ in 20 steps from τ_{min} = 0.02 ms to τ_{max} = 0.6 ms. The range of τ, as well as other parameters of the protocol, was kept the same for all the mixing times used in the experiments. Diffusion was measured for 15 t_m = 0.2–40 ms, which enabled the achievement of b-values from the range of 0–5.97 $\times 10^{11}$ sm^{-2}. The values of the parameters of the SSE pulse sequence are summarized in Table S1. The normalized echo attenuation for SSE is given by [15]:

$$\frac{E}{E_0} = \exp\left(-\gamma^2 G^2 \tau^2 \left(t_m + \frac{2}{3}\tau\right) D - \frac{2\tau}{T_2} - \frac{t_m}{T_1}\right), \quad (1)$$

where γ (T^{-1}s^{-1}) is gyromagnetic ratio, G (Tm^{-1}) is gradient strength and T_1 and T_2 are the longitudinal and transverse relaxation times, respectively.

T_1 and T_2 relaxation times were obtained from T_1 and T_2 distributions. The T_2 relaxation curve was acquired with the application of a Carr-Purcell-Meiboom-Gill (CPMG) pulse sequence for the following parameters: TE/RD = 40 µs/6200 ms, number of echoes = 4096, NoS = 256. T_1 was measured with the application of a saturation recovery sequence using TE/RD = 40 µs/3500 ms, number of echoes = 2048, NoS = 16.

2.4. Models for Diffusion in Cellular System

Three models of diffusion in yeast were tested on the collected data: a two-compartmental (Model 0 when fitted in the full range of b-values, Model 0B when fitted in a given interval of b-values), a two-compartmental with an intercept (Model 1) and a three-compartmental model (Model 2). All of the models were fitted to the data in OriginPro2018b software. The overall formula for the echo attenuation in the sample for a particular t_m is:

$$\frac{E}{E_0} = \left(e^{-\frac{2\tau}{T_2}} \cdot e^{-\frac{t_m}{T_1}}\right) \cdot \sum_{i=1}^{n} p_i \cdot e^{-(\gamma^2 G^2 \tau^2 (t_m + \frac{2}{3}\tau)) D_i} + y_0, \quad (2)$$

where T_1 and T_2 relaxation times were taken from the distributions shown in Figure 1, i is i-th compartment in the sample, n is the number of compartments, E is the echo amplitude for the given τ and t_m and E_0 is the echo amplitude for the minimal τ and t_m [13], p_i is the molar fraction of i-th population and $\sum_{i=1}^{n} p_i = 1$, D_i (m^{2}s^{-1}) is the apparent diffusion coefficient in the i-th compartment, and:

$$(\gamma G \tau)^2 \left(t_m + \frac{2}{3}\tau\right) = b, \quad (3)$$

which is a diffusion weighting factor in units (sm^{-2}). y_0 is the intercept and is equal to zero for Model 0, Model 0B and Model 2.

2.5. Time-Dependent Diffusion Coefficient (TDDC)

The multi-compartmental model of diffusion in yeast used further in this paper was based on images obtained from Transmission Electron Microscopy (TEM) or Scanning Electron Microscopy (SEM) reported in the literature (e.g., [16]), where at least one region of a significant size is visible, regarding nucleus, vacuoles, mitochondria or cell wall. Each of these regions is characterized by the self-diffusion coefficient dependent on diffusion time, which for $t_m \gg \tau$ is equal to t_m, and will be hereafter called the time-dependent diffusion coefficient (TDDC). TDDC on the log-log scale evinces a characteristic S-shape with three distinct regions (Figure S3): I—free diffusion, II—restricted diffusion (localization regime) and III—hindered diffusion (motional averaging regime). Region I is described by Mitra's relation [17]:

$$D_i(t_m) = D_{0i} - \frac{4}{3W\sqrt{\pi}} \cdot \frac{S_i}{V_i} \cdot {D_{0i}}^{\frac{3}{2}} \cdot \sqrt{t_m}, \quad (4)$$

where W is the number of space dimensions in which diffusion occurs, $D_{0i}\left(\mathrm{m^2 s^{-1}}\right)$ is the bulk self-diffusion coefficient in i-th compartment for $t_m \to 0$ and $\frac{S_i}{V_i}\left(\frac{1}{m}\right)$ is the Surface-area-to-Volume ratio. In this region, diffusion signal is independent of microgeometry, meaning that all structures with similar D_0 contribute to one, i-th compartment. The arrow-marked region in II (Figure S3) can be described by the Einstein-Smoluchowski equation [11]:

$$\left\langle Z_i^2 \right\rangle = 2dD_i t_m, \quad (5)$$

where $\left\langle Z_i^2 \right\rangle \left(\mathrm{m^2}\right)$ is the root-mean-square displacement of water molecules during t_m and d is the number of dimensions. This equation concerns diffusion in a non-permeable confinement. In reality, the power of diffusion time may be slightly higher than -1 [18] due to the permeable boundaries, i.e., cell membranes [10]. In this region, the diffusion coefficient is dependent on the microgeometry, which means that i-th compartment will be composed of structures having similar sizes. In the limit: $\tau \ll \frac{R_i^2}{D_{0i}}$, $t_m \gg \frac{R_i^2}{D_{0i}}$, the root mean square displacement can be expressed as ([6] and references therein):

$$\left\langle Z^2 \right\rangle = \frac{2}{2+d} \cdot R^2, \quad (6)$$

where R (m) is a half distance between boundaries (e.g., radius of sphere). d is, again, the number of dimensions, and in our case $d = 1$.

2.6. Simulations

In order to determine the contribution of each compartment to the signal attenuation during t_m, Monte Carlo Random Walk (RW) simulations were conducted in the cell, in which random walkers reflected diffusing particles. Simulations were conducted in MATLAB (R2019b) (Natick, MA, USA, The MathWorks Inc.). The modeled two-dimensional (2D) geometry consisted of a cell wall, nucleus, mitochondrion, vacuole and intracellular space, in which we assumed completely reflecting boundaries. A non-exchangeable system was assumed based on the lifetimes reported in the literature for yeast (see Section 4.5). Particle jump duration was set to be $t_s = 5$ µs (step length was dependent on the self-diffusion coefficient, D_{0i}, $\sigma = \sqrt{4D_{0i}t_s}$). Number of RW steps depended on t_m based on the relation $N = t_m/t_s$ and was in the range of 40–8000, while the number of particles was equal to 5000. From the root-mean-square displacements of each particle the mean displacements r_m in compartments during t_m were calculated. By using $r_m(t_m)$ and Equations (4) and (5), apparent diffusion coefficients were calculated and plotted versus t_m. There was a certain time t_m at which D_i from Equations (4) and (5) were equal. To the left of this point we used D_i from Equation (4), while to the right, we used D_i from Equation (5). From these $D_i(t_m)$ signal attenuations, $E/E_0(b)$ in each compartment was simulated using the Stejskal-Tanner equation, by the calculation of b for a priori taken E/E_0(from 1 to 0.01).

2.7. Permeability

In the absence of osmotic gradients, no net water flux is observed during transmembrane water molecule exchange. In this case, water exchange is described by the diffusional membrane permeability, P_d, which for spherical compartments can be calculated as:

$$P_{di} = \frac{R_i}{3\tau_i}, \tag{7}$$

where τ_i is the lifetime of water in i-th compartment. It can be determined from the curve fitting to the time-dependent molar fractions, given by:

$$p_i = p_{0i} \cdot e^{-\frac{t_m}{\tau_i}}, \tag{8}$$

where p_{0i} is the compartmental molar fraction for $t_m \to 0^+$ and represents the normalized (to the volume of the whole sample) volume of the compartment.

3. Results

The collected data in the diffusion experiments are a set of echo attenuations for different mixing times. It contains information about TDDC and molar fractions for all the modeled regions, which are treated as fitting parameters.

3.1. Relaxation Times

The T_1 and T_2 time distributions of a sample obtained in NMR-MoUSE are shown in Figure 1. T_2 s are apparent T_2 relaxation times, decreased compared to the bulk fluid's T_2, due to the high diffusion impact resulting from the application of the high gradient. However, these T_2 s are visible in the diffusion experiment in the same system. T_2 times of the peaks were found to be equal to 2 ms and 29.2 ms, while T_1 = 215 ms. The peak with T_2 = 2 ms can be neglected due to a very low contribution. Peaks with T_2 = 29.2 ms constitute 99.63% of a whole relaxation signal, meaning all cellular structures have similar relaxational properties, and come from the free fluids in the cell system. We can assume that in the diffusion experiment, the attenuation of a signal due to relaxation will be associated with T_2 = 29.2 ms and T_1 = 215 ms.

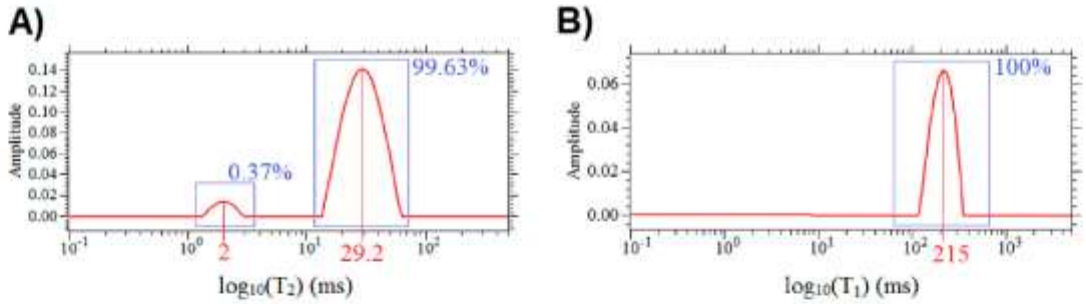

Figure 1. T_2 (**A**) and T_1 (**B**) distributions of a fresh yeast sample. Contributions of peaks to the whole distribution are presented in percentages.

3.2. Choosing the Appropriate Diffusion Model

First, we adapted the most common, two-compartmental model (model 0, Figure 2A), in which two non-exchangeable (t_m much smaller than water lifetimes reported for yeast) regions are associated with extra- and intracellular water. However, even for the low t_ms, model 0 does not fit the data well and for higher t_ms, it does not even converge on the data points for b values higher than approximately 1×10^{10} sm^{-2}. To see whether this situation is due to systematic errors (resulting for example from

inequality of T_2s in the compartments [5]), a two-exponential model with intercept (model 1) was adapted (Figure 2). Model 1 indeed fits the data better for the low t_ms, but the intercept y_0 consisted of as much as 10% of a signal. Additionally, molar fractions p_i from model 1 did not exhibit an exponential decay; rather, they are randomly distributed. Furthermore, y_0 revealed a very strong discontinuity at t_m between 1 and 2 ms (Figure 2C). A rapid increase of p_2 in connection with a rapid drop of p_1 values at t_m = 2–5 ms is in accordance with the D_1 and D_2 discontinuity point (Figure 2B). It looks like D_2 was composed of two decaying regions II (marked with arrow in the Figure S3) separated at t_m = 2–5 ms. In case of D_1, the points start to decay even for the very small t_ms and then remain constant. Considering that this component is associated with extracellular space, it is unlikely that region II is observed for very low t_ms, meaning that diffusion is restricted. Due to its size, extracellular space enables water to diffuse freely for a relatively long time. On this basis, we can suspect that the third compartment of slowly diffusing water is visible in the experiments. For very low t_ms (<1 ms), it gives almost no attenuation to the total signal and appears as a high intercept y_0, while for high t_ms, it will have high impact on the attenuation curve (especially for the second half of b-values for which the first two compartments are rather fully attenuated, but the signal is still detectable).

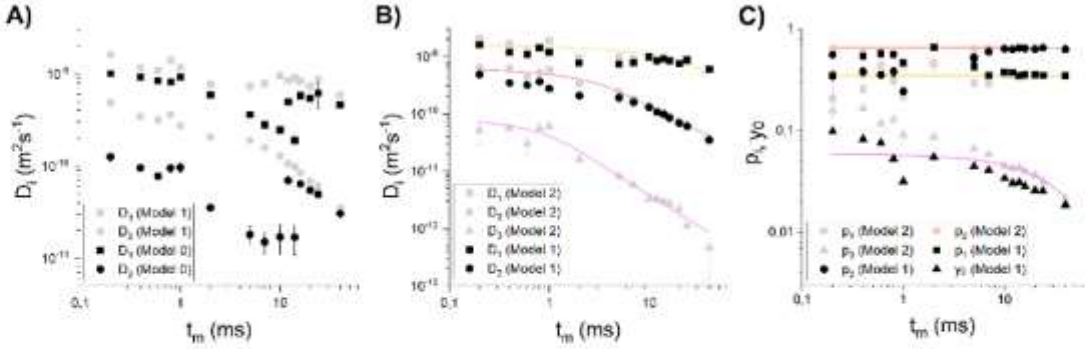

Figure 2. (**A**) Comparison of results from the fitting of the model 0 and 1. (**B**) Comparison of results from the fitting of the Model 1 and 2. The lines are fitted to $D_i(t_m)$ from model 2 with the application of (4) and (5). (**C**) Molar fractions obtained from model 1 and 2 with fitted lines for t_m = 10–40 ms.

The first qualitative analysis shows that three-compartmental is the most preferable. Assuming that all of the three compartments will contribute to the signal attenuation for all t_ms for a given b-values range, model 2 was fitted. Next, a quantitative comparison of the model 1 and 2, was made. The models were compared via statistical tests—Akaike's (AIC) and Bayesian Information Criterion. Figure S4 shows that for almost all cases, there is a higher probability (Akaike's weight) that model 2 is a true model. For extreme mixing times, Akaike's weights are higher for model 1, but BIC is inconclusive. These findings suggest that signal attenuation depends on the three components simultaneously, only for some t_ms, while for the very short and long t_ms signal is attenuated mostly due to diffusion in two compartments. Considering that D_is for $t_m \to 0$ are of the order of $\sim 1 \times 10^{-9}$, $\sim 1 \times 10^{-10}$, $\sim 1 \times 10^{-11}$, it is supposed that for short t_ms, the signal is attenuated mostly by the fastest and the intermediate components, while for long t_ms by the intermediate and slowest ones.

To find out for which diffusion weighting, b, the signal from the fastest component is completely attenuated and for which b the slowest one starts to contribute to the total signal attenuation, we simulated diffusion signal behavior E_1/E_{01}, E_2/E_{02} and E_3/E_{03} in compartment 1 (the fastest diffusion, extracellular water), 2 (intermediate diffusion, cytoplasm) and 3 (the slowest diffusion, different cellular organelles), respectively. Then, $E_{1,2,3}/E_0$ was analyzed. However, a particle's diffusive behavior will be different in different geometries (i.e., planar, spherical or cylindrical). For this reason, compartments had to be matched with a concrete water pools and their geometry characterized by size, shape, molar fractions and self-diffusion coefficients. The preliminary information about compartments was taken from the TDDCs resulting from the fitting of model 2.

3.3. Relating Compartments with Cellular Structures

Firstly, the three compartments were characterized by the approximate self-diffusion coefficients D_{0i} and sizes R_i. Considering that D_1 is rather constant and similar to D_{bulk}, the first compartment was assigned to the extracellular water assumed earlier, with $D_{01} \approx D_{b1} \approx 1 \times 10^{-9}$ m^{2}s^{-1}. Since $D_1 \approx$ const., E_1/E_{01} (b) obtainment did not require the simulation of random walks in extracellular space in order to determine $D_1(t_m)$ from root-mean-square displacement. Intermediate and slow components show typical S-shape decay (Figure S3) and regions I and II can be recognized (Figure 2B)). Equations (4) and (5) were fitted to the regions I and II, respectively. For the diffusion coefficient of cytoplasm, D_2, the two curves merge perfectly at t_m = 5 ms. D_{02} obtained from the fitting of (4) was equal to 0.676 ± 0.041 × 10^{-9} m^{2}s^{-1}, while compartment size R_2 from the fitting of (5) was equal to 2.79 ± 0.11 µm. The reason why the second's compartment size is better determined from (5) than from the S_2/V_2 will be explained in Section 4.4. For the slowest component, (4) was fitted in the range 0.2 ms to 2 ms, i.e., the first point after the plateau in region I, which delivered D_{03} = 0.095 ± 0.011 × 10^{-9} m^{2}s^{-1}. A linear part of TDDC is clearly visible in the range of t_m = 0.8–40 ms. The lines fitted in the region I and II merge satisfactorily at $t_m \cong$ 1.5 ms. As in the case of the intermediate component, an allometric function was fitted that yielded a compartment size R_3 = 0.277 ± 0.048 µm.

Molar populations, p_i, in the range of 0.2–7 ms do not lie on the fitted lines. For t_m < 10 ms they are chaotically distributed, which results from the application of model 2 in the whole range of b-values and t_m. p_is tend to decrease mono-exponentially from 10 ms for all compartments, where (8) was fitted. The poor fit of a mono-exponential function to the p_3 suggests that $p_3(t_m)$ dependency has a bi-exponential character. However, due to the erroneous p_1 and p_2, the short-time behavior of the p_is form model 2 is not analyzed, and therefore, there is no need for bi-exponential fitting. Mono-exponential fitting delivered approximate equilibrium molar fractions p_{01} = 0.3513 ± 0.0073, p_{02} = 0.6501 ± 0.0089 and p_{03} = 0.0648 ± 0.0037 for compartments 1, 2 and 3, respectively. The sum of p_{0i} > 1, which is due to the fitting three components for high t_m. This, together with short/intermediate-time behavior, is further explained in the next subsection.

Identification of cellular structures associated with the third compartment was based on the comparison of R_3, p_{03} and D_{03} with literature values shown in Table 1. Taking into consideration that $p_{03}/p_{02} \approx 0.1$, ratios of total volume of structure and intracellular volume, f, as well as $f \cdot p_{02}$ are presented. Most of the structures are characterized by the self-diffusion coefficient similar to that of the second component—cytoplasmic water. D_{03} is of the same order of magnitude as D_0 of a cell wall and nucleus. Considering the determined D_{03} and R_3, it is possible that the third compartment contains an averaged signal coming from several structures. RW simulations were conducted separately for cytoplasm, nucleus, mitochondrion, vacuole and the cell wall. Calculated TDDCs are presented in Figure 3.

Table 1. Literature values of parameters characterizing cellular structures in yeast cell; N_s—number of structures in a single cell, V_t—total volume calculated from geometrical calculations, f—total volume and intracellular space volume ratio, D_0—self-diffusion coefficient of water in the structure found in the literature, p_{02}—equilibrium molar fraction of intracellular water.

Cell Structure	Size (µm)	N_s	V_t (µm^3)	f	D_0 (×10^{-9} m^2/s)	$f\,p_{02}$
Whole cell	~3	1	113	–	–	–
Intracellular space (whole cell without CW)	2.82–2.92	1	93.9–104	1	~0.5–0.7 [5,6,9,19]	0.65
Nucleus	1 [20,21]	1	4.19	0.04	~0.01–0.1 [22], 0.23 (erythrocyte) [23], 0.04 (oligonucleotides) [24]	0.026–0.029

Table 1. *Cont.*

Cell Structure	Size (μm)	N_s	V_t (μm^3)	f	D_0 (×10^{-9} m^2/s)	fp_{02}
Cell Wall (CW) and cell membrane (combined)	0.0792–0.180 [25]	1	8.72–19.2	0.08–0.204	~0.03 (weighted mean of CW and cell membrane)	0.054–0.133
Cell membrane	0.0092 [26]	1	0.922–0.989	0.00989–0.00922	0.44 (water between lipid bilayer), <0.0006 (lipids) [27]	0.0062–0.0063
Cell Wall (CW)	0.070–0.1708 [28]	1	7.73–18.2	0.07–0.194	0.032 ± 0.014 (Carboxyfloresceine in Thale cress) [29]	0.048–0.126
Mitochondrion	0.25 [30,31]	2.3 [32]	0.151	0.0014–0.0016	0.58 (liver mitochondrion) [23], ~0.01–0.1 D_{bulk} [33]	0.00104
Vacuole	1 [34]	2.7 [35]	11.3	0.11–0.12	0.34 (Besidiomycete fungi at 20 °C) [36], 1.7 (apples) [37]	0.0704–0.0783

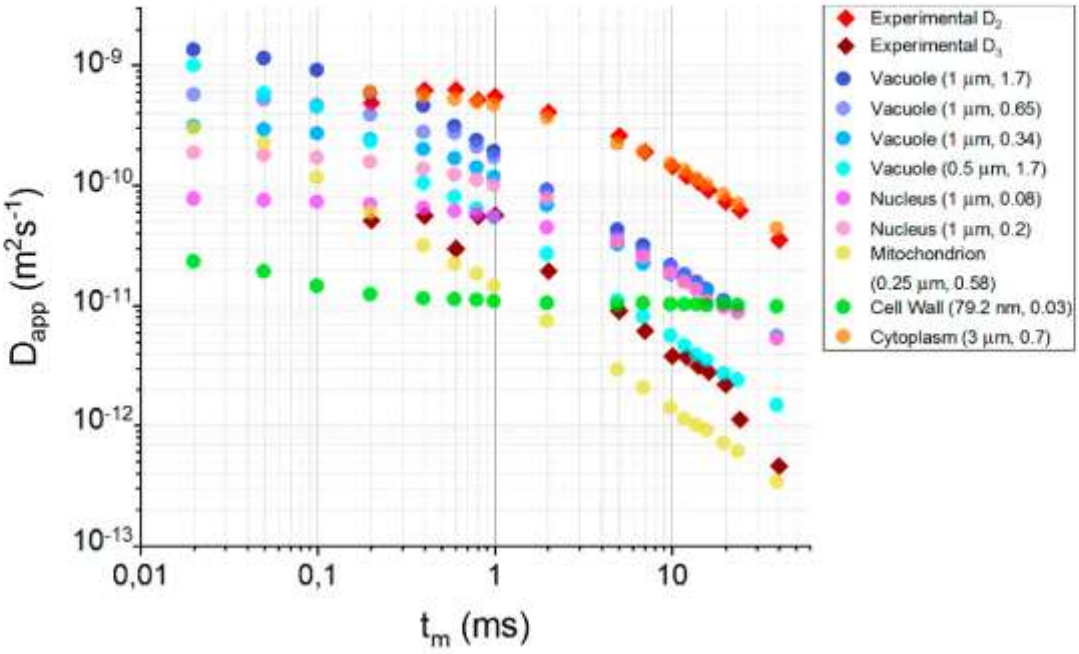

Figure 3. Time-Dependent Diffusion Coefficients (TDDCs) obtained in the experiments with comparison to simulations conducted for cytoplasm and cellular organelles; the legend presents the name of the structure with its size and literature value of self-diffusion coefficient in units $\cdot 10^{-9}$ m^{2}s^{-1} put in the bracket.

3.4. Simulation of the Diffusion Behavior in Cells

Diffusion coefficients simulated for different water pools in the sample are shown in Figure 3. In the next step, with the use of these coefficients, we simulated signal intensities, which are shown in Figure 4. As we can see, cellular structures do not significantly attenuate the total signal for $b < b_{16}$ (null attenuation from the third compartment), for $b < b_{13}$ and for $b < b_8$ for t_m = 0.2, 0.4 and 0.6 ms, respectively. In these ranges, two-compartmental model 1 can be applied instead of the more parametric model 2, where the intercept y_0 reflects non-attenuating p_3. However, for t_m = 0.6 ms, seven points seem to be too few (erroneous fitted parameters), thus, one of the parameters had to

be constrained (in our case we arbitrarily chose D_1). The signal from extracellular space is rapidly attenuated for $t_m > 2$ ms. This signal is virtually null for the fourth, third and the second b-value for t_ms equal to 5–7 ms, 10–24 ms and 40 ms, respectively. This means that the first component obtained from the fitting of model 2 to the experimental attenuation curves (Figure 5A) was fitted to only several points. It is highly probable that for higher t_m, the first exponent was partly fitted to the points for which in practice the attenuation came from the second compartment. As a result, fitting could deliver D_1, but also p_1, which are associated partly with the first compartment and partly with the second (i.e., averaged D_1 and p_1). In consequence, D_1 is underestimated, while p_1 overestimated (therefore, the sum of p_{0i} in the previous subsection was higher than 1). Hence, for $t_m > 2$ ms, it was reasonable to exclude the first 2, 3 or 4 points from the data set and to perform the less parametric, two-exponential fitting to the signal coming only from the second and the third compartment. This approach is called model 0B fitting, which delivered the experimental D_2 and D_3 values shown in Figure 3.

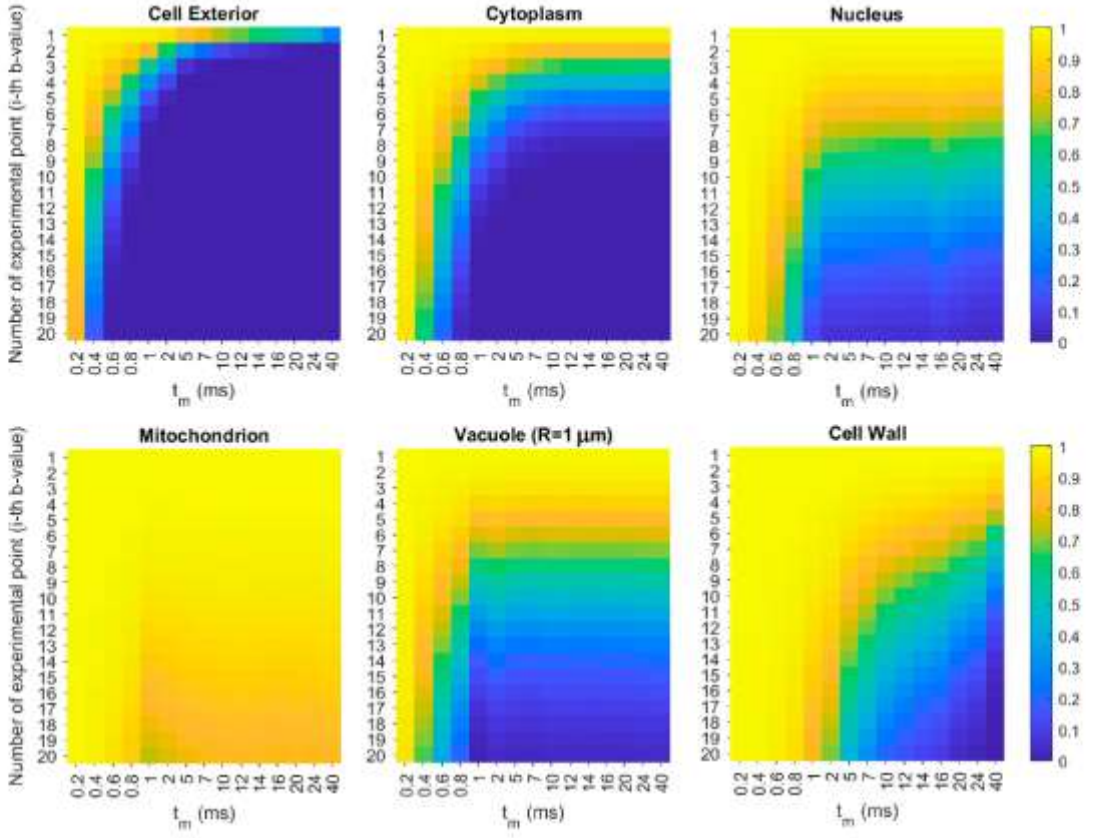

Figure 4. Simulated signal intensities in the given cell structure and extracellular space (E_j/E_{0j}, where j corresponds to the given pool (Cell Exterior, Cytoplasm, Nucleus, Mitochondrion, Vacuole and Cell Wall, while E_j and E_{0j} are signals registered with and without diffusion weighting) dependent on b-value and mixing times, t_m.

Attenuation of the signal coming from the cytoplasm is visible in the full range of t_m. For $t_m > 1$ ms, the signal from cytoplasm is null in the second half of experimental data points. For these points (b-values), the diffusion signals are still intensive for the nucleus, mitochondrion, vacuole and cell wall that comprise the third compartment. Hence, the two-exponential fitting seems to be a good approach, since the number of fitted parameters in each half is a few times lower than the number of data points.

In Figure 3 we can see that the experimental D_2s coincide almost perfectly with the D_2s obtained in the simulations, which confirms that the second compartment is associated with cytoplasm. Figure 3 also shows apparent diffusion coefficients obtained in the simulations for the cell's structures with

comparison to the experimental third component, D_3. Considering the amounts of signal in the organelles (Figure 4) and the alignment of the experimental D_3 with respect to the simulated TDDCs of organelles (Figure 3), the third compartment is probably associated with all of these organelles; however, in the experiment we can observe the averaged signal, D_3. Moreover, the contribution of each organelle will depend on their signal's attenuation rate for a given t_m.

3.5. Extraction of Compartmental Characteristics from TDDCs

Based on Figure 4, it was possible to approximately identify the b-values for each t_m, for which the signal from the first compartment is attenuated. Fitting the sum of two exponents in this range was called model 0B fitting. The choice of this approach was explained in the previous section. The sample's microgeometry was characterized based on TDDCs and molar fractions decays obtained from the fitting of model 0B for $t_m > 2$ ms (Figure 5). This approach delivered compartment sizes $R_2 = 2.252 \pm 0.053$ µm and $R_3 = 0.277 \pm 0.058$ µm. The equilibrium of molar fractions calculated from interpolation of lines obtained from the fitting of (8) were $p_{01} = const. = 0.2188 \pm 0.0075$, $p_{02} = 0.6959 \pm 0.0052$, $p_{03a} = 0.070 \pm 0.021$ and $p_{03b} = 0.060 \pm 0.028$ (yielding total $p_{03} = 0.130 \pm 0.035$), while residence times $\tau_2 = 390 \pm 56$ ms, $\tau_{3a} = 3.3 \pm 2.0$ ms and $\tau_{3b} = 39 \pm 28$ ms. In the case of extracellular water, it was not possible to genuinely determine water lifetimes from the (8) for t_ms for which the extracellular signal is not completely attenuated ($D_1(t_m)$ and $p_1(t_m)$ are approximately constant there—see the red lines in Figure 5). In practice, using model 0B over model 2 allows a more accurate determination of D_2 and D_3, which results in slightly different compartments sizes, as well as p_2 and p_3, which leads to the obtainment of residence times that are up to two times higher.

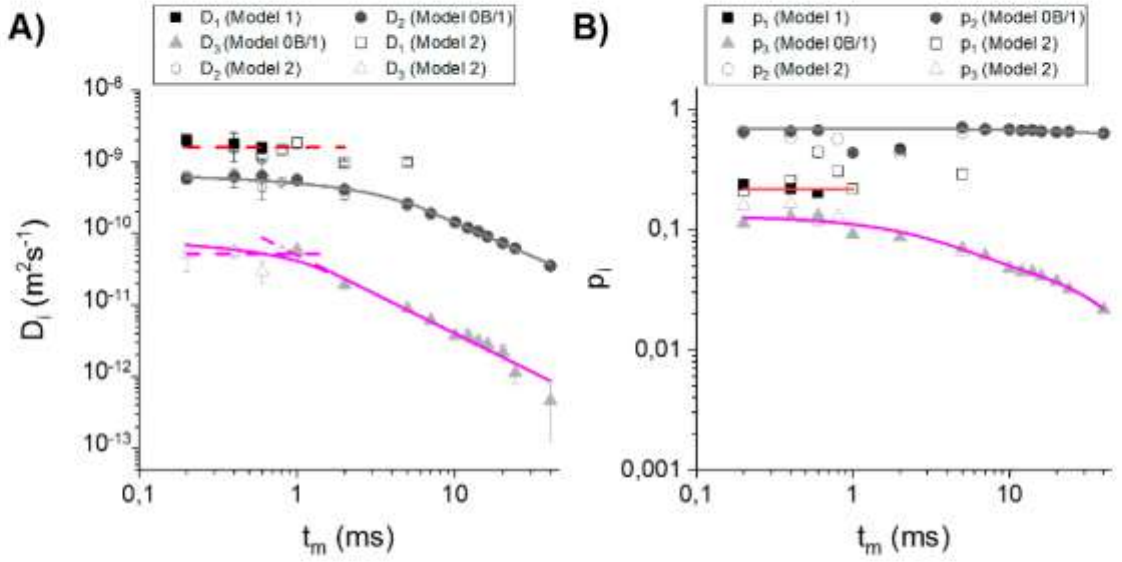

Figure 5. TDDCs (**A**) and molar fractions (**B**) of the three compartments obtained from the fitting of model 0B in the range $t_m \gg \tau$ for which t_m is equal to diffusion time. Additionally, results from the fitting of model 2 are presented.

4. Discussion

NMR diffusometry was performed for several mixing times, which were much smaller than the lifetimes of water molecules in the extra- and intracellular space reported in the literature for yeast [5,11,38]. Based on this knowledge, we assumed that there is no exchange between the interior and exterior of the cell during the experiments. The very strong magnetic field gradient imposed very large b-values (Table S1) that significantly exceeded 5×10^9 sm^{-2}, above which it is said that the intracellular signal can be predominantly detected [39]. Such a strong diffusion weighting led us to suppose that

there was another, very slowly diffusing component to be detected. We qualitatively compared the three diffusion models in yeast: two-compartmental (or Kärger model [40], which is a simple model of diffusion in two compartments between which water exchanges; model 0), two-compartmental with intercept (model 1) and three-compartmental (model 2). Model 0 was not satisfactory, especially for t_ms for which b values exceeded ~1×10^{10} sm^{-2}, and was excluded from further analysis. In the next step, model 1 and model 2 were qualitatively as well as quantitatively compared via AIC and BIC (Figure S4). Inconclusive results for extreme t_ms indicated that in our experiments different components influence signal attenuation depending on the b-value range. Identification of those ranges was possible after RW simulations (Figures 3 and 4) with the application of the literature values of sizes and self-diffusion coefficients of yeast's cellular structures (Table 1). Knowledge of the approximate b-values for which extracellular water is attenuated allowed us to apply the simpler, two-compartmental model (model 0B) associated with the cytoplasm and cellular organelles.

4.1. Violation of the $t_m \gg \tau$ Condition

TDDC analysis requires the fulfillment of the Short Gradient Pulse (SGP) or in other words- $t_m \gg \tau$ condition. In our experiments, the condition was violated for some experimental points τ_i for $t_m < 1$ ms, where t_m was not equal to the real diffusion time, $t_d = \left(t_m + \frac{2}{3}\tau\right)$ and t_d was not constant during the acquisition of the single signal attenuation curve. However, the fitting lines in the region I and II connect almost perfectly, while the points simulated based on the fitted parameters coincide with the experimental data. Mean error in the short-time regime was equal to ~11% (t_m = 0.2–1 ms). It is possible that taking into account all of the cellular organelles in the cellular geometry modeling during the simulations of RW would reduce the mean error. More intracellular restrictions would cause shorter root-mean-square displacements and, in consequence, slightly higher D_2s, like those obtained experimentally. More ambiguous values can be observed for the $p_i(t_m)$ dependence, which is a smooth, single exponential dependence only above the short-time limit. It is hard to say whether the evident two-exponential $p_i(t_m)$ dependency or the points not lying on the fitted lines result from the erroneous fit, physiological processes (namely diffusive exchange) in the system or the non-compliance of the time-related requirements ($t_d \neq const.$). Based on these observations we can say that under conditions of $t_m \gg \tau$ violation causing $t_d \neq const.$, distortions are visible for the molar fractions, while for $D_i(t_m)$ they are minor.

4.2. Comparison of the Diffusion Models

As shown in the Results section, three compartments cannot be characterized in the full range of b-values by using model 1, because the observations show that the 2% drop of signal coming from an organelle with a molar fraction of several percent is already visible in the experiment with high SNR (in this work—128 scans). The intercept values in model 1 were equal to 10% of the total signal, which is a significant amount considering the capabilities of a NMR-MoUSE system to detect very slow (D~10^{-15} m^{2}s^{-1}), low-populated components (even 1% of the total population according to Williamson [41]). Model 2, which delivers smooth TDDC, but biased parameters, can be applied only for the determination of approximate values of parameters. The results suggested that signal attenuation results from the three different components depending on the t_m range—fast and intermediate for short t_ms (low b-values) and intermediate and slow for longer t_ms (high b-values), forcing interval fitting. Fitting the simpler model 1 in the interval of low b-values and low t_m yielded more accurate values of $D_{1,2}$ and $p_{1,2}$ associated with extracellular water and cytoplasm. The second interval included attenuation due to the diffusion in cytoplasm and cellular structures and embraced b-values for which extracellular signal is fully attenuated. In this interval, the fitting of the simpler model 0B was beneficial and delivered more accurate parameters in comparison to model 2 as mentioned in Section 3.5.

Interval fitting using model 1 and model 0B over model 2 was advantageous due to the less fitted parameters and reduced risk of fitting a component to the points, for which this component is attenuated in reality. The percentage differences between the fitted parameters from the models 2 and

0B were equal to 0.1–21.3% with a mean of 7.7%, 0.7–22.6% with a mean 9.0%, 0.1–37.9% with a mean of 10.1% and 0.1–10.2% with a mean of 7.6% for D_2, D_3, p_2 and p_3, respectively. In the case of parameters obtained from model 2 and 1, the percentage difference was equal to 4.9–31.3% with a mean of 14.7%, 0.1–42.4% with a mean of 17.5%, 14.7–54.6% with a mean of 28.1%, 2.4–52.0% with a mean of 28.1% and 0.1–10.2% with a mean of 7.6% for D_1, D_2, p_1, p_2 and p_3, respectively. The analysis shows that model 2 can be incorporated into the signal attenuation curve fitting in the whole range of applied t_ms and b-values yielding reasonable outcomes, especially when it is unable to identify the attenuation rate or signal amount associated with a particular component in a given range. A significant improvement due to the application of simpler models was observed particularly in the short-time regime and especially for molar fractions. From an analytical point of view, the improvement relies on the fact that by the elimination of 2/3/4 experimental points, the number of points per number of fitted parameters increases from 3.33 up to 4.75, while the total number of points, N (= 18, 17, 16), is much higher than the number of fitted exponents.

4.3. Characterization of the Compartments Based on TDDCs

Based on the TDDCs, compartment characteristics were obtained in Section 3.4. Additional information can be inferred from Figures 3 and 4. The first compartment visible in Figure 5 is associated with the extracellular water. For t_m = 0.2–1 ms, the mean diffusion coefficient $D_{01} = 1.64 \pm 0.15 \cdot 10^{-9}$ m^2s^{-1} (Figure 5A)), which is similar to the self-diffusion coefficient 1.6×10^{-9} m^2s^{-1} reported for extracellular fluid [5]. Extracellular space size cannot be accurately determined from (4) ($V_1/S_1 \cong R_1$ = 2.84 ± 0.36 μm), because there are very few data points for which the extracellular signal is still detectable, which means that the first exponent contains averaged information about the first and the second compartment and the obtained D_1s are underestimated. It cannot also be successfully compared with reported sizes, due to the significantly lower water content (~24% compared to 80% water content in the work of Suh [11], who obtained extracellular space sizes equal to 15–20 μm). Nonetheless, D_1 can be slightly time-dependent and R_1 can be reduced, because fresh yeast's extracellular space size is smaller than in commonly studied suspensions or sediments. Model 1 delivered $p_{01} = 0.2188 \pm 0075$, which is similar to the theoretical and experimental molar fractions of extracellular space reported by Conway and Downey [42] equal to 0.26 and 0.22–0.24, respectively. On the other hand, they reported that extracellular space can be increased to 0.33–0.34 and seen as a thick cell wall. This is in accordance with our analysis.

The second and third compartments are associated with different structures depending on the t_m. It is well-known that in the short-time regime (region I in Figure S3), the diffusion signal is independent of the microgeometry (free diffusion regime). Therefore, D_2 and D_3 in this regime will encompass all structures with a similar self-diffusion coefficient. In the short-time limit, the second compartment, D_2, reflects the diffusion signal in the cytoplasm ($D_{0,cytoplasm}$ equal to 0.5×10^{-9} m^2s^{-1} [19], up to 1.0×10^{-9} m^2s^{-1} [37]), vacuoles (if we assume a vacuolar size of 1 μm and $D_{0,vacuole}$ equal to 0.34×10^{-9} m^2s^{-1} [36] or $0.61 \cdot 10^{-9}$ m^2s^{-1} calculated based on the Stokes relation [19] using a vacuolar viscosity equal to 2.52 cP [43] or $1.7 \cdot 10^{-9}$ m^2s^{-1} [37]) and mitochondria (if we assume $D_{0,mitochondrion} = 0.58 \times 10^{-9}$ m^2s^{-1} [23]; however, it is the apparent diffusion coefficient calculated for water-mitochondria suspension). D_3 in the short-time limit can be connected with the nucleus ($D_{0,nucleus}$ = 0.01–0.1 $\times 10^{-9}$ m^2s^{-1}), cell wall combined with cellular membrane ($D_{0,CWSmembrane} = 0.03 \times 10^{-9}$ m^2s^{-1}) and mitochondrion (if we assume $D_{0,mitochondrion}$ = 0.01–0.1 D_{bulk}). This is well depicted in Figure 4, where experimental D_3 in the short-time regime lies near the nuclear (light and dark pink dots), cell wall's (green dots) and mitochondrion's (red dots) TDDCs. The very low fraction of mitochondrion volume in relation to the whole cell's volume suggests that its signal is of minor importance.

In the region II of TDDC (Figure S3), the diffusion signal becomes dependent on the confining geometry (localization regime). Thus, TDDCs will be associated with structures having similar sizes. First of all, D_3 will no longer depend on the nucleus signal. This is due to the fact that the nuclear pore complexes are relatively large (~100 nm [44]) and molecules up to 20–40 kDa can diffuse freely

through them [45]. The high permeability of the nuclear envelope leads to water residence time in the nucleus being very short (using the dependency of osmotic permeability versus permeant's radius obtained on the basis of the values presented by Paine for oocytes [46], nuclear water residence time in the conditions of osmotic gradient is approximately 0.03 ms, while it is ~0.1–1 ms when considering that the diffusive permeability is 4–70 times lower than osmotic one [47]). Hence, the $t_m > 1$ ms signal coming from the nucleus will already be mixed with the cytoplasm signal (motional averaging) and will contribute to the second compartment, D_2. D_3 above the short-time limit will mostly depend on the diffusion in vacuoles, but it is possible that their sizes are slightly smaller than those found in the literature (Table 1), which can be seen in Figure 3 (blue dots representing vacuolar radius equal to 0.5 µm). The transmission electron micrographs presented by Baba and Osumi [48] (for example Figure 5 therein) clearly show that vacuoles are significantly smaller than the nucleus and have a diameter of ~1 µm.

Incorporating theoretical $p_{01} = 0.2$ and sizes of structures determined in this study (the exception was the vacuole, for which we assume a radius of 0.5 µm), we estimated the expected molar fractions for each compartment. Based on the contributions to each compartment in the short-time limit, the determined fractions were equal to 0.69 and 0.11 for the second and third compartment, respectively. These values are in very good agreement with the experimental molar fractions obtained in the study. In the case of $p_3(t_m)$, similarly to the first compartment, bi-exponential dependence can also be seen. Fitting the second component to the $p_3(t_m)$ in the short-time regime delivers $p_{03} = 0.129 \pm 0.016$, which is even closer to the theoretical value of 0.11.

4.4. Characterization of the Sample's Microgeometry

The cell radius obtained from the fitting of (5) in region II in the study was $R_2 = 2.252 \pm 0.053$ µm, which is in very good agreement with the cell radius calculated from S_2/V_2 equal to 2.35 ± 0.40 µm. Small discrepancies may result from the effect of different surface-area and volume of the second compartment in the free and localization diffusion regime. Åslund reported a yeast cell radius of 2.48 µm [6], Tanner and Stejskal obtained a yeast cell diameter equal to 4.1 µm [9], while Cory obtained a radius of 5 µm [49] and Suh identified yeast cell radii equal to 2.3 ± 0.2, 3.0 ± 0.2 and 2.7 ± 0.2 µm for incubation times equal to 9, 24 and 48 h, respectively [11]. As we can see, our values are in the range of the abovementioned cell sizes. The difference between R_2 obtained from the fitting of (5) and from the S_2/V_2 results from the fact that signal from nucleus in the short-time limit is associated with the third compartment, not the second one. A cytoplasm is characterized by the self-diffusion coefficient $D_{02} = 0.692 \pm 0.060 \times 10^{-9}$ m^{2}s^{-1}, which is similar to the value for the intracellular self-diffusion coefficient reported in the literature for the two-compartmental model. For example, Tanner and Stejskal obtained a value of 0.68×10^{-9} m^{2}s^{-1} [9], while Aslund obtained a value of 0.65×10^{-9} m^{2}s^{-1} [6]. The slightly higher value may result from the SGP violation or from the fact that it is associated with relatively high diffusivity cytoplasm, not the whole cell interior.

The size of the third compartment in the short-time regime obtained in the study is a weighted mean size of the nucleus and cell wall as mentioned in Section 4.3. Assuming a literature value of the extracellular molar fraction $p_{01} = 0.2$ (and correspondingly $p_{02} = 1 - p_{01} = 0.8$), the molar weights of cellular structures were determined. Applying these values in a short-time limit, we estimated the weighted mean size $R_3 = 0.422$ µm, which is in a very good agreement with $R_3 = 0.415 \pm 0.016$ µm determined from S_3/V_3 from Mitra's relation fitted to $D_3(t_m)$. In the analysis of the region II of D_3, the estimated $R_3 = 0.278 \pm 0.040$ µm, which reflects the weighted mean size of the cell wall and the average vacuolar size. Based on the work of Baba [48] and our results, we can assume that *S. cerevisiae* cells in the studied sample also contained vacuoles with a radius of 0.5 µm or less.

4.5. Diffusive Permeabilities

The diffusive permeability of the vacuolar membrane P_{d3} was determined based on (7) and was equal to 2.38 ± 0.66 µm/s. This value is within the range of the two limiting values of permeability for

sphingomyelin/cholesterol and phosphatidylcholine/cholesterolbilayer membranes at 25 °C equal to 0.81 and 5.73 μm/s, respectively [38]. The diffusive permeability of yeast cell membrane P_{d2} determined based on (7) was equal to 1.93 ± 0.10 μm/s, which is very similar to 0.92 μm/s [38] and 0.185–1.35 μm/s [50]. Interestingly these values are relatively low compared to the value of 6.3 ± 0.6 μm/s estimated by Suh [11]. The same situation occurs for intracellular lifetimes reported to date, which differ among papers. Exemplary values are 0.833 s [38], 0.240 s, 0.450 s and 0.400 s [11], which are very similar to the value of 0.390 s determined in this work. All characteristic parameters for the model cell system used in the work are summarized in Table 2.

Table 2. Characteristic parameters for three compartments obtained in the study; *i* means the *i*-th compartment, D_0 is a self-diffusion coefficient, *S*/*V* is the Surface-area-to-Volume ratio, p_{0i} is the equilibrium molar fraction of compartment, τ is the lifetime of water, R_i is the compartment size, P_d is the diffusive permeability of the compartment's boundary.

i	D_{0i}(×10^{-9} m^2s^{-1})	S_i/V_i (μm^{-1})	P_{0i}	τ_i (s)	R_i (μm)	P_d (μm/s)
1	1.64 ± 0.15	–	0.2188 ± 0.0075	0.201 ± 0.039	–	–
2	0.692 ± 0.060	1.28 ± 0.22	0.6985 ± 0.0068	0.390 ± 0.056	2.252 ± 0.053	1.93 ± 0.10
3	0.095 ± 0.011	7.22 ± 0.28	0.070 ± 0.021 0.060 ± 0.028	3.3 ± 2.0 0.039 ± 0.028	0.277 ± 0.048	2.38 ± 0.66

5. Conclusions

An NMR-MoUSE with a very high steady gradient (24 T/m) was used in the characterization of living cells by means of diffusion NMR. The three-compartmental model was tested and favored for the diffusion in the middle range of applied t_ms. Accurate characterization of compartments was supplemented by random walk simulations and theoretical calculations supported by an extensive literature review. Complex analysis, including the theoretical behavior of diffusion and the analysis of biophysical processes in cells, was necessary to understand the physical results reflected by signal attenuations obtained in our system. This work shows that NMR diffusometry can be used to explore biophysical processes occurring far below the extra- and intracellular level. A very good level of agreement between the experimental and theoretical results proves that cellular organelles can be studied in terms of their biophysical properties by the application of NMR-MoUSE, something never previously achieved by diffusion NMR without the isolation of a given structure. Additionally, we presented the signal behavior depending on the SSE sequence parameters in the work, which can be used as a guide for choosing the appropriate values of *b*-values or t_m for measurements oriented towards specific compartment studies.

In the MoUSE system, in which RF pulses are applied with a constantly present high gradient, the excited slice thickness is of the order of 100 micrometers. Considering this fact, detecting a signal from low-populated components such as water in nuclei is beneficial with regard to the small amount of samples that scientists often have at their disposal. To sum up, self-diffusion coefficients, sizes and molar fractions of extracellular water, cytoplasm and cellular structures can be obtained from the analysis of a time-dependent diffusion coefficient using single-sided NMR-MoUSE.

Supplementary Materials: The following are available online at http://www.mdpi.com/2073-4409/9/9/2124/s1, Section S1. Materials and methods, Figure S1: The construction scheme of the NMR-MoUSE device, Figure S2: The Stimulated Spin Echo (SSE) pulse sequence used in the experiment. Table S1: Parameters of the protocol used in diffusion measurements. Figure S3: Log-log plot of diffusion coefficient dependency on diffusion time, Section S2. Theory of model comparison based on Akaike's (AIC) and Bayesian Information Criterion (BIC), Figure S4: Results from the comparison of Model 1 and Model 2 based on Akaike's weights and ΔBIC.

Author Contributions: Conceptualization, A.T.K.; methodology, A.T.K. and W.M.; validation, A.T.K. and W.M.; formal analysis, W.M.; investigation, W.M.; resources, A.T.K.; data curation, W.M. and A.T.K.; writing—original draft preparation, W.M.; writing—review and editing, A.T.K.; visualization, W.M.; supervision, A.T.K.; project

administration, A.T.K.; funding acquisition, A.T.K. All authors have read and agreed to the published version of the manuscript.

Funding: This research was funded by the National Centre of Research and Development (contract No. STRATEGMED2/265761/10/NCBR/2015. W.M. was partly supported by the EU Project POWR.03.02.00-00-I004/16.

Acknowledgments: The authors are grateful to I. Habina for the fruitful discussions and help with planning the experiments.

Conflicts of Interest: The authors declare no conflict of interest.

References

1. Setter, T.L.; Flannigan, B.A. Water deficit inhibits cell division and expression of transcripts involved in cell proliferation and endoreduplication in maize endosperm. *J. Exp. Bot.* **2001**, *52*, 1401–1408. [CrossRef] [PubMed]
2. Ames 3rd, A.; Nesbett, F.B. Pathophysiology of Ischemic Cell Death: II. Changes in Plasma Membrane Permeability and Cell Volume. *Stroke* **1982**, *14*, 227–233. [CrossRef] [PubMed]
3. Reuss, L. Water Transport Across Cell Membranes. In *eLS*; John Wiley Sons Ltd.: Hoboken, NJ, USA, 2012; p. 8. [CrossRef]
4. Latour, L.L.; Mitra, P.P.; Kleinberg, R.L.; Sotak, C.H. Time-Dependent Diffusion Coefficient of Fluids in Porous Media as a Probe of Surface-to-Volume Ratio. *J. Magn. Reson.* **1993**, *101*, 342–346. [CrossRef]
5. Åslund, I.; Nowacka, A.; Nilsson, M.; Topgaard, D. Filter-exchange PGSE NMR determination of cell membrane permeability. *J. Magn. Reson.* **2009**, *200*, 291–295. [CrossRef] [PubMed]
6. Åslund, I.; Topgaard, D. Determination of the self-diffusion coefficient of intracellular water using PGSE NMR with variable gradient pulse length. *J. Magn. Reson.* **2009**, *201*, 250–254. [CrossRef] [PubMed]
7. Cho, C.; Hong, Y.; Kang, K.; Volkov, V.I.; Skirda, V.; Lee, C.J.; Lee, C. Water self-diffusion in Chlorella sp. studied by pulse field gradient NMR. *Magn. Reson. Imaging* **2003**, *21*, 1009–1017. [CrossRef]
8. Schoberth, S.M.; Ba, N.; Kra, R. Pulsed High-Field Gradient in Vivo NMR Spectroscopy to Measure Diffusional Water Permeability in Corynebacterium glutamicum. *Anal. Biochem.* **2000**, *279*, 100–105. [CrossRef]
9. Tanner, J.E.; Stejskal, E.O. Restricted Self-Diffusion of Protons in Colloidal Systems by the Pulsed-Gradient, Spin-Echo Method. *J. Chem. Phys.* **1968**, *49*, 1768–1777. [CrossRef]
10. Latour, L.L. Time-dependent diffusion of water in a biological model system. *Proc. Natl. Acad. Sci. USA* **1994**, *91*, 1229–1233. [CrossRef]
11. Suh, K.; Hong, Y.; Skirda, V.D.; Volkov, V.I. Water self-diffusion behavior in yeast cells studied by pulsed field gradient NMR. *Biophys. Chem.* **2003**, *104*, 121–130. [CrossRef]
12. Fischer, E.; Kimmich, R. Constant time steady gradient NMR diffusometry using the secondary stimulated echo. *J. Magn. Reson.* **2004**, *166*, 273–279. [CrossRef] [PubMed]
13. Rata, D.G.; Casanova, F.; Perlo, J.; Demco, D.E.; Blümich, B. Self-diffusion measurements by a mobile single-sided NMR sensor with improved magnetic field gradient. *J. Magn. Reson.* **2006**, *180*, 229–235. [CrossRef] [PubMed]
14. Stanisz, G.J.; Szafer, A.; Wright, G.A.; Henkelman, R.M. An Analytical Model of Restricted Diffusion in Bovine Optic Nerve. *Magn. Reson. Med.* **1997**, *37*, 103–111. [CrossRef] [PubMed]
15. Blümich, B.; Haber-Pohlmeier, S.; Zia, W. *Compact NMR*, 1st ed.; Walter deGruyter GmbH: Berlin, Germany, 2014; ISBN 9783110266283.
16. Wei, D.; Jacobs, S.; Modla, S.; Zhang, S.; Young, C.L.; Cirino, R.; Czymmek, K. High-resolution three-dimensional reconstruction of a whole yeast cell using focused-ion beam scanning electron microscopy. *Biotechniques* **2012**, *54*, 41–48. [CrossRef] [PubMed]
17. Mitra, P.P.; Sen, M.P.N.; Schwartz, L.M.; Doussal, P. Le Diffusion Propagator as a Probe of the Structure of Porous Media. *Phys. Rev. Lett.* **1992**, *68*, 3555–3558. [CrossRef]
18. Obata, T.; Kershaw, J.; Tachibana, Y.; Miyauch, T.; Abe, Y.; Shibata, S.; Kawaguchi, H.; Ikoma, Y.; Takuwa, H.; Aoki, I. Comparison of diffusion-weighted MRI and anti-Stokes Raman scattering (CARS) measurements of the inter-compartmental exchange- time of water in expression- controlled aquaporin-4 cells. *Sci. Rep.* **2018**, *8*, 1–11. [CrossRef]
19. Novak, I.L.; Kraikivski, P.; Slepchenko, B.M. Diffusion in Cytoplasm: Effects of Excluded Volume Due to Internal Membranes and Cytoskeletal Structures. *Biophys. J.* **2009**, *97*, 758–767. [CrossRef]

20. Jorgensen, P.; Edgington, N.P.; Schneider, B.L.; Rupes, I.; Tyers, M.; Futcher, B. The Size of the Nucleus Increases as Yeast Cells Grow. *Mol. Biol. Cell* **2007**, *18*, 3523–3532. [CrossRef]
21. Oeffinger, M.; Zenklusen, D. To the pore and through the pore: A story of mRNA export kinetics. *Biochim. Biophys. Acta* **2012**, *1819*, 494–506. [CrossRef]
22. Misteli, T. Physiological importance of RNA and protein mobility in the cell nucleus. *Histochem. Cell Biol.* **2008**, *129*, 5–11. [CrossRef]
23. García-Pérez, A.; López-Beltrán, E.; Klüner, P.; Luque, J.; Ballesteros, P.; Cerdán, S. Molecular crowding and viscosity as determinants of translational diffusion of metabolites in subcellular organelles. *Arch. Biochem. Biophys.* **1999**, *362*, 329–338. [CrossRef] [PubMed]
24. Politz, J.C.; Browne, E.S.; Wolf, D.E.; Pederson, T. Intranuclear diffusion and hybridization state of oligonucleotides measured by fluorescence correlation spectroscopy in living cells. *Proc. Natl. Acad. Sci. USA* **1998**, *95*, 6043–6048. [CrossRef] [PubMed]
25. Milani, M.; Batani, D.; Bortolotto, F.; Botto, C.; Baroni, G.; Cozzi, S.; Costato, M.; Pozzi, A.; Salsi, F.; Allott, R.; et al. *Differential Two Colour X-ray Radiobiology of Membrane/Cytoplasm Yeast Cells; TMR Large-Scale Facilities Access Programme*; Rutherford Appleton Laboratory: Milan, Italy, 1998.
26. Schneiter, R.; Brügger, B.; Sandhoff, R.; Zellnig, G.; Leber, A.; Lampl, M.; Athenstaedt, K.; Hrastnik, C.; Eder, S.; Daum, G.; et al. Electrospray ionization tandem mass spectrometry (ESI-MS/MS) analysis of the lipid molecular species composition of yeast subcellular membranes reveals acyl chain-based sorting/remodeling of distinct molecular species en route to the plasma membrane. *J. Cell Biol.* **1999**, *146*, 741–754. [CrossRef] [PubMed]
27. Karakatsanis, P.; Bayerl, T.M. Diffusion measurements in oriented phospholipid bilayers by 1NMR in a static fringe field gradient. *Phys. Rev. E* **1996**, *54*, 1785–1790. [CrossRef]
28. Srinorakutara, T. Determination of yeast cell wall thickness and cell diameter using new methods. *J. Ferment. Bioeng.* **1998**, *86*, 253–260. [CrossRef]
29. Kramer, E.; Frazer, N.; Baskin, T. Measurement of diffusion within the cell wall in living roots of Arabidopsis thaliana. *J. Exp. Bot.* **2007**, *58*, 3005–3015. [CrossRef]
30. Partikian, A.; Ölveczky, B.; Swaminathan, R.; Li, Y.; Verkman, A.S. Rapid Diffusion of Green Fluorescent Protein in the Mitochondrial Matrix. *J. Cell Biol.* **1998**, *140*, 821–829. [CrossRef]
31. Jiang, H.; Song, C.; Chen, C.-C.; Xu, R.; Raines, K.S.; Fahimian, B.P.; Lu, C.-H.; Lee, T.-K.; Nakashima, A.; Urano, J.; et al. Quantitative 3D imaging of whole, unstained cells by using X-ray diffraction microscopy. *Proc. Natl. Acad. Sci. USA* **2010**, *107*, 11234–11239. [CrossRef]
32. Visser, W.; van Spronsen, E.; Nanninga, N.; Pronk, J.; Gijs Kuenen, J.; van Dijken, J. Effects of growth conditions on mitochondrial morphology in Saccharomyces cerevisiae. *Antonie Leeuwenhoek* **1995**, *67*, 243–253. [CrossRef]
33. López-Beltrán, E.A.; Maté, M.J.; Cerdán, S. Dynamics and Environment of Mitochondrial Water as Detected by 1H NMR. *J. Biol. Chem.* **1996**, *271*, 10648–10653. [CrossRef]
34. Michaillat, L.; Baars, T.; Mayer, A. Cell-free reconstitution of vacuole membrane fragmentation reveals regulation of vacuole size and number by TORC. *Mol. Biol. Cell* **2012**, *23*, 881–895.
35. Chan, Y.-H.M.; Marshall, W.F. Organelle Size Scaling of the Budding Yeast Vacuole Is Tuned by Membrane Trafficking Rates. *Biophys. J.* **2014**, *106*, 1986–1996. [CrossRef] [PubMed]
36. Darrah, P.R.; Tlalka, M.; Ashford, A.; Watkinson, S.C.; Fricker, M.D. The Vacuole System Is a Significant Intracellular Pathway for Longitudinal Solute Transport in Basidiomycete Fungi. *Eukaryot. Cell* **2006**, *5*, 1111–1125. [CrossRef] [PubMed]
37. van Dusschoten, D.; de Jager, P.A.; Van As, H. Extracting Diffusion Constants from Echo-Time-Dependent PFG NMR Data Using Relaxation-Time Information. *J. Magn. Reson. Ser. A* **1995**, *116*, 22–28. [CrossRef]
38. Zhang, Y.; Poirier-quinot, M.; Springer, C.S.; Balschi, J.A. Active Trans-Plasma Membrane Water Cycling in Yeast Is Revealed by NMR. *Biophys. J.* **2011**, *101*, 2833–2842. [CrossRef] [PubMed]
39. Pfeuffer, J.; Provencher, S.W.; Gruetter, R. Water diffusion in rat brain in vivo as detected at very large b values is multicompartmental. *Magn. Reson. Mater. Physics, Biol. Med.* **1999**, *8*, 98–108. [CrossRef]
40. Kärger, J. NMR Self-Diffusion studies in heterogeneous systems. *Adv. Colloid Interface Sci.* **1985**, *23*, 129–148. [CrossRef]

41. Williamson, N.H.; Ravin, R.; Benjamini, D.; Merkle, H.; Falgairolle, M.; Donovan, M.J.O.; Ide, D.; Cai, T.X.; Ghorashi, N.S.; Bai, R.; et al. Magnetic resonance measurements of cellular and sub-cellular membrane structures in live and fixed neural tissue. *eLife* **2019**, *8*, e51101. [CrossRef]
42. Conway, E.J.; Downey, M. An Outer Metabolic Region of the Yeast Cell. *Biochem. J.* **1950**, *47*, 347–355. [CrossRef]
43. Puchkov, E.O.; Wiley, J. Brownian motion of polyphosphate complexes in yeast vacuoles: Characterization by fluorescence microscopy. *Yeast* **2010**, *27*, 309–315. [CrossRef]
44. Wente, S.R.; Rout, M.P. The Nuclear Pore Complex and NuclearTransport. *Cold Spring Harb. Perspect. Biol.* **2010**, *2*, 1–19. [CrossRef] [PubMed]
45. Miao, L.; Schulten, K. Probing a Structural Model of the Nuclear Pore Complex Channel through Molecular Dynamics. *Biophys. J.* **2010**, *98*, 1658–1667. [CrossRef] [PubMed]
46. Paine, P.L.; Moore, L.C.; Horowitz, S.B. Nuclear envelope permeability. *Nature* **1975**, *254*, 109–114. [CrossRef] [PubMed]
47. Fraser, P.A. Diffusional and Osmotic Permeability to Water. In *Physiology and Pharmacology of the Blood-Brain Barrier*; Bradbury, M.W.B., Ed.; Springer-Verlag: Berlin/Heidelberg, Germany, 1992; pp. 53–64. ISBN 978-3-642-76896-5.
48. Baba, M.; Osumi, M. Transmission and Scanning Electron Microscopic Examination of Intracellular Organelles in Freeze-Su bstituted Kloeckera and Saccharomyces cerevisiae Yeast Cells. *J. Electron Microsc. Tech.* **1987**, *5*, 249–261. [CrossRef]
49. Cory, D.G.; Garroway, A.N. Measurement of Translational Displacement Probabilities by NMR: An Indicator of Compartmentation. *Megnetic Reson. Med.* **1990**, *14*, 435–444. [CrossRef]
50. Avilova, I.A.; Vasil, S.G.; Rimareva, L.V.; Serba, E.M.; Volkova, L.D.; Volkov, V.I. Water Metabolism in Cells of Saccharomyces Cerevisiae of Races Y-3137 and Y-3327, According to Pulsed-Field Gradient NMR Data. *Russ. J. Phys. Chem. A* **2015**, *89*, 710–714. [CrossRef]

Received: 27 August 2021 | Revised: 4 November 2021 | Accepted: 22 December 2021

DOI: 10.1111/jcmm.17178

ORIGINAL ARTICLE

WILEY

Nuclear magnetic resonance footprint of Wharton Jelly mesenchymal stem cells death mechanisms and distinctive in-cell biophysical properties in vitro

Artur T. Krzyżak[1] | Iwona Habina-Skrzyniarz[1] | Weronika Mazur[1,2] | Maciej Sułkowski[3] | Marta Kot[3] | Marcin Majka[3]

[1]Faculty of Geology, Geophysics and Environmental Protection, AGH University of Science and Technology, Cracow, Poland

[2]Faculty of Physics and Applied Computer Science, AGH University of Science and Technology, Cracow, Poland

[3]Department of Transplantation, Faculty of Medicine, Institute of Pediatrics, Jagiellonian University Medical College, Cracow, Poland

Correspondence
Artur T. Krzyżak, Faculty of Geology, Geophysics and Environmental Protection, AGH University of Science and Technology, al. Mickiewicza 30, 30-059 Cracow, Poland.
Email: akrzyzak@agh.edu.pl

Funding information
Narodowe Centrum Badań i Rozwoju, Grant/Award Number: POWR.03.02.00-00-I004/16 and STRATEGMED2/265761/10/NCBR/2015

Abstract

The importance of the biophysical characterization of mesenchymal stem cells (MSCs) was recently pointed out for supporting the development of MSC-based therapies. Among others, tracking MSCs in vivo and a quantitative characterization of their regenerative impact by nuclear magnetic resonance (NMR) demands a full description of MSCs' MR properties. In the work, Wharton Jelly MSCs are characterized in a low magnetic field (LF) in vitro by using different approaches. They encompass various settings: MSCs cultured in a Petri dish and cell suspensions; experiments- 1D-T_1, 1D-T_2, 1D diffusion, 2D T_1-T_2 and D-T_2; devices- with a bore aperture and single-sided one. Complex NMR analysis with the aid of random walk simulations allows the determination of MSCs T_1 and T_2 relaxation times, cells and nuclei sizes, self-diffusion coefficients of the nucleus and cytoplasm. In addition, the influence of a single layer of cells on the effective diffusion coefficient of water is detected with the application of a single-sided NMR device. It also enables the identification of apoptotic and necrotic cell death and changed diffusional properties of cells suspension caused by compressing forces induced by the subsequent cell layers. The study delivers MSCs-specific MR parameters that may help tracking MSCs in vivo.

KEYWORDS
in vitro characterization, intracellular self-diffusion, magnetic resonance parameters, mesenchymal stem cells, single-sided NMR

1 | INTRODUCTION

Mesenchymal stem cells (MSCs) were discovered in the last century by Friedenstein. He observed that bone marrow contains cells that form fibroblast-like colonies in vitro.[1] Further studies revealed that MSCs are able to differentiate into different cell lineages namely osteo, chondro and adipo. They can be characterized by the expression of several markers like CD73, CD90 and CD105 and the lack of hematopoietic markers including CD45 and CD34.[2] Wharton Jelly MSCs, derived from human umbilical cord, represent promising source of stem cells able to differentiate into such cells types as astrocytes, adipocytes, myocytes, cardiomyocytes and neurons.[2,3]

Recently, MSCs attracted considerable attention in the biomedical field as they have been shown to ameliorate symptoms in a number of diseases including neurological and cardiovascular ones.[4,5] Most studies suggest that MSCs secrete numbers of factors

activating the regeneration processes in injured tissues.[6] For that purpose, MSCs will have to stay alive in the regenerating tissues for a prolonged period of time. However, we are still unable to efficiently trace MSCs in patients after transplantation. Due to the lack of full knowledge about their biology and behaviour after injection, the MSCs cannot be fully utilized in regenerative medicine. Thus, new methods that help to solve these problems are urgently needed. NMR enables the study of porous material or biological systems in a non-invasive manner and in vitro or in vivo conditions.[7,8] Tracking the migration of transplanted stem cells with the use of NMR techniques has several years of practice. However, most of the recent research is based on contrast agents labelling the cells,[9–11] T_2 relaxation times or diffusion coefficients, D, as biomarkers have only been used in a few papers.[12,13]

The long-term purpose of the study of live stem cells by means of truly non-invasive NMR, that is also without contrast agents, is twofold. First of all, it concerns the determination of specific parameters 'seen' by low field NMR (LF-NMR), such as relaxation times T_1, T_2, T_1-T_2 and D-T_2 maps, or diffusion coefficients, which are characteristic for Wharton Jelly MSCs. The proposed multi-parametric characterization is also implemented to obtain a set of MR parameters in order to minimize the possibility of overlapping signals from other cells. These parameters may be useful in-cell detection when studying animal models or patients by means of MRI in vivo. A similar approach was developed and implemented for porous and heterogeneous systems.[14,15] Secondly, NMR parameters characterizing in vitro cell suspensions can be used to determine their quantitative and qualitative characteristics, such as size, self-diffusion coefficient and viability. For this purpose, besides results from the characterization of MSCs by LF-NMR, a single-sided Mobile Universal Surface Explorer (MoUSE) was used. MoUSE allows the study of a sample using an extremely strong magnetic field gradient (~24 T m^{-1}) and short diffusion times, which leads to higher diffusion weighting without coming into motional averaging between compartments. New promising cell studies, carried out under these conditions and considering several signal components from cell samples, have appeared recently.[16,17] Another advantage is the ability to test samples in open geometry with the use of mobile apparatus,[8] which increases the potential of future uses in the case of finding optimal measurement protocols and parameters dependent on cells characteristics.

2 | MATERIALS AND METHODS

2.1 | Experimental model

The umbilical cords were collected after Caesarean sections. Written consents were obtained from parents. The umbilical cords were washed with phosphate-buffered saline supplemented with antibiotic-antimycotic solution, cut into small explants and plated into a plastic flask. Explants were cultured with a growth medium for MSCs (DMEM Low Glucose, Biowest), supplemented with the platelet lysate in standard culture conditions under 21% of O_2 and 5% of CO_2 at 37°C. Next, the explants were removed, and the cells were passaged using the Accutase cell detachment solution (BioLegend). After reaching the appropriate number of cells, WJMSCs were used for further experiments.

2.2 | WJMSCs characterization

The phenotype of WJMSCs was analysed according to the International Society of Cellular Therapy standards. Briefly, cells cultured at passage 3 or 4 were collected and stained with antibodies against CD73, CD90, CD105, CD3, CD45, CD34, CD14 and CD19 (Becton Dickinson) for 30 min at 4°C in darkness. Appropriate isotype controls were used to exclude non-specific binding. Cells were analysed using Attune Nxt Flow cytometer (Thermo Fisher Scientific, Waltham, MA, USA), and data were analysed using Attune NxT Software v2.2.

WJMSCs were tested for their three-lineage differentiation potential using MesenCult Adipogenic Differentiation Medium, MesenCult Osteogenic Differentiation and MesenCult ACF Chondrogenic Differentiation Medium (all from StemCell Technologies, Vancouver, CA-BC, Canada). For analysis, cells were seeded into 12-well plate at a density of 1.3×10^3 cells/cm^2 and cultured in the standard medium until the culture reached appropriate confluence and the medium was replaced by differentiation medium. At the end of differentiation, cell was stained with Oil Red O (adipocytes) (Sigma-Aldrich) Alizarin Red (MERC) (osteoblasts) and Alcian Blue staining (chondrocytes) (Sigma-Aldrich) according to standard procedures.

2.3 | Experiments in a LF-NMR system with a bore aperture

A suspension of MSCs from Wharton Jelly in a PBS buffer was put into glass pipette and centrifuged. Then, the glass pipette was closed and so the prepared samples were examined on a Magritek Rock Core Analyzer at a magnetic field of 0.05 T. Samples with 5 and 15 million cells in a volume of 0.5–1 ml were tested (suspensions a–d, see Table 1). The Inversion Recovery (IR) and Carr-Purcell-Meiboom-Gill (CPMG) sequences were used for 1D-T_1 (inter-experiment delay, ID = 5 s, T_1 delay range: 0.1–5 s) and T_2 (ID = 7.5 s, echo time, TE = 200–400 μs, number of echoes in CPMG encoding train, NoE = 50,000) measurements, respectively. 2D T_1-T_2 correlation maps were obtained with IR-CPMG sequence ID = 3 s for buffer, ID = 350 ms for cells, T_1 delay range: 0.1–5 s, TE = 400 μs, NoE = 20,000). In order to enhance the signal from cells, shorter inter-experiment delays were applied for T_1-T_2 (350 ms) than in the case of 1D experiments. For 2D complementary diffusion experiments, a diffusion-weighted pulsed-field gradient spin-echo (PGSE) sequence was applied with an increasing gradient amplitude to 0.5 T m^{-1} and CPMG sequence for detection (ID = 350 ms, TE = 400 μs, NoE = 10,000, gradient pulse length, δ = 6 ms for

TABLE 1 Peak positions from 1D-T_1, T_2 distributions (A) and 2D T_1-T_2 (B) and D-T_2 (C) correlation maps

A. Results from 1D-T_1 and T_2 distributions						
Sample	MSC: V_{tot} [no of cells: ml]	T_2 [ms] Peak 1	T_2 [ms] Peak 2	$T_{2,\text{log-mean}}$ [ms]	T_1 [ms]	$T_{1,\text{log-mean}}$ [ms]
Buffer (a)	0: 1	2584.2	-	2640.3	2439.6	2479.6
Cells (b)	5: 1	2770.0	117.6	2857.8	2158.0	2108.2
Cells (c)	5: 0.5	2584.2	227.5	1846.3	2294.0	2166.4
Cells (d)	15: 0.5	4201.2; 1162.3	310.8	1884.6	1795.3	1815.6

B. Results from T_1-T_2 correlation maps									
Sample	MSC: V_{tot} [no of cells: ml]	T_1 [ms] Peak 1	T_2 [ms] Peak 1	T_1 [ms] Peak 2	T_2 [ms] Peak 2	T_1 [ms] Peak 3	T_2 [ms] Peak 3	T_1/T_2 Peak 1	T_1/T_2 Peak 2
Buffer (a)	0: 1	2740	2740	-	-	-	-	1	-
Cells (c)	5: 0.5	3090	3310	923	240	-	-	0.93	3.8
Cells (d)	15: 0.5	3490	3145	1120	333	-	-	1.11	3.4

C. Results from D-T_2 correlation maps									
Sample	MSC: V_{tot} [no of cells: ml]	D_1 [$\times 10^9$ m^2/s] Peak 1	T_2 [ms] Peak 1	D_2 [$\times 10^9$ m^2/s] Peak 2	T_2 [ms] Peak 2	D_3 [$\times 10^9$ m^2/s] Peak 3	T_2 [ms] Peak 3	D_1/D_2	D_1/D_3
Buffer (a)	0: 1	2.08	2300	-	-	-	-	-	-
Cells (c)	5: 0.5	2.04	2340	0.93	185	0.163	238	2.19	12.55
Cells (d)	15: 0.5	2.19	2880	1.45	240	0.216	266	1.51	10.14

suspensions a and c, $\delta = 8$ ms for suspension d, interval between two gradient pulses, $\Delta = 20$ ms). The maximum b-value achieved for suspensions a and c was equal to 11.6×10^9 sm^{-2} and 19.8×10^9 s m^{-2} for suspension d. All the experiments were conducted in seven separate experimental series, and for each cell concentration measurement with the same parameters was repeated at least once. In the work, representative data were shown.

2.4 | Experiments in a LF-NMR single-sided system

For the NMR measurements in a constant time-steady gradient, a single-sided MoUSE scanner (NMR-MoUSE, Magritek) was used with a magnetic field, B_0 of 0.5 T and constant time-steady magnetic field gradient of 24 T m^{-1} (1030 MHz mm^{-1}) set perpendicularly to B_0 and longitudinally to slice thickness. A profile sequence was used to localize the bottom of the Petri dish (repetition time, RT = 2 s, TE = 128.5 μs, Δ = 10 ms, number of echoes in CPMG encoding train, NoE = 512, slice thickness, ST = 10 μm) or cylindrical container (RT = 6.2 s, TE = 50.5 μs, Δ = 20 ms, NoE = 4098, ST = 20 μm) and the presence of the examined material. The precise lift in the MoUSE device allowed us to set the position of the slices. Echo decays with tau from 0.01 to 0.05 ms for Petri dishes, which corresponded to b-values from 0.04 to 1.03×10^9 s m^{-2} and 0.01 to 0.2 ms (b-value in the range of 0.08–33.1 $\times 10^9$ s m^{-2}) for cylindrical container were registered. Then, the obtained data were calculated using the Inverse Laplace Transform (ILT) (L&H algorithm, Prospa software) and fitted independently using a one- or bi-exponential model.

2.5 | Quantification and statistical analysis

The registered data were analysed using ILT with Lawson&Hanson and FISTA algorithms,[18] allowing us to obtain 1D distributions and 2D maps, respectively (Prospa software, Magritek). Data from single-sided NMR-MoUSE were additionally processed by fitting independently a mono- or bi-exponential diffusion model (for descriptions please see for example in the work of Mazur and Krzyżak[16]) in Statistica (TIBCO Software Inc.).

3 | RESULTS

3.1 | WJMSCs characterization

The WJMSCs show the minimal criteria outlined for MSCs by the International Society of Cellular Therapy. They adhere to plastic surface in standard culture conditions and display fibroblast-like morphology (Figure 1A). Cytometric analysis revealed high expression of specific mesenchymal markers. More than 90% of cells were CD73, CD90 and CD105 positive, whereas they do not express hematopoietic antigens (CD45, CD14, CD19, CD34 and CD3) (Figure 1B). We have also confirmed multipotent differentiation potential of

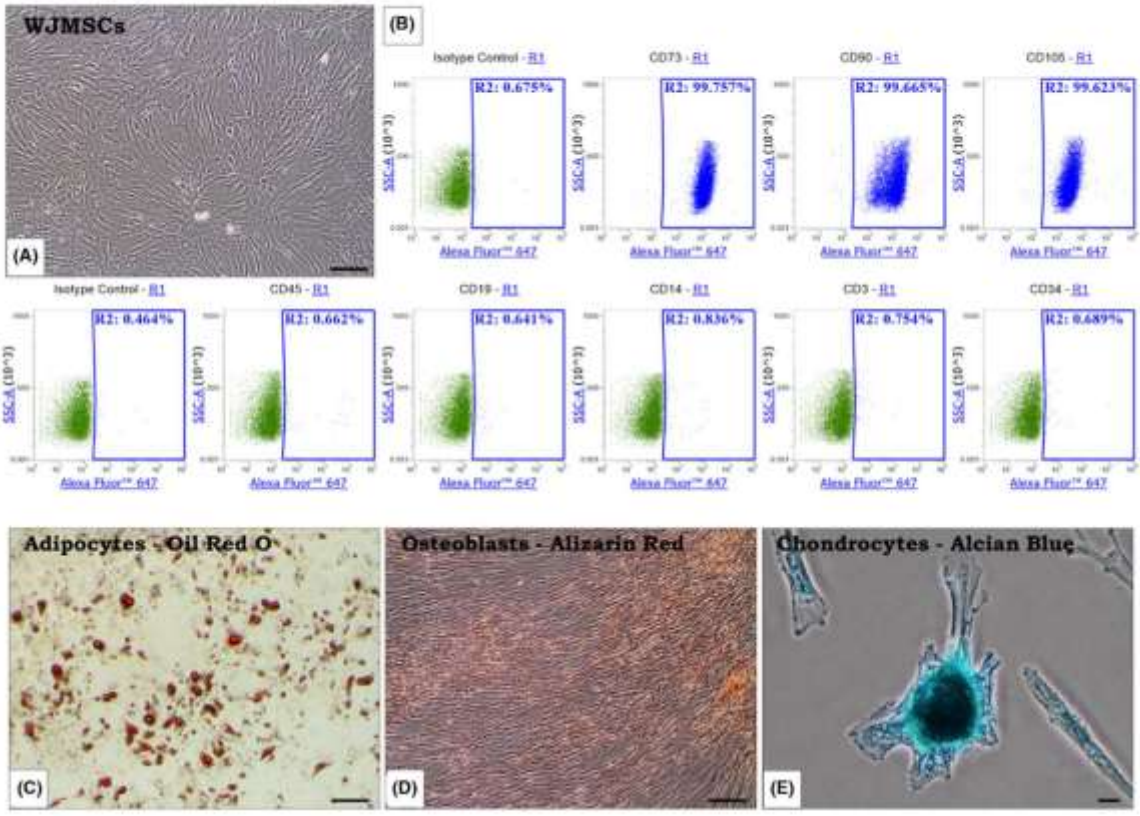

FIGURE 1 Characterization of WJMSCs in standard culture conditions; light microscopy, magnification ×100, bar =100 μm (A). The expression of surface markers characteristic for MSCs: CD73, CD90 and CD105 (over 90% positive cells). The cells are negative for hematopoietic antigens: CD45, CD19, CD14, CD34, CD3; flow cytometry analysis (B). Trillineage differentiation potential of WJMSCs: adipocytes (Oil Red O staining) (C), osteoblasts (Alizarin Red s staining) (D) and chondrocytes (Alcian blue staining) (E); light microscopy, magnification ×100, bar =100 μm

WJMSCs. These cells demonstrated strong capacities for differentiation towards adipogenic (Figure 1C), osteogenic (Figure 1D) and chondrogenic (Figure 1E) lineages.

3.2 | T_1 and T_2 relaxation

In Figure 2, the T_1 and T_2 distributions for MSCs samples with various amounts of cells in a specified volume are presented, and in Table 1, the relaxation times at maximum and $T_{1,2}$ log-mean values are collected. In the case of T_1 distributions only one peak is visible, for both the buffer and for the cell samples (see Figure 2, left panel), having T_1 from 2.16 to 1.8 s for suspensions b to d, respectively. The lack of a clearly separated peak derived from the cells is probably caused by the close values of T_1 for buffer and cells samples, which makes it difficult to separate these two components using ILT.

On T_2 distributions (Figure 2 right panel), a separate peak for MSCs can be seen even for the lowest cells concentration. T_2 of MSCs was equal to 118, 228 and 311 ms for suspensions b, c and d, respectively (the difference is caused by the effect of different amount of MSCs signal on ILT). Suspension d probably contained cells clusters with intercellular spaces resulting in additional component with T_2 = 1162 ms.

3.3 | T_1-T_2 and D-T_2 correlation maps

In Figure 3A–C, T_1-T_2 maps are presented corresponding to the 1D distributions from Figure 2 for suspension a, c and d. A peak with an increasing intensity and area for the cell samples, located at T_2 about 130–350 ms and not present for the pure buffer sample, is the main observation for these measurements. Its T_1/T_2 values were a few times higher than for a free water, which is another confirmation of the assumption that the signal originates from the restricted region of the sample.

A comparison of D-T_2 maps for the pure buffer and MSCs samples is shown in Figure 3D–F. It can be observed that for the used PGSE parameters signal with T_2 from the range of 130–350 ms was

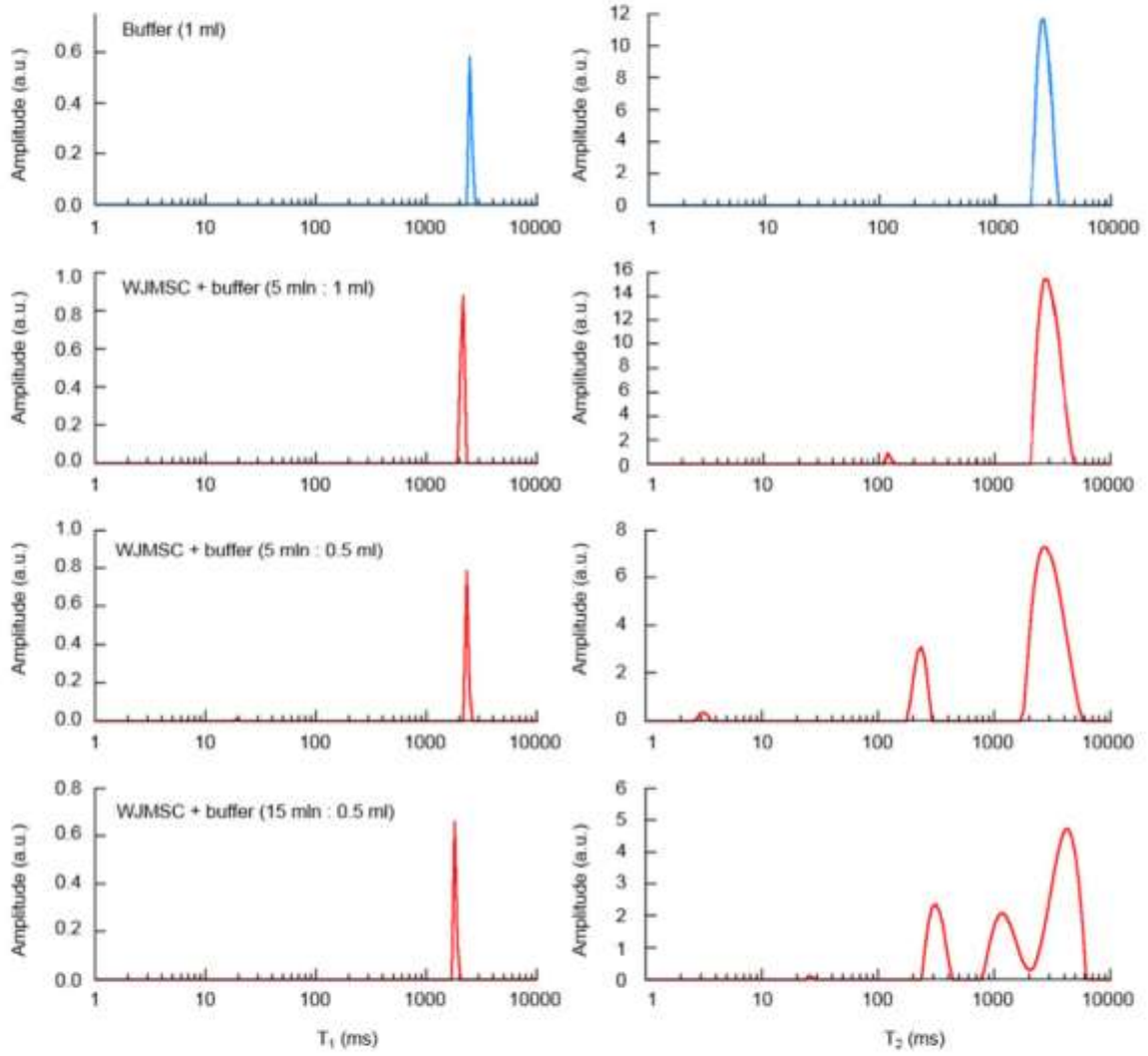

FIGURE 2 Relaxation times 1D distributions. T_1 (left panel) and T_2 (right panel) relaxation times distributions obtained for different cells concentration in the suspensions

separated into two components with different diffusion coefficients, which was the most visible for the suspension d. For this concentration, the first component (Figure 3F) is characterized by diffusion coefficient of 1.45×10^{-9} m^2 s^{-1}, and the latter: 0.216×10^{-9} m^2 s^{-1}, which is 1.5 and 10.1 lower than the diffusion coefficient for the main peak, originating from free water within this sample. For the lower concentration (suspension c), the corresponding components have values of 0.93×10^{-9} m^2 s^{-1} and 0.163×10^{-9} m^2 s^{-1}, respectively. The lowest diffusion may be related to the water compartment with the highest restriction—probably intracellular spaces, while the second component might originate from the restricted areas between cells, and may be the same as the signal at 1162 ms of 1D-T_2 distribution.

3.4 | Diffusion measurements of cells cultured in a Petri dish

In Figure 4A–D and F–I, diffusion distributions obtained for samples of stem cells cultured on Petri dishes are shown and compared with the results of pure water examined under the same conditions. Four slices of 10 μm were registered for two samples prepared independently—bottom slices are assigned as '1' and top slices as '4'. Simultaneously, effective (ie averaged for all of the water pools) diffusion coefficients were fitted using a mono-exponential function (results shown in Table 2) and presented in Figure 4E and J. Effective diffusion coefficients for the bottom slices of the stem cell samples (slice 1, Figure 4D and I) were

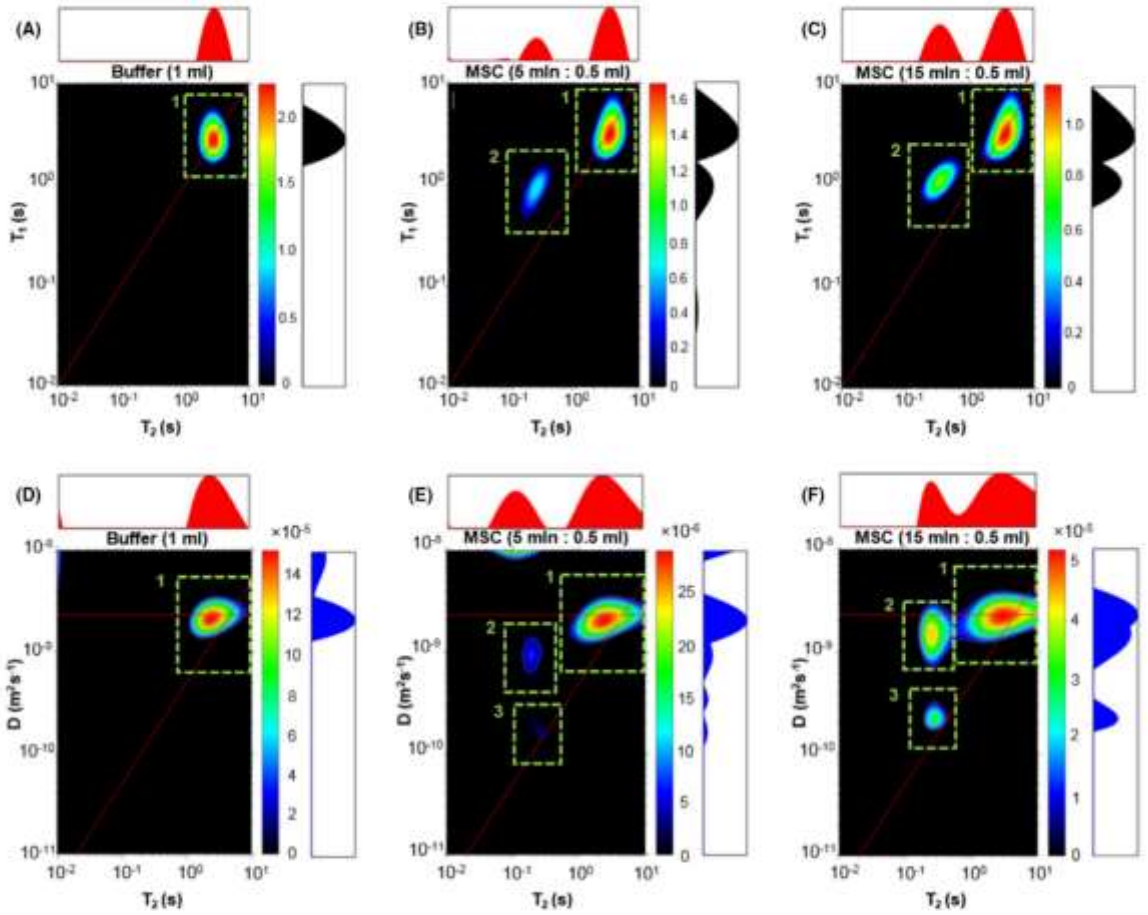

FIGURE 3 Correlation maps from 2D experiments. T_1-T_2 correlation maps (A–C) and D-T_2 correlation maps (D–F) for buffer and MSCs samples with peaks numbered from 1 to 3

1.2–1.5 times lower than values of coefficients obtained for slices situated above them (slices 2–4). Diffusion coefficients for slice '1' for cells were also 1.2–1.5 times lower than for each water measurement. Results for slices 2–4 are close to the water diffusion coefficients.

3.5 | Diffusion measurements of cell suspension in a cylindrical container

In order to obtain the results of diffusion coefficients for cells less biased by water present between them, samples of a centrifuged cell suspension were examined in a cylindrical container. Distributions of diffusion coefficient for four slices with width of 50 μm are compared in Figure 5A–D. Results of fitted values using bi-exponential model are listed in Table 2 and visualized in Figure 5E. Measurements for these samples were also repeated after 6 days (see Figures 2J and 5F–I).

For samples measured immediately after preparation, significantly lower, 1.7–2.2 times, diffusion coefficients D_1 for all the examined slices than the corresponding values for water can be noticed. Values from 1.36 to 1.14×10^{-9} m^2 s^{-1} were registered, in comparison with 2.31–2.48×10^{-9} m^2 s^{-1} obtained for water. Moreover, second diffusion component with D_2 ranging between 0.052 and 0.068×10^{-9} m^2 s^{-1} was possible to obtain. For samples examined after 6 days of incubation at room temperature, a significant decrease of diffusion coefficients was observed (1.5–3 times). The lowest values of the diffusion coefficient for the bottom slice and generally increasing values for higher located slices can be noticed.

4 | DISCUSSION

In the work, different NMR approaches were applied in order to characterize MSCs. Each of them delivered distinct information which was complementary to the others, and all are discussed below.

TABLE 2 Results of fitting of mono-exponential functions for stem cells and water sample in a Petri dish for slices of 10 μm (A) and bi-exponential functions for stem cells and mono-exponential for water sample in a cylindrical container for slices of 50 μm (B)

A. Petri dish				
Slice number	Slice width [μm]	Water	Stem cells (experiment 1)	Stem cells (experiment 2)
		D_{eff} [$\times 10^9$ m^2/s]	D_{eff} [$\times 10^9$ m^2/s]	D_{eff} [$\times 10^9$ m^2/s]
1 (bottom)	10	2.13 ± 0.06	1.58 ± 0.07	1.80 ± 0.04
2	10	2.31 ± 0.07	2.15 ± 0.06	2.27 ± 0.08
3	10	2.28 ± 0.06	2.32 ± 0.09	2.16 ± 0.05
4 (top)	10	2.32 ± 0.05	2.38 ± 0.10	2.28 ± 0.08

B. Cylindrical container						
Slice number	Slice width [μm]	Water	Stem cells	Stem cells	Stem cells after 6 days	Stem cells after 6 days
		D [$\times 10^9$ m^2/s]	D_1 [$\times 10^9$ m^2/s]	D_2 [$\times 10^9$ m^2/s]	D_1 [$\times 10^9$ m^2/s]	D_2 [$\times 10^9$ m^2/s]
1 (bottom)	50	2.31 ± 0.003	1.36 ± 0.07	0.068 ± 0.026	0.46 ± 0.09	0.042 ± 0.014
2	50	2.47 ± 0.05	1.19 ± 0.07	0.052 ± 0.027	0.65 ± 0.06	0.082 ± 0.015
3	50	2.50 ± 0.03	1.16 ± 0.08	0.064 ± 0.030	0.56 ± 0.03	0.031 ± 0.015
4 (top)	50	2.48 ± 0.03	1.14 ± 0.06	0.055 ± 0.026	0.78 ± 0.05	0.084 ± 0.023
Mean	50	2.44 ± 0.03	1.21 ± 0.07	0.0598 ± 0.027	0.61 ± 0.06	0.0598 ± 0.017

4.1 | Determination of the MSCs' size

Mesenchymal stem cells' diameter ranges from d_{min} = 15 μm to d_{max} = 30 μm.[19] For these values and real suspension volumes, theoretical cellular fractions were calculated and compared with the ones from D-T_2 experiment (Figure 3). Fractions coincide for d_{min} =15 μm, which is assumed to be real MSCs size. Note that MSCs size cannot be determined from T_1-T_2 maps, because extra- and intracellular water can have very similar relaxation times[16] and they may combine into a single peak disenabling fractions comparison.

4.2 | The influence of MSCs cultured in a Petri dish on an apparent diffusion coefficient

Mesenchymal stem cells cultured on a Petri dish were traced by applying a very small slice thickness, which was possible due to the use of a single-sided NMR-MoUSE device. The slice thickness of 10 μm ensured a single layer of cells to be examined in a single slice. Due to the considerable reduction of the effective diffusion coefficient in the bottom slice, the presence of a significant number of cells is suspected. Results for slices 2–4 are similar to water diffusion coefficients, suggesting that the diffusion coefficient is only affected by the presence of cells in the first and the lowest layer on the bottom of the Petri dish. Using $D_{cyto}(t_d$ = 10 ms) from simulations (see Section 4.4.), cells fraction on the bottom of a Petri dish can be estimated to be in the range of 23–34%. Hence, cells did not completely cover the surface and the proportion of water between the cells strongly influenced the detection of a true intracellular self-diffusion coefficient. However, these findings seem useful for understanding the impact of MSCs on the apparent (ie dependent on diffusion time) diffusion coefficient of water in vivo measured in a clinical practice. The effective diffusion coefficient may reflect the amount of MCSs accumulating on tissue after a medical intervention.

4.3 | Monitoring of diffusion and viability of MSCs cultured in a cylindrical container

Values of D_1 for samples examined in the cylindrical container are much lower than those measured in Petri dishes. This is probably because of a lower proportion of water between cells in the samples prepared in this way. This may suggest obtaining closer values of effective diffusion coefficient to the true self-diffusion intracellular coefficients in MSCs. The second diffusion component may originate from structures located within the cells which cause greater water restriction. Immediately after the preparation of the cell suspension, the dependence of the diffusion coefficient on the slice location is rather random and they can be averaged in order to obtain more reliable values. Mean diffusion coefficients can be used for the identification of the second component, D_2.

4.3.1 | Evidence of diffusion in the in-cell structures

The MSCs nucleus is a large and round cellular structure[20] and was suspected in the first place to contribute to the second diffusion component. For example, in yeast, nuclear to cellular volume ratio is equal to about 8%,[21] which is associated with a nuclear radius of ~1 μm.[22] In the

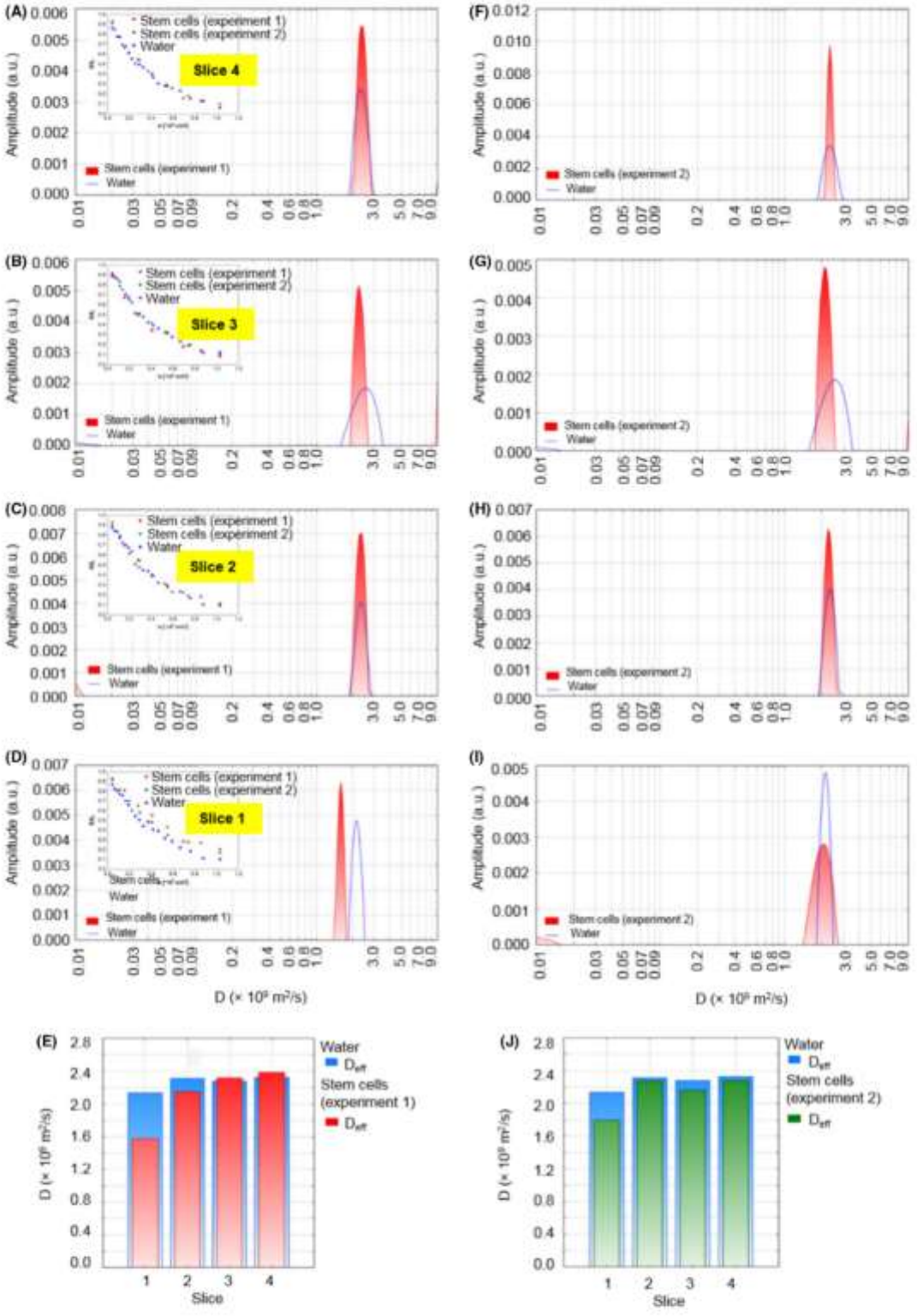
(A)
Stem cells (experiment 1)
Stem cells (experiment 2)
Water
Slice 4
Stem cells (experiment 1)
Water
(B)
Slice 3
(C)
Slice 2
(D)
Slice 1
(F)
Stem cells (experiment 2)
(G)
(H)
(I)
Amplitude (a.u.)
D (× 10⁹ m²/s)
(E)
Water
D_eff
Stem cells (experiment 1)
(J)
Stem cells (experiment 2)
Slice

FIGURE 4 Two independent diffusion experiments in Petri dishes. Data in the left column represent experiment 1, while in the right column: experiment 2, conducted independently. Diffusion coefficient distributions for water and cells samples in Petri dishes, sequentially for the layers from the highest ('4') to the lowest ('1') (A–D, F–I). Inset graphs present attenuation of signals, E/E_0, vs. b-value. Column plots comparing diffusion coefficients $D_{0,fr}$ for cells and water sample (E), (J)

mouse MSCs, the ratio of cell and nucleus diameters was reported to be equal to about 63%.[23] In human MSCs, the ratio of nuclear to cellular diameters is equal to 26–31%.[24] Assuming the cell radius of 7.5 μm estimated in Section 4.1, nucleus radius, R_{nucl}, is equal to ~2 μm. This size and $D_{0,nucl} = 0.095 \times 10^{-9}$ m^2 s^{-1} reported by Mazur and Krzyżak[16] yielded $D_{nucl}(t_d = 20\,ms) = 0.0602 \times 10^{-9}$ m^2 s^{-1}, which is in a good agreement with the mean value of D_2 equal to 0.06×10^{-9} m^2 s^{-1}. Therefore, it is highly possible that nuclei in the examined cells have a radius of $R_{nucl} = 2$ μm.

4.3.2 | Cell viability reflected in the effective diffusion coefficient

For samples examined after 6 days of incubation at room temperature, a significant decrease of diffusion coefficients was observed (1.5–3 times). This may be related to structural damage to the cells over time, as well as with partial water evaporation. The lowest values of diffusion coefficient for the bottom slice and generally increasing values for higher located slices can be noticed. Lower values of diffusion coefficients for the bottom slice may be caused by the gravitational fall of cells and their squeezing due to the higher pressure exerted by the slices located above them. The decrease of D_2 cannot be counteracted by the partially or to a greater extent damaged internal structure of cells.

Mean molar fractions f_1 and f_2 of D_1 and D_2, respectively, changed after 6 days of incubation (Table 2). Mean f_1 decreased from 0.97 to 0.8 with a mean D_1 drop from 1.21×10^{-9} m^2 s^{-1} to 0.61×10^{-9} m^2 s^{-1}, while f_2 increased from 0.0725 to 0.2 with no change of a mean D_2. If no cellular death and only cell condensation occurred, f_1 would be unchanged in favour of f_2, only D_1 would change (higher cells fraction with significantly smaller D). Therefore, the most possible scenario is that some part of the cells died in the process of necrosis or apoptosis. The part of apoptotic cells would release apoptotic bodies with membrane-enveloped DNA fragments. They would have similar properties to the nucleus and collocate with a nuclear signal, giving a higher molar fraction of a D_2 component. Both cell death mechanisms result in DNA release and medium coagulation leading to the decrease of D_1 diffusion coefficient. Hence, it is suspected that f_2 increase was mostly due to apoptosis, while D_1 decrease was associated with the rise of density and viscosity resulting from DNA issued from cells destroyed by necrosis and partly by apoptosis.

4.4 | Determination of MSCs' self-diffusion coefficient

In the previous work,[16] it was proposed to use simulations of a time-dependent diffusion coefficient (TDDC) for the diffusion times applied in the real experiments to identify cellular compartments. Experimental TDDC is associated with a given cellular structure if it corresponds with the simulated one for this structure (details of simulations used in this study are presented in Section S1). However, simulations require prior knowledge on the free (ie for $t_d \to 0$) self-diffusion coefficient, D_0, associated with a given water pool. Hence, simulations for MSCs are quite inconvenient due to the lack of information about in-cell D_0s. This is in a total contrast to other cells like yeast, which are well-characterized in the literature. Therefore, a slightly different pattern was applied for the estimation of intracellular self-diffusion coefficients.

Firstly, this analysis derives from experiments conducted in a constant time-steady gradient, from which the nuclear size and self-diffusion coefficient were determined (see Section 4.4.). Considering that nuclear residence time, τ_{nucl}, is significantly shorter than applied diffusion times,[16] peak 3 (Figure 3E,F) originates from the effective diffusion coefficient of exchanging water cytoplasm and nucleus, $D_{intra}(t_d) = f_{nucl} \cdot D_{nucl}(t_d) + f_{cyto} \cdot D_{cyto}(t_d)$, where f_{nucl}, f_{cyto}, D_{nucl} and D_{cyto} are molar fraction of nuclear water, molar fraction of cytoplasmic water, diffusion coefficient in the nucleus and diffusion coefficient cytoplasm, respectively.

It is important that for $t_d < \tau_{nucl}$, signal attenuation due to diffusion in nucleus would be so small that would require a very high signal-to-noise ratio to be distinguished as a separate component, especially in small samples for which f_{nucl} is low (in this study it is equal to ~0.24%–1.5% of a total signal). Practically, if pulsed-field gradient (PFG) techniques are used, most of the attenuation will come from diffusion in cytoplasm. Therefore, for $t_d \gg \tau_{nucl}$ effective/intracellular diffusion coefficients D_{intra} will be observed, while for $t_d \to 0$ $D_{0,intra} \to D_{0,cyto}$. Based on the fact that intracellular self-diffusion coefficients of 0.68×10^{-9} m^{2}s^{-1} [25] and 0.65×10^{-9} m^2 s^{-1} [26] were obtained for yeast cells, while self-diffusion coefficient of 0.69×10^{-9} m^2 s^{-1} [16] was obtained for yeast's cytoplasm, the $D_{0,intra} \approx D_{0,cyto}$ approximation seems to be justified for PFG in moderate gradient strengths. Since self-diffusion coefficient of nucleus is known, $D_{cyto}(t_d)$ was extracted from $D_{intra}(t_d)$ and used for determination of $D_{0,cyto}$. Estimated $D_{0,cyto}$ was equal to 0.22×10^{-9} m^2 s^{-1} and 0.29×10^{-9} m^2 s^{-1} for $D_{cyto}(t_d) = 0.165 \times 10^{-9}$ m^2 s^{-1} and 0.219×10^{-9} m^2 s^{-1}, respectively (for details of estimation of $D_{0,cyto}$ required for simulations see Section S2).

4.4.1 | Verification of $D_{0,cyto}$ by comparison with simulated TDDCs

For several theoretical $D_{0,cyto}$s from the range of 0.2×10^{-9} m^2 s^{-1} to 1.0×10^{-9} m^2 s^{-1}, TDDCs were simulated and

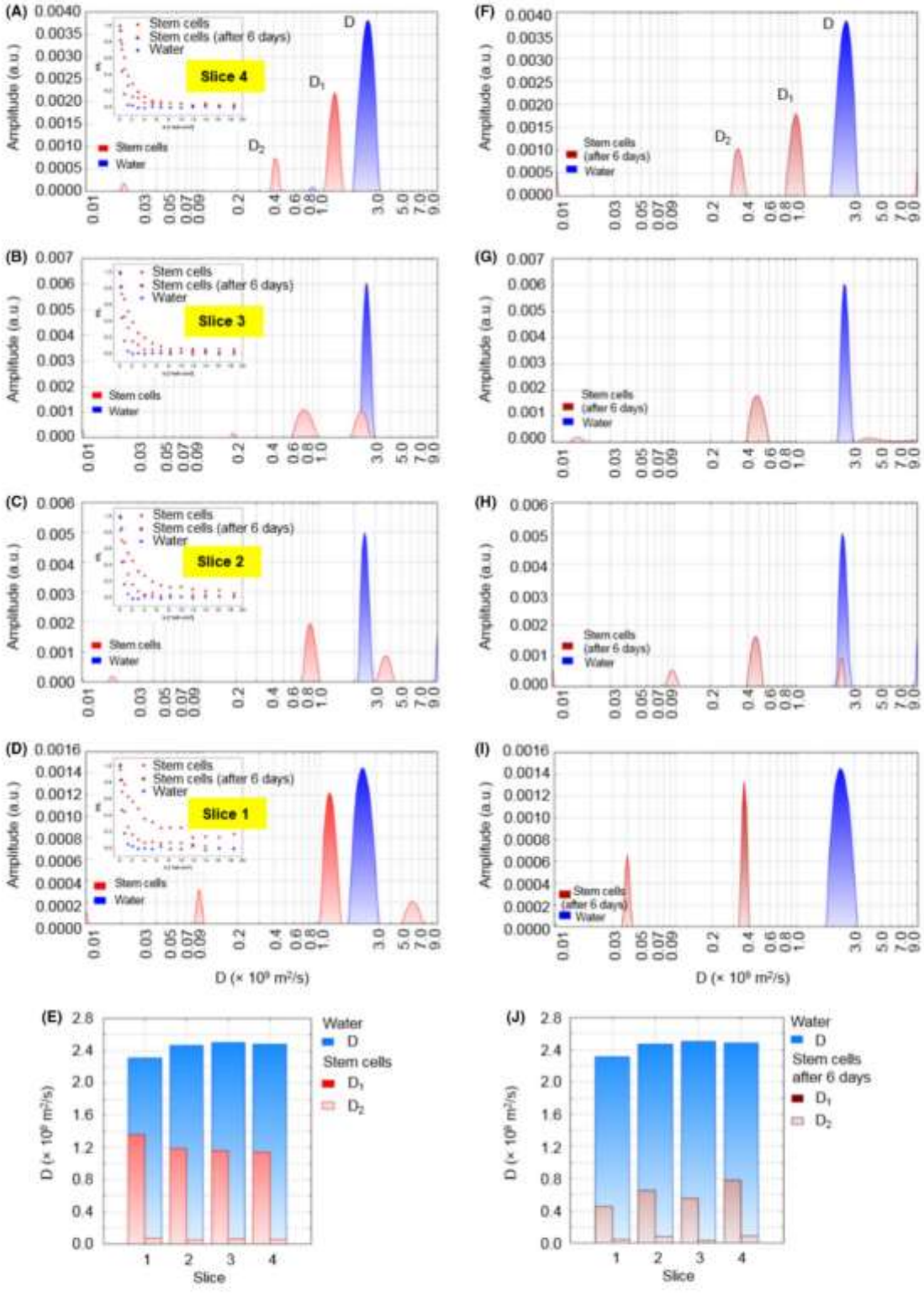
(A)
(B)
(C)
(D)
(F)
(G)
(H)
(I)
Amplitude (a.u.)
Stem cells
Stem cells (after 6 days)
Water
Slice 4
Slice 3
Slice 2
Slice 1
D
D1
D2
D (× 10⁹ m²/s)
(E)
(J)
Water
D
Stem cells
D1
D2
Stem cells after 6 days
Slice

FIGURE 5 Diffusion experiments in cylindrical container. Data in the left column represent samples measured immediately after preparation, while in the right column: after 6 days. Diffusion coefficient distributions for water and cells samples within a cylindrical container, sequentially for the layers from the highest ('4') to the lowest ('1') (A–D, F–I). Inset graphs present the attenuation of signals, E/E_0, vs. b-value. Column plots comparing diffusion coefficients D_1 and D_2 for cells and D for water samples (E), (J)

experimental $D_{cyto}(t_d)$ were compared with them. In Figure S1C, it can be seen that experimental $D_{cyto}(t_d)$ lie close to the simulated TDDC assuming $D_{0,cyto} = 0.22 \times 10^{-9}$ m^2 s^{-1} and 0.29×10^{-9} m^2 s^{-1} for $D_{cyto}(t_d) = 0.165 \times 10^{-9}$ m^2 s^{-1} and 0.219×10^{-9} m^2 s^{-1}, respectively. Based on Figure S1C, it can be concluded that in the restricting geometry with the diameter of $d = 15$ μm, for $D_0 \leq 0.8 \times 10^{-9}$ m^2 s^{-1} molecules are in the free diffusion regime in the range of $t_d = 0.1$–50 ms, where Mitra's relation is valid. Therefore, more reliable $D_{0,cyto} \sim D_{0,intra}$ can be estimated from Mitra's formula and is equal to 0.205×10^{-9} m^2 s^{-1} and 0.283×10^{-9} m^2 s^{-1} for $D_{cyto}(t_d) = 0.165 \times 10^{-9}$ m^2 s^{-1} and 0.219×10^{-9} m^2 s^{-1}, respectively.

Taking into consideration that $D_{cyto}(t_d) = 0.219 \times 10^{-9}$ m^2 s^{-1} results from the higher cells concentration, it can be suspected that ILT was more accurate in comparison with the three times lower concentration and the real $D_{0,cyto}$ can be assumed to be equal to $\sim 0.283 \times 10^{-9}$ m^2 s^{-1}. This value is in the range of 0.15–0.63×10^{-9} m^2 s^{-1} obtained by Tanner for the intracellular self-diffusion coefficient of different cells in vitro.[27] Such small diffusivity indicates rather high cytoplasmic viscosity. For example, ~3 times higher viscosity of blood compared with water at 37 °C results in an about two to three times smaller diffusivity ($0.9–1.65 \times 10^{-9}$ m^2 s^{-1} [28]). Taking into consideration that the viscosity of MSCs at 20°C is equal to ~2.71 Pa s,[29] $D_{0,cyto}$ of MSCs suggests that their cytoplasm contains either higher dry weight (resulting in a considerable D_0 reduction), ions (brine shrimp cells in the work of Tanner[27] had $D_0 = 0.35 \times 10^{-9}$ m^2 s^{-1}) or lipids ($D_0 = 0.015 \times 10^{-9}$ m^2 s^{-1} [27]).

4.5 | New insights in the context of current MRI applications for the investigation of MSCs

Despite the ongoing investigations concerning MSCs (eg differentiation, viability, ontogenesis), attempts at the clinical applications of MSCs, especially for the civilization-driven conditions, are boosted. Over the years, many studies on the application of MRI to MSCs monitoring have been reported. Most of them were oriented towards in vivo experiments, mainly related to the characterization of treatment effects[30,31] or tracking MRI-labelled cells.[32–34] Treatment effects are usually evaluated through the change of volume or size of a given region (eg tumour, infarct and cartilage) on MR images or T_1, T_2 and apparent diffusion coefficient (ADC) mapping. MRI-labelled cells are tracked by shortened T_2 or T_2^* values, which result from the uptake of nanoparticles by the MSCs.

From the point of view of this study, tracking and differentiation of MSCs are particularly meaningful. As mentioned, MRI usage for this purpose is inextricably connected to the application of contrast agents (CAs), such as iron-oxide or gadolinium-based. The role of CAs is to change MRI-derived parameters (T_1, T_2, ADC) in order to differentiate MSCs from the tissue. The meaning of the characterization of biophysical properties of MSCs for their distinguishing from primary, cancer and differentiated cells was pointed out.[35,36] Through our approach, we provide complementary parameters obtained non-invasively for MSCs *in vitro*. The characterization of MSCs by means of 1D and 2D relaxometry revealed several MSCs-specific features, including diffusional and relaxational behaviour. First of all, MSCs are characterized by a significantly smaller intracellular self-diffusion coefficient, $D_{0,intra} = 0.283 \times 10^{-9}$ m^2 s^{-1}, in comparison with many other human cell types. For example, a diffusion coefficient of 0.45×10^{-9} m^2 s^{-1} was reported for astrocytes, 1.06×10^{-9} m^2 s^{-1} for cardiomyocytes,[37] $0.9–1.6 \times 10^{-9}$ m^2 s^{-1} for axons measured longitudinally, while $0.3–0.5 \times 10^{-9}$ m^2 s^{-1} for axons measured perpendicularly,[38] $\sim 1 \times 10^{-9}$ m^2 s^{-1} for glia,[39] 1.38×10^{-9} m^2 s^{-1} for chondrocytes,[40] $\sim 0.8 \times 10^{-9}$ m^2 s^{-1} for white matter and $\sim 1.2 \times 10^{-9}$ m^2 s^{-1} for grey matter.[41] This gives potential to differentiate MSCs in these tissues. As shown in Sections 3.2 and 3.3, such a value strongly influences not only the effective diffusion coefficient in the layer of MSCs but also in the volume of suspended cells. Therefore, it seems that diffusion can be used as a potential biomarker for tracking MSCs non-invasively, without the necessity of using CAs to change the intracellular properties of the cells.

5 | SUMMARY

The study revealed the capability of a low field system to detect signals from cells in the samples with a low concentration of cells in the suspensions or low amounts of the sample without any contrasting agents. To sum up, based on the results from 1D: T_1, T_2, D, 2D: T_1-T_2, D-T_2 measurements it was possible to:

- determine specific parameters for WJMSC of T_2 *relaxation times*, T_2 = 118–350 ms, and *diffusion coefficients* $D_{intra} = 0.0163–0.0216 \times 10^{-9}$ m^2 s^{-1} and $D_{extra} = 0.93–1.45 \times 10^{-9}$ m^2 s^{-1} corresponding to intra- and extracellular water pools, respectively;
- estimate *MSCs' size* equal to ~15 μm from D-T_2 measurements;
- assess the effective diffusion coefficient for a *single layer of MSCs* cultured in a Petri dish, $D_{eff} = 1.69 \times 10^{-9}$ m^2 s^{-1} allowing the determination of cells fraction (~28%);
- find evidence of *diffusion in the in-cell structures* associated mainly with the nucleus characterized by $D_{0,nucl} = 0.095 \times 10^{-9}$ m^2 s^{-1} and radius $R_{nucl} = 2$ μm;
- determine cell *viability* reflected in the effective diffusion coefficients ($D_{eff,t} = 0.46–0.78 \times 10^{-9}$ m^2 s^{-1}) reflecting apoptosis and necrosis of cells after 6 days of incubation;

- register D_{str}s indicating changed physical properties of the suspension due to *cell destruction* and the increase of *DNA-rich components* with properties similar to a nucleus;
- estimate *MSCs' intracellular self-diffusion coefficient*, $D_{Sintra} = 0.283 \times 10^{-9}\ m^2\ s^{-1}$.

In further research, the known specific NMR parameters will be used to estimate the location of stem cells in organs undergoing therapy in MRI diagnosis *in vivo*, as well as to learn about their quantitative and qualitative characteristics in *in vitro* suspensions. A very important issue that has to be addressed in the further, research on our method is the possibility of distinguishing different fractions of cells in their mixture in an *in vitro* experiment. Another challenge will be to try to distinguish MSCs from other cell types *in vivo* through clinical MRI imaging.

6 | CONCLUSIONS

The determination of specific parameters for MSCs in LF-NMR opens up the possibility of research on the detection of these cells *in vivo* as well as attempts at the determination of their quantity or vitality in the source tissues, such as the umbilical cord, in *in vitro* studies. The application of a single-sided NMR device with a strong magnetic field gradient allowed the attainment of very thin slices and the detection of a single cell layer in the Petri dish. This introduces the possibility of examination of MSCs properties and their differences at the individual cell layer. The cells setting in the Petri dish also has the advantage of imitating the *in vivo* environment. It relies on the presence of a limited number of cells in the watery ambience, similarly to the case of cells reposition on the tissue. In this way, the character of diffusivity change can reflect the presence and amount of MSCs.

Experiments in the cylindrical container enabled studying cell viability through the change of the diffusion coefficients and components' fraction. In order to determine the MSCs lifetime, the viability curve has to be examined. The two surveys carried out within a six-day interval were aimed at tracking any evidence of cell death by the change of diffusivities, something which was accomplished. This indicates that diffusion can be proposed as a natural biomarker of a cell viability. Based on the obtained results, it seems that necrosis and apoptosis can be distinguished, which can be achieved thanks to the ability of NMR-MoUSE device to detect low diffusivity components, similar to a nucleus. This provides the opportunity to trace tissue destruction or tissue remodelling through the evidence of elements of cell dissolution. However, reference studies, such as microscopy, are required.

ACKNOWLEDGEMENTS

The work was financed by the National Centre for Research and Development, contract no. STRATEGMED2/265761/10/NCBR/2015. W.M. was partly supported by the EU Project POWR.03.02.00-00-I004/16.

CONFLICT OF INTEREST

The authors declare that they have no competing interests.

AUTHOR CONTRIBUTIONS

Artur T. Krzyżak: Conceptualization (lead); data curation (equal); funding acquisition (equal); investigation (equal); methodology (equal); project administration (equal); software (equal); supervision (lead); validation (equal); writing – original draft (equal); writing – review and editing (equal). **Iwona Habina-Skrzyniarz:** Data curation (equal); formal analysis (equal); investigation (equal); software (equal); visualization (equal); writing – original draft (equal). **Weronika Mazur:** Conceptualization (supporting); data curation (equal); formal analysis (equal); software (equal); validation (equal); visualization (equal); writing – original draft (equal); writing – review and editing (equal). **Maciej Sułkowski:** Data curation (supporting); investigation (supporting); resources (equal); visualization (supporting); writing – original draft (supporting). **Marta Kot:** Data curation (supporting); investigation (supporting); resources (supporting); visualization (supporting); Writing – original draft (supporting). **Marcin Majka:** Conceptualization (equal); funding acquisition (equal); methodology (equal); project administration (equal); resources (equal); supervision (equal); validation (equal); writing – review and editing (equal).

DATA AVAILABILITY STATEMENT

The data that support the findings of this study are openly available in Mendeley Data repository at http://dx.doi.org/10.17632/n3sfpcyp4z.1. Simulations code supporting the current study have not been deposited in a public repository, because it is similar to the widely used and commonly available variants of random walk approach for diffusion simulations (The MathWorks Inc.), but are available from the corresponding author on request.

ORCID

Artur T. Krzyżak https://orcid.org/0000-0002-1709-9831
Weronika Mazur https://orcid.org/0000-0002-6131-2097
Marcin Majka https://orcid.org/0000-0002-0429-681X

REFERENCES

1. Friedenstein A, Chailkhjan R, Lalykina K. The development of fibroblast colonies in monolayer cultures of guinea-pig bone marrow and spleen cells. *Cell Tissue Kinet*. 1970;3(4):393-403. doi:10.1111/j.1365-2184.1970.tb00347.x
2. Dominici M, Le BK, Mueller I, et al. Minimal criteria for defining multipotent mesenchymal stromal cells. The International Society for Cellular Therapy position statement. *Cytotherapy*. 2006;8(4):315-317. doi:10.1080/14653240600855905
3. Bobis S, Jarocha D, Majka M. Mesenchymal stem cells: characteristics and clinical applications. *Folia Histochem Cytobiol*. 2006;44(4):215-230.
4. Milczarek O, Jarocha D, Starowicz-Filip A, et al. Multiple autologous bone marrow-derived CD271+ mesenchymal stem cell transplantation overcomes drug-resistant epilepsy in children. *Stem Cells Transl Med*. 2018;7(1):20-33. doi:10.1002/sctm.17-0041

5. Musialek P, Mazurek A, Jarocha D, et al. Myocardial regeneration strategy using Wharton's jelly mesenchymal stem cells as an off-the-shelf "unlimited" therapeutic agent: results from the Acute Myocardial Infarction First-in-Man Study. *Adv Interv Cardiol*. 2015;11(2):100-107
6. Majka M, Sulkowski M, Badyra B, et al. Concise review: mesenchymal stem cells in cardiovascular regeneration: emerging research directions and clinical applications. *Stem Cells Transl Med*. 2017;6(10):1859-1867. doi:10.1002/sctm.16-0484
7. Blümich B, Casanova F, Appelt S. NMR at low magnetic fields. *Chem Phys Lett*. 2009;477(4–6):231-240. doi:10.1016/j.cplett.2009.06.096
8. Blümich B, Perlo J, Casanova F. Mobile single-sided NMR. *Prog Nucl Magn Reson Spectrosc*. 2008;52(4):197-269. doi:10.1016/j.pnmrs.2007.10.002
9. Modo M, Beech J, Meade T, et al. A chronic 1 year assessment of MRI contrast agent-labelled neural stem cell transplants in stroke. *NeuroImage*. 2009;47 Suppl 2(0 2):T133-T142. doi:10.1016/j.neuroimage.2008.06.017
10. Zhang F, Chen S-Q, Tong M-M, et al. 7.0 tesla high resolution MRI study on intracerebral migration of magnet-labeled neural stem cells in a mouse model of Alzheimer's disease. *Magn Reson Imaging*. 2018;54:58-62. doi:10.1016/j.mri.2018.08.005
11. Park H-H, Lee K-Y, Park DW, et al. Tracking and protection of transplanted stem cells using a ferrocenecarboxylic acid-conjugated peptide that mimics hTERT. *Biomaterials*. 2018;155:80-91. doi:10.1016/j.biomaterials.2017.11.009
12. Ko S-F, Yip H-K, Lee C-C, et al. Apparent diffusion coefficient is a useful biomarker for monitoring adipose-derived mesenchymal stem cell therapy of renal ischemic-reperfusion injury. *Mol Imaging Biol*. 2018;20:750-760. doi:10.1007/s11307-018-1184-0
13. Bontempi P, Busato A, Bonafede R, et al. MRI reveals therapeutical efficacy of stem cells: An experimental study on the SOD1(G93A) animal model. *Magn Reson Med*. 2018;79(1):459-469. doi:10.1002/mrm.26685
14. Krzyżak AT, Habina I. Low field 1H NMR characterization of mesoporous silica MCM-41 and SBA-15 filled with different amount of water. *Microporous Mesoporous Mater*. 2016;231:230-239. doi:10.1016/j.micromeso.2016.05.032
15. Habina I, Radzik N, Topór T, et al. Insight into oil and gas-shales compounds signatures in low field 1H NMR and its application in porosity evaluation. *Microporous Mesoporous Mater*. 2017;252:37-49. doi:10.1016/j.micromeso.2017.05.054
16. Mazur W, Krzyżak AT. Attempts at the characterization of in-cell biophysical processes non-invasively – quantitative. *Cells*. 2020;9(9):2124. doi:10.3390/cells9092124
17. Williamson NH, Ravin R, Benjamini D, et al. Magnetic resonance measurements of cellular and sub-cellular membrane structures in live and fixed neural tissue. *eLife*. 2019;8:e51101. doi:10.7554/eLife.51101
18. Teal PD, Eccles C. Adaptive truncation of matrix decompositions and efficient estimation of NMR relaxation distributions. *Inverse Probl*. 2015;31(4):045010. doi:10.1088/0266-5611/31/4/045010
19. Krueger TEG, Thorek DLJ, Denmeade SR, et al. Concise review: mesenchymal stem cell-based drug delivery: the good, the bad the ugly, and the promise. *Stem Cells Transl Med*. 2018;7(9):651-663. doi:10.1002/sctm.18-0024
20. Joel MDM, Yuan J, Wang J, et al. MSC: immunoregulatory effects, roles on neutrophils and evolving clinical potentials. *Am J Transl Res*. 2019;11(6):3890-3904.
21. Jorgensen P, Edgington NP, Schneider BL, et al. The size of the nucleus increases as yeast cells grow. *Mol Biol Cell*. 2007;18(9):3523-3532. doi:10.1091/mbc.E06
22. Kanimura K, Tsuchiya E, Miyakawa T, et al. Isolation and characterization of the nuclei from *Saccharomyces cerevisiae*. *Curr Microbiol*. 1981;6:175-180. doi:10.1007/BF01642394
23. Lipowsky HH, Bowers DT, Banik BL, et al. Mesenchymal stem cells deformability and implications for microvascular sequestration. *Ann Biomed Eng*. 2018;46(4):640-654. doi:10.1007/s10439-018-1985-y.Mesenchymal
24. Galarza Torre A, Shaw JE, Wood A, et al. An immortalised mesenchymal stem cell line maintains mechano-responsive behaviour and can be used as a reporter of substrate stiffness. *Sci Rep*. 2018;8(1):8981. doi:10.1038/s41598-018-27346-9
25. Tanner JE, Stejskal EO. Restricted self-diffusion of protons in colloidal systems by the pulsed-gradient, Spin-Echo Method. *J Chem Phys*. 1968;49(4):1768-1777. doi:10.1063/1.1670306
26. Åslund I, Topgaard D. Determination of the self-diffusion coefficient of intracellular water using PGSE NMR with variable gradient pulse length. *J Magn Reson*. 2009;201(2):250-254. doi:10.1016/j.jmr.2009.09.006
27. Tanner JE. Intracellular diffusion of water. *Arch Biochem Biophys*. 1983;224(2):416-428. doi:10.1016/0003-9861(83)90228-X
28. Funck C, Laun FB, Wetscherek A. Characterization of the diffusion coefficient of blood. *Magn Reson Med*. 2018;79:2752-2758. doi:10.1002/mrm.26919
29. Tan SCW, Pan WX, Ma G, et al. Viscoelastic behaviour of human mesenchymal stem cells. *BMC Cell Biol*. 2008;9(1):40. doi:10.1186/1471-2121-9-40
30. Iijima H, Isho T, Kuroki H, et al. Effectiveness of mesenchymal stem cells for treating patients with knee osteoarthritis: a meta-analysis toward the establishment of effective regenerative rehabilitation. *Npj Regen Med* 2018;3:15. doi:10.1038/s41536-018-0041-8
31. Charles CJ, Li RR, Yeung T, et al. Systemic mesenchymal stem cell-derived exosomes reduce myocardial infarct size: characterization with MRI in a porcine model. *Front Cardiovasc Med*. 2020;7(November):601990. doi:10.3389/fcvm.2020.601990
32. Alf AAA, Shahror RA, Chen K-Y. Efficient labeling of mesenchymal stem cells for high sensitivity long-term MRI monitoring in live mice brains. *Int J Nanomedicine*. 2020;15:97-114.
33. Tangchitphisut P, Srikaew N, Phongkitkarun S, et al. Using iron sucrose-labeled adipose-derived mesenchymal stem cells in 1.5 and 3 T MRI tracking: an in vitro study. *Heliyon*. 2020;6(8):e04582. doi:10.1016/j.heliyon.2020.e04582
34. Rosenberg JT, Yuan X, Grant S, et al. Tracking mesenchymal stem cells using magnetic resonance imaging. *Brain Circ*. 2016;2:108-113. doi:10.4103/2394-8108.192521
35. Chen Y, Liu Y, Liu Y, et al. Bio- chemical and physical characterizations of mesenchymal stromal cells along the time course of directed differentiation. *Sci Rep*. 2016;6:31547. doi:10.1038/srep31547
36. Rando TA, Ambrosio F. Regenerative rehabilitation: applied biophysics meets stem cell therapeutics. *Cell Stem Cell*. 2018;22(3):306-309. doi:10.1016/j.stem.2018.02.003
37. Liess C, Radda GK, Clarke K. Metabolite and water apparent diffusion coefficients in the isolated rat heart: effects of ischemia. *Magn Reson Med Sci*. 2000;44(2):208-214. doi:10.1002/1522-2594(200008)44:2<208:aid-mrm7>3.0.co;2-i
38. Beaulieu C. The basis of anisotropic water diffusion in the nervous system – a technical review. *NMR Biomed*. 2002;15:435-455. doi:10.1002/nbm.782
39. Pfeuffer J, Flo U, Dreher W, et al. Restricted diffusion and exchange of intracellular water: theoretical modelling and diffusion time dependence of 1H NMR measurements on perfused glial cells. *NMR Biomed*. 1998;11:19-31. doi:10.1002/(SICI)1099-1492(199802)11:1<19:AID-NBM499>3.0.CO;2-O

40. Burstein D, Gray ML, Hartman AL, et al. Diffusion of small solutes in cartilage as measured by nuclear magnetic resonance (NMR) spectroscopy and imaging. *J Orthop Res*. 1993;11:465-478.
41. Ingo C, Brink W, Ercan E, et al. Studying neurons and glia non-invasively via anomalous subdiffusion of intracellular metabolites. *Brain Struct Funct*. 2018;223:3841-3854. doi:10.1007/s00429-018-1719-9

SUPPORTING INFORMATION

Additional supporting information may be found in the online version of the article at the publisher's website.

How to cite this article: Krzyżak AT, Habina-Skrzyniarz I, Mazur W, Sułkowski M, Kot M, Majka M. Nuclear magnetic resonance footprint of Wharton Jelly mesenchymal stem cells death mechanisms and distinctive in-cell biophysical properties in vitro. *J Cell Mol Med*. 2022;00:1–14. doi:10.1111/jcmm.17178

diagnostics

MDPI

Case Report

Diffusion as a Natural Contrast in MR Imaging of Peripheral Artery Disease (PAD) Tissue Changes. A Case Study of the Clinical Application of DTI for a Patient with Chronic Calf Muscles Ischemia

Weronika Mazur [1,2], Małgorzata Urbańczyk-Zawadzka [3], Robert Banyś [3], Rafał Obuchowicz [4], Mariusz Trystuła [5] and Artur T. Krzyżak [1,*]

1 Faculty of Geology, Geophysics and Environmental Protection, AGH University of Science and Technology, Mickiewicza Avenue 30, 30-059 Cracow, Poland; Weronika.Mazur@fis.agh.edu.pl
2 Faculty of Physics and Applied Computer Science, AGH University of Science and Technology, Mickiewicza Avenue 30, 30-059 Cracow, Poland
3 Department of Radiology and Diagnostic Imaging, John Paul II Hospital, Prądnicka Street 80, 31-202 Cracow, Poland; gosia_urbanczyk@poczta.onet.pl (M.U.-Z.); p.banys@szpitaljp2.krakow.pl (R.B.)
4 Department of Diagnostic Imaging, Jagiellonian University Medical College, Jakubowskiego 2, 30-688 Cracow, Poland; rafalobuchowicz@su.krakow.pl
5 Department of Vascular Surgery with Endovascular Procedures Subdivision, John Paul II Hospital, Prądnicka Street 80, 31-202 Cracow, Poland; m.trystula@szpitaljp2.krakow.pl
* Correspondence: akrzyzak@agh.edu.pl

Abstract: This paper reports a first application of diffusion tensor imaging with corrections by using the B-matrix spatial distribution method (BSD-DTI) for peripheral artery disease (PAD) detected in the changes of diffusion tensor parameters (DTPs). A 76-year-old male was diagnosed as having PAD, since he demonstrated in angiographic images of lower legs severe arterial stenosis and the presence of lateral and peripheral circulation and assigned to the double-blind RCT using mesenchymal stem cells (MSCs) or placebo for the regenerative treatment of implications of ischemic diseases. In order to indicate changes in diffusivity in calf muscles in comparison to a healthy control, a DTI methodology was developed. The main advantage of the applied protocol was decreased scanning time, which was achieved by reducing b-value and number of scans (to 1), while maintaining minimal number of diffusion gradient directions and high resolution. This was possible due to calibration via the BSD method, which reduced systematic errors and allowed quantitative analysis. In the course of PAD, diffusivities were elevated across the calf muscles in posterior compartment and lost their anisotropy. Different character was noticed for anterior compartment, in which diffusivities along and across muscles were decreased without a significant loss of anisotropy. After the intervention involving a series of injections, the improvement of DTPs and tractography was visible, but can be assigned neither to MSCs nor placebo before unblinding.

Keywords: diffusion tensor imaging; peripheral artery disease; diffusion tensor tractography; BSD calibration

Citation: Mazur, W.; Urbańczyk-Zawadzka, M.; Banyś, R.; Obuchowicz, R.; Trystuła, M.; Krzyżak, A.T. Diffusion as a Natural Contrast in MR Imaging of Peripheral Artery Disease (PAD) Tissue Changes. A Case Study of the Clinical Application of DTI for a Patient with Chronic Calf Muscles Ischemia. *Diagnostics* **2021**, *11*, 92. https://doi.org/10.3390/diagnostics11010092

Received: 14 December 2020
Accepted: 5 January 2021
Published: 8 January 2021

1. Introduction

Peripheral arterial disease (PAD) is a condition in which blood supplied to peripheral tissues arteries is obstructed, which leads to ischemia of these tissues. In the chronically progressive deficit in oxygenated blood inflow in the course of PAD, the muscle tissue that uses the most oxygen during its work is the first to manifest this clinically. While walking, pain in the calf muscles occurs; the greater the restriction of the inflow, i.e., the restriction of oxygen supply, the faster it occurs. In extreme cases, if we do not improve blood flow, all tissues, including muscles, are necrotized.

The main diagnostic methods before qualifying the patient for revascularization are ultrasound examination with color imaging, angiography or computed tomography angiography. In patients with critical ischemia of the lower extremities, in whom revascularization is not possible, in addition to imaging small yet patent arteries, the assessment of blood supply to the muscles of the lower extremities may be helpful.

Healthy muscles have an anisotropic structure. Changes in the muscle tissue caused by ischemia lead to gradual degradation of cell structures (including protein denaturation), cytoplasm swelling, and disintegration of the cell membrane, and thus disrupt the anisotropic structure of the muscles. As magnetic resonance (MR) diffusion tensor imaging (DTI) is very sensitive to microgeometry, it can be used to detect muscle structural changes caused by ischemia. So far, DTI has been used to detect nervous system injuries [1], in skeletal muscle injuries [2,3], heart muscle injuries [4,5] and in innervation disorders [6–8]. It has also been shown that the second (λ_2) and third (λ_3) eigenvalues reflect the size of the endomysium and myofiber, respectively [9–11].

Stem cells used in regenerative medicine are the primary cells of the body that have the ability to multiply and transform into various, specialized types of daughter cells. These, in turn, can become the starting material for damaged tissue or organ. They are used for the regeneration of nerves, joints, skin, heart muscle and skeletal muscles by acting directly on damaged tissues and indirectly by stimulating the formation of collateral microcirculation (neo-angiogenesis), which in turn improves blood supply to the muscles and allows regeneration.

In this case study, DTI is used to examine the calf muscles of a patient with PAD who have received intraarterial and intramuscular injections of CardioCell based on mesenchymal stem cells (MSCs) or placebo which was produced according to GMP rules at PBTiK UJ CM (license no. 145/0323/15), in a double-blind RCT. The aim of this report is twofold: to outline the development of the approach for the non-invasive diagnosis of PAD by DTI and to monitor the condition of the calf muscles after the administration of therapeutic injections by detecting changes of the diffusion tensor parameters (DTPs) and tractography.

2. Case Study

The diagnostic approach described in the next section was tested on a patient selected randomly from a group of 55 patients from N-O CLI clinical trial, registered under EudraCT No. 2016-004684-40, conducted in accordance with GCP requirements. A 76-year-old male was referred to the Outpatient Clinic of the Vascular Surgery Department of the John Paul II Hospital in Cracow, due to critical ischemia of the right lower limb. This condition was caused by atherosclerosis, diabetes mellitus and possibly also immune responses in the course of rheumatoid arthritis. The patient was a heavy smoker in the past. These conditions had caused the build-up of atherosclerotic plaques in the arteries, causing a state of ischemia in many organs, but especially in his right lower limb. The symptom of such a critical supply to the leg tissues of oxygen carried by the blood is pain, in the first place in the muscles, not only during exercise, i.e., while walking, but even at rest. The extreme stage of ischemia is tissue necrosis, and when the inflow of oxygenated blood is not improved, necrotic changes require limb amputation.

During the last few years, this patient was operated upon many times, both by endovascular methods (arterial recanalization with angioplasty and stent implantation), and by performing open surgery (endarterectomy and by-passes). Due to the exhaustion of all possibilities of revascularization, he was offered an experimental method of treatment using mesenchymal cells (so-called stem cells) in a double-blind RCT. These cells were isolated from Wharton's jelly of neonatal umbilicals. In this program, research was focused on creating a new network in arterial microcirculation through stimulation with stem cells. As a result, it would improve the blood supply to the limb and save it from amputation.

The intraarterial and intramuscular injections in a double-blind RCT intervention was initiated following the first DTI examination (E1). Therapy encompassed three injections every seven weeks and after the whole series (83 days after E1) the DTI examination

was repeated (E2; first follow-up). One healthy volunteer was enrolled in the study (control). The study protocol was designed according to the guidelines of the Declaration of Helsinki and Good Clinical Practice standards and conducted at the Vascular Surgery Department with Endovascular Procedures Subdivision, John Paul II hospital in Cracow, Poland. The Institutional Ethical Committee on Human Research approved the studies and the publication of anonymized medical images. Informed consent was also collected from the patient.

3. DTI Procedure Developed for the Diagnosis and Intervention Monitoring

Both DTI examinations were performed on a 3T MR system (Siemens Skyra 3 T, Erlangen, Germany) with the application of an eight-channel TORSO body coil. Lower legs were examined axially in terms of T_1-weighted MR images (repetition time, TR = 440 ms, echo time, TE = 10.8 ms) and T_2-weighted MR images (TR = 3800, TE = 70 ms) with fat suppression by using a Fast Spin Echo (FSE) sequence. The images were primarily used to depict the anatomical structures and detect muscle edema. DTI were acquired using the Echo Planar Imaging (EPI) sequence with six diffusion gradient directions. In the DTI protocol b-value = $350 \cdot 10^3$ s/mm^2, TR/TE, 5200/64 ms, FOV = 59 × 39 cm^2, Number of Scans, NoS = 1, 384 × 300 Px matrix; slice thickness was equal to 8 mm, while no interleaved slices were assured. Each DTI acquisition lasted about 2.5 min.

Additionally, since the analysis is quantitative, the B-matrix spatial distribution (BSD) method was applied in order to eliminate the systematic errors in DTI [12,13]. The approach relies on the determination of real B–matrices on a voxel-by-voxel basis with the application of anisotropic phantoms. After the BSD calibration of a gradient field, the diffusion tensor can be more accurately determined, while the bias due to systematic errors is eliminated [14]. The application of this method is especially important in fiber tracking, in which fiber tracts are more reliably determined, and changes can be better detected [15].

Images were analyzed in terms of mean diffusion tensor parameters (DTPs) and fiber tracking using the in-house BSD-DTI software (BSD-DTI ver. 2.0, AGH UST, Cracow, Poland). DTPs analyzed in the study were fractional anisotropy (FA), mean diffusivity (MD) and three eigenvalues (λ_1, λ_2, λ_3). ROIs were selected in the regions of three muscles: Gastrocnemius Medialis (GM), Soleus (SOL) and Tibialis Anterior (TA), which were identified based on T_1-weighted images. ROIs were circles with a radius consisting of four pixels.

Fiber tracking was performed by applying seeding ROIs (with each seed step equal to 1 voxel) allowed for bidirectional tracking with the integration step set to 0.1 voxel. The seeding ROIs were drawn based on the T_1-weighted images in the SOL muscle. FA range was equal to 0.15-1, and an angle change was set to be smaller than 45 per integration step. In the images, seven slices were subjected to analysis, in which the seeding ROIs were circles having a radius equal to eight pixels. The location of the ROI was chosen on the basis of cuts made on a frozen cadaver (Visible Human Project U.S National Library of Medicine). The obtained fiber tracts were analyzed qualitatively and quantitatively via the fiber tracts density (FTD) parameter. This is calculated as the ratio of the number of tracts per volume of voxels in a cylinder obtained from stacking ROIs from all slices.

4. Results and Discussion

The BSD-DTI method eliminates systematic errors present during the calculation of a diffusion tensor. The method relies on the Generalized Stejskal-Tanner equation; the importance of the application to nervous system diagnostics based on diffusion tensor tractography was pointed out recently [12–18]. The effectiveness of even the lean approach was also shown (in relation to the BSD method), where the effective value of the B-matrix was calibrated on the basis of isotropic phantom measurements [19]. There is also an alternative approach to correct the DTI images based on the knowledge of the coil tensor, L, obtained from the manufacturer or experimentally [20]. Currently, however, it is not possible to apply this approach in practice and there is no clear evidence of its effectiveness

(the impact of factors other than heterogeneity of the gradient coils on the distribution of gradient fields for different diffusion sequences). In our study, the observed effect of the calibration using the BSD method is not the same for all of the subjects. It can be seen in Figure 1, that FA and λ_1 are significantly underestimated for control, while overestimated for the patient when calculated from the uncalibrated tensor. Considering that the differences determining muscle status can be subtle, the application of BSD-DTI seems essential for the use of diffusion as a disease marker.

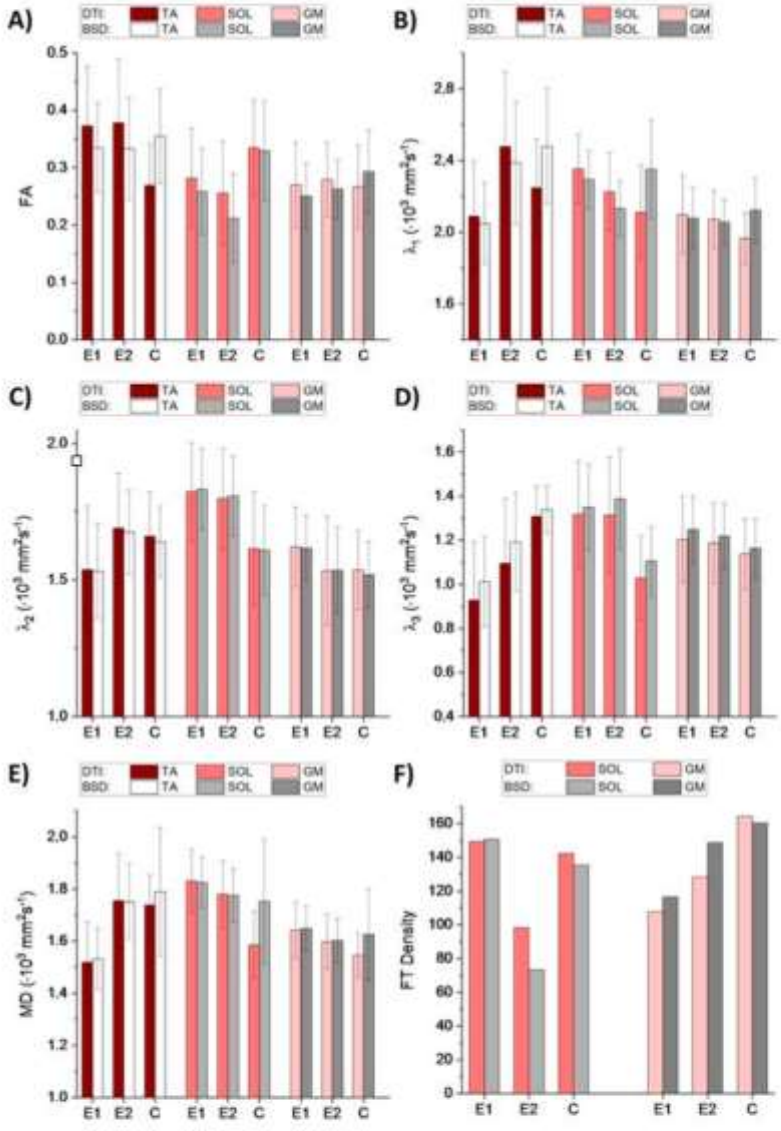

Figure 1. Diffusion tensor parameters: fractional anisotropy (FA) (**A**), λ_1 (**B**), λ_2 (**C**), λ_3 (**D**), mean diffusivity (MD) (**E**) and fiber tracts (FT) density (**F**) obtained for the patient before (E1) and after (E2) the intervention and the control (C) with and without the calibration of a gradient field using the B-matrix spatial distribution (BSD) method.

As shown in the Section 1, DTPs can reflect muscle status. Increased MD may indicate broadened spaces within an analyzed volume of interest. Increased λ_2 and λ_3 indicate elevated diffusivity across the muscle's long axis, which means that the cross-sectional areas of the muscle and endomysium are extended. In the case of PAD, it is expected that fatty accumulation, newly-formed vessels (collateral circulation), fibrosis and undernourished muscles (see Figure 2) will cause changes in the abovementioned parameters. These changes are clearly discernible in Figure 1. In the diseased muscles, the partial loss of anisotropy compared to the healthy ones can be seen, especially in the SOL (Figure 1A). Transversal diffusivity (reflected in λ_2 and λ_3) in SOL is increased, possibly due to fatty accumulation. Longitudinal diffusivity (λ_1) is very similar to the healthy muscle, which may be caused by the presence of multiple blood vessels, that can increase diffusion coefficient in the direction of a blood flow. In GM muscle, differences in diffusivities correspond to SOL, but they are more subtle due to fewer blood vessels and lower fatty infiltration. In the anterior compartment the character of changes is different than in the posterior one. In TA muscle all diffusivities (λ_1, λ_2, λ_3 and MD) are decreased, with FA almost not affected. This may result from fibrosis in the muscle (Figure 2). It was hypothesized by Sanz-Requena et al. [21] that the fat content in lower leg muscles would cause a decrease of apparent diffusion coefficient. Therefore, decrease of diffusivities in the patient's TA muscle may also indicate its dehydration.

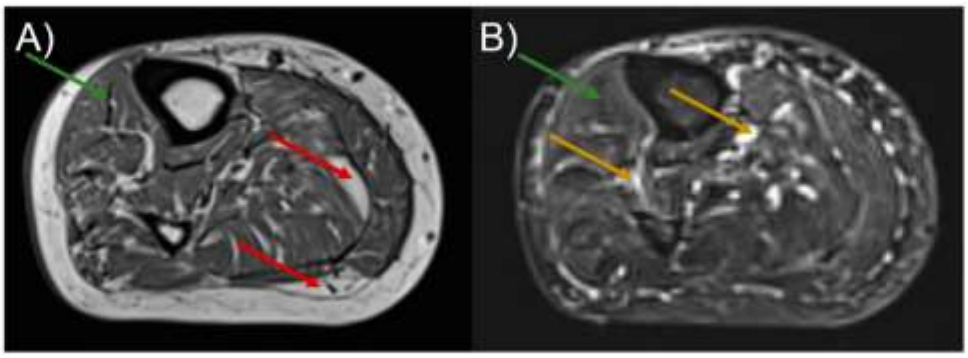

Figure 2. T_1-weighted (**A**) and T_2-weighted (**B**) images of the patient's calf acquired before the intervention (following the E1 diffusion tensor imaging (DTI) examination). Red, green and yellow arrows indicate fatty accumulation in muscles, fibrosis and blood vessels, respectively.

Comparing E1 and E2 examinations with the control, it can be seen that in TA and GM the DTPs from E2 become closer to the values obtained for the control. In SOL, the differences are higher after the intervention. However, fiber tracts (Figure 3) evince improvement in terms of the fiber tract directions in both SOL and GM. It is clearly visible that tractography for E2 contains more vertical (blue), organized fibers than for E1, and becomes more similar to the tractography for healthy legs. The density of fibers is only improved for GM (Figures 1F and 3). However, considering that this paper is based on the preliminary results from an ongoing project, it is as yet unknown whether these results reflect the patient's actual condition.

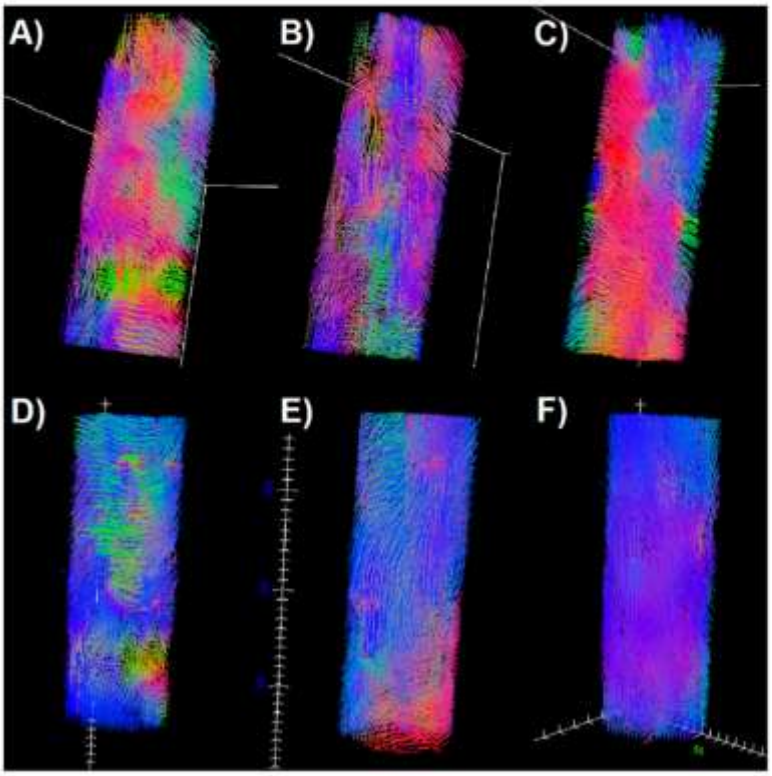

Figure 3. Fiber tracts obtained for the soleus (SOL) (upper row) and gastrocnemius medialis (GM) (lower row) muscles for the patient in the first examination (**A**,**D**), for the patient after the intervention (**B**,**E**) and for the healthy control (**C**,**F**).

5. Conclusions

In this paper, diffusion was proposed as a natural marker of skeletal muscle condition in PAD. Diffusion tensor parameters and tractography after the correction by using the BSD method were compared for examinations conducted for patient before and after the injections in the double-blind RCT, and with a healthy control. This case study shows that in the course of PAD, both anterior and posterior compartments are distinguished by the change of DTPs in comparison to control, while the character of these changes is compartment-dependent. Moreover, diffusivity and anisotropy changes are different for the muscles containing fibrosis, fatty accumulation, and depend on the degree of the angiogenesis. After injections, a very good improvement was observed for DTPs in the TA muscle, and a discernible improvement was seen in the GM muscle. In the SOL, the differences between the patient and the control increased in the follow-up examination. In terms of fiber tracking, the tracts in E2 were more similar to the control in terms of directions (SOL, GM) and density (GM). This may indicate the progression of muscle anisotropy and structure, respectively. The progression will be assigned to the MSCs therapy or placebo after the unblinding.

Author Contributions: Conceptualization, A.T.K., R.B. and R.O.; methodology, A.T.K., R.B., M.T. and R.O.; software, A.T.K.; validation, R.O., M.U.-Z. and M.T.; formal analysis, W.M., R.O.; investigation, R.B., A.T.K., M.T.; resources, M.U.-Z., A.T.K.; data curation, W.M., R.B., R.O., M.T.; writing—original draft preparation, W.M., A.T.K.; writing—review and editing, M.T., A.T.K., R.O., M.U.-Z., W.M.; visualization, W.M., A.T.K.; supervision, A.T.K., R.O., M.T.; project administration, M.U.-Z., R.B.,

A.T.K., M.T.; funding acquisition, A.T.K. All authors have read and agreed to the published version of the manuscript.

Funding: This research was funded by the National Centre of Research and Development (contract No. STRATEGMED2/265761/10/NCBR/2015. W.M. was partly supported by the EU Project POWR.03.02.00-00-I004/16.

Institutional Review Board Statement: The study was conducted according to the guidelines of the Declaration of Helsinki and approved by the Institutional Review Board of John Paul II hospital in Cracow. Positive opinion no. 1072.61201.17.2017 dated on 21/12/2017 was issued by the Bioethics Committee of the Jagiellonian University.

Informed Consent Statement: Informed consent was obtained from all subjects involved in the study.

Data Availability Statement: The data presented in this study are available on request from the corresponding author.

Acknowledgments: The authors are grateful to Marcin Majka from the Department of Transplantation at the Jagiellonian University in Krakow and Jakub Baran from the Polish Stem Cells Bank (FamiCord Group) for providing MSCs or placebo and facilitating the therapy.

Conflicts of Interest: The authors declare that they have no conflict of interest.

References

1. Krzyżak, A.T.; Jasiński, A.; Kwieciński, S.; Kozłowski, P.; Adamek, D. Quantitative Assessment of Injury in Rat Spinal Cords In Vivo by MRI of Water Diffusion Tensor. *Appl. Magn. Reson.* **2008**, *34*, 3–20. [CrossRef]
2. Zaraiskaya, T.; Kumbhare, D.; Noseworthy, M.D. Diffusion tensor imaging in evaluation of human skeletal muscle injury. *J. Magn. Reson. Imaging* **2006**, *24*, 402–408. [CrossRef] [PubMed]
3. Hall, M.N.; Hall, J.K.; Cadwallader, A.B.; Pawlikowski, B.T.; Doles, J.D.; Elston, T.L.; Olwin, B.B. Transplantation of Skeletal Muscle Stem Cells. *Comput. Biol.* **2017**, *1556*, 237–244. [CrossRef]
4. Musialek, P.; Mazurek, A.; Jarocha, D.; Tekieli, L.; Szot, W.; Kostkiewicz, M.; Banys, R.P.; Urbanczyk, M.; Kadzielski, A.; Trystula, M.; et al. Myocardial regeneration strategy using Wharton's jelly mesenchymal stem cells as an off-the-shelf 'unlimited' therapeutic agent: Results from the Acute Myocardial Infarction First-in-Man Study. *Adv. Interv. Cardiol.* **2015**, *11*, 100–107. [CrossRef]
5. Yu, H.; Lu, K.; Zhu, J.; Hu, W. Stem cell therapy for ischemic heart diseases. *Br. Med. Bull.* **2017**, *121*, 135–154. [CrossRef] [PubMed]
6. Zhang, J.; Zhang, G.; Morrison, B.M.; Mori, S.; Sheikh, K.A. Magnetic resonance imaging of mouse skeletal muscle to measure denervation atrophy. *Exp. Neurol.* **2008**, *212*, 448–457. [CrossRef] [PubMed]
7. Jarocha, D.; Milczarek, O.; Wedrychowicz, A.; Kwiatkowski, S.; Majka, M. Continuous Improvement after Multiple Mesenchymal Stem Cell Transplantations in a Patient with Complete Spinal Cord Injury. *Cell Transplant.* **2015**, *24*, 661–672. [CrossRef] [PubMed]
8. Csobonyeiova, M.; Polák, Š.; Zamborsky, R.; Danisovic, L. Recent Progress in the Regeneration of Spinal Cord Injuries by Induced Pluripotent Stem Cells. *Int. J. Mol. Sci.* **2019**, *20*, 3838. [CrossRef]
9. Galbán, C.J.; Maderwald, S.; Uffmann, K.; Ladd, M.E. A diffusion tensor imaging analysis of gender differences in water diffusivity within human skeletal muscle. *NMR Biomed.* **2005**, *18*, 489–498. [CrossRef] [PubMed]
10. Carlier, P.G.; Marty, B.; Scheidegger, O.; De Sousa, P.L.; Baudin, P.-Y.; Snezhko, E.; Vlodavets, D. Skeletal Muscle Quantitative Nuclear Magnetic Resonance Imaging and Spectroscopy as an Outcome Measure for Clinical Trials. *J. Neuromuscul. Dis.* **2016**, *3*, 1–28. [CrossRef] [PubMed]
11. Berry, D.B.; Regner, B.; Galinsky, V.; Ward, S.R.; Frank, L.R. Relationships between tissue microstructure and the diffusion tensor in simulated skeletal muscle. *Magn. Reson. Med.* **2017**, *80*, 317–329. [CrossRef] [PubMed]
12. Borkowski, K.; Krzyżak, A.T. The generalized Stejskal-Tanner equation for non-uniform magnetic field gradients. *J. Magn. Reson.* **2018**, *296*, 23–28. [CrossRef] [PubMed]
13. Borkowski, K.; Kłodowski, K.; Figiel, H.; Krzyżak, A.T. A theoretical validation of the B-matrix spatial distribution approach to diffusion tensor imaging. *Magn. Reson. Imaging* **2017**, *36*, 1–6. [CrossRef] [PubMed]
14. Borkowski, K.; Krzyżak, A.T. Assessment of the systematic errors caused by diffusion gradient inhomogeneity in DTI-computer simulations. *NMR Biomed.* **2019**, *32*, e4130. [CrossRef] [PubMed]
15. Borkowski, K.; Krzyżak, A.T. Analysis and correction of errors in DTI-based tractography due to diffusion gradient inhomogeneity. *J. Magn. Reson.* **2018**, *296*, 5–11. [CrossRef] [PubMed]
16. Kwon, H.G.; Chang, C.H.; Jang, S. Diagnosis of Dizziness Due to a Core Vestibular Projection Injury in a Patient with Intracerebral Hemorrhage. *Diagnostics* **2020**, *10*, 220. [CrossRef]
17. Kierońska, S.; Sokal, P.; Dura, M.; Jabłońska, M.; Rudaś, M.; Jabłońska, R. Tractography-Based Analysis of Morphological and Anatomical Characteristics of the Uncinate Fasciculus in Human Brains. *Brain Sci.* **2020**, *10*, 709. [CrossRef] [PubMed]

18. Obuchowicz, R.; Krzyżak, A.T. Improvement of Brain Tractography Using the BSD-DTI Method on the Example of Subcortical U-Fibers Visualization. In Proceedings of the European Congress of Radiology, Vienna, Austria, 27 February–3 March 2019. [CrossRef]
19. Lee, Y.; Kettinger, A.O.; Wilm, B.J.; Deichmann, R.; Weiskopf, N.; Lambert, C.; Pruessmann, K.P.; Nagy, Z. A comprehensive approach for correcting voxel-wise b-value errors in diffusion MRI. *Magn. Reson. Med.* **2019**, *83*, 2173–2184. [CrossRef] [PubMed]
20. Hansen, C.B.; Rogers, B.P.; Schilling, K.G.; Nath, V.; Blaber, J.A.; Irfanoglu, O.; Barnett, A.; Pierpaoli, C.; Anderson, A.W.; Landman, B.A. Empirical field mapping for gradient nonlinearity correction of multi-site diffusion weighted MRI. *Magn. Reson. Imaging* **2021**, *76*, 69–78. [CrossRef] [PubMed]
21. Sanz-Requena, R.; Martínez-Arnau, F.M.; Pablos, A.; Flor-Rufino, C.; Barrachina-Igual, J.; García-Martí, G.; Martí-Bonmatí, L.; Pérez-Ros, P. The Role of Imaging Biomarkers in the Assessment of Sarcopenia. *Diagnostics* **2020**, *10*, 534. [CrossRef] [PubMed]

Diffusion tensor imaging as a tool to assess the structure of lower limb muscles invisible on T1- and T2-weighted images in the course of the chronic phase of peripheral artery disease

Weronika Mazur[1,2], Małgorzata Urbańczyk-Zawadzka[3], Robert Banyś[3], Rafał Obuchowicz[4], Mariusz Trystuła[5], Artur T. Krzyżak[1]

[1]Faculty of Geology, Geophysics and Environmental Protection, AGH University of Science and Technology, Krakow, Poland
[2]Faculty of Physics and Applied Computer Science, AGH University of Science and Technology, Krakow, Poland
[3]Department of Radiology and Diagnostic Imaging, John Paul II Hospital, Krakow, Poland
[4]Department of Diagnostic Imaging, Jagiellonian University Medical College, Krakow, Poland
[5]Department of Vascular Surgery with Endovascular Procedures Subdivision, John Paul II Hospital, Krakow, Poland

Adv Interv Cardiol 2022; 18, 3 (69):
DOI: https://doi.org/10.5114/aic.2022.121343

A patient with peripheral artery disease (PAD) was selected randomly from a group of 55 patients from the N-O CLI clinical trial, registered under EudraCT No. 2016-004684-40, conducted in accordance with GCP requirements. A 76-year-old woman was referred to the Outpatient Clinic of the Vascular Surgery Department of the John Paul II Hospital in Krakow, due to critical ischemia of the right lower limb. She was offered an experimental method of treatment using mesenchymal stem cells (MSCs). The patient was submitted to magnetic resonance imaging (MRI) examination before (E1) and after (E2) the intraarterial and intramuscular injections of CardioCell based on mesenchymal stem cells (MSCs) or placebo which was produced according to the rules of good manufacturing practices at Jagiellonian University Collegium Medicum, Pracownia-Bank Tkanek i Komórek (PBTiK) Zakładu Transplantologii UJ CM (license no. 145/0323/15), in a double-blind RCT. Therapy encompassed three injections every seven weeks and after 398 days after E1 the condition of the lower extremities was once again checked by MRI. The study was conducted according to the guidelines of the Declaration of Helsinki and approved by the Institutional Review Board of John Paul II hospital in Krakow. Positive opinion no. 1072.61201.17.2017 dated on 21/12/2017 was issued by the Bioethics Committee of the Jagiellonian University.

Muscles' condition was evaluated based on T_1- (T1WI) and T_2-weigthed images (T2WI; Figure 1), obtained transversely on a 3T MR system (Siemens Skyra 3 T, Erlangen, Germany) using an eight-channel TORSO body coil with the application of turbo spin echo (TSE) and turbo inversion recovery magnitude (TIRM) with fat suppression pulse sequences, respectively. Complementarily, diffusion tensor imaging (DTI) was performed using the Echo Planar Imaging (EPI) sequence with six diffusion gradient directions. In the DTI protocol, *b*-value = 350 s/mm^2, number of scans, NoS = 1, while slice thickness was equal to 8 mm. The BSD-DTI calibration method [1, 2] was applied before the quantitative analysis, for which it was shown recently to have substantial applicability [3]. The following DTI parameters were analyzed: the second and third eigenvalues (λ_2 and λ_3, respectively), mean (MD), longitudinal (DL) and transversal (DT; mean of λ_2 and λ_3) diffusivity, and fractional anisotropy (FA), by using the in-house BSD-DTI software (BSD-DTI ver. 2.0, AGH UST, Krakow, Poland). For comparison, mean parameters for 3 healthy volunteers were presented (control, C). A single muscle from each compartment was chosen as representative: tibialis anterior (TA), soleus (SOL) and gastrocnemius medialis (GM).

Recently it was shown that the BSD-DTI method is crucial for the quantitative evaluation of the muscle condition and intervention effect in PAD. In this study we found that diffusion can also reflect different disease courses. MRI of the patient from this work revealed chronic muscle denervation that resulted in atrophy with

Corresponding author:
Artur T. Krzyżak, Faculty of Geology, Geophysics and Environmental Protection, AGH University of Science and Technology, Krakow, Poland, e-mail: akrzyzak@agh.edu.pl
Received: 13.05.2021, **accepted:** 13.10.2022.

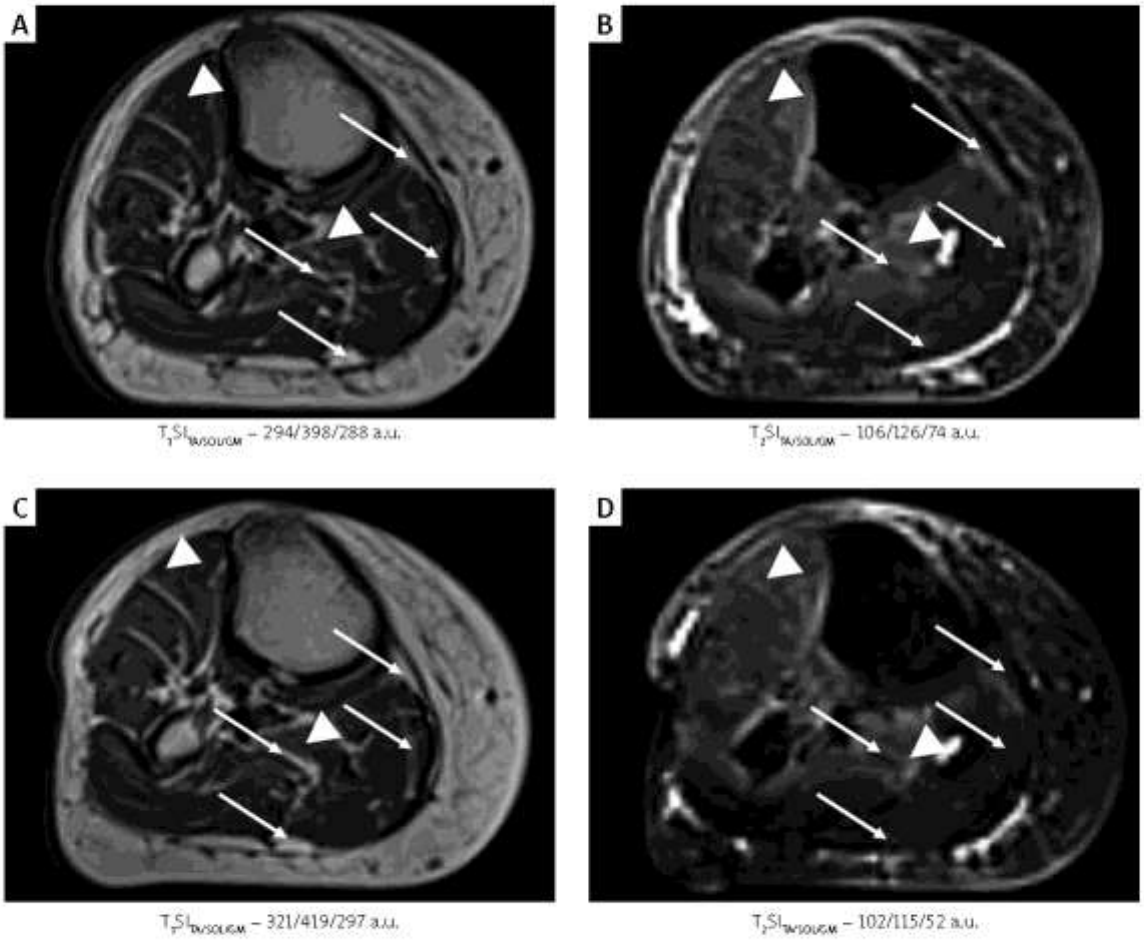

Figure 1. Axial T1-weighted FSE (T1WI) and T2-weighted TIRM (T2WI) images of calf of a 76-year-old woman with PAD. **A**, **B** – T1WI (A) and T2WI (**B**) before the medical intervention (examination E1); **C**, **D** – T1WI (**C**) and T2WI (**D**) after the injections of CardioCell based on mesenchymal stem cells (MSCs) or placebo in a double-blind RCT (examination E2). Regions of fatty infiltration (arrows) and edema-like signal (arrowheads) can be recognized. In the picture, analyzed calf muscles are indicated by the following abbreviations: tibialis anterior (TA), soleus (SOL), gastrocnemius medialis (GM), for which T1 and T2 signal intensities (T1SI and T2SI, respectively) are shown below the image

fatty infiltration reflected in a hyperintense signal on T1WI and a corresponding low-intensity signal on T2WI [4], similarly to a previously reported patient [3]. In contrast, anterior and deep posterior compartments showed a high-intensity, edema-like signal on T2WI (Figure 1), while neoangiogenesis in the muscle bulk was hardly recognized, which is opposite to the previously reported patient [3].

According to Mazur *et al.* [3], each muscle change in PAD can be reflected in diffusive properties. λ_2 and λ_3 reflect the transverse diffusion in the endomysium and myofiber, respectively. Hence, λ_3 is sensitive to fatty infiltration, which relies on the replacement of muscle fibers by fat characterized by a smaller diffusion coefficient than water. Increased diffusivities in general, but especially DT, λ_2 and λ_3, can indicate edema. Interestingly, the patient did not demonstrate increased diffusivities in E1. Visibly lower DT resulting from the lower λ_3 was observed for SOL, suggesting the highest fatty deposit. In TA the highest DT, λ_2, λ_3 and *MD* are correlated with the strongest edema. GM muscle condition was not severe based on T1WI/T2WI, and among the three analyzed muscles it had only slightly increased diffusivities.

After the intervention (E2) all muscles are characterized by higher T_1 signal intensity (T_1SI) and lower T_2 signal intensity (T_2SI) (Figures 1 C and D, respectively), which is associated with T_1 and T_2 decreasing. This means that they approached the values reported for normal muscles

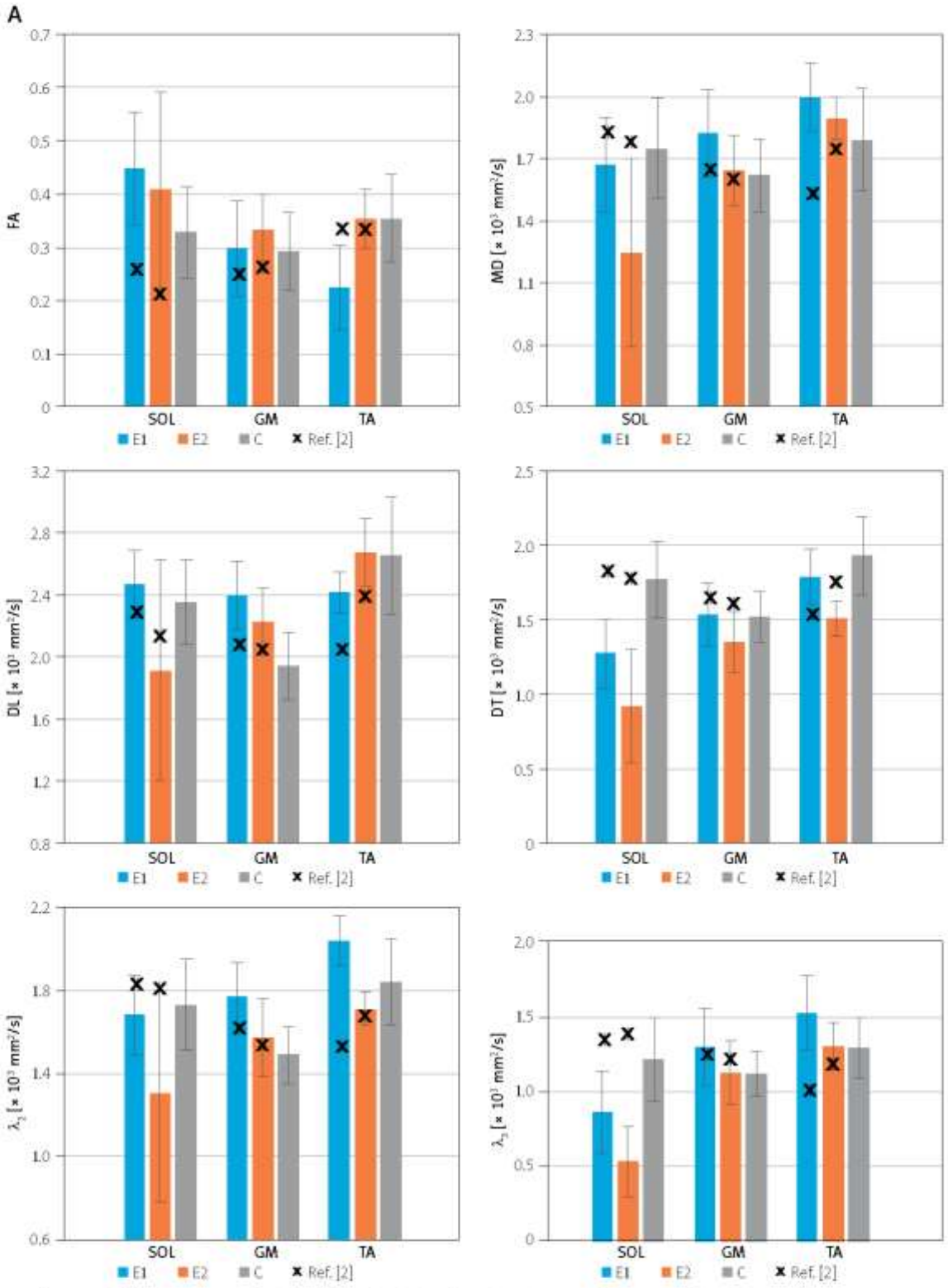

Figure 2. Diffusion tensor imaging (DTI) of calf muscles of a 76-year-old woman with PAD. **A** – DTI parameters (fractional anisotropy, FA, mean diffusivity, MD, longitudinal diffusivity, DL, transverse diffusivity, DT, the second eigenvalue, λ_2, and the third eigenvalue, λ_3) obtained before (E1) and after (E2) the intervention consisting of the injections of CardioCell based on mesenchymal stem cells (MSCs) or placebo in a double-blind RCT, with comparison to the values obtained for healthy control (**C**) and the patient in Ref. 2 [2]

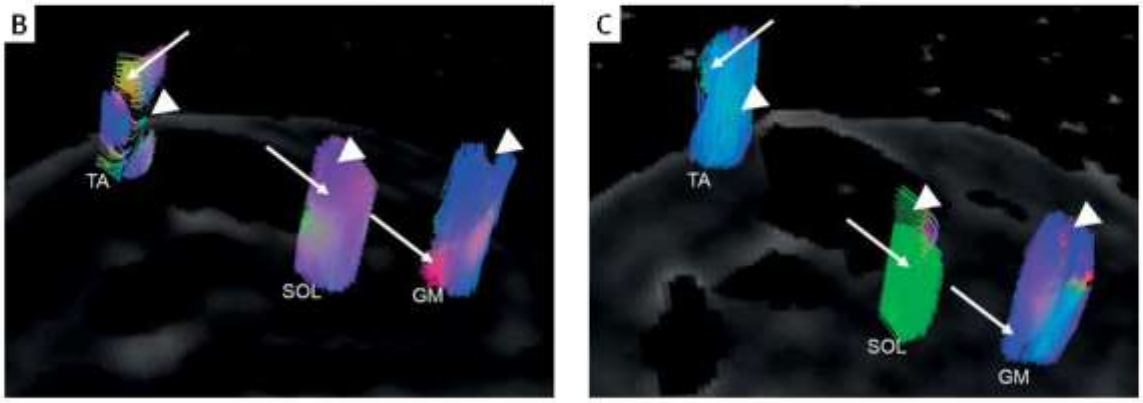

Figure 2. Cont. **B**, **C** – DTI tractography for calf muscles for a given region of interest in E1 (**B**) and E2 (**C**). Regions of improved fiber tract direction (arrows) and density (arrowheads) can be recognized. In the picture, analyzed calf muscles are indicated by the following abbreviations: tibialis anterior (TA), soleus (SOL), gastrocnemius medialis (GM)

(T_2 = 27–38 ms [5] and T_1 = 1420 ms [6] in comparison to T_2 = 133 ms for fat [6]). At the same time, MD and DT decreased, which suggests the reduction of the edema. Moreover, GM and TA showed improved muscle anisotropy and FA, visible also as the improved structure (density and direction of fibers) on the tractographic DTI representation (Figures 2 B and C). A slight decrease of λ_2 and λ_3 in TA and GM seems to be connected with edema recovery rather than fatty degeneration. In SOL, apart from decreased DT, λ_2, λ_3 and MD indicatory for detumescence, fiber tract density (Figures 2 B and C, arrowheads), FA and DL decreases can also be observed, which suggests overall muscle dehydration. The intervention caused changes from peripheral to internal compartments, which will be assigned to the MSC therapy or placebo after the unblinding.

In conclusion, without DTI no information about muscle structure can be obtained from T1WI/T2WI. As a reference we showed results from the previous study, in which T1WI/T2WI indicated more collateral circulation and fatty replacement in the patient's calves, suggesting more disrupted muscles than for the patient in this study. The same intervention procedure caused more subtle changes towards the healthy control's diffusivities and anisotropy, meaning that despite advanced lower limb ischemia, collateral circulation, even though intruding the muscle bulk, allowed the muscle structure to be preserved and the muscles to remain nourished. Surprisingly, the patient in this study was found to have more damaged muscle structure in SOL, while demonstrating a great improvement in anterior and posterior compartments after the intervention.

Acknowledgments

The authors are grateful to Marcin Majka from the Department of Transplantation at the Jagiellonian University in Krakow and Jakub Baran from the Polish Stem Cell Bank (FamiCord Group) for providing MSCs or placebo and facilitating the therapy.

This research was funded by the National Centre of Research and Development (contract No. STRATEGMED2/265761/10/NCBR/2015. W.M. was partly supported by the EU Project POWR.03.02.00-00-I004/16.

Conflict of interest

The authors declare no conflict of interest.

References

1. Borkowski K, Krzyżak AT. The generalized Stejskal-Tanner equation for non-uniform magnetic field gradients. J Magn Reson 2018; 296: 23-8.
2. Borkowski K, Kłodowski K, Figiel H, Krzyżak AT. A theoretical validation of the B-matrix spatial distribution approach to diffusion tensor imaging. Magn Reson Imaging 2017; 36: 1-6.
3. Mazur W, Urbańczyk-Zawadzka M, Banyś R, et al. Diffusion as a natural contrast in MR imaging of peripheral artery disease (PAD) tissue changes. A case study of the clinical application of DTI for a patient with chronic calf muscles ischemia. Diagnostics 2021; 11: 92.
4. Kim S, Choi JY, Huh YM, et al. Role of magnetic resonance imaging in entrapment and compressive neuropathy – what, where, and how to see the peripheral nerves on the musculoskeletal magnetic resonance image: Part 1. Overview and lower extremity. Eur Radiol 2007; 17: 139-49.
5. Psatha M, Wu Z, Gammie FM, et al. A longitudinal MRI study of muscle atrophy during lower leg immobilization following ankle fracture. J Magn Reson Imaging 2012; 35: 686-95.
6. Gold GE, Han E, Stainsby J, et al. Musculoskeletal MRI at 3.0 T: relaxation times and image contrast. AJR Am J Roentgenol 2004; 183: 343-51.

THE JOURNAL OF PHYSICAL CHEMISTRY C

pubs.acs.org/JPCC Article

Identification of Proton Populations in Cherts as Natural Analogues of Pure Silica Materials by Means of Low Field NMR

Artur T. Krzyżak,* Weronika Mazur, Jacek Matyszkiewicz, and Alicja Kochman

Cite This: J. Phys. Chem. C 2020, 124, 5225−5240 Read Online

ACCESS | Metrics & More | Article Recommendations | Supporting Information

ABSTRACT: Recent theories about the sources of silica in bedded and nodular cherts do not fit the origin of cherts from the Kraków−Częstochowa Upland. Since siliceous sponges as a single source of silica is questionable, assumptions about additional sources have to be verified. In order to do so, three samples of nodular cherts and one representative sample of bedded chert were studied by means of ^{1}H LF-NMR 1D and 2D relaxometry and complementary geochemical methods. The results were compared with the literature and standard silica materials which helped to identify five types of ^{1}H signal. The very distinct 1D-T_2 spectra of the dried samples indicated the existence of closed pores which, after comprehensive analysis, were identified as inclusions filled with different types of siliceous materials. Saturation revealed the differences between nodular and bedded cherts that were visible mainly in the amount and size of open porosity. The principal component analysis of NMR parameters showed the excellent separation of these two groups of samples and this is well visible on the biplots. Additionally, the estimated pore size distribution revealed that the total porosity of around 2% consisted primarily of mesopores (2−50 nm in diameter) and macropores (diameter >50 nm). In bedded cherts, open porosity is dominated by macropores, while the share of mesopores and macropores is similar in nodular cherts.

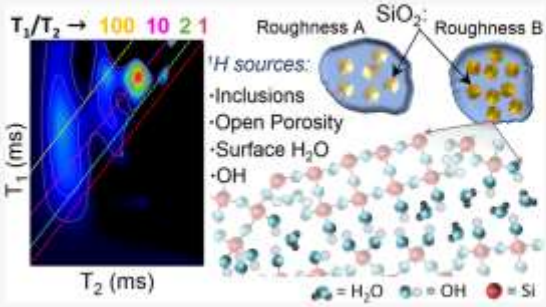

1. INTRODUCTION

Cherts are a type of sedimentary, nonporous, highly siliceous rocks composed of quartz. Silicon in cherts may occur in various forms, such as silica or silanols (in the magnetic resonance nomenclature Q_4 or Q_3, Q_2, Q_1, Q_0, where an index corresponds to the number of oxygen atoms).[1] Two forms of cherts exist, nodular (concretions) or bedded, and their origin is sometimes problematic to discern. However, the differentiation of cherts is important from the geological, archeological[2−5] and petrological[6] point of view. The origin of both the chert nodules and the bedded cherts in the Fanerozoic sediments has attracted the attention of many authors. Generally, these rocks are interpreted as the products of synsedimentary, or early- to late-diagenetic, or epigenetic processes (see, e.g., refs 7−32). One of the regions of the occurrence of cherts is the Kraków-Częstochowa Upland (KCU). The KCU is located in southern Poland and is a part of the Silesian-Kraków Homocline—the regional tectonic unit built up of the Triassic, Jurassic and Cretaceous sediments deposited unconformably onto the Precambrian and Paleozoic formations, and transected by the major the Kraków-Lubliniec Fault Zone.[33] Various assumptions as to the origin of silica in bedded and nodular cherts have been made. The assumption that siliceous skeletons of sponges were the main source of silica for chert nodules forming horizons in biostrome-like Oxfordian bedded limestones has already been presented in the literature.[34−37] However, the origin of silica in bedded cherts hosted in calciturbidites from the Oxfordian/Kimmeridgian turn has only been discussed in a single publication by Matyszkiewicz,[38] who suggested the accumulations of radiolarians abruptly buried in sediments by density flows as the source of silica, in accordance with the model after Bustillo and Ruiz-Ortiz.[30] Recently, the concept of siliceous sponges skeletons as practically the sole source of silica for chert nodules hosted in the Upper Jurassic microbial-sponge megafacies of the KCU (as a part of the Tethyan northern margin) has been questioned due to three facts: (i) the lack of a clear correlation between the abundance of siliceous sponges in bedded limestones[39−41] and the accumulations of chert nodules, which only occasionally form horizons in the Middle Oxfordian bedded, biostrome-like limestones,[35,42] (ii) the occurrence of chert nodules within the calciturbidites from the Oxfordian/Kimmeridgian turn, whereas the share of siliceous sponges in *in situ* sediments of that age is lower than in the Middle Oxfordian sediments and while radiolarians are present in marly sediments overlying the calciturbidites,[38,42] and (iii)

Received: December 20, 2019
Revised: January 30, 2020
Published: February 7, 2020

Table 1. Chemical Composition (Major Elements) of the Samples Obtained from FUS-ICP Analysis

major elements	SiO_2 (%)	Al_2O_3 (%)	Fe_2O_3(T) (%)	MnO (%)	MgO (%)	CaO (%)	Na_2O (%)	K_2O (%)	TiO_2 (%)	P_2O_5 (%)	LOI (%)	total (%)
AK1	98.44	0.13	0.92	0.01	0.01	0.08	0.04	0.03	0.00	<0.01	0.39	100.1
AK2	98.26	0.10	1.26	0.01	0.02	0.14	0.05	0.04	0.01	0.01	0.92	100.8
AK3	98.20	0.13	1.37	0.01	0.01	0.09	0.05	0.04	0.02	<0.01	0.67	100.6
AK4	97.93	0.14	1.45	0.014	0.02	0.08	0.06	0.05	0.01	<0.01	1.04	100.8

the just documented, multistage silicification of the Upper Jurassic neptunian dykes cutting through these sediments.[43] These facts imply the contribution of additional sources of silica related to the appearance of radiolarians, as well as the periodic transfer of hydrothermal solutions along deep fracture zones generated by an extensional tectonic regime. The occurrence of chert nodules and bedded cherts in calciturbidites from the Oxfordian/Kimmeridgian turn cannot be related exclusively to the presence of Hexactinellida sponges since these organisms formed rather limited accumulations in that part of the stratigraphic column. However, these sediments contained radiolarians which may have provided a potential source of silica for bedded cherts.[24,30,38,44]

Apart from the full mineralogical and petrographic characterization supported by specialized analytical methods, the genetic concepts of cherts should be confronted with a comprehensive sedimentological, paleontological and tectonic characterization. In the literature, we may encounter numerous reports about research on their identification and characterization by means of instrumental methods ranging from infrared spectroscopy (IR),[45,46] X-ray diffraction (XRD),[47] emission and atomic absorption spectroscopy,[48] and energy-dispersive X-ray fluorescence (EDXRF)[49] to neutron activation analysis (NAA).[50] The development of nuclear magnetic resonance (NMR) techniques over the last 50 years has meant that NMR has been applied as an alternative method for geological purposes. Due to the high abundance of silicon and their crystal structure, solid state NMR (magic angle spinning NMR, MAS NMR) has been widely used for the study of cherts.[51] In contrast to other sedimentary rocks, such as sandstones or shales, cherts have been poorly analyzed by proton nuclear magnetic resonance (^{1}H NMR). We propose ^{1}H low field NMR as a nondestructive tool for distinguishing cherts of different types or with varying provenances. Low field NMR is commonly used for the investigation of sandstones, shales, and carbonates, and it can also be applicable for studies on cherts as it has a number of advantages. Primarily, it is noninvasive and nondestructive to rock core samples, and thus, the analysis is repeatable. Second, we obtain a signal from the water (protons) present in several forms, including microporosity free water, adsorbed water or even protons in the crystal lattice. These types of "water" have very short relaxation times due to their strong interactions with adsorbent surface or bonding. Also, every magnetic susceptibility difference causes the induction of internal gradients that arise in higher magnetic fields and distort the interpretation of obtained data. A low field helps to overcome these problems, because we can attain low values of echo time and operate at a low magnetic field strength. This enables us to register short relaxation times and, when the difference between susceptibilities of water and rock matrix is small and pores are nanometric, ignore the diffusion impact from internal gradients (which we will show in the work), respectively.

Silicon is present in various forms in geology, but also, due to its wide range of properties, in technology. Many silica structures, such as mesopores, nanotubes, silicagels, silicate glass, and cherts, have been investigated by NMR. Results show that different proton populations are possible to identify in these materials. ^{1}H low field NMR relaxometry revealed that in MCM-41 and SBA-15 mesopores, three water populations can be seen and they are associated with inner bulk water, surface water and OH groups.[52] T_1 and T_2 relaxation times measurements in low field enabled adsorbed water to be distinguished on the surface of silica nanotubes which helped to estimate the number of functional groups with which a nanotube can bond.[53] Relaxation times and diffusion coefficients also enabled three types of water to be detected in silica gels that were related to free water and the first and second layer of water.[54] Protons from OH groups and molecular H_2O demarcation by ^{1}H wide-line and MAS NMR experiments helped to determine water content in hydrous silicate glass that alters in the presence of specific cations and changes the physical properties of the glass.[55] It is also possible to investigate the chemical properties of silica. T_1 and T_2 distributions from ^{1}H MAS NMR of nonporous silica yielded information about molecular dynamics and interactions of fluid particles with the adsorbent's surface (different relaxation times for subsequent layers of water, cross-polarization).[56] These colloidal silica particles can be used as a model of water- or 1-heptanol-bearing rocks. NMR spectroscopy (^{29}Si MAS NMR) also helped to trace the depolymerization process of amorphous silica due to ASR (alkali silica reaction) reaction on the grounds of dominant peak location (the Q_4 peak disappeared and a Q_3, Q_2 or Q_1 peak appeared).[57] The same experiment allowed the identification of protons associated with silanol (Q_3) on the surface of structural defects in flints and the estimation of water and OH protons content that can change the physical and chemical properties of rocks.[51]

In this work, ^{1}H-LF-NMR is applied for the first time to chert studies. This technique allowed us to characterize the differences in porosity (including size and distribution of pore spaces) of chert nodules and bedded cherts.

2. MATERIALS AND METHODS

2.1. Characterization of Samples. Four chert core samples from different places from the KCU are the subject of the study, and in the paper, we distinguish between them by using the form AKi, where i = 1, 2, 3, 4 is the number of a sample. The samples vary in color. Samples of nodular and bedded cherts were studied in thin sections and examined using a scanning electron microscope (SEM). In the description of samples, a classification after Folk and Pittman[58] has been used. It was assumed that the limit of the diameter for distinguishing between quartz and microquartz is 20 μm. Within the microquartz there are equant and fibrous quartz types. Microflamboyant quartz (flamboyant lutecite after Folk and Pittman[58] or quartz with flamboyant spectral extinction

https://dx.doi.org/10.1021/acs.jpcc.9b11790
J. Phys. Chem. C 2020, 124, 5225−5240

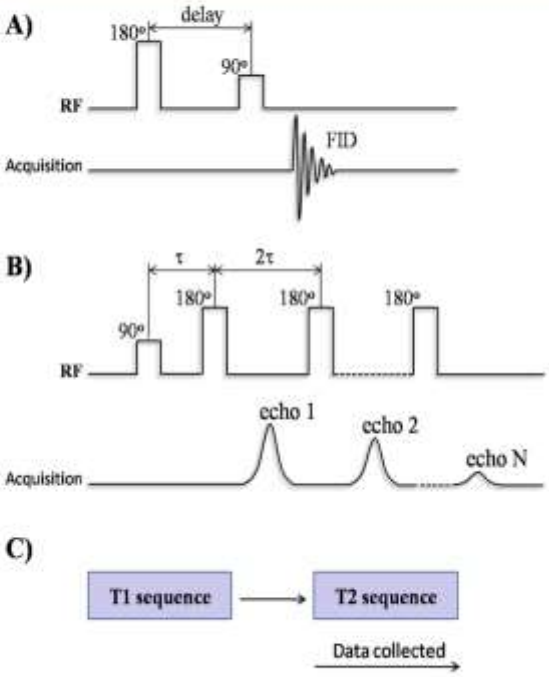

Figure 1. Schemes of sequences used in the experiments: (A) 1D-T_1, inversion recovery free induction decay (IR-FID); (B) 1D-T_2, CPMG with N echoes; (C) 2D T_1−T_2 correlation experiment that delivered T_1−T_2 maps.

after Chowns and Elkins[59]) has a fabric which is between the equant and fibrous quartz types.

The AK1 sample is the typical bedded chert, forming regular, flat, or lens-shaped horizons up to 1.2 m in length and 0.5 m thick with distinguished zonation. It occurs in calciturbidites,[38] characterized by the excellent sorting of carbonate grains within the Bouma sequence. The groundmass of the cherts is mainly composed of microcrystalline quartz. In the SEM view, it is a dense, nonporous mass. Rare relicts of bioclasts are filled with megaquartz. Chalcedonic and opal aggregates are absent.

The AK2−4 samples are nodular cherts forming irregular, flat or regular lens shaped nodules up to 20 cm in diameter. The groundmasses of the cherts are mainly composed of opal-CT, but microcrystalline quartz and chalcedony also occur. Inside the cherts, microflamboyant quartz aggregates cutting the fossils were also found. The textures of the host rock are recognizable, especially in the outermost parts of cherts, and are composed of wackestone or packstone. Carbonate fossils are replaced by megaquartz, and quartzine and chalcedony occur as a cement.

2.2. Chemical Composition of Samples. The geochemical analyses were carried out at the Activation Laboratories Ltd. (Actlabs) in Ancaster in Canada. The major element in the composition was analyzed using fusion-inductively coupled plasma (FUS-ICP). Samples are prepared and analyzed in a batch system. Each batch contains a method reagent blank, certified reference material and 17% replicates. Samples are mixed with a flux of lithium metaborate and lithium tetraborate and fused in an induction furnace. The molten melt is immediately poured into a solution of 5% nitric acid containing an internal standard and mixed continuously until completely dissolved (about 30 min). The samples are run for major oxides on a combination simultaneous/sequential Thermo Jarrell-Ash ENVIRO II ICP. Results are shown in Table 1.

2.3. NMR Experiments. NMR experiments were carried out using a Magritek Rock Core Analyzer (Aachen, Germany) spectrometer with a 0.05 T (2 MHz) magnetic field. Inversion Recovery (IR) and Carr−Purcell−Meiboom−Gill (CPMG) sequences were applied to obtain 1D-T_1, 1D-T_2 and T_1−T_2 maps. The schemes of the applied sequences are shown in Figure 1. 1D distributions were calculated using Inverse Laplace Transform (ILT), Hanson and Lawson method, while T_1−T_2 correlation maps used the FISTA algorithm. Table 2 shows the protocol used in each experiment.

All of the experiments were performed for three saturation states of rock core samples: native (N), dry (D), and saturated (S). Native samples were measured and then dried for 12 h in 200 °C in vacuum conditions. Dry samples were measured and then saturated with water in vacuum conditions. The saturated samples were wrapped tightly in plastic foil in order to prevent the evaporation of water prior to measuring. 1D-T_1 and 1D-T_2 distributions of signal coming from hydrogen species in the samples in three saturation states (N, D, S) delivered relaxation times (peaks locations) and relative contributions (peaks integrals) of each hydrogen population. Additionally, we subtracted raw data from the measurements of saturated and dry samples and obtained differential data (SD). Peaks in the 1D-T_2 distributions were numbered N*i*, D*i*, S*i*, and SD*i*, while in the 1D-T_1 n*i*, d*i*, s*i*, sd*i*, where i = 1, 2, 3, 4, and 5 is the number of a peak beginning from the left side on a time axis and corresponds to a given time range, R*i*. It should be noted that for 1D-T_1 distribution, lowercase was applied to highlight the fact that D1 and d1 do not necessarily come from the same hydrogen population. The integrals of peaks were called I_1 and I_2 for peaks concerning 1D-T_1, 1D-T_2 distributions, respectively. In addition, we determined the total porosity, ϕ, and logarythmic means of T_1 and T_2 distributions called T_1lm and T_2lm, respectively. Peaks in the T_1−T_2 maps were matched to

Table 2. Protocols Applied in the Experiments[a]

Experiment name	IE-delay (ms)	TE = 2τ (μs)	NoS	NoE	min delay (ms)	max delay (ms)	min τ (ms)	max τ (ms)
1D-T_1	5000	–	24	–	0.05	5000	–	–
1D-T_2	1500	60	512	10000	–	–	–	–
T_1−T_2	1500	60	128	10000	–	–	0.1	5000

[a]IE-delay is an inter-experiment delay, i.e., time between subsequent scans, NoS is the number of scans, NoE is the number of echoes, min./max. delay is the minimum/maximum time between 180 and 90 pulses in IR sequence, min./max. τ is minimum/maximum time between 90 and 180 pulses in CPMG sequence.

https://dx.doi.org/10.1021/acs.jpcc.9b11790
J. Phys. Chem. C 2020, 124, 5225−5240

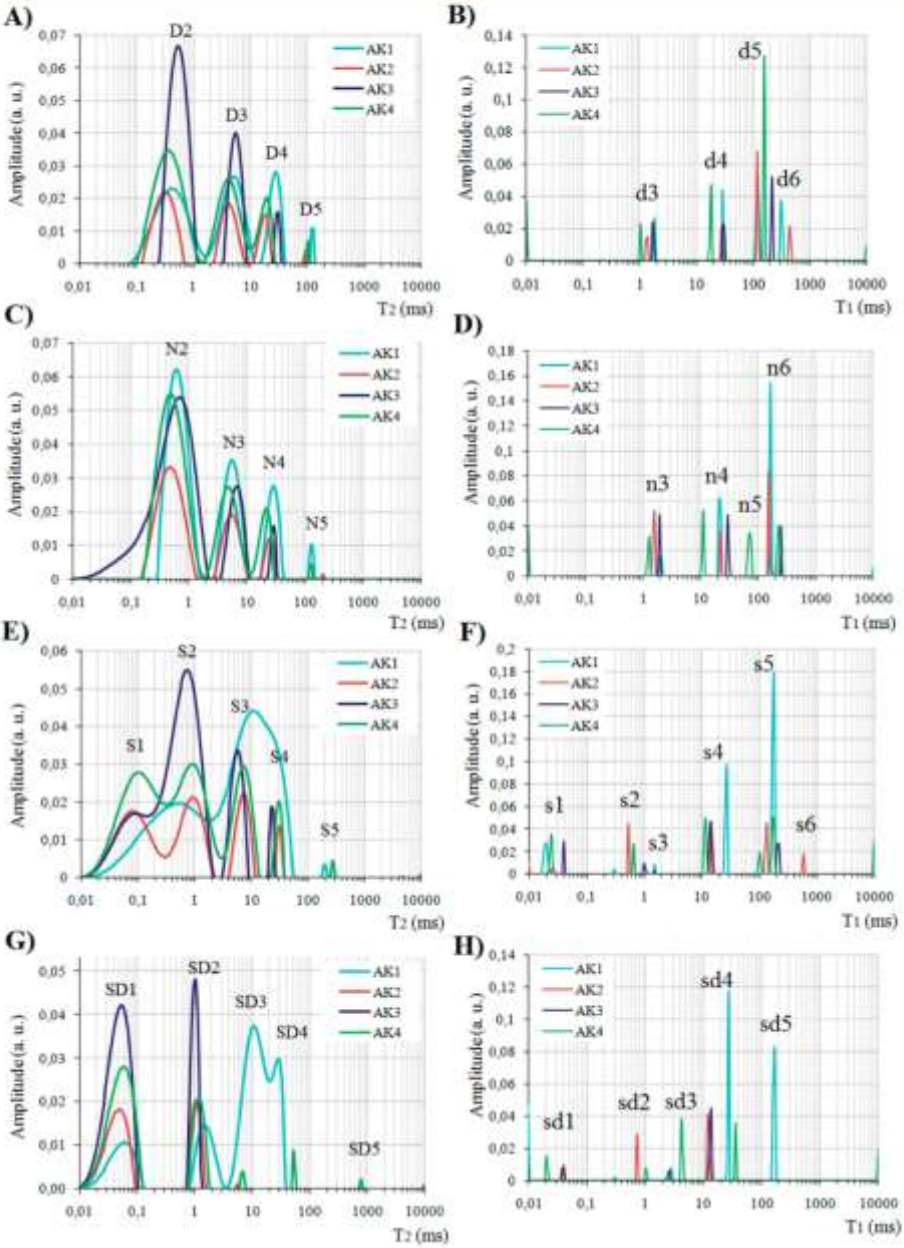

Figure 2. 1D-T_2 and 1D-T_1 distributions for different saturation states of samples: (A) T_2 dry state; (B) T_1 dry state; (C) T_2 native state; (D) T_1 native state; (E) T_2 saturated state; (F) T_1 saturated state; (G) T_2 differential distribution of saturated and dry states; (H) T_1 differential distribution of saturated and dry states. The numeration of peaks was taken from the left to the right side of a distribution. It should be noted that for 1D-T_1 distribution, lowercase was applied to highlight the fact that, e.g., D1 and d1 do not necessarily come from the same hydrogen population. The corresponding T_1 and T_2 times for the population should be taken from T_1−T_2 maps.

those from 1D-T_2 distributions and marked with the same number.

2.4. Principal Component Analysis (PCA). The 1D data was analyzed qualitatively by using PCA in PQStat software. PCA is a procedure that enables the transformation of a set of correlated variables to another set of new variables, called Principal Components (PCs), that are no longer linearly correlated. This transformation usually leads to the reduction of variables and simplifies the process of finding samples that have similar features.

The original variables in the PCA were relaxational parameters, i.e. T_1, T_2, I_1, I_2 of peaks N*i*, D*i*, S*i*, SD*i*, n*i*, d*i*,

https://dx.doi.org/10.1021/acs.jpcc.9b11790
J. Phys. Chem. C 2020, 124, 5225−5240

si, and sd*i*. PCA transforms this relaxational data into new variables, PCs, which the original variables have a certain contributions in. The number of PCs is always less or equal to the number of original variables, and the transformation ensures that the first PC explains the largest percentage of the total variance of the data. In our case, the number of PCs was equal to 3, however, the first two PCs, PC 1 and PC 2, explained the satisfactory percentage of the total variance and results of the analysis for these two PCs will be presented on the biplots. For a more detailed description of the PCA, the reader is referred to Supporting Information.

2.5. Pore Size Distribution (PSD). In porous systems, the T_2 relaxation time determined experimentally is dependent on three components:[60]

$$\frac{1}{T_2} = \frac{1}{T_{2bulk}} + \frac{1}{T_{2surface}} + \frac{1}{T_{2diffusion}} \cong a\left(\frac{\eta}{T_K}\right) + \rho_2\left(\frac{S}{V}\right)_{pore} + \frac{D(\gamma GTE)^2}{12} \quad (1)$$

where a is a constant dependent on fluid type, η is viscosity (Pa·s), T_K is temperature (°C), ρ_2 is the surface relaxivity of the pore walls (m/s), $\left(\frac{S}{V}\right)_{pore}$ is the surface-to-volume ratio of a pore (m^{-1}), D is diffusion coefficient (m^2/s), γ is gyromagnetic ratio (MHz/T), G is magnetic field gradient (T/m) and TE is echo time (s).

PSD was estimated based on T_2 distributions of saturated samples. The calculations were conducted assuming cylindrical pore geometry, for which

$$\left(\frac{S}{V}\right)_{pore} = \frac{4}{d} \quad (2)$$

where d is a pore diameter (m). Surface relaxivity for a given sample in the second component in (1) is assumed to be $\rho_{2\,Sample} = f_{SiO_2} \cdot \rho_{2SiO_2} + f_{Fe_2O_3} \cdot \rho_{2Fe_2O_3}$, which is a sum weighted by the fractions of SiO_2 and Fe_2O_3 showed in the Table 1, where ρ_{2SiO_2}=0.18 μm/s is a mean value of surface relaxivities for pure silica materials MCM-41 and SBA-15 reported by Krzyżak and Habina[52] and $\rho_{2Fe_2O_3}$ is the additional contribution from Fe_2O_3 to surface relaxivity calculated from the relationship proposed in ref 61. In practice, the surface relaxivity is dominated by the impact of iron(III) oxide. We can assume that magnetic field gradient results from differences between magnetic susceptibilities, $\Delta\chi$, of water and a matrix of samples,

$$\Delta\chi = \chi_{H_2O} - \chi_{Sample} \quad (3)$$

where χ_{H_2O} is a magnetic susceptibility of water equal to -9.02×10^{-6} and χ_{Sample} is a magnetic susceptibility of a sample. χ_{Sample} value was calculated as a sum of χ_{SiO_2} and $\chi_{Fe_2O_3}$ weighted by their fractions in a given sample. The volume magnetic susceptibility of SiO_2 was assumed to be equal to -10.55×10^{-6}, while 500×10^{-6}[62] for iron(III) oxide. In pore of size d, the induced gradient is

$$G = \frac{\Delta\chi B_0}{d} \quad (4)$$

where B_0 is a magnetic field induction (T) and in our case B_0 = 0.05 T. Substituting for (2) and (4) in (1), and introducing $C = \frac{1}{T_2} - \frac{1}{T_{2bulk}}$ and $F = \frac{(\gamma\Delta\chi B_0 TE)^2}{12}$, we obtain the quadratic equation for d:

$$Cd^2 - 4\rho_2 d - \mathrm{FD} = 0 \quad (5)$$

which has two roots

$$d = \frac{4\rho_2 \pm \sqrt{(-4\rho_2)^2 - 4C(-\mathrm{FD})}}{2C} \quad (6)$$

Only positive roots will be considered. The diameter of a pore for a given time step was calculated assuming $T_{2\,bulk}$ = 2.2 s.

In the second approach, typically assumed to be valid for small B_0 and short echo time, TE,[60,63] the diffusional component in (1) was omitted and a pore size was calculated as

$$d = 4 \cdot \rho_2 \cdot T_{2surface} \quad (7)$$

The amplitude of the PSD consists of a normalized amplitude in the time step from the 1D-T_2 distribution.

3. RESULTS AND DISCUSSION

3.1. 1D Distributions. Different types of porosity were estimated from the T_2 distributions shown in Figure 2. The total recorded porosity value for dry samples ranges from 0.65% for AK2 to 1.31% for AK3 and AK4. For the native state, we observe an increase in porosity by 0.3−0.4% on average, and in most cases the maintenance or slight decrease

Table 3. Coordinates of Peaks from 1D-T_2 Distributions Shown in Figure 2, Parts A, C, E, and G[a]

Saturation state	Sample	T_2 relaxation time (ms)					Logarythmic Mean, T_2lm (ms)	Porosity, ϕ (%)
		Peak number						
DRY		D1	D2	D3	D4	D5		
	AK1		0.42	5.2	29.3	126.0	2.2	1.22 ± 0.05
	AK2		0.32	4.2	18.0	95.5	1.4	0.65 ± 0.04
	AK3		0.56	5.5	31.4		1.2	1.31 ± 0.06
	AK4		0.37	4.2	19.3	102.3	1.3	1.31 ± 0.06
NATIVE		N1	N2	N3	N4	N5		
	AK1		0.60	5.5	29.3	126.0	2.1	1.6 ± 0.02
	AK2		0.46	5.5	25.5	204.9	1.2	0.92 ± 0.02
	AK3		0.64	6.8	29.3		0.7	1.79 ± 0.10
	AK4		0.46	4.8	22.2	126.0	1.2	1.59 ± 0.04
SATURATED		S1	S2	S3	S4	S5		
	AK1		0.52	11.1	29.3	204.9	3.2	2.34 ± 0.08
	AK2	0.080	0.98	7.3	31.4		0.55	1.08 ± 0.06
	AK3	0.092	0.79	5.9	22.2		0.62	2.00 ± 0.10
	AK4	0.106	0.91	7.3	31.4	270.5	0.64	1.98 ± 0.08
SATURATED-DRY		SD1	SD2	SD3	SD4	SD5		
	AK1	0.06	1.48	10.73	28.35		3.82	1.20 ± 0.10
	AK2	0.05	1.05	5.54			0.12	0.44 ± 0.09
	AK3	0.05	1.05				0.10	1.00 ± 0.20
	AK4	0.06	1.20	6.83	51.11	766.3	0.13	0.70 ± 0.10

[a]Peaks were located in the five regions, for which T_2 was consecutively one order larger, and numbered from 1 to 5, from the left to the right side of the distributions. In addition to the number, the peaks have a letter that corresponds to the saturation state for which the distributions were obtained: dry, D, native, N, saturated, S and for differential data of saturated and dry samples, SD. The last two columns consist of T_2 logarithmic means (T_2lm) and total porosities (ϕ) calculated from 1D-T_2 distributions for the samples in each saturation state.

https://dx.doi.org/10.1021/acs.jpcc.9b11790
J. Phys. Chem. C 2020, 124, 5225−5240

Table 4. Coordinates of the Peaks from T_1-T_2 Correlation Maps for Different Saturation States[a]

Saturation state	Sample	Peak number														
		D1			D2			D3			D4			D5		
DRY		T_2 (ms)	T_1 (ms)	T_1/T_2	T_2 (ms)	T_1 (ms)	T_1/T_2	T_2 (ms)	T_1 (ms)	T_1/T_2	T_2 (ms)	T_1 (ms)	T_1/T_2	T_2 (ms)	T_1 (ms)	T_1/T_2
	AK1	0.119	23.7	199				1.58	158	100	16.8	141	8.4	63.1	200	3.2
	AK2	0.079	12.6	159				1.68	158	94	12.6	150	12	75	168	2.2
	AK3				0.266	2.99	11	2.24	141	63	14.1	126	8.9	112	200	1.8
	AK4	0.089	15	169	0.708	23.7	33	0.944	168	178	15.8	158	10	89.1	237	2.7
NATIVE		N1			N2			N3			N4			N5		
		T_2 (ms)	T_1 (ms)	T_1/T_2	T_2 (ms)	T_1 (ms)	T_1/T_2	T_2 (ms)	T_1 (ms)	T_1/T_2	T_2 (ms)	T_1 (ms)	T_1/T_2	T_2 (ms)	T_1 (ms)	T_1/T_2
	AK1	0.063	16.8	267	0.708	17.8	25				18.8	133	7.1	75	211	2.8
	AK2				0.316	1.41	4.5	2.11	141	67	14.1	150	11	70.8	168	2.4
	AK3				0.708	3.98	5.6	1.19	188	158	12.6	133	11	79.4	158	2.0
	AK4				0.708	11.2	16	1.26	141	112	13.3	158	12			
SATURATED		S1			S2			S3			S4			S5		
		T_2 (ms)	T_1 (ms)	T_1/T_2	T_2 (ms)	T_1 (ms)	T_1/T_2	T_2 (ms)	T_1 (ms)	T_1/T_2	T_2 (ms)	T_1 (ms)	T_1/T_2	T_2 (ms)	T_1 (ms)	T_1/T_2
	AK1				0.237	9.44	40	2.11	89.1	42	12.6	106	8.4			
	AK2				0.335	1.41	4.2				9.44	133	14	28.2	188	6.7
	AK3				0.708	7.5	11				8.91	141	16	39.8	188	4.7
	AK4				0.447	11.9	27				7.94	141	18	35.5	200	5.6
SATURATED-DRY		SD1			SD2			SD3			SD4			SD5		
		T_2 (ms)	T_1 (ms)	T_1/T_2	T_2 (ms)	T_1 (ms)	T_1/T_2	T_2 (ms)	T_1 (ms)	T_1/T_2	T_2 (ms)	T_1 (ms)	T_1/T_2	T_2 (ms)	T_1 (ms)	T_1/T_2
	AK1				0.75	14.1	19				12.6	84.1	6.7			
	AK2				0.501	8.91	18				18.8	23.7	1.3			
	AK3	0.079	15.8	200	0.841	9.44	11				16.8	28.2	1.7			
	AK4				0.447	10.6	24				6.68	22.4	3.4	44.7	94.4	2.1

[a] T_2 and T_1 are transverse and longitudinal relaxation times, respectively, and T_1/T_2 is the T_1 to T_2 ratio; if a given peak does not occur on the map, it is marked by a dark gray cell.

in T_2bm: from 2.1 to 2.2 ms for AK1, and from 1.2 to 1.4 ms for AK2 and AK4. Only for AK3 there is a clear decrease of T_2lm from 1.2 to 0.7 ms. In the saturated state we observe a further increase in porosity, the largest for AK1 by 1.2% to the maximum observed value of 2.32%. A further decrease in the T_2bm value to 0.5−0.6 ms was also recorded, with the exception of AK1, where we noticed a clear increase in value to 3.2 ms (Table 3).

T_2 experiments revealed very similar distributions for all samples, with peak coordinates virtually coinciding (Table 3; coordinates of peaks from 1D-T_1 distributions are shown in the Table S1). Each peak number, i (ranging from 1 to 5), represents the same region regardless of saturation state. In the distributions of dry and native samples (Figure 2A,C) four different peaks (i = 2−5) can be seen. After saturation, we can additionally distinguish another peak S1 with the shortest T_2 time, in the order of 0.06−0.1 ms (Figure 2E). The least significant peak, with i = 5, that has the highest T_2 does not occur for AK3. Peaks D2−D5 are slightly shifted toward shorter T_2 times with respect to N2−N5. Sample AK1 distinguishes itself in the saturated state. Since it was not possible to separate modes to five peaks, we observe trimodal distribution. Figure 2G shows distributions of differential data of saturated and dry samples, which reveals areas where water migrates after saturation. The most significant contribution can be observed for the SD1 and SD2 having maxima between 0.06 and 0.1 ms and 0.4−1 ms, respectively. These peaks are very distinct and almost coincide for all samples, except for AK1. In addition, SD3 and SD4 appear and cover for most samples, however, they have a negligible contribution to the T_2 distribution.

Thus, based on the obtained T_2 distributions, we made a fairly obvious division into 5 hydrogen signal regions R1−R5. The regions are characterized by the maxima of peaks that are in the following ranges: 0.05−0.2 ms (R1), 0.2−2 ms (R2), 2−12 ms (R3), 18−40 ms (R4), and 90−300 ms (R5).

T_1 distributions provide complementary information (see Figure 2, parts B, D, F, and H). The connection of the peaks with those from the T_1 distributions is possible after taking into account the data from the T_1-T_2 maps.

3.2. T_1-T_2 Maps. The T_1-T_2 maps correlate T_1 and T_2 times observed in 1D experiments, enabling a better assessment of relaxation centers. The association of the T_1/T_2 ratio with the T_2 relaxation time provides important information about the strength of hydrogen bonding and its source. The recorded T_1/T_2 values, depend on the region, R (R1−R5), and the degree of water saturation, and range from ~2 to nearly 300 (Table 4). This suggests the existence of water confined tightly in the pores, as well as very strongly bound and the existence of a signal from OH groups.

The T_1-T_2 correlation maps of dried samples (Figure 3) revealed four distinct peaks that are shown in Table 4. The peaks D1 and D2 are usually combined in one averaged spot (seen as D1 or D2), except for the AK4 sample, where five peaks are visible on the map. D1 did not occur on the 1D-T_2 distributions at all. It is likely that D2 on 1D-T_2 distributions represents the average of D1 and D2 from the map (see for example T_2 times of D1 and D2 for AK4 in Table 4, their average is very similar to the T_2 of D2 from the 1D

https://dx.doi.org/10.1021/acs.jpcc.9b11790
J. Phys. Chem. C 2020, 124, 5225−5240

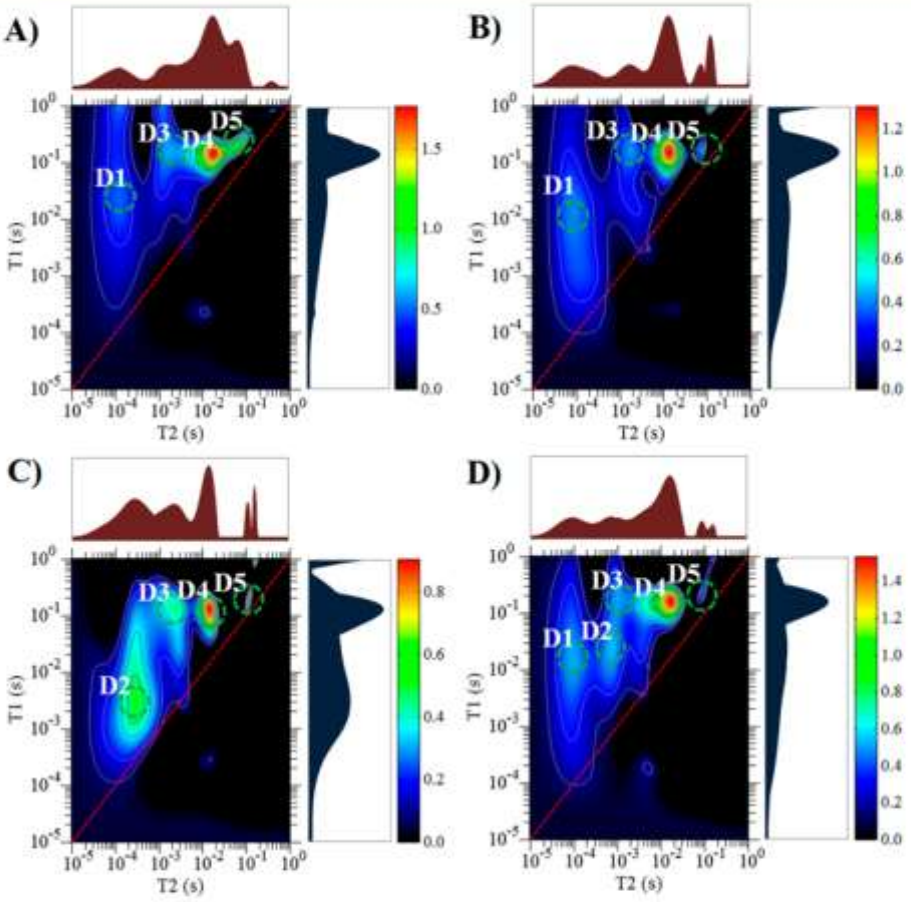

Figure 3. T_1-T_2 correlation maps of dry samples: (A) AK1; (B) AK2; (C) AK3; (D) AK4. Peaks are numbered according to the location in the T_2 time domain, while the letter "D" corresponds to the abbreviation of the Dry state. Additionally, the projections of the maps on the two time domains (T_1 and T_2) are shown.

experiments, Table 3). For the native state, associated with a higher degree of water saturation, we observe a pattern of N1−N5 spots similar to the dried samples, with a tendency to average or overlap in areas of N1 and N2 (Figure 4). The impact of the further increase of water saturation visible on the maps of saturated samples (Figure 5) indicates that chert rock core samples are able to absorb water, causing an increase in porosity by 0.4−1.2% (Table 3). Regions that are reflected by peak 2 on the maps are refilled with water, which we observe as the appearance of S2 or an increase in its amplitude. Hydrogen populations reflected by peaks 4 and 5 also absorb water, mainly in the case of AK1 (Figure 5A), which additional averaging of signals associated with peaks S4 and S5 occur for.

Differential maps of saturated and dried samples (Figure 6) additionally help in the interpretation of maps for different saturation states and deliver information about open porosity. Saturation effects for AK2−AK4 samples are seen mainly in regions R1 and R2 (SD1 and SD2), and for AK1 in R4. On these maps, peaks lie close to the red-dotted line and have T_1/T_2 equal to 11−24 for SD2 and 1.3−6.7 for SD3. Only AK4 (Figure 6D) absorbs water in bigger spaces reflected by SD4, which has $T_1/T_2 = 2.1$ and corresponds to poorly bound water in the pores. Differential maps, especially for AK2 (Figure 6B) and AK3 (Figure 6C), show a trail for very short T_2s, which extends to the wide range of T_1. This is probably related to the formation of new OH groups (this kind of pattern on the maps for the observed T_2 times is characteristic to hydroxyls).

After the initial characterization of samples based on 1D and 2D experiments, the following chapters will discuss the issue of porosity distribution and its types.

3.3. Estimation of Pore Size Distribution in Cherts. As demonstrated in ref 60, at low B_0 and for short value of echo time in the CPMG measurement, PSD can usually be calculated from eq 7, and in practice, it is dominated by surface relaxation. This approach has been repeatedly verified, but rather on rock cores which have much larger pore diameters[60,63] in comparison to the cherts examined in our study. That is why we decided to analyze the possible impact of diffusion on PSD for cores with a large population of pores having diameters of several nanometers. For comparison, both eqs 1 and 7 were applied.

The diffusion coefficient D was estimated based on theoretical[64−66] and experimental[59,67,68] results. According to these, the D of water confined in silica nanopores varies

https://dx.doi.org/10.1021/acs.jpcc.9b11790
J. Phys. Chem. C 2020, 124, 5225−5240

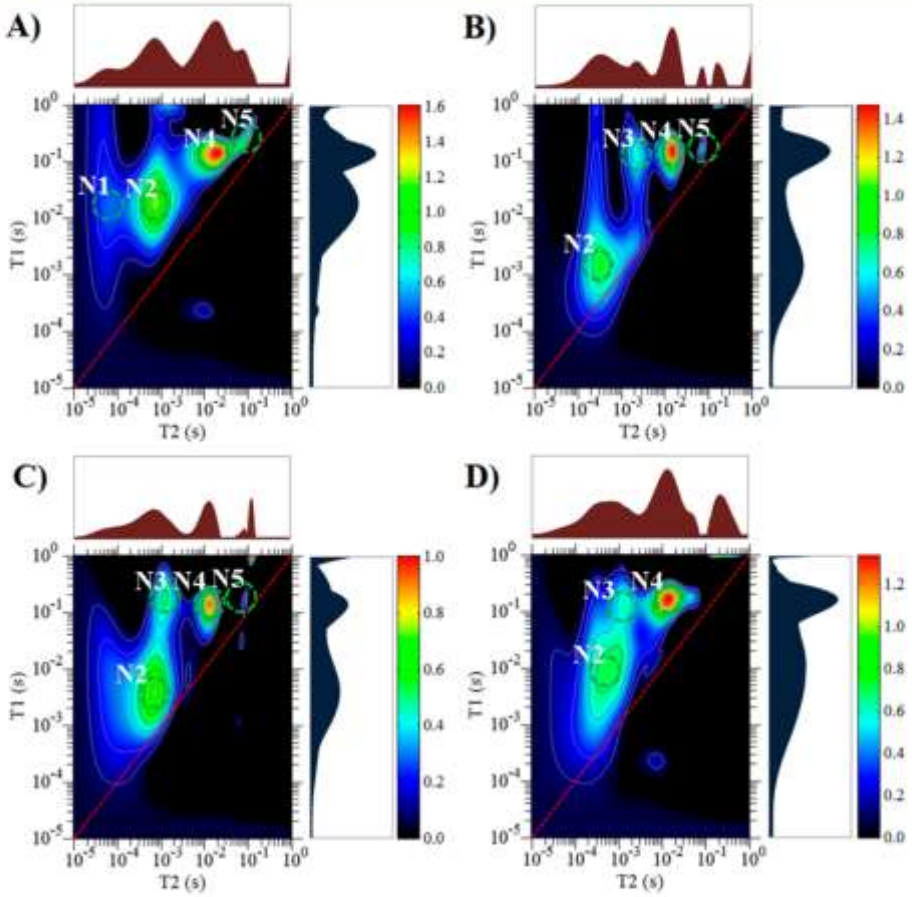

Figure 4. T_1-T_2 correlation maps of native samples: (A) AK1; (B) AK2; (C) AK3; (D) AK4. Peaks are numbered according to the location in the T_2 time domain, while the letter "N" corresponds to the abbreviation of the native state. Additionally, the projections of the maps on the two time domains (T_1 and T_2) are shown.

strongly for pore size between 0.7 and 4 nm (Table 5). Below and above this range it is almost constant and equal to 0.45 × 10^{-10} (the most strongly bound first water monolayer) and 2.3 × 10^{-9} m^2/s (bulk water), respectively. The obtained PSD's based on the T_2 distributions of saturated and dried samples as well as their difference are shown in Figure 7. At the same time, they correspond to the total, closed and open porosity distribution, respectively. The influence of diffusion and induced gradients on PSDs is additionally shown for a few pore diameters in Table 5. In general, noticeable changes are visible in the range of 1−10 nm. The effect of gradients outside this range is negligible. As we can see in our case, PSDs are completely dominated by the influence of surface relaxivity. However, as we show in theoretical considerations for an identical PSD system, in the absence of iron(III) oxide or its negligible amount, the dependence on diffusion would be significant if one does not account for the decrease of the diffusion coefficient of water confined in nanopores (Figure S1 in Supporting Information). Although in our case (diffusion coefficient that is smaller for nanometer pores, small differences between volume magnetic susceptibilities of water and sample) the use of a linear relationship (eq 7) for PSD estimation is sufficient in practice.

3.4. Porosity in Cherts. As mentioned in subsection 3.2, *T_1-T_2 Maps*, the T_1/T_2 parameter reflects the strength of hydrogen bonding.[69] Combining 1D and 2D data, we can assume that in the R1 region is a signal from OH groups and water, while in the R2−R5 regions, the source is water in various pore systems. Although we also note high T_1/T_2 values in the R3 region, taking into account the results of other researchers,[52,70,71] we are inclined to ascribe to the thesis that the hydrogen population in R3 comes from water that is strongly bound to the surface rather than chemically bound hydrogen. In the study of water adsorbed on silica gel, two hydrogen relaxation centers were recorded. The first, strongly bound to the surface, with a T_2 of 0.06−0.2 ms and $T_1/T_2 \approx$ 400−500, assigned to OH in silanol[52,71] and the second, less strongly, with a T_2 of 1−6 ms and $T_1/T_2 \approx$ 4−100.[52,70,71] In our case, this suggests the existence of water bound on silica surface with a very high roughness. The above considerations regarding the sources of proton signals are supported by recent reports describing the processes of hydroxylation of quartz

https://dx.doi.org/10.1021/acs.jpcc.9b11790
J. Phys. Chem. C 2020, 124, 5225−5240

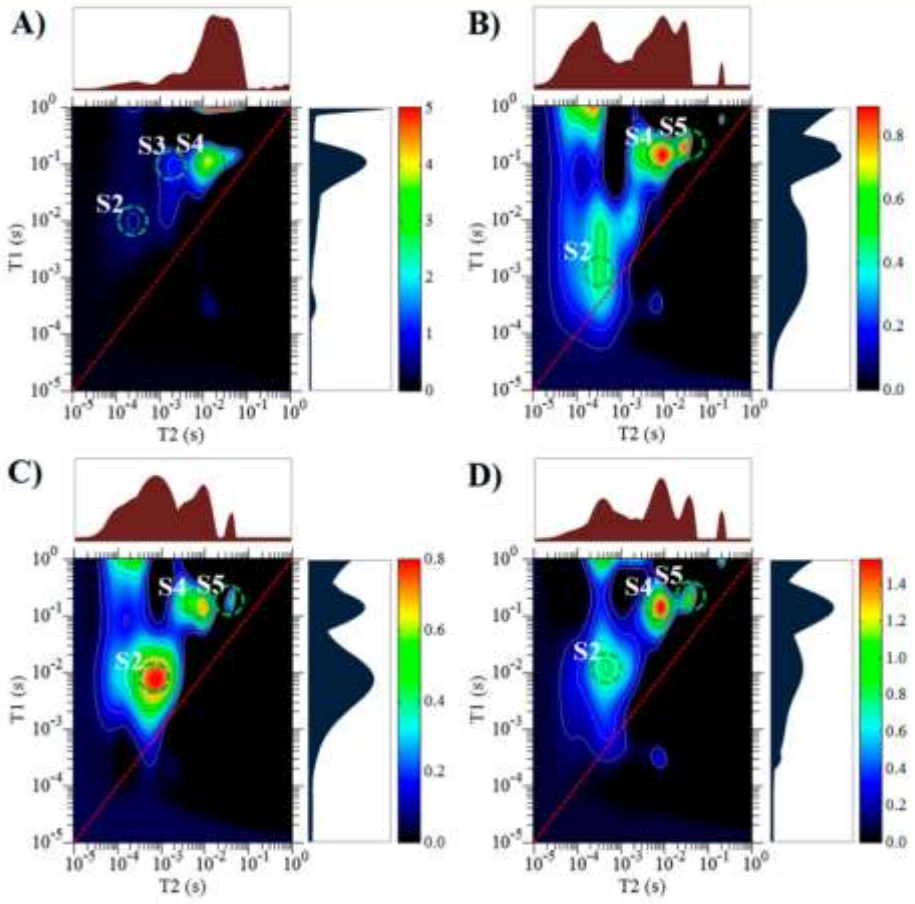

Figure 5. T_1-T_2 correlation maps of saturated samples: (A) AK1; (B) AK2; (C) AK3; (D) AK4. Peaks are numbered according to the location in the T_2 time domain, while the letter "S" corresponds to the abbreviation of the saturated state. Additionally, the projections of the maps on the two time domains (T_1 and T_2) have been shown.

surfaces as well as the creation of preferred hydrogen bonds.[72,73]

Based on the PSDs (Figure 7), we can conclude that total porosity consists primarily of mesoporosity (R1−R2) and macroporosity (R3−R5) (according to IUPAC classification). We can also extract trace amounts of microporosity (R1) and a clear signal (R1) for very short T_2 (0.05−0.1 ms) and very high T_1/T_2 (>200), as mentioned corresponding to compounds containing hydroxyl groups.

The total porosity, which varies from 1.08 to 2.32% depending on the sample, can be divided into closed and open. Closed porosity (0.65−1.31%) is composed of inclusions perfectly visible on T_2 distributions registered for rock cores in the "dry" state. During the drying process (12 h at 200 °C in a vacuum) we got rid of both physically and chemically bound water, therefore the observed signals (D2−D5) come from water in inclusions. Open porosity (0.4−1.2%), revealed in the saturation process, is located in different regions. In the case of AK1 (bedded chert) we observe the largest increase in total porosity (1.2%), associated with an increase of T_2lm (from 2.2 to 3.2 ms), in a very wide range from R1 to R4 and four maxima: SD1, SD2, SD3, and SD4, which correspond to the dominance of macropores (Figures 2G and 6A). In the case of nodular cherts (AK2−4), the signals in areas R1 and R2 (SD1, SD2) dominate, with a simultaneous decrease in the T_2lm values from 1.2 to 1.4 ms to 0.55−0.65 ms, which corresponds to the formation of open porosity by microporosity, a few nanometer mesoporosity and newly formed hydroxyl groups (Figure 2G, 6B-D). Table 6 sums up the values of different types of porosities.

We provide further information on the PSD of chert cores by comparing them with model porous systems built of pure silica particles with mesoporosity in the following sections.

3.5. Standards of Mesoporous Systems Made up of Silica. Considering that the studied cherts consist of up to 98% of silica, it is reasonable to analyze them in comparison to standard porous systems structured from SiO_2, assuming that magnetic impurities will have a fine or identifiable impact on a signal. Such standards can be, for example, synthetic systems MCM-41 and SBA-15, made from pure silica with a 100 nm to 1−2 μm particles size. The particles contain pores with diameters equal to 3−4 nm and 8−10 nm for MCM-41 and SBA-15, respectively. These kind of standards were studied by LF-NMR in regard to their relaxational properties (T_1, T_2

https://dx.doi.org/10.1021/acs.jpcc.9b11790
J. Phys. Chem. C 2020, 124, 5225−5240

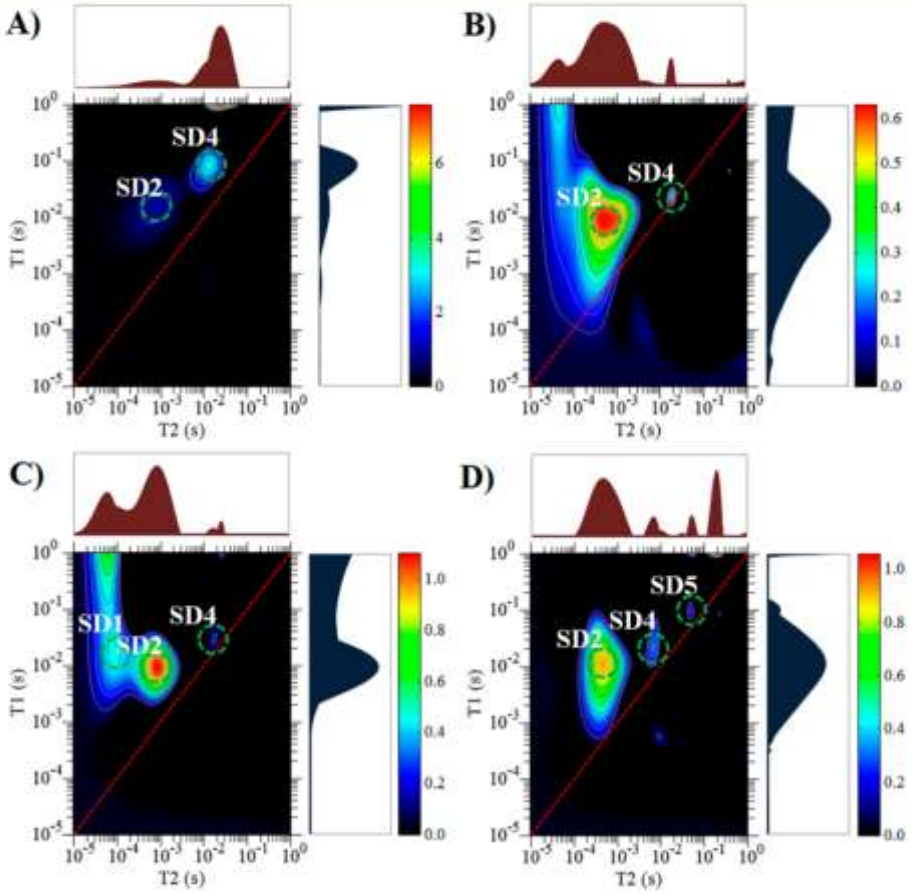

Figure 6. T_1-T_2 correlation maps of differential data of saturated and dry samples: (A) AK1; (B) AK2; (C) AK3; (D) AK4. Peaks are numbered according to the location in the T_2 time domain, while the letters "SD" correspond to the abbreviation of the differential data from saturated and dry state. Additionally, the projections of the maps on the two time domains (T_1 and T_2) are shown.

Table 5. Comparison of Pore Sizes Determined Using Two Approaches—with and without Diffusional Component in Equation 1[a]

d_t (nm)	D ($\cdot 10^{-9}$ m^2/s)	d (nm) (calculated based on (6))				d (nm) (calculated based on (7))			
		AK1	AK2	AK3	AK4	AK1	AK2	AK3	AK4
0.3	0.045								
0.6	0.045	0.59				0.59			
1	0.24	1	1.06	1.02	1.01	0.96	0.99	0.94	0.93
4	1.86	4.16	4.03	4.09	4.05	4.41	3.99	4.04	3.99
10	2.28	10.22	9.88	10.01	9.89	10.2	9.84	9.97	9.84
50	2.3	50.38	48.62	49.29	48.64	50.36	48.58	49.24	48.6
100	2.3	100.89	97.33	98.66	97.37	100.87	97.29	98.61	97.33

[a]Diffusion coefficients D for exemplary, theoretical pore sizes, d_t, are shown.

relaxation times, T_1-T_2 maps) for different water content.[52] A signal was detected for water volume, ranging from a value that exceeded the calculated pore volume several times, to a value lower than required for the total surface of all pores to be covered by a single layer of water. These extreme water contents correspond to the different relaxation mechanisms that dominate the signal, i.e. interparticle water relaxation and intraparticle surface relaxation associated with dipolar coupling effects among water molecules and/or between water molecules and OH groups. T_1 and T_2 distributions and T_1-T_2 maps presented in ref 52 revealed significant changes when decreasing water content evincing the domination of bulk, surface and chemically bound water (OH groups) in the signal. It is worth noticing that, despite the information provided by the producer that both MCM-41 and SBA-15 are pure silica samples, T_1/T_2 ratios reflecting the desorption energy, i.e. the

https://dx.doi.org/10.1021/acs.jpcc.9b11790
J. Phys. Chem. C 2020, 124, 5225−5240

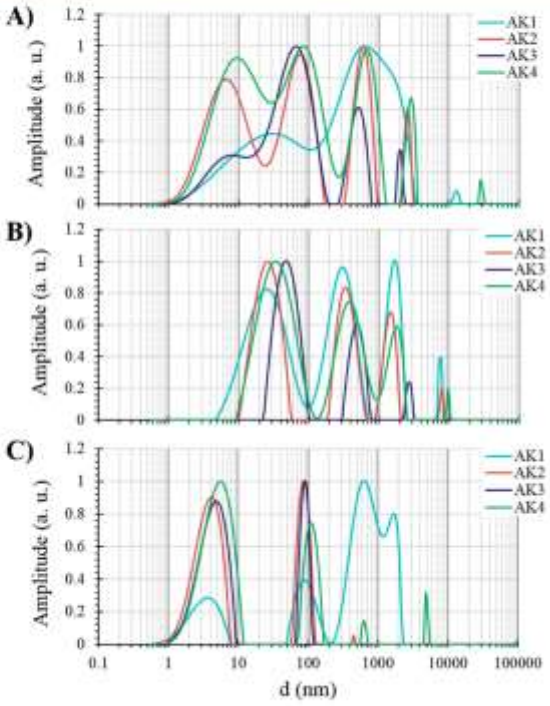

Figure 7. PSD calculated based on T_2 distributions of saturated (A) and dry (B) samples and differential data of saturated and dry samples (C), which corresponds to the total (A), closed (B), and open (C) porosity, respectively. Pore size was determined from eq 6 assuming that samples are composed of SiO_2 and Fe_2O_3, and that diffusion coefficient D is influenced by the size of confinement up to $d = 10$ nm, for which D is equal to the diffusion coefficient of a bulk water.

bonding energy with the surface,[69] are much higher for SBA-15 even though it has larger pores compared to MCM-41. It is probably connected with different surface roughness and associated with the existence of stronger interactions between hydrogen atoms and the surface.[69] Results from the study on MCM-41 and SBA-15 which are relevant to this paper are shown in Table 7, while for further details the reader is referred to ref 52.

Table 7. Values of T_2, T_1 Times and T_1/T_2 Ratios for the Different Hydrogen Populations in the Reference Silica Porous Systems: MCM-41 and SBA-15 (Based on Reference 52)

	T_2 (ms)			
sample	OH groups	surface water	filled pores	overfilled pores
MCM-41	0.06	1.4	5.8	6−31.4
SBA-15	0.05	2	8.6	9−65.1
	T_1 (ms)			
sample	OH groups	surface water	filled pores	overfilled pores
MCM-41	25−30	10.4	25.6	26−94
SBA-15	20−25	175	678	679−1835
	T_1/T_2			
sample	OH groups	surface water	filled pores	overfilled pores
MCM-41	400−500	7.4	4.4	4.3−3
SBA-15	400−500	87.5	78.8	75.4−28.2

3.6. Comparison of Chert Rock Core Samples with Standard Systems. Studies on pure silica systems deliver valuable information for the interpretation of results from the measurements conducted on the chert rock core samples. A first glance at the T_2 times (Table 3 and 4) and T_1/T_2 (Table 4) ratios from the experiments on cherts suggests that the studied systems are constructed from silica particles with a mesoporous structure. Moreover, dry chert rock core samples are characterized by distinct T_1 and T_2 distributions with four coinciding modes. On the basis of this observation, it is possible that samples contain inclusions, in which different amount of water and silica occur (the reasoning is explained in section 3.7 Inclusions in Cherts). High, but different, T_1/T_2 ratios suggest the strong bonding of water in mesopores that have surfaces with different roughness and/or content of paramagnetic compounds. Of particular interest is the fact that T_2 distributions are very similar for all of the samples, despite that they have different origin (two sampling sites). This might be evidence of potentially similar conditions of rock formation. After saturation, a new peak (S1, Figure 2C) appears in the region of $T_2 = 60−100$ μs, which, according to the literature, together with high T_1/T_2 (of an order of several hundred; Table 4) corresponds to OH groups. It is especially visible in Figure 2D, which shows the distribution of differential data of saturated and dry samples. Peak S1/SD1 is associated with a signal probably originating from SiOH that forms after

Table 6. Different Types of Porosities Determined Based on the PSDs of Saturated (Microporosity, ϕ_{micro}, Mesoporosity, ϕ_{meso} Macroporosity, ϕ_{macro}, Total Porosity), Dry (Closed Porosity), and Differential Data of Saturated and Dry Samples (Open Porosity)

		porosity value (%)			
porosity type	pore size range	AK1	AK2	AK3	AK4
microporosity, ϕ_{micro}	<2 nm	0.02	0.02	0.02	0.02
mesoporosity, ϕ_{meso}	2−50 nm	0.63	0.53	0.92	0.95
macroporosity, ϕ_{macro}	50−280 nm	0.44	0.27	0.69	0.52
	0.280−1.4 μm	0.92	0.21	0.31	0.38
	1.4−4 μm	0.32	0.05	0.05	0.10
	4−40 μm	0.009	0	0	0.007
	0−40 μm (total ϕ_{macro})	1.691	0.531	1.056	1.015
total porosity	0−40 μm	2.34	1.08	1.99	1.98
closed porosity	0−40 μm	1.22	0.65	1.31	1.31
open porosity	0−40 μm	1.2 ± 0.1	0.44 ± 0.09	1.0 ± 0.2	0.7 ± 0.1

https://dx.doi.org/10.1021/acs.jpcc.9b11790
J. Phys. Chem. C 2020, 124, 5225−5240

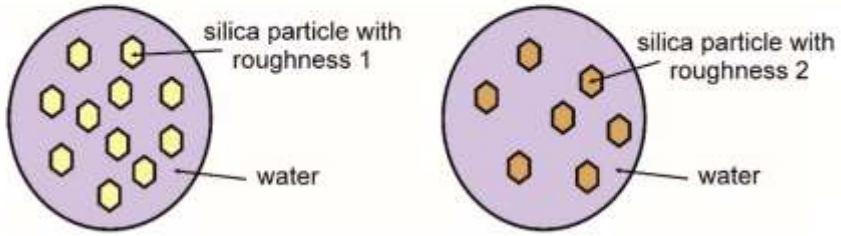

Figure 8. Schematic model of inclusions. Inclusions may differ in the type of silica as well as its quantity and water solution content.

Table 8. Average Values of T_2 and T_1/T_2 from Tables 3 and 4[a]

inclusion	T_2 (ms)	d (nm)	T_1/T_2	roughness
1	0.45	36	22	comparable to SBA-15
2	4.8	3.9×10^2	109	greater than SBA-15
3	24.5	1.9×10^3	10	between MCM-41 and SBA-15
4	108	9.1×10^3	2.5	comparable to MCM-41

[a]The estimated value of the pore diameter, d, is the average apparent porosity for various mixtures of silica particles and water. The roughness, which is reflected by the T_1/T_2 ratio, is compared with the standards MCM-41 and SBA-15 from the Table 7.

saturation in the open porosity of the crystal lattice. On the same distribution (Figure 2D) we can see the rise of the signal in the range of 1 ms marked as SD2. In relation to T_1/T_2 = 20−30 we can suspect that this signal comes from water bonded to the surface of open mesopores characterized by roughness (after comparison with standards) between MCM-41 and SBA-15. It is likely that water forms a H-bonding with surface silanols and gives rise to this peak in such a form. A similar T_2 was observed for the surface water in pure silica pores (Table 7).[52] Peaks S1/SD1 and S2/SD2, despite having different amplitudes depending on the sample number, occur for all of them. For AK1, the more visible differences appear for peaks SD3 and SD4. A significant rise of T_2 signal in the range of 5−30 ms, with practically no signal in this region for other samples having been observed (Figure 2E, G). This indicates that open porosity in the rock core sample appeared in the form of slits in the microcrystalline quartz. Thus, except for the mesoporous water signal, we can observe a signal originating from water in pores that have larger diameters, located between crystallites. This situation is similar to the overfilled pores state of standard systems (Table 7).

3.7. Inclusions in Cherts. Distinct, regular T_2 distributions of chert rock core samples, after heating in 200 °C and vacuum, clearly indicate closed inclusions. It is very interesting that regardless of the core sample (i.e., sampling site), we observe four aligned peaks (Figure 2A). Due to the fact that inclusion size is stochastic and would impact T_2 time in the same manner (T_2 scales with the pore size), the occurrence of four identically localized peaks has to be triggered by something else. The most plausible explanation seems to be that the inclusions are filled with different proportions of silica and water which leads to different T_2 and T_1/T_2 values. This statement is based on the previous studies on MCM-41 and SBA-15 (Table 7),[52] since the T_2 (Table 3 and 4) and T_1/T_2 (Table 4) obtained in this work suggest a similar situation. Additionally, four clearly separated peaks that align for all the samples of different types of chert (Figure 2A) suggests that different formation conditions (temperature, pressure, and the composition and origin of the fluid), rather than origin, were responsible for this mutual feature. The above statements lead to the model describing inclusions (Figure 8 and Table 8). It should be noted that for the system of natural nanometric inorganic pores, we recorded water signals characterized by unusually high T_1/T_2 values.[74,75] In the case of inclusions, it is even up to 100. In contrast, for open pores the ratio is of the order of 20. This suggests the existence of the structures shown schematically in Figure 8 and Table 8.

3.8. Differentiation between Bedded and Nodular Cherts. Figure 9 shows biplots for different saturation states obtained from PCA. The first two PCs make the coordinate system, and axes labels include a percentage of a total variance that is explained by the particular PC. Vectors on the biplots are rather divided into groups which have different colors. Table S2 shows original variables that are incorporated into each coloristic group. As we can see, sample AK1 stands out for each saturation state, but for the saturated state (Figure 9C) or differential data (Figure 9D) there is a clear division of samples into two coherent groups. For these two states, AK1 has the minimal value of PC 1, which indicates that original variables that have the highest contribution to this PC differentiate this sample.

The results of the PCA analysis correspond well with the observations of T_2 distributions and T_1-T_2 maps. AK1 is always characterized by the highest T_1lm and T_2lm, which indicates that the distributions are shifted toward higher T_2s that result from the biggest pores among the samples. Additionally, it has the highest porosity independently on saturation state. The most noticeable difference is the type of pores that saturates most preferably. For AK2-AK4 we observed a significant increase in the signal from OH-groups and mesoporosity, while for AK1 this was from macropores.

3.9. Summary.

- T_2 distributions and T_1-T_2 maps revealed that cherts contain protons associated with hydroxyl groups (R1: T_2 ~ 0.06−0.2 ms) and molecular water (R2−R5: T_2 > 0.4−2 ms) with total porosity varying from 1.08 to 2.32%.
- PSDs, determined based on the T_2 distributions, indicate that the rock core samples contain a wide range of pores size, including mainly mesopores (R1−R2: T_2< 2 ms) and macropores (R3−R5: T_2> 2 ms) with a very low content of micropores (R1: T_2 < 0.03 ms).
- Very distinct peaks on the T_2 distributions and the T_1-T_2 maps in the dry state of the samples revealed the existence of the kind of closed porosity (0.65−1.31%) associated with inclusions possibly filled with different amounts of silica particles and water.
- Types of inclusions are characterized by a large diversity of T_1/T_2 and T_2 parameters, which is probably

https://dx.doi.org/10.1021/acs.jpcc.9b11790
J. Phys. Chem. C 2020, 124, 5225−5240

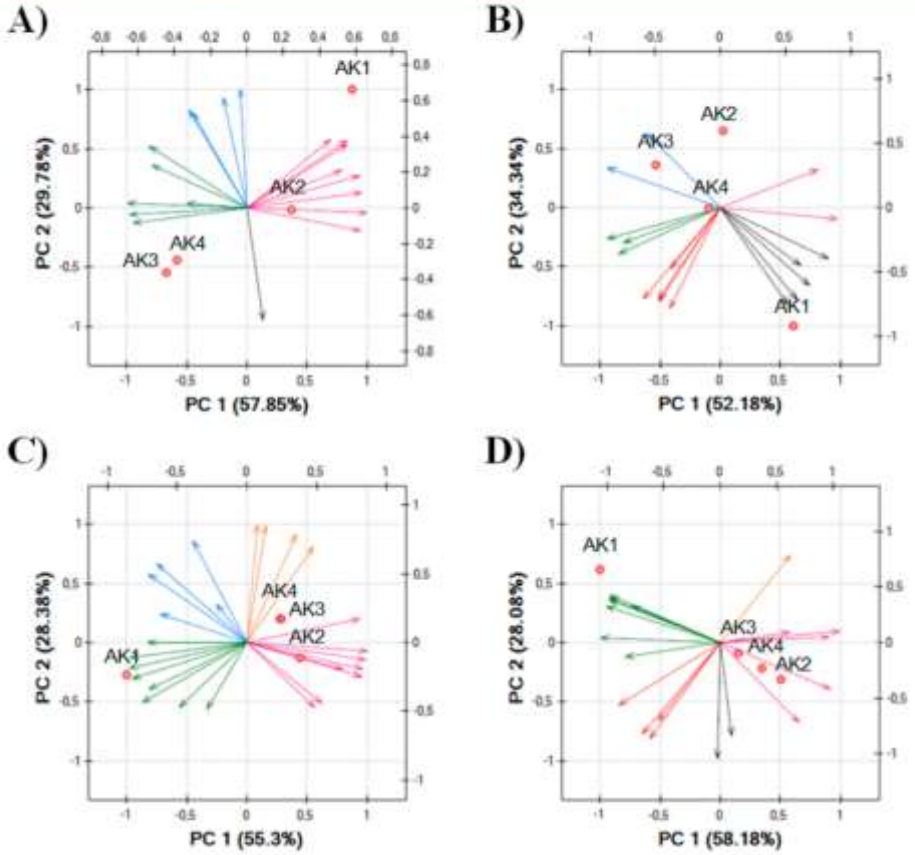

Figure 9. Biplots from PCA: (A) dry samples data; (B) native samples data; (C) saturated samples data; (D) differential data of saturated and dry samples. Vectors reflect the load of original variables into PCs and are divided into coloristic groups (the contents of each group are shown in Table S2).

associated with various geological processes accompanying their formation.

- The registered open porosity (0.4−1.2%) is composed of a considerable volume of macropores in bedded cherts and mesopores in nodular cherts and, in addition, a visible increase in the signal from the newly formed OH groups (probably in silanols) in both cases.
- Existence of unusually high T_1/T_2 values (inclusions: up to ∼100, open pores: ∼20) for water in inorganic nanometric pores suggests the occurrence of pores that may differ in the type of silica as well as its quantity and water solution content (Figure 8, Table 8).
- PCA helped to distinguish AK1 (bedded chert) from others, yielding a set of variables which differentiate the sample the most.
- Finally, LF-NMR relaxometry in the three saturation states delivers a complete and sufficient set of information, based on which bedded and nodular cherts can be distinguished.

4. CONCLUSIONS

The analysis of natural inorganic porous systems showed that we were dealing with samples that have porosity at the level of 1−2%, consisting of several clear hydrogen signal sources. A significant part of the pore volume was inaccessible and were considered to be inclusions. Depending on chert type, different pore types were saturated. Bedded chert seems to have bigger pores in a fairly wide range and hence higher porosity than nodular cherts. Therefore, saturation leads to the filling of a considerable number of macropores in bedded cherts and mesopores in nodular ones and, in addition, a visible increase in the signal from the newly formed OH groups in both cases. Moreover untypical for inorganic pores high values of T_1/T_2 factor equal to ∼100 and ∼20 was registered for T_2 in the range of several and over a dozen milliseconds, respectively. The identification of pore types was possible due to the chemical analysis of the elemental composition of rock core samples, which revealed that they consist of at least 98% pure silica. With this information it was possible to compare them with standard models built from pure silica, MCM-41 and SBA-15, as well as making an estimation of PSD using its relationship with 1D-T_2 distribution. The analysis of PSD showed that for samples containing Fe_2O_3, the influence of diffusion on transverse magnetization decay is negligible. Hence, PSD can be sufficiently accurately determined from the linear relationship between pore size and surface relaxation time. In addition, the performed experiments delivered a sufficient set of variables for PCA, which turned out to be the

https://dx.doi.org/10.1021/acs.jpcc.9b11790
J. Phys. Chem. C 2020, 124, 5225−5240

right tool for the clear division of cherts into two groups. This means that the differences between the parameters obtained from relaxometry for bedded and nodular cherts were statistically significant. The outcomes indicate the possible use of the LF-NMR method for the noninvasive and effective distinction of cherts types expected by geologists, archeologists, and petrographers.

■ ASSOCIATED CONTENT

Supporting Information

The Supporting Information is available free of charge at https://pubs.acs.org/doi/10.1021/acs.jpcc.9b11790.

Principal component analysis—theory and interpretation method; coordinates of peaks from 1D-T_1 distributions (Table S1); original variables that were considered in the PCA (Table S2); and pore size distribution (PSD) determined from 1D-T_2 distributions of saturated samples, assuming that they are composed of 100% SiO_2 (Figure S1) (PDF)

■ AUTHOR INFORMATION

Corresponding Author

Artur T. Krzyżak − *Department of Fossil Fuels, Faculty of Geology, Geophysics and Environmental Protection, AGH University of Science and Technology, 30-059 Kraków, Poland;* orcid.org/0000-0002-1709-9831; Email: akrzyzak@agh.edu.pl

Authors

Weronika Mazur − *Department of Fossil Fuels, Faculty of Geology, Geophysics and Environmental Protection, AGH University of Science and Technology, 30-059 Kraków, Poland*

Jacek Matyszkiewicz − *Department of Environmental Analysis, Geological Mapping and Economic Geology, Faculty of Geology, Geophysics and Environmental Protection, AGH University of Science and Technology, 30-059 Kraków, Poland*

Alicja Kochman − *Department of Environmental Analysis, Geological Mapping and Economic Geology, Faculty of Geology, Geophysics and Environmental Protection, AGH University of Science and Technology, 30-059 Kraków, Poland*

Complete contact information is available at: https://pubs.acs.org/10.1021/acs.jpcc.9b11790

Notes

The authors declare no competing financial interest.

■ ACKNOWLEDGMENTS

This research was funded by the National Science Centre, Poland, on the basis of Contract No. UMO-2017/27/B/ST10/00594 (J.M., A.K.) and by the National Centre of Research and Development (Contract No. STRATEGMED2/265761/10/NCBR/2015) (W.M., A.T.K.). W.M. has been partly supported by the EU Project POWR.03.02.00-00-I004/16.

■ REFERENCES

(1) Van den Boorn, S. H. J. M. *Silicon Isotopes and the Origin of Archaean Cherts*. Ph.D. Thesis; 2008.

(2) Jones, D. L.; Murchey, B. Geologic Significance of Paleozoic and Mesozoic Radiolarian Chert. *Annu. Rev. Earth Planet. Sci.* **1986**, *14* (4), 455−492.

(3) Olivares, M.; Tarrino, A.; Murelaga, X.; Baceta, J. I.; Castro, K.; Etxebarria, N. Non-Destructive Spectrometry Methods to Study the Distribution of Archaeological and Geological Chert Samples. *Spectrochim. Acta, Part A* **2009**, *73*, 492−497.

(4) Hassler, E. R.; Swihart, G. H.; Dye, D. H.; Li, Y. S. Non-Destructive Provenance Study of Chert Using Infrared Reflectance Microspectroscopy. *J. Archaeol. Sci.* **2013**, *40*, 2001−2006.

(5) Purdy, B.; Brooks, H. Thermal Alteration of Silica Minerals: An Archaeological Approach. *Science* **1971**, *173*, 322−325.

(6) Kenyon, W.; Howard, J. Pore-Size Distribution and NMR in Microporous Cherty Sandstones. *Trans. SPWLA Ann.* **1989**, *i*, LL.

(7) Degens, E. T.; Epstein, S. Relationship between O18/O16 Ratios in Coexisting Carbonates, Cherts and Diatomites. *AAPG Bull.* **1962**, *46*, 534−542.

(8) Kolodny, Y. Petrology of Siliceous Rocks in the Mishash Formation (Negev, Israel). *J. Sediment. Res.* **1969**, *39*, 166−175.

(9) Hesse, R. Silica Diagenesis: Origin of Inorganic and Replacement Cherts. *Earth-Sci. Rev.* **1989**, *26*, 253−284.

(10) Gao, G. Q.; Land, L. S. Nodular Chert from the Arbuckle Group, Slick Hills, SW Oklahoma - a Combined Field, Petrographic and Isotopic Study. *Sedimentology* **1991**, *38*, 857−870.

(11) Knauth, L. P. A Model for the Origin of Chert in Limestone. *Geology* **1979**, *7*, 274−277.

(12) Knauth, L. P.; Clauer, N.; Chaudhuri, S. Origin and Diagenesis of Cherts: An Isotopic Perspective. *Isotopic Signatures and Sedimentary Records Lect. Notes Earth Sci.* **1992**, *43*, 123−152.

(13) Genedi, A. Formation of the Upper Cretaceous Cherts in Northeastern Sinai, Egypt. *J. Afr. Earth Sci.* **1998**, *26*, 297−311.

(14) McBride, E. F.; Abdel-Wahab, A.; El-Younsy, A. R. M. Origin of Spheroidal Chert Nodules, Drunka Formation (Lower Eocene), Egypt. *Sedimentology* **1999**, *46*, 733−755.

(15) Umeda, M. Precipitation of Silica and Formation of Chert-Mudstone-Peat Association in Miocene Coastal Environments at the Opening of the Sea of Japan. *Sediment. Geol.* **2003**, *161*, 249−268.

(16) Pieńkowski, G.; Gutowski, J. Origin of the Upper Oxfordian Flints in Krzemionki Opatowskie, Poland. *Tomy Jurajskie* **2004**, *2*, 29−36.

(17) Migaszewski, Z. M.; Gałuszka, A.; Durakiewicz, T.; Starnawska, E. Middle Oxfordian − Lower Kimmeridgian Chert Nodules in the Holy Cross Mountains, South-Central Poland. *Sediment. Geol.* **2006**, *187*, 11−28.

(18) Tribovillard, N. The Ge/Si Ratio as a Tool to Recognize Biogenic Silica in Chert. *C. R. Geosci.* **2013**, *345*, 160−165.

(19) Kolodny, Y. The Origin of Cherts as Members of High Productivity Sequences: Isotopic Evidence. In *The Scientific Study of Flint and Chert*; Sieveking, G. D., Hart, M. B., Eds.; Cambridge Univ. Press: 1986; pp 55−62.

(20) Chiari, M.; Baumgartner, P. O.; Bernoulli, D.; et al. Late Triassic, Early and Middle Jurassic Radiolaria from Ferromanganese-Chert 'Nodules' (Angelokastron, Argolis, Greece): Evidence for Prolonged Radiolarite Sedimentation in the Maliac-Vardar Ocean. *Facies* **2013**, *59*, 391−424.

(21) Aghaei, A.; Mahboubi, A.; Harami, R. M.; et al. Carbonate Diagenesis of the Upper Jurassic Successions in the West of Binalud - Eastern Alborz (NE Iran). *J. Geol. Soc. India* **2014**, *83*, 311−328.

(22) Spence, G. H.; Finch, E.; Spence, G. H.; Redfern, J.; Aguilera, R.; Bevan, T. G.; Cosgrove, J. W.; Couples, G. D.; Daniel, J.-M. Influences of Nodular Chert Rhythmites on Natural Fracture Networks in Carbonates: An Outcrop and Two-Dimensional Discrete Element Modelling Study. *Geol. Soc. Spec. Publ.* **2014**, *374*, 211−249.

(23) Dong, L.; Shen, B.; Lee, C.-T. A.; Shu, X.; Peng, Y. Germanium/Silicon of the Ediacaran-Cambrian Laobao Cherts: Implications for the Bedded Chert Formation and Paleoenvironment Interpretations. *Geochem., Geophys., Geosyst.* **2015**, *16*, 751−763.

(24) Gül, M. Occurrences of Chert in Jurassic-Cretaceous Calciturbidites (SW Turkey). *Cent. Eur. J. Geosci.* **2015**, *7*, 446−464.

(25) Bustillo, M. Á.; Díaz-Molina, M.; López-García, M. J.; et al. Geology and Paleontology of Tresjuncos (Cuenca, Spain), a New Diatomaceous Deposit with Konservat-Lagerstätte Characteristics from the European Late Miocene. *J. Iber. Geol.* **2017**, *43*, 395−411.

(26) Knauth, L. P.; Epstein, S. Hydrogen and Oxygen Isotope Ratios in Nodular and Bedded Cherts. *Geochim. Cosmochim. Acta* **1976**, *40*, 1095−1108.
(27) Kolodny, Y.; Epstein, S. Stable Isotope Geochemistry of Deep Sea Cherts. *Geochim. Cosmochim. Acta* **1976**, *40*, 1195−1209.
(28) Wheeler, W. H.; Textoris, D. A. Limestone and Chert of Playa Origin in North Carolina. *J. Sediment. Res.* **1978**, *48*, 765−776.
(29) Bromley, R. G.; Ekdale, A. A. Flint and Fabric in the European Chalk. In: Sieveking, G. de G., Hart, M. B. (Eds.). In *The Scientific Study of Flint and Chert*; 1986; pp 71−82.
(30) Bustillo, M. Á.; Ruiz-Ortiz, P. A. Chert Occurrences in Carbonate Turbidites: Examples from the Upper Jurassic of the Betic Mountains (Southern Spain). *Sedimentology* **1987**, *34*, 611−621.
(31) Maliva, R. G.; Siever, R. Pre-Cenozoic Nodular Cherts: Evidence for Opal-CT Precursors and Direct Quartz Replacement. *Am. J. Sci.* **1988**, *288*, 798−809.
(32) Maliva, R. G.; Siever, R. Nodular Chert Formation in Carbonate Rocks. *J. Geol.* **1989**, *97*, 421−433.
(33) Habryn, R.; Buła, Z.; Nawrocki, J. The Kraków Sector of the Kraków-Lubliniec Tectonic Zone in the Light of Data Obtained from New Boreholes of Trojanowice 2 and Cianowice 2. *Biul. Państwowego Inst. Geol.* **2014**, *459*, 45−60.
(34) Alexandrowicz, S. W. Geological Structure of the Vicinity of Tyniec. *Biul. Inst. Geol.* **1960**, *152*, 5−93.
(35) Matyszkiewicz, J. Sedimentation and Diagenesis of the Upper Oxfordian Cyanobacterial-Sponge Limestones in Piekary near Kraków. *Ann. Soc. Geol. Polym.* **1989**, *59*, 201−232.
(36) Świerczewska, A. *Sylifikacja Diagenetyczna w Wapieniach Górnojurajskich Jury Krakowsko-Wieluńskiej*; Polish Academy of Sciences: 1990.
(37) Świerczewska, A. Early Diagenetic Silicification in the Upper Jurassic Biohermal and Interbiohermal Facies. In *Man and Flint*; Schild, R., Sulgostkowska, Z., Eds.; 1997; pp 357−361.
(38) Matyszkiewicz, J. The Significance of Saccocoma-Calciturbidites for the Analysis of the Polish Epicontinental Late Jurassic Basin: An Example from the Southern Cracow-Wieluń Upland (Poland). *Facies* **1996**, *34*, 23−40.
(39) Trammer, J. Sponge Bioherms in the Jasna Góra Beds (Oxfordian of the Polish Jura Chain). *Przegląd Geol.* **1985**, *33*, 78−81.
(40) Trammer, J. Lower to Middle Oxfordian Sponges of the Polish Jura. *Acta Geol. Polym.* **1982**, *32*, 1−39.
(41) Trammer, J. Middle to Upper Oxfordian Sponges of the Polish Jura. *Acta Geol. Polym.* **1989**, *39*, 49−91.
(42) Matyszkiewicz, J.; Felisiak, I.; Hoffmann, M.; Kochman, A.; Kołodziej, B.; Krajewski, M.; Olchowy, P. Transgressive Callovian Succession and Oxfordian Microbial-Sponge Carbonate Buildups in the Kraków Upland. In *Guidebook for field trips accompanying 31 IAS meeting of sedimentology held in Kraków*; Haczewski, G., Ed.; Polskie Towarzystwo Geologiczne, 2015; pp 51−73.
(43) Matyszkiewicz, J.; Krajewski, M.; Kochman, A.; Kozłowski, A.; Duliński, M. Oxfordian Neptunian Dykes with Brachiopods from the Southern Part of the Kraków-Częstochowa Upland (Southern Poland) and Their Links to Hydrothermal Vents. *Facies* **2016**, *62*, 12.
(44) Bąk, M.; Bąk, K.; Górny, Z.; Stożek, B. Evidence of Bacteriogenic Iron and Manganese Oxyhydroxides in Albian-Cenomanian Marine Sediments of the Carpathian Realm (Poland). *Ann. Soc. Geol. Pol.* **2015**, *85*, 371−385.
(45) Vahur, S.; Kriiska, A.; Leito, I. Investigation of the Adhesive Residue on the Flint Insert and the Adhesive Lump Found From the Pulli Early Mesolithic Settlement Site (Estonia) By Micro-Atr-Ft-Ir Spectroscopy. *Est. J. Archaeol.* **2011**, *15* (1), 3.
(46) Cintă Pînzaru, S.; Pop, D.; Nemeth, L. FT-Raman and FT-Infrared Investigations of Archaeological Artefacts from Foeni Neolithic Site (Banat, Romania). *Stud. Univ. Babes-Bolyai* **2008**, *53* (1), 31−37.
(47) Aliyu, M. M.; Murphy, W.; Collier, R.; Lawrence, J. A. Classification of Flints for Drill Wear Potential. In *Future Developments of Rock Mechanics*; 2015.
(48) Sieveking, G. de G.; Bush, P.; Ferguson, J.; Craddock, P. T.; Hughes, M. J.; Cowell, M. R. Prehistoric Flint Mines and Their Identification as Sources of Raw Material. *Archaeometry* **1972**, *14* (2), 151−176.
(49) Hughes, R. E.; Högberg, A.; Olausson, D. The Chemical Composition of Some Archaeologically Significant Flint from Denmark and Sweden. *Archaeometry* **2012**, *54* (5), 779−795.
(50) Aspinall, A.; Feather, S. W. Neutron Activation Analysis of Prehistoric Flint Mine Products. *Archaeometry* **1972**, *14* (1), 41−53.
(51) Adams, S. J.; Hawkes, G. E.; Curzon, E. H. A Solid State 29Si Nuclear Magnetic Resonance Study of Opal and Other Hydrous Silicas. *Am. Mineral.* **1991**, *76* (11−12), 1863−1871.
(52) Krzyżak, A. T.; Habina, I. Low Field 1H NMR Characterization of Mesoporous Silica MCM-41 and SBA-15 Filled with Different Amount of Water. *Microporous Mesoporous Mater.* **2016**, *231*, 230−239.
(53) Yuan, L.; Chen, L.; Chen, X.; Liu, R.; Ge, G. In Situ Measurement of Surface Functional Groups on Silica Nanoparticles Using Solvent Relaxation Nuclear Magnetic Resonance. *Langmuir* **2017**, *33* (35), 8724−8729.
(54) Oulkadi, D.; Yemloul, M.; Desobry-Banon, S.; Canet, D. Water Behavior in Hybrid Silica Gels as Studied by 1H Nuclear Magnetic Resonance Relaxometry. Evidence of Two Hydration Layers. *Microporous Mesoporous Mater.* **2013**, *172*, 213−216.
(55) Schaller, T.; Sebald, A. One- and Two-Dimensional 1H Magic-Angle Spinning Experiments on Hydrous Silicate Glasses. *Solid State Nucl. Magn. Reson.* **1995**, *5* (1), 89−102.
(56) Totland, C.; Steinkopf, S.; Blokhus, A. M.; Nerdal, W. Water Structure and Dynamics at a Silica Surface: Pake Doublets in 1H NMR Spectra. *Langmuir* **2011**, *27* (8), 4690−4699.
(57) Khouchaf, L.; Hamoudi, A.; Cordier, P. Evidence of Depolymerisation of Amorphous Silica at Medium- and Short-Range Order: XANES, NMR and CP-SEM Contributions. *J. Hazard. Mater.* **2009**, *168* (2−3), 1188−1191.
(58) Folk, R. L.; Pittman, J. S. Length-Slow Chalcedony: A New Testament for Vanished Evaporites. *J. Sediment. Res.* **1971**, *41* (4), 1045−1058.
(59) Chowns, T. M.; Elkins, J. E. The Origin of Quartz Geodes and Cauliflower Cherts through the Silicification of Anhydrite Nodules. *J. Sediment. Res.* **1974**, *44* (3), 885−903.
(60) Kleinberg, R. L.; Horsfield, M. A. Transverse Relaxation Processes in Porous Sedimentary Rock. *J. Magn. Reson.* **1990**, *88* (1), 9−19.
(61) Foley, I.; Farooqui, S. A.; Kleinberg, R. L. Effect of Paramagnetic Ions on NMR Relaxation of Fluids at Solid Surfaces. *J. Magn. Reson., Ser. A* **1996**, *123* (1), 95−104.
(62) Hunt, P.; Moskowitz, B. M.; Banerjee, S. K. Magnetic Properties of Rocks and Minerals. *Rock Physics & Phase Relations: A Handbook of Physical Constants* **2013**, *3*, 189−204.
(63) Hürlimann, M. D. Effective Gradients in Porous Media Due to Susceptibility Differences. *J. Magn. Reson.* **1998**, *131* (2), 232−240.
(64) Bourg, I. C.; Steefel, C. I. Molecular Dynamics Simulations of Water Structure and Diffusion in Silica Nanopores. *J. Phys. Chem. C* **2012**, *116* (21), 11556−11564.
(65) Lerbret, A.; Lelong, G.; Mason, P. E.; Saboungi, M. L.; Brady, J. W. Water Confined in Cylindrical Pores: A Molecular Dynamics Study. *Food Biophys* **2011**, *6* (2), 233−240.
(66) Milischuk, A. A.; Ladanyi, B. M. Structure and Dynamics of Water Confined in Silica Nanopores. *J. Chem. Phys.* **2011**, *135* (17), 174709.
(67) Takahara, S.; Nakano, M.; Kittaka, S.; Kuroda, Y.; Mori, T.; Hamano, H.; Yamaguchi, T. Neutron Scattering Study on Dynamics of Water Molecules in MCM-41. *J. Phys. Chem. B* **1999**, *103* (28), 5814−5819.
(68) Takahara, S.; Sumiyama, N.; Kittaka, S.; Yamaguchi, T.; Bellissent-Funel, M. C. Neutron Scattering Study on Dynamics of Water Molecules in MCM-41. 2. Determination of Translational Diffusion Coefficient. *J. Phys. Chem. B* **2005**, *109* (22), 11231−11239.

https://dx.doi.org/10.1021/acs.jpcc.9b11790
J. Phys. Chem. C 2020, 124, 5225−5240

(69) D'Agostino, C.; Mitchell, J.; Mantle, M. D.; Gladden, L. F. Interpretation of NMR Relaxation as a Tool for Characterising the Adsorption Strength of Liquids inside Porous Materials. *Chem. - Eur. J.* **2014**, *20* (40), 13009−13015.

(70) Woessner, D. E.; Zimmerman, J. R. NUCLEAR TRANSFER AND ANISOTROPIC MOTIONAL SPIN PHENOMENA: RELAXATION TIME TEMPERATURE DEPENDENCE STUDIES OF WATER ADSORBED ON SILICA GEL. IV. *J. Phys. Chem.* **1963**, *67* (8), 1590−1600.

(71) O'Reilly, D. E.; Leftin, H. P.; Hall, W. K. Nuclear Magnetic Resonance of Proton Dilute Silica Gel and Silica-Aluminas. *J. Chem. Phys.* **1958**, *29*, 970−971.

(72) Musso, F.; Sodupe, M.; Corno, M.; Ugliengo, P. H-Bond Features of Fully Hydroxylated Surfaces of Crystalline Silica Polymorphs: A Periodic B3LYP Study. *J. Phys. Chem. C* **2009**, *113* (41), 17876−17884.

(73) Robinson, N.; Robertson, C.; Gladden, L. F.; Jenkins, S. J.; D'Agostino, C. Direct Correlation between Adsorption Energetics and Nuclear Spin Relaxation in a Liquid-Saturated Catalyst Material. *ChemPhysChem* **2018**, *19* (19), 2472−2479.

(74) Khatibi, S.; Ostadhassan, M.; Xie, Z. H.; Gentzis, T.; Bubach, B.; Gan, Z.; Carvajal-Ortiz, H. NMR Relaxometry a New Approach to Detect Geochemical Properties of Organic Matter in Tight Shales. *Fuel* **2019**, *235*, 167−177.

(75) Habina, I.; Radzik, N.; Topór, T.; Krzyżak, A. T. Insight into Oil and Gas-Shales Compounds Signatures in Low Field 1H NMR and Its Application in Porosity Evaluation. *Microporous Mesoporous Mater.* **2017**, *252*, 37−49.

https://dx.doi.org/10.1021/acs.jpcc.9b11790
J. Phys. Chem. C 2020, 124, 5225−5240

AGU ADVANCING EARTH AND SPACE SCIENCE

JGR Solid Earth

RESEARCH ARTICLE
10.1029/2021JB023299

Prospects and Challenges for the Spatial Quantification of the Diffusion of Fluids Containing ^{1}H in the Pore System of Rock Cores

A. T. Krzyżak[1], W. Mazur[1,2], A. Fheed[1], and W. P. Węglarz[3]

[1]Faculty of Geology, Geophysics and Environmental Protection, AGH University of Science and Technology, Kraków, Poland, [2]Faculty of Physics and Applied Computer Science, AGH University of Science and Technology, Kraków, Poland, [3]Department of Magnetic Resonance Imaging, The Henryk Niewodniczański Institute of Nuclear Physics, Polish Academy of Sciences, Kraków, Poland

Abstract Nuclear magnetic resonance (MR) (NMR) is commonly used for the determination of rock porosity, as well as pore size distribution (PSD) and tortuosity, required to handle hydrocarbon exploitation. Emerging technologies for NMR equipment now enable the visualization of porosity using magnetic resonance imaging (MRI). Currently, single-point imaging is the most common MRI technique employed, but diffusion-weighted imaging has been attracting the attention of geologists and geophysicists. In this study, a more advanced technique, diffusion tensor imaging (DTI), is proposed for the characterization of rock core samples. The main purpose of this paper is to demonstrate the usefulness of DTI in the petrophysical characterization of rocks and discuss its strengths. As an example, a carbonate core sample was examined using DTI. The diffusion tensor (DT) was obtained and DT parameters (mean diffusivity, *MD*; fractional anisotropy, *FA*; three eigenvalues; DT components; and proton density, *PD*) were visualized in 2D and 3D. Each parameter was described and its utility in terms of pore space characterization was analyzed. In addition, a new parameter, principal diffusion tracts, was introduced based on the DT tractography performed in the study. The analysis is summarized in a set of DT parameters and a resultant ellipsoid that delivers complementary information about the sample's pore network microgeometry, including referential measurements of anisotropic phantoms. The applications of DTI for the determination of pore size distribution, tortuosity and conductivity are also shown. The study ends with a consideration of the potential prospects and challenges for DTI-based examination of rock core samples.

Plain Language Summary An advanced nuclear magnetic resonance technique, diffusion tensor imaging (DTI), is proposed here for the characterization of rock core samples. As an example, a carbonate core sample was subjected to DTI examination, from which the diffusion tensor (DT) was obtained and DT parameters (mean diffusivity, *MD*; fractional anisotropy, *FA*; three eigenvalues; DT components and proton density, *PD*) were visualized in 2D and 3D. Potential examples of the practical applications of the data obtained from the DTI experiment are demonstrated. Importantly, we can now provide spatial and quantitative data which is closely related to the studied microstructure using DTI. The application of DTI for the determination of pore size distribution, tortuosity and conductivity are also shown. The study ends with a consideration of the potential prospects and challenges for the DTI-based examination of rock core samples.

Key Points:

- Diffusion tensor imaging enables, rotationally invariant, 3D spatial quantification of diffusion in rocks, reflecting porosity features
- Principal diffusion tracts may reflect permeability anisotropy and correspond to the conductivity tensor
- DTI ellipsoid delivers a set of parameters describing the microgeometry of average or spatially resolved pores

Supporting Information:

Supporting Information may be found in the online version of this article.

Correspondence to:

A. T. Krzyżak,
akrzyzak@agh.edu.pl

Citation:

Krzyżak, A. T., Mazur, W., Fheed, A., & Węglarz, W. P. (2022). Prospects and challenges for the spatial quantification of the diffusion of fluids containing ^{1}H in the pore system of rock cores. *Journal of Geophysical Research: Solid Earth*, *127*, e2021JB023299. https://doi.org/10.1029/2021JB023299

Received 25 SEP 2021
Accepted 28 FEB 2022

Author Contributions:

Conceptualization: A. T. Krzyżak
Data curation: A. T. Krzyżak, W. Mazur, A. Fheed
Formal analysis: A. T. Krzyżak, W. Mazur, A. Fheed
Funding acquisition: A. T. Krzyżak, A. Fheed, W. P. Węglarz
Investigation: A. T. Krzyżak, A. Fheed, W. P. Węglarz
Methodology: A. T. Krzyżak
Project Administration: A. T. Krzyżak
Resources: A. T. Krzyżak
Software: A. T. Krzyżak, A. Fheed

1. Introduction

Research on the diffusion of fluids filling rock pores with the application of techniques using nuclear magnetic resonance (NMR) is mainly related to the measurement of the diffusion coefficient, D, in one- or two-dimensional correlation experiments (D-T_1, D-T_2; Hürlimann & Venkataramanan, 2002; Mitchell et al., 2015) and, in recent years, diffusion-weighted imaging (DWI; Fheed et al., 2020). In the former, where D-T_2 is the most popular and will be central to our further considerations, the NMR signal is analyzed after the transformation by Inverse Laplace Transform (ILT) instead of Fast Fourier Transform (FFT) as in the case of DWI. After the calculations by means of ILT or FFT, projections of the diffusion coefficient maps are obtained along the experimentally defined diffusion gradient vector (Dale et al., 2015). Both methods deliver different information and are complementary. First of all, D-T_2 enables distinctions to be drawn between various liquids (water, different types of oil and gas), as well as the estimation of pore size distribution (PSD) and permeability by analyzing the T_2 relaxation

Supervision: A. T. Krzyżak
Validation: A. T. Krzyżak, A. Fheed, W. P. Węglarz
Visualization: A. T. Krzyżak, W. Mazur, A. Fheed
Writing – original draft: A. T. Krzyżak, W. Mazur, A. Fheed
Writing – review & editing: A. T. Krzyżak, W. Mazur, A. Fheed, W. P. Węglarz

spectra (Daigle & Dugan, 2011; Kleinberg & Horsfield, 1990; Krzyżak, Habina-Skrzyniarz et al., 2020; Krzyżak & Habina, 2016). DWI enables the spatial imaging of diffusion coefficient distributions, for example, it shows the arrangement of fissures in rock cores or allows indirect conclusions to be drawn regarding the permeability of a reservoir sample (Fheed et al., 2020). In both cases, the obtained diffusion coefficients of water or hydrocarbons contain information about diffusion along a specific gradient direction, meaning that their values are ambiguous and different, depending not only on the gradient direction, but also on the orientation of the sample within a magnet bore. In fact, D-T_2 and DWI deliver a projection (simplification) of a symmetrical tensor of the second order. In anisotropic media, the diffusion tensor is a correct, full representation of the diffusion of fluid molecules, which unambiguously describes the microstructure of the sample, regardless of the reference system (its position in the magnet bore or the diffusion gradient vector scheme used). To obtain full information about the tensor, a diffusion tensor imaging (DTI) experiment has to be performed (Kingsley, 2006). This technique is well-known and used extensively in the biomedical sphere, but has yet to be applied in geology or geophysics (Alexander, 2006).

Both hydrocarbon recovery and underground gas storage require detailed knowledge about the internal rock structure which controls the movement of fluids through the reservoir. In the case of carbonate rocks, the ultimate pore network is a product of a complicated course of both sedimentary and diagenetic processes (Flügel, 2004). Therefore, it seems that bridging the gap between geology and DTI is worth considering. In particular, the use of quantitative values of diffusion tensor offered by DTI in petrophysical aspects could help to determine the degree of pore space connectivity more precisely. The architecture of the pores controls the permeability of rocks and thus the potential rate of oil and gas production (Zhang et al., 2020) or optimal energy extraction from geothermal environment (Watanabe et al., 2020; Yasuhara et al., 2006). The DTI results could be further compared with permeability tensors, defined similarly to the DTI approach and thus enabling potential relations between diffusion and permeability to be revealed (Lang et al., 2014). Another potential application of DTI could be the selection of sites for the efficient underground storage of CO_2, an application which is currently enjoying a considerable amount of interest (Ajayi et al., 2019; Arif et al., 2017; Raza et al., 2017). In this case, the parameters describing the DT and related to pore size and geometry would facilitate the selection of such locations.

Despite the petrophysical potential of DTI related to its ability to deliver direct information on pore size and/or geometry, there are only few references dealing with some aspects of this technique. Furthermore, none of these works shows the actual meaning of DTI, that is, the registration of spatial maps of the diffusion tensor (most often water) in an examined object (see the literature review below). This is related to the considerable difficulties in using magnetic resonance imaging (MRI), and especially DTI in these areas, due to the shortening of T_2 relaxation times and local differences in magnetic susceptibilities in samples, with greater complications with increases in the magnetic field (Hürlimann, 1998; Krzyżak, Mazur, et al., 2020). This work documents the use of DTI to examine a carbonate rock core for the first time. Quantitative diffusion tensor (DT) parameters such as fractional anisotropy (*FA*), mean diffusivity (*MD*) and three DT eigenvalues ($\lambda_{1/2/3}$) are provided. The main tracks of the diffusion tensor, which are solely dependent on the microstructure of the tested sample (Mori et al., 1999), are also visualized. In addition, also discussed are the current state of the art, potential geophysical or geological applications, and the challenges of developing this technique for the purposes of imaging a fluid diffusion tensor in rock cores.

1.1. From Diffusion-Weighted NMR to DTI

To date, the diffusion phenomenon has been frequently utilized in NMR-based reservoir characterization (Coates et al., 1999). As highlighted earlier, besides porosity investigation, the majority of the research concentrates around fluid typing using diffusion-weighted NMR (Luo et al., 2015; Matenoglou et al., 2016). D-T_2 correlation maps are commonly used to locate different reservoir fluids within samples (Ahr et al., 2005; Luo et al., 2015). The persistent interest in this field of study has recently promoted the development of more complex fluid typing workflows. For instance, by comparing the functions of diffusion-relaxation distributions, Mutina and Hürlimann (2008) showed the existence of obvious differences corresponding to the underlying structures of the tested fluids and proved that the D-T_2 measurements can trace the paths of complex fluids.

Diffusion-weighted NMR was also frequently utilized to derive the absolute pore size distribution, so that the T_2 relaxation times are assigned specific pore sizes, typically using the pulsed field gradient methods (Mitra

et al., 1992; Pomerantz et al., 2007). Other authors have also utilized diffusion-related NMR research to study pore space geometry, tortuosity, or the degree of its communication (Delgado, 2006; Wang et al., 2018).

Papers dealing with or describing the use of DTI for petrophysical purposes are few and far between. Moreover, there has been a tendency to misuse the term *diffusion tensor imaging*, since some articles referring to DTI in fact do not implement full tensor imaging. To the best of our knowledge, only two works have demonstrated some of the useful aspects of DTI in geosciences (Matenoglou et al., 2016; Porion et al., 2018). The work of Matenoglou et al. (2016) provides a complete workflow for studying the wettability of rocks, especially when more than one reservoir fluid is present. These researchers used an EPI sequence with several values of the diffusion-weighting factor (*b*-value) in order to facilitate the separation of the signal coming from oil and water, based on different diffusion coefficients. However, because Matenoglou et al. (2016) only applied a single (axial) diffusion gradient direction during the measurements, it should be clarified that DTI was not fully implemented and the methodology can be downgraded to DWI in one direction. Moving forward, Fheed et al. (2020) proposed the implementation of DWI in three orthogonal directions to study the dynamics of fluid motions in narrow channel porosity. Similarly, however, a DTI approach was not yet fully implemented.

Porion et al. (2018) presented a different application of the spatially resolved diffusion coefficients. The authors proposed utilizing pulsed-field gradient spin echo NMR (PGSE-NMR) in six diffusion gradient directions and single point imaging (SPI) to characterize the mobility of water in a dense clay sediment with respect to the compression axis. Even though the self-diffusion tensor was calculated, the utilization of a spectrometer only allowed the determination of a mean tensor representing the whole volume of the sample. For spatially heterogeneous samples such as porous rocks, the information obtained in this manner is very general. Nonetheless, this work utilized more than one diffusion gradient direction and the determination of a diffusion tensor.

The emerging popularity of diffusion-based NMR imaging techniques in geosciences and related branches is a promising trend. Although unrelated to rocks or fossilized material, the paper of van Schadewijk et al. (2018) can be mentioned as an example here. The authors employed DWI with six, isotropically distributed gradient directions to realize an *in-vivo* study of green algae, known to have the capability of producing oils in their lipid bodies. Thanks to DWI and other supplementary studies, the researchers managed to visualize the main routes of oil migration and revealed the microstructure of algae, the analogue of which is frequently found in fossilized material (cf. Raczyński et al., 2017).

As we have seen, none of the abovementioned papers covers the full implementation of voxel-based DTI to study the geometry of pores in rocks. Therefore, our proposal of employing the DTI procedure on carbonate rock samples seems to be both novel and justified.

1.2. Theory

As already mentioned, D-T_2 and DWI measurements deliver apparent diffusion coefficients (D_{app}s), that depend on the chosen gradient direction and sample orientation. This is elegantly depicted in Figure 1, where four general pore types are schematically presented and some possible displacement vectors of the molecule are marked. For fully isotropic pores (types A and B), displacement vectors have the same length (r_A and r_B) and neither the sample orientation nor the gradient direction influence D_{app}. However, for anisotropic pores (types C and D), potential molecule displacement paths have different lengths, and therefore D_{app} varies with sample orientation and gradient direction. Moreover, the higher the anisotropy, the higher the differences between particular D_{app}s. This means, that D_{app} from D-T_2 and DWI are rotationally variant and give ambiguous information about the pore geometry.

In contrast, DTI relies on the application of diffusion-weighted impulses of magnetic field gradients in at least 6 directions. Based on the 6 diffusion-weighted and 1 baseline (no diffusion-weighting) images, the elements of a diffusion tensor:

$$\boldsymbol{D} = \begin{bmatrix} D_{xx} & D_{xy} & D_{xz} \\ D_{yx} & D_{yy} & D_{yz} \\ D_{zx} & D_{zy} & D_{zz} \end{bmatrix} \tag{1}$$

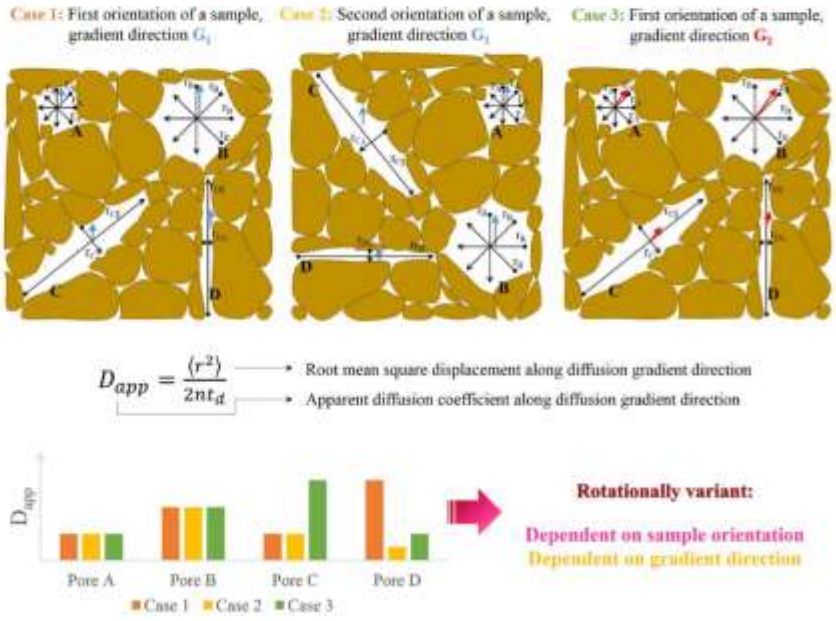

Figure 1. Scheme visualizing the changes in apparent diffusion coefficients (D_{app}) in D-T_2 and a single DWI, resulting from the choice of sample orientation and different gradient directions. The relation for D_{app} contains parameters n and t_d, representing the number of spatial dimensions in which diffusion occurs and diffusion time, respectively.

are calculated from the generalized Stejskal-Tanner Equation 2 for each voxel of a magnetic resonance (MR) image (Borkowski & Krzyżak, 2018).

$$\ln\left(\frac{S(b(r))}{S(b_0(r))}\right) = -b(r) : D = -\sum_{i=1}^{3}\sum_{j=1}^{3} b_{ij}(r)D_{ij} \tag{2}$$

where $S(b(r))$ and $S(b_0(r))$ are MR signals in a voxel with spatial coordinates $r = [x, y, z]$ obtained with and without diffusion-weighting, respectively; $b_{ij}(r)$ are spatially dependent components of the diffusion gradient matrix $b(r)$; D_{ij} are components of the diffusion tensor D; the colon designates the generalized dot product. As shown in Figure 2, sample rotation influences the diffusion tensor components. However, DTI has some advantages over DWI in three orthogonal directions in a laboratory frame. First, D_{xx}, D_{yy} and D_{zz} in DTI are calculated based on the six diffusion-weighted images, while in DWI one image serves for the determination of one coefficient. This means that the signal-to-noise ratio (SNR) in DTI is higher and orthogonal coefficients can be more accurately determined. Second, the only derivative from orthogonal methods is *MD*, calculated as a mean of the three orthogonal diffusion coefficients. Since the off-diagonal tensor's elements are calculated in DTI, additional geometric parameters can be obtained.

In order to determine the rotationally invariant geometry descriptors solely related to the microstructure of a sample, the tensor is diagonalized. After diagonalization, three eigenvalues and associated eigenvectors are obtained. The diagonalized tensor has the following form:

$$\Lambda = \begin{bmatrix} \lambda_1 & 0 & 0 \\ 0 & \lambda_2 & 0 \\ 0 & 0 & \lambda_3 \end{bmatrix} \tag{3}$$

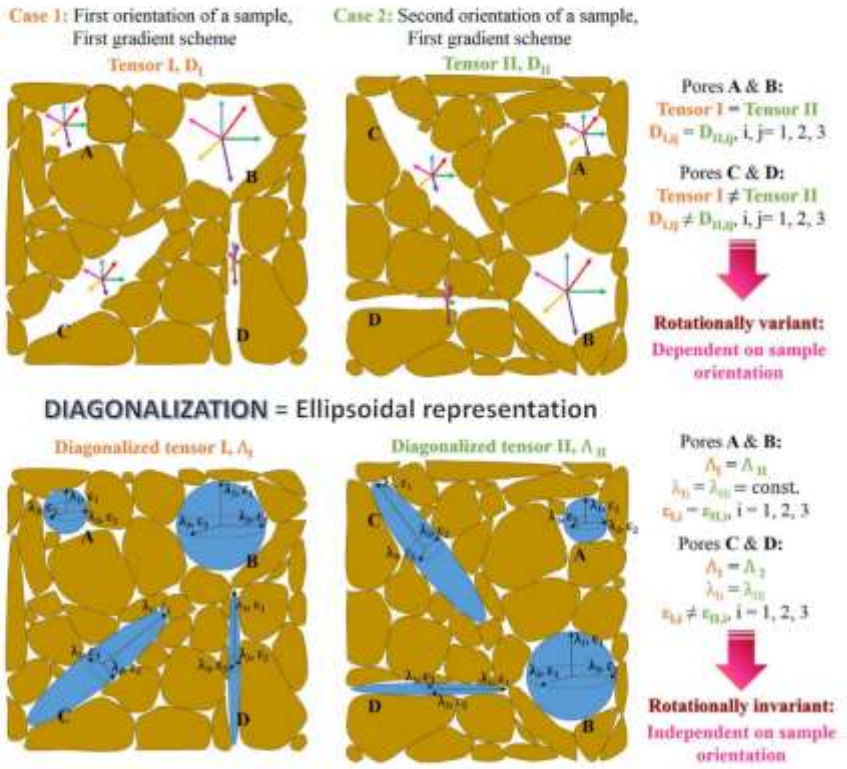

Figure 2. Scheme visualizing the effect of tensor diagonalization. Pores A–D are described as ellipsoids with dimensions represented by eigenvalues λ_1, λ_2 and λ_3, with orientation with respect to the laboratory frame indicated by eigenvectors e_1, e_2 and e_3. Diagonalization delivers three diffusion coefficients along the orthogonal axes associated with pore geometry.

where eigenvalues λ_1, λ_2 and λ_3 represent the amount of diffusion in each of three orthogonal directions in a coordinate system associated with geometry of a diffusion medium (e_1, e_2 and e_3) and are sorted from the highest (λ_1) to the lowest (λ_3) diffusivity. Eigenvectors indicate the directions of three orthogonal diffusion paths with respect to the laboratory frame of reference. Based on the diagonalized tensor, **Λ**, diffusion can be visualized in the shape of an ellipsoid. The orientation of the ellipsoid with respect to the laboratory frame is indicated by the eigenvectors, while its shape is shown by the eigenvalues (see Figure 2). From a mathematical point of view, this corresponds to the probability density function of the position of the fluid molecules after the diffusion time. Most importantly, the coefficients of the diffusion tensor, as well as the parameters computed from them (see the results), are actually quantitative. This makes a significant difference in relation to diffusion-based D-T_2 or DWI measurements, for instance. Simultaneously, it is a source of potential progress and represents the introduction of a new, more precise method of studying fluid diffusion in rocks.

2. Materials and Methods

2.1. Sample Collection and Evaluation

In this study we focus on one carbonate sample. The sample was used for all of the experiments presented in this paper. The details of sample extraction, preparation and evaluation using transmitted-light microscopy (TLM) and complementary methods are elaborated in Section S1 in Supporting Information S1. The studied sample is

a part of the Upper Permian, Zechstein Limestone (Ca1) formation of West Poland and comes from the Brońsko Reef (see Fheed et al., 2022; Peryt et al., 2012).

Complementary information about the sample was obtained by means of mercury intrusion capillary pressure (MICP) and 1D-T_2 NMR experiments (for details see Section S1 in Supporting Information S1). According to MICP research, permeability and porosity of the sample were equal to 22 mD and 14.65%, respectively. 1D-T_2 NMR delivered porosity of 13.90 ± 0.01% and logarithmic mean T_2 time, $T_{2log\,mean}$, of 362 ms. By using MICP and 1D-T_2 data, it was possible to determine the transverse surface relativity, ρ_2, for the sample which was equal to 7.44 μm/s. The characteristic parameters of the sample are summarized in Table S1 in Supporting Information S1.

2.2. Anisotropic Phantoms

Reference DTI measurements were carried out on layered and capillary anisotropic phantoms (Mazur et al., 2019). The fabrication of the layered phantom was as follows: 99 square glass plates, with a thickness of about 180 μm, were stacked in a 2 × 2 × 2 cm cube. The plates were separated in order to ensure planar, longitudinal, equidistant pores with sizes of 20 μm. A capillary phantom was made of 824 quartz photonic fibers, 21 mm long and 830 μm in diameter. Each fiber contains 300 tubes, which are cylindrical, longitudinal pores with a diameter equal to 30 μm. Finally, the anisotropic structures were placed in cylindrical, plexiglas enclosures, 46 mm in diameter, and filled with water. The magnetic susceptibilities of the anisotropic phantoms were matched with the one for water, diminishing the induced gradients (Klodowski & Krzyżak, 2016).

2.3. DTI

The DTI of the rock core sample was conducted on a 9.4 T Bruker BioSpec 94/20USR scanner using a spin echo DtiStandard pulse sequence with the following acquisition parameters: echo time, TE = 20 ms; repetition time, TR = 13 s; number of averages, NoA = 4; number of slices, n_s = 26; slice thickness, ST = 500 μm; number of diffusion sensitizing gradient directions, N = 6; b-value, b = 800 s/mm^2; diffusion encoding time, δ = 5 ms; diffusion gradients interval, Δ = 8.52 ms; field of view, FOV = 32 × 32 mm^2; matrix size 128 × 128 pixels.

For the DTI of the anisotropic phantoms, the protocol for the spin echo DtiStandard sequence was as follows: TE = 20 ms, TR = 2,500 ms, ST = 2 mm, n_s = 11, Δ = 10 ms, δ = 6 ms, N = 6, NoA = 2, FOV = 30 × 30 mm^2, matrix size 64 x 64 pixels.

Tensor visualization and tractography were performed using in-house software (BSD-DTI ver. 2.0, AGH Kraków).

2.4. X-Ray Microtomography (μCT)

The purpose of implementing μCT was to verify the internal pore structure of the sample and obtain basic information regarding the size and shape of pores. The details of μCT method are shown in Section S2 in Supporting Information S1.

3. Results

Images from DTI experiments provide a series of spatial data describing the rock core sample. Due to the application of multiple slices, the data can be presented in three dimensions, as depicted in Figure 3. From the *PD* images, the porosity distribution can be obtained. For the determined porosity, more comprehensive data can be inferred after the calculation of a diffusion tensor. Besides the distribution of the diffusion tensor, other parameters derived from the tensor, such as *MD*, *FA*, as well as the distribution of the main diffusion paths, that is, the privileged diffusion directions of the tested fluid molecules, can be analyzed spatially. Brief descriptions of the parameters obtained, including their petrophysical importance, are presented below.

3.1. *PD*

PD images store information about the amount of fluid containing hydrogen. The intensity of the signal in *PD* images is proportional to this amount within a voxel. Hence, a higher intensity will be associated with regions of

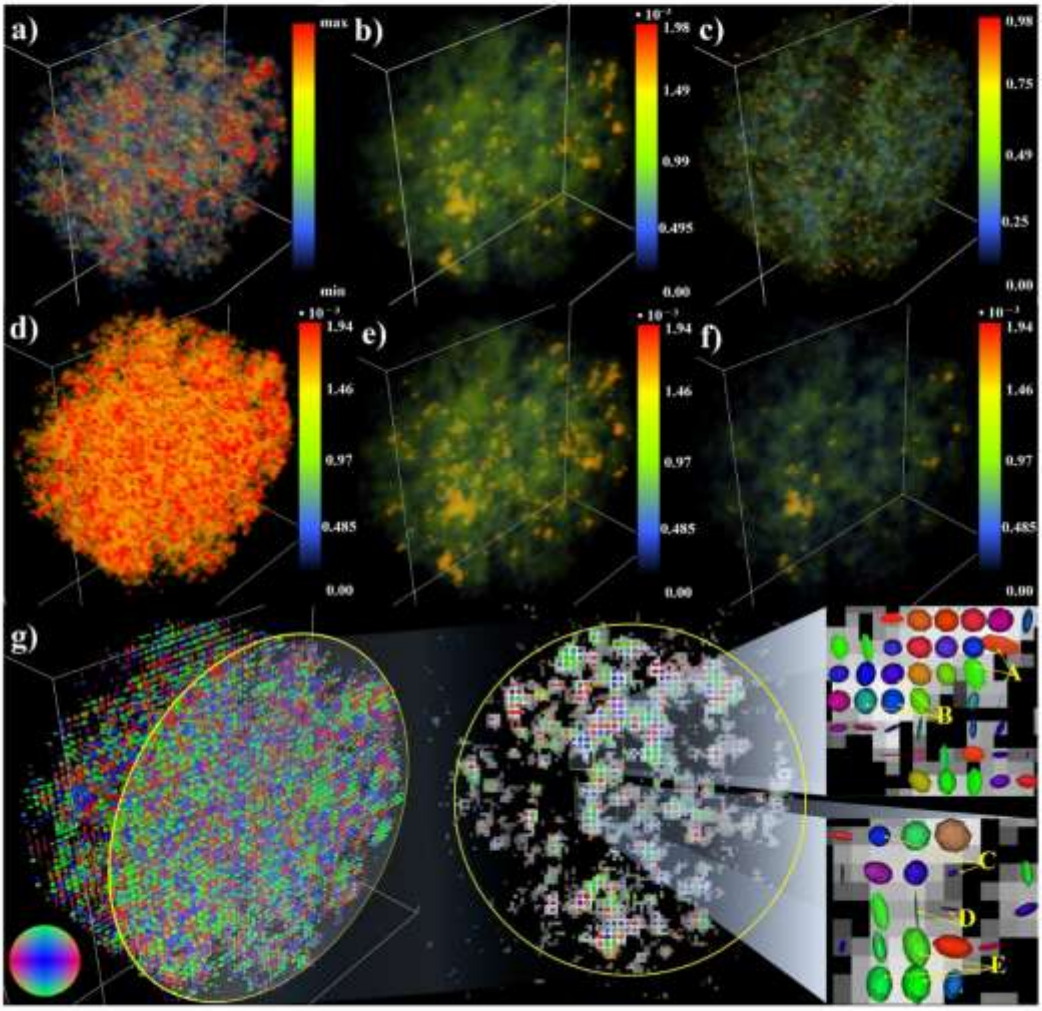

Figure 3. 3D distributions obtained from the diffusion tensor: (a) proton density representing porosity distribution; (b) mean diffusivity; (c) fractional anisotropy; (d) λ_1; (e) λ_2; (f) λ_3; (g) ellipsoidal representation of the diagonalized diffusion tensor, for which one slice was chosen in order to depict various shapes of ellipsoids (yellow letters A, B, C, D and E) that are associated with different diffusive properties within a voxel.

higher porosity – either more voids or larger pore spaces. Therefore, the primary information that can be inferred from DTI is the spatial distribution of porosity in a sample (Figure 3a).

After the elimination of all pixels with intensity equal to the background values, the basic images were generated (Figure 4). 3D (for all slices) porosity distribution in the sample was normalized to the value of $13.90 \pm 0.01\%$ obtained from 1D-T_2 experiment conducted in a low magnetic field (0.05 T; see Section S1, Table S1 and Figure S4 in Supporting Information S1), which is the method of choice for the accurate determination of total porosity (Krzyżak, Habina-Skrzyniarz et al., 2020; Mukhametdinova et al., 2021). The images in Figure 4 additionally depict slice-to-slice porosity distribution, which after normalization to 1D-T_2 can be characterized quantitatively (see Section 4.2) There is only one reservation regarding such normalization, that the contribution to the total

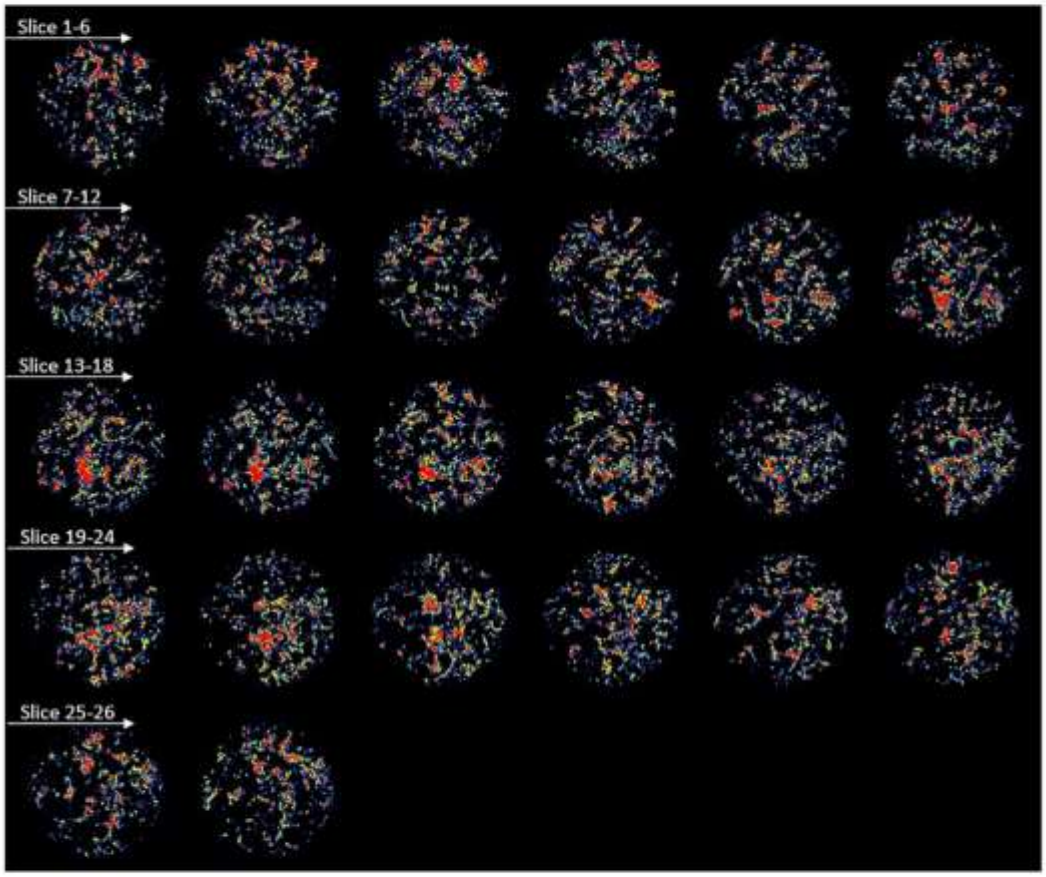

Figure 4. Porosity distribution (i.e., *PD* images) in each imaged 500 μm-thick slice.

porosity of 0.425% is underestimated via DTI due to considerable relaxation mechanisms in proton populations with $T_2 \leq TE$.

In petrophysics, locating porous reservoir regions is of tremendous importance since they may host hydrocarbons. Geological factors controlling the development of a pore network, such as cementation (low *PD* values), dissolution and fracturing (high *PD* values), might be better understood using *PD* data. Based on the *PD*, one can directly infer the degree of pore space connectivity. If some of the isolated pores are also filled with fluids and the pore system has a significant total volume, artificial reservoir fracturing or acid treatment may be accurately designed to increase the permeability.

3.2. *MD*

MD is the average of the three eigenvalues. The obtained distributions of eigenvalues and *MD* are shown in Figures 3d–3f and Figure 3b, respectively. In contrast, for DWI in three orthogonal directions (x, y and z), the *MD* is calculated as a mean of D_x, D_y and D_z and can differ from the *MD* calculated from $\mathbf{\Lambda}$. Since the eigenvalues depend on the size of a void (see Figure 2), individual voxels will be attributed a particular *MD* value reflecting the average size of the included pores. The larger the *MD* value, the greater the expected size of a pore. The

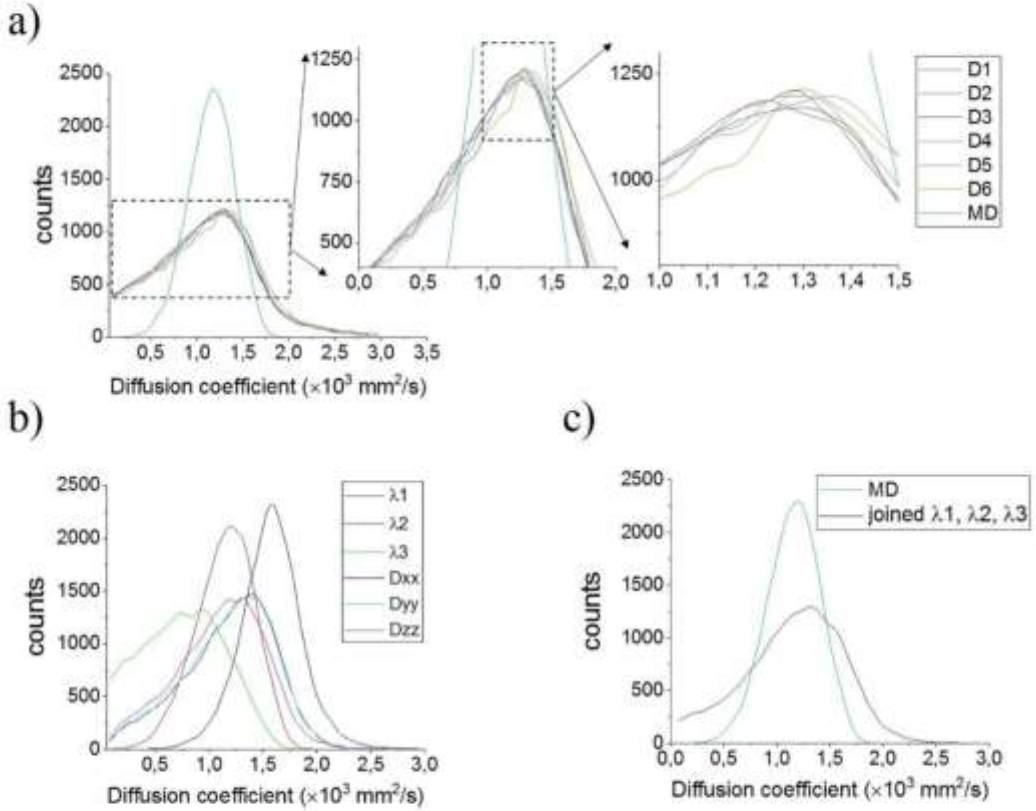

Figure 5. Distributions of diffusion coefficients from diffusion-weighted imaging (DWI) and diffusion tensor imaging (DTI) in the pore space; (a) comparison of D_{app}s from DWI (D1-D6 for each of the six diffusion gradients) with mean diffusivity (*MD*) from DTI; (b) comparison of orthogonal diffusion coefficients in the laboratory frame (D_{xx}, D_{yy} and D_{zz}) with the orthogonal ones in the sample axis frame (λ_1, λ_2 and λ_3); (c) comparison of *MD* with the aggregate distribution of the three eigenvalues (joined λ_1, λ_2, λ_3).

relatively low standard deviation of *MD* for all analyzed voxels may thus indicate low degree of heterogeneity in terms of pore size. In the case of carbonate rocks, the largest pores with high *MD* may correspond to dissolution vugs or similar large voids which have a considerable influence on the storage capacity of a reservoir. The *MD* values may also be helpful in depicting the zones subjected to dolomitization – the process by means of which calcite transforms to dolomite, hence generating additional intercrystalline porosity. Such voids may occur when the pore size is relatively small and unimodal.

Additionally, we would like to draw attention to the authentically quantitative nature of the *MD* distribution, related only to the microstructural characteristics of the tested sample. In the case of D-T_2 or individual DWI pictures, subjective information related to the direction of observation of diffusion changes is always provided. This is well illustrated in Figure 5, where the distributions of the diffusion coefficients obtained in the DTI (*MD*) and single DWI (Di, i = 1–6) experiments are shown.

3.3. *FA*

FA is a coefficient that provides information about the degree of anisotropy. The coefficient is calculated from diffusion tensor eigenvalues (Equation 4) and therefore it is rotationally invariant, meaning it is only associated

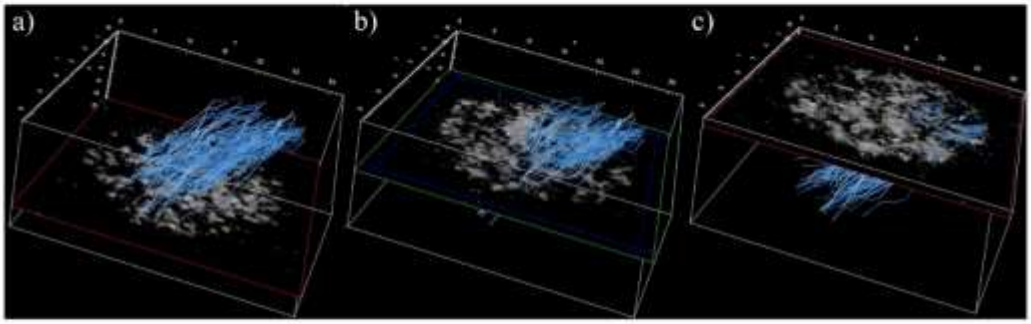

Figure 6. Principal diffusion tract obtained for the sample visualized with the bottom (a), middle (b) and top (c) slice.

with pore geometry and not the orientation of a sample with respect to the laboratory frame. *FA* changes from 0 to 1, corresponding to the isotropic (sphere) and completely anisotropic (line) geometry, respectively. In other words, *FA* reflects the pore shape. Low anisotropy values tend to indicate spherical pores (types B, C, E based on Figure 3g), while higher ones suggest elongated or oblate structures (pore types D, A from Figure 3g, respectively).

$$FA = \sqrt{\frac{3}{2}} \cdot \frac{\sqrt{(\lambda_1 - MD)^2 + (\lambda_2 - MD)^2 + (\lambda_3 - MD)^2}}{\sqrt{\lambda_1^2 + \lambda_2^2 + \lambda_3^2}} \tag{4}$$

where anisotropic diffusion predominates, meaning that the diffusion is restricted in at least one direction, elongated pores such as fractures, dissolution channels or other similar voids can be expected (see Figure S1 in Supporting Information S1). The detection of fractures or similar, elongated or oblate pore space components might be decisive in terms of understanding any increase in permeability. Other applications include the detection of tectonic or karst-related structures. Additionally, the *FA* distribution might enable the estimation of the tortuosity of a pore system, which is the case in calculating the pore size distribution, for example.

3.4. Fiber Tracking (FT)

The last type of tensor visualization that introduces more sophisticated information is tractography. It is chiefly used in medicine (mainly for the visualization of the nervous system), and relies on the first eigenvalue, λ_1, and associated eigenvector, e_1. In this visualization method, in general, diffusion fiber tracts are generated by connecting subsequent voxels that fulfill certain requirements (an angle between eigenvectors in adjacent voxels, minimal tract length, etc.). For biological samples, fiber tracts correspond directly to the microgeometry of tissues. DTI in medicine is conducted for relatively large voxels, reaching the size of approximately $1 \times 1 \times 1$ mm^3. The diffusion tensor in a single voxel (macroscale) usually accurately represents the microgeometry due to the high organizational nature of the tissues within a voxel and among voxels as well as their continuity. It is then possible to think about diffusion fiber tracts in the same manner that one might think of a tissue.

In geological samples, the pores are often smaller and much more heterogeneous, even within a single voxel. Moreover, pores can be open or closed and not necessarily organized, especially in carbonate rocks, where extreme complexity can be expected (Fheed, 2019; Fheed et al., 2018). The size, type and orientation of voids are often stochastically distributed both within a voxel and among voxels (for example see Figures 1 and 2). Therefore, fiber tracking does not just reflect a kind of a network of interconnected pores. In this case, fiber tracts have to be imagined as the highest probability density of diffusion direction in a sample. The interpretation of the tracts through their direction and density (as in the case of medical sciences) is no longer accurate. Thus, it is reasonable to introduce a new term – principal diffusion tracts (*PDTs*). *PDTs* determined for the examined sample are shown in Figure 6. The *PDT* parameter, in conjunction with *FA*, provides information about the anisotropy of the studied pore network. We can interpret it as a new kind of information about the expected directions of the greatest fluid permeability, in addition to the recently developed approaches (Jin et al., 2019; Li et al., 2020).

From a phenomenological point of view, this parameter defines the tracts which may be understood as lines joining two regions in space, characterized by coherent properties of adjacent voxels. In this case, the coherency is related to the fact that each immediately adjacent voxel has to have the same dominative diffusion direction. In petrophysics, this means that such tracts would represent optimal routes of communication among local pore systems. Finding highly connected regions is of primary interest when thinking about the permeability of a reservoir (Daigle & Dugan, 2011). Unfortunately, natural pore systems, and especially those of carbonate rocks, tend to be extremely complex. To put it simply, it can be assumed that some pore spaces in rocks are a superposition of two types: capillary and laminar, with the emphasis on the former. Figures 8b and 8c show corresponding reference phantoms along with the parameters obtained from the DTI experiments. While the determination of the course of the main tracts for capillary systems can be carried out in a similar manner to nerve fibers in medicine, the determination of the main diffusion direction in the case of laminar systems is ambiguous. Therefore, in assessing the correctness and usefulness of the *PDT* course for a given pore system, the shape of the ellipsoids characterizing a given pore system must be taken into account (Figure 8). Nevertheless, fiber tracking enriches any static model, such as proton density distribution, with dynamic information regarding the fluid motion possibilities, thus allowing for better management of reservoir's exploitation. It seems that *PDT* should be most useful for tracking the course of fractures or other elongated pore types (Chan et al., 2014; Clavaud et al., 2008; Isakov et al., 2001; Mêheust & Schmittbuhl, 2001).

3.5. Characterization of the Sample Based on DTI

The studied sample is a bioclastic limestone whose mineralogical composition is dominated by calcite. The sample is shown in Figure S1 in Supporting Information S1. Texturally, it can be defined as a bryozoan-rich packstone or grainstone, cemented with drusy calcite. Porosity in the sample follows clearly marked, sometimes chaotically distributed paths, probably reflecting the dissolution of encrusting foraminifers and other fossils, including a possible contribution of microbialites. The pore system largely consists of amalgamated moulds showing a high degree of communication. The majority of pores are small, commonly less than 0.1 mm in diameter. Single pores approach the size of even 1 mm, but they may be invisible to the NMR equipment if they are isolated and not filled with water.

For the porosity distribution shown in Figure 4, further analysis of the sample properties was conducted. All of the 3D distributions supply complementary information. High values of *PD* indicate a large amount of water, and thus an increase in local porosity (Figures 3a and 4). These regions are represented by a red color and comply with regions having high *MD* values (Figure 3b). As can be noted from the *PD* distribution, the pores are mainly well-connected in the studied case (Figures 3a and 4). This is mainly because the studied plug was taken from a conventional carbonate reservoir, where the distribution of fossils and their alteration had a significant impact on porosity enhancement (Fheed, 2019).

Most of the pores have a *MD* below 1.49×10^{-3} mm^2/s (Figures 3b and 5), but several spots with higher values are also visible. These regions are probably associated with larger voids. No intercrystalline voids (pores accommodated between dolomite crystals due to dolomitization process) were recognized, which is consistent with microscope analyzes. Where larger pores are concerned, it is worth noting that high *MD* does not always correspond with very low *FA* (black to dark blue voxels in Figure 3c). This means that the pores are to some extent anisotropic. Therefore, it is worth comparing eigenvalue distributions for the identification of their expected shape. λ_1 is rather high for all pores (at least as high as λ_2; Figures 3d and 5), and the shape will be dependent on the other two eigenvalues. Voxels that have high λ_2 and λ_3 (yellow to red spots in Figures 3e and 3f) are associated with spherical pores. Regions for which λ_2 is high, but λ_3 is observably smaller correspond to oblate voids. The higher the difference between λ_2 and λ_3, the more the ellipsoid is flattened in one direction. In the sample of interest, the pores have a diversified degree of anisotropy (shapes). A very high *FA* observable in Figure 3c is rather sparse (red spots). Most of the pore spaces have a *FA* around 0.5 (green regions) or lower (blue regions). Mean *FA* for pores is equal to 0.36 (with a mode equal to 0.204), but the standard deviation is comparable to the mean (0.20), suggesting a very heterogeneous pore space in the sample, which is typical for reef carbonates and is in agreement with the characteristics of the studied plug (see Section S3 and Figure S5 in Supporting Information S1 with μCT visualizations).

It is also interesting to examine the distributions of diffusion coefficients shown in Figure 5 obtained for voxels through which the *PDT* pass (Figure S2 in Supporting Information S1). First of all, the mean *FA* for these voxels

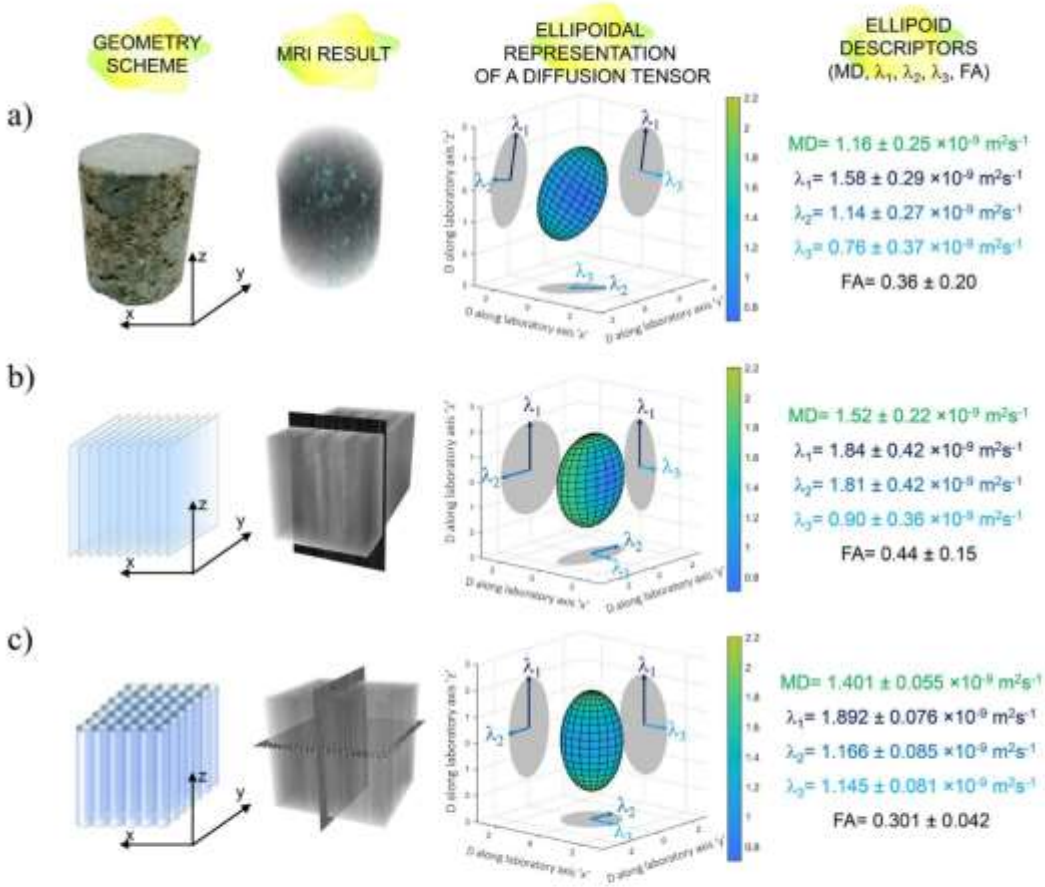

Figure 7. (a) Rock core sample's parameter set (mean diffusivity, *MD*; three eigenvalues, $\lambda_{1,2,3}$; fractional anisotropy, *FA*) corresponding to the descriptors of the average ellipsoid representing the mean tensor for the whole plug. For comparison, sets and ellipsoids are presented for the laminar (b) and capillary (c) anisotropic phantoms with a well-known structure and alignment in a magnet bore, that have pore sizes equal to 20 and 30 μm, respectively.

is higher and equals 0.44 ± 0.21. Moreover, λ_2 and λ_3, unlike λ_1, are shifted toward the left with respect to the distributions from Figure 5. *MD* distribution also has a peak for the lower value, which stems from the decreased λ_2 and λ_3 values. This analysis supports the understanding of the information delivered by *PDT*. As shown quantitatively, *PDT* are developed in regions that have higher *FA* in relation to the whole pore volume and have the highest impact on the determination of the macroscopic anisotropy for the whole sample.

4. Discussion

4.1. Parameter Set From DTI to Evaluate the Pore System

We propose a set of parameters that quantify the pore system (Figure 7). Here we want to indicate the eigenvalues of the diffusion tensor (λ_1, λ_2, λ_3), along with a visual description in the form of an ellipsoid (the third column in Figure 7). In addition, these are the *FA* and *MD* parameters that describe the system anisotropy, as well as the quantitatively averaged diffusion value for the pore system. The *PDT* will be especially useful for the analysis of capillary pore spaces.

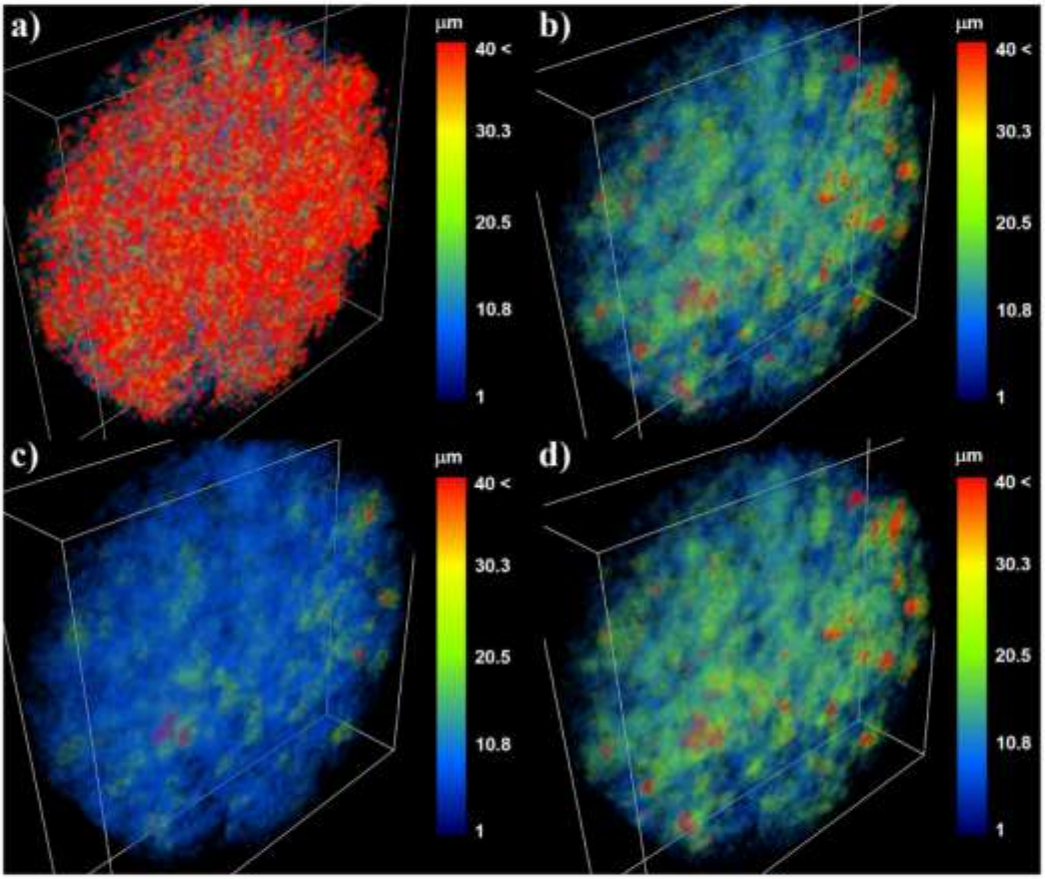

Figure 8. Three-dimensional pore size distribution obtained from diffusion tensor imaging parameters: λ_1 (a), λ_2 (b), λ_3 (c), *MD* (d).

In order to better visualize the meaning of these parameters, we show their values for two standard phantoms representing the capillary and laminar pore system, respectively (Figures 7b and 7c). It should be emphasized that the approach, apart from additional parameters such as *FA* and *PDT*, includes diffusion coefficients, now in a truly quantitative version. Thus, this workflow allows typical geophysical parameters to be determined using diffusion coefficients: PSD, pore geometry, permeability, wettability, fluid structure, etc (Maerki et al., 2004; Mitra et al., 1992; Mutina & Hürlimann, 2008; Watanabe et al., 2020; Zhang et al., 2020), with much greater precision and regardless of the location of the sample in the laboratory frame. The challenge is to use the workflow for nanopore rocks such as shales (Krzyżak, Mazur, et al., 2020; Saif et al., 2017). This issue is described in more detail in the following paragraphs.

4.2. Geophysical Quantities Derived From DTI

The potential examples of practical applications of the data obtained from the DTI experiment are demonstrated below. There are more potential applications related to spheres where geophysicists or petrophysicists explore diffusion to determine various parameters and features of rock cores. Importantly, thanks to the use of DTI, we can now provide spatial and quantitative data which is closely related to the microstructure under study.

4.2.1. Porosity Distribution

In Section 3.1, the porosity distribution in each slice was shown and the quantitative analysis of the porosity can be realized by normalization to the very accurate porosity value obtained by T_2 NMR equal to 13.90% (Table S1 in Supporting Information S1). By DTI it is possible to analyze porosity locally, qualitatively, but also quantitatively. We presented slice-to-slice porosity distribution, for which the contributions to the total porosity are shown in Table S2 in Supporting Information S1, but technically it can be done in any direction through the sample.

4.2.2. PSD

In contrast to bulk volumes, in which diffusion is free, diffusion in porous systems is restricted by the pore boundaries. This is observed by the reduction of diffusion coefficient from its bulk/free value, D_0 (m^2/s), depending on the diffusion time, t_d (s). However, the character of changes of a diffusion coefficient varies according to the diffusion regime or, in other words, time limit. In the short-time limit, only a few molecules which are near the pore surface experience restriction from the pore walls, which is not enough for the diffusion coefficient to rapidly decrease (free diffusion regime). This corresponds to the condition $d^2 \ll D_0 t_d$, where d (m) is a pore length. In this regime, diffusion is almost independent of the microgeometry, while the time-dependence of the diffusion coefficient, $D(t_d)$, follows Mitra's relation according to (Equation 5; Mitra et al., 1992). Increasing t_d results in $d^2 \approx D_0 t_d$ and a higher number of water molecules to contact pore walls and consequently a larger decrease in the diffusion coefficient (intermediate time-limit or restricted diffusion regime). Then, the $D(t_d)$ dependence follows the Einstein-Smoluchowski equation (Equation 6; Islam, 2004), for which the slope is proportional to the pore size. For very long t_ds (long-time limit), $t_d \to \infty$, $d^2 \gg D_0 t_d$, which means that all molecules traveled the pore several times and further t_d increase does not influence the value of D. This is called the hindered diffusion regime, in which diffusion coefficient approaches the constant value D_∞. There is no consensus on the D_∞ formula, but several equations have been proposed for different models of a porous system, such as periodic array of parallel, permeable barriers and solution of reflecting spheres as described by (Equation 7; Latour et al., 1994) and (Equation 8; De Swiet & Sen, 1996), respectively. In our case, we used (Equation 7) for a single pore as an individual compartment and (Equation 8) for the sample as a macroscopic porous system.

$$D(t_d) = D_0 - \frac{4}{3W\sqrt{\pi}} \cdot \left(\frac{S}{V}\right)_{pore} \cdot D_0^{\frac{3}{2}} \cdot \sqrt{t_d} \tag{5}$$

where W is the number of space dimensions in which diffusion occurs, D_0 (m^2/s) is the bulk self-diffusion coefficient for $t_d \to 0$, and $(S/V)_{pore}$(m^{-1}) is the Surface-area-to-Volume ratio of a pore.

$$D(t_d) = \frac{<z^2>}{2W t_d} \tag{6}$$

where $<z^2>$ (m) is a root-mean-square displacement of water molecules during t_d, and $<z^2> \sim d^2$.

$$\frac{1}{D_\infty} \to \frac{1}{D_0} + \frac{1}{Pd} \tag{7}$$

where P (m/s) is permeability and d (m) is pore diameter.

$$\frac{D(t_d)}{D_0} \to \alpha + \frac{\beta}{t_d} + \frac{\gamma}{t_d^{\frac{3}{2}}} + \ldots \tag{8}$$

where α, β, γ are assumed to depend on the microgeometry of pores. They cannot be predicted, but some authors, for example, de Swiet and Sen, found their relation to the pore characteristics, where $\alpha = (1-f^{1/2})$, $\beta = (f(d/2)^2/4D_0)$, $\gamma = (f/4\sqrt{\pi})((d/2)^2/D_0)^{3/2}$, while f is a volume fraction of reflecting phase (solid phase).

In order to determine pore size from experimental $D(t_d)$, it would be necessary to identify the diffusion regime by estimating $\xi = D_0 t_d / d^2$. $\xi \gg 1$ indicates that the measurement was conducted in a short-time limit, while in an intermediate- and long-time limit when $\xi \approx 1$ and $\xi \gg 1$, respectively. Since the pore diameter, d, is unknown, we simulated ξ for a wide range of d and then $D(t_d)$ for the time conditions applied in the DTI experiment. Simulations delivered $D(t_d)$s for each diffusion regime boundaries. By comparing the experimental $D(t_d)$ with the simulated ones, it was possible to identify a regime and determine average pore size in each voxel from the appropriate

formula (Equations 5–7). The 3D PSD is shown in Figure 8, while 1D PSDs for the whole volume and each slice are presented in Figure S3 in Supporting Information S1.

4.2.3. Tortuosity

Tortuosity in geoscience is a term reflecting the complexity of a porous system and determines the fluid flow paths. Thus, it is one of the fundamental quantities describing a rock core sample's void architecture and is very useful for the determination of other geophysical parameters, such as conductivity. There are many methods for determining tortuosity, while no consensus has been established for the best choice of model or methodology for either analytical or empirical approaches. Therefore, obtaining information on tortuosity remains challenging. One way, is to use the diffusion data to calculate diffusive tortuosity, τ_d:

$$\tau_d = \frac{D_0}{D_\infty} \tag{9}$$

where D_0 (m^2/s) is free diffusion coefficient and D_∞ (m^2/s) is long-time diffusion coefficient for the whole pore system, that is, the whole sample.

Based on PSD obtained from DTI, the mean pore diameter, d_{mean}, was determined. Knowing that long-time diffusion limit starts to apply when $\xi \gg 1$, assuming $\xi = 10$ diffusion time, $t_d = \xi \cdot d_{mean}^2 / D_0$, was calculated for which D_∞ for the sample was simulated using (Equation 8) and assuming $D_0 = 2 \cdot 10^{-9}$ m^2/s. The obtained $d_{mean} = 9.9$ μm and $t_d \approx 500$ ms delivered $D_\infty \approx 1.17 \cdot 10^{-9}$ m^2/s, which was consistent with $D(t_d = 500$ ms) from a referential, independent PGSE measurement of the sample, that yielded $D_\infty = 1.13 \cdot 10^{-9}$ m^2/s. All parameters delivered diffusive tortuosity of $\tau_d = 1.71$. This value is within the range of 1.46–2.33 estimated by using different models adopting porosity (Allen & Sun, 2017).

4.2.4. Electrical Conductivity Tensor

The physical relationship of the conductivity tensor C with the water diffusion tensor D is based on the assumption of the existence of the same eigenvectors (Sen & Torquato, 1989). This leads to a linear relationship between the diffusion and conductivity tensors $C = \eta \cdot D$ (Tuch et al., 2001). Several methods for calculating the η coefficient have been proposed, primarily for biomedical purposes related to brain research (Katoch et al., 2021). The optimal solution in the first approach is the Force Equilibrium Model (FEM) where, from the equilibrium condition between electric and viscous forces and from the Stokes-Einstein equation showing the relationship between the viscosity and the diffusion coefficient, it can be shown (Katoch et al., 2021) that the proportionality coefficient $\eta = 0.76q^2N/k_BT$, where k_B (J/K) is Boltzmann's constant, T(K) is the absolute temperature, $q = 1.6 \cdot 10^{-19}$ C is elementary electric charge, and $N = 2 \cdot 10^{25}$ m^{-3}. Thus, the distributions of the diffusion tensor D and the parameters based on it presented in Figure 3 correspond directly, after scaling, to the conductivity tensor C. Notably, the tensors provide spatial and quantitative information solely dependent on the pore microstructure.

4.2.5. The Application of the Set of Tensor's Parameters

The new parameter set of the diffusion tensor D to characterize the rock core proposed in paragraph 4.1, takes on a new meaning. The values of MD, (λ_1, λ_2, λ_3) and FA now correspond to the mean value of the conductivity tensor C, its eigenvalues and the anisotropy coefficient, equal to: 0.111 S/m, 0.152 S/m, 0.109 S/m, 0.073 S/m and 0.36, respectively. These values were obtained using the FEM model. The described procedure for determining the main tracts of the diffusion tensor (paragraph 3.4) is also gaining new significance. These tracks also connect the voxels with the highest electrical conductivity of a water-saturated rock core.

4.3. DTI Data Comparison Possibilities

It is possible to compare DTI data with the results from supplementary methods, for instance the low-field NMR relaxation measurements (see Figure S4 in Supporting Information S1). Low-field NMR is currently the first selection technique for the precise determination of PSD distribution, regardless of the dominant pore size and type in the sample (Kleinberg & Horsfield, 1990). PSD is an important addition to the PD raw data, while not showing quantitatively resolved pore sizes. Bearing in mind that low-field NMR relaxometry is the optimal solution for the determination of PSD and is an unattainable benchmark for MRI-based imaging techniques, we

focused exclusively on the latter in order to verify and identify their strengths. For this purpose, we have put together a wealth of DTI capabilities (including *PD* and DWI images, diffusion tensor components maps, and corresponding parameters such as *FA* or *MD*) with the naturally complementary imaging modality – μCT. In Section S3 in Supporting Information S1, the DTI results are compared to the results obtained from μCT, yielding additional information regarding the analyzed pore network.

4.4. Existing Restrictions for MRI in Rock Cores

Carbonates are a special case in terms of the rock types which are suitable for DTI examination. The main limitations of the wider application of MRI for the study of other rock types are related to the significant reduction of T_2 time for fluids in the pore spaces due to the presence of large magnetic field gradients (Hürlimann, 1998). In addition, strong effects of type II scalar relaxation can be observed, where the decisive role is played by the extremely short relaxation time of the spin of the electron shell of ferro- or paramagnetic dopants (Kleinberg & Horsfield, 1990). These phenomena make it practically impossible to image a significant part of the rock population. In practice, the NMR signal, due to T_2 relaxation, decays earlier than when the MRI sequence becomes recordable or the image is distorted due to strong, induced local magnetic field gradients, rendering it unsuitable for analysis. We experienced this for most tight rocks (shales, sandstones), although MRI is successful with some of them (Węglarz et al., 2016, 2018). For carbonate rocks, on the other hand, which constitute about half of the reservoirs which are important from the petrophysical (hydrocarbon exploitation) or geothermal point of view (Montanari et al., 2017), this problem is much less important due to the relatively lower doping and similar magnetic susceptibility of carbonates and water (Fheed et al., 2018). This is confirmed by the very good agreement between the porosity values obtained from DTI and μCT in this study. In our case, we performed a full DTI imaging of the rock core sample for the first time, as a continuation of the previously initiated research on DWI applications (Fheed et al., 2020; Matenoglou et al., 2016). The emerging interest in DWI in geoscience-related literature is an promising sign for DTI, as DTI is nothing more than the simultaneous analysis of data from several (minimum 7) DWI images recorded for different directions of the diffusion gradient vector. Therefore, in the case of the mentioned publications (Matenoglou et al., 2016), DTI could also be used. Of course, the problems with the destructive influence of local gradients on the image are not entirely eliminated. It is also true that there is a paper showing the potential for imaging in a curvilinear space (i.e., one in which the gradient distribution is constant), however, this application requires further theoretical work and experimental verification (Borkowski & Krzyżak, 2018). Currently, in order to perform MRI on rock cores, we have to limit ourselves to the existing technical solutions, which unfortunately significantly confine the applicability of DTI to a limited range of rocks, as well as prevent quantitative and comparative analyzes. Formerly, the result depended more on the type of doping with paramagnetic and ferromagnetic minerals and on induced gradients than on pore distribution (Weiger & Pruessmann, 2019; Węglarz et al., 2016, 2018). This type of imaging is therefore more illustrative than quantitative, but carbonate rocks are an exception here.

The core sample studied comes from a conventional carbonate reservoir where the rocks are characterized by the prevalent part of the T_2 distribution above 10 ms and have a similar magnetic susceptibility to water (−13 ppm and −9 ppm for calcite and water, respectively), which prevents the induction of large magnetic field gradients, and therefore this type of lithology was chosen for diffusion tensor imaging. In this work, the DTI of the carbonate rock core sample was successfully conducted despite the high magnetic field induction (9.4 T), to which induced gradients are directly proportional. This conclusion, which justified further work with the acquired data, was based on several factors including: (a) the acceptable signal level based on the preliminary results obtained for the lower resolution (pores having sizes large enough for the diffusion measurements without the total vanishing of the signal due to transverse, namely surface, relaxation); (b) a satisfactory level of signal for the high-resolution images; and (c) no recognized deformations (that might result from the broad baseline or resonance line-shape distortions due to short *TE*). Moreover, the MR-derived porosity was in a very good agreement with the value obtained from μCT.

4.5. Perspectives

This study is based on experiments conducted in a high magnetic field (9.4 T), which may cause the generation of large internal magnetic field gradients in the sample. However, the applied system is currently the one of choice for rocks, because it affords the opportunity to obtain a very short TE in MRI and a high SNR. In addition, based

on the μCT results (Figure S5 in Supporting Information S1), it could also be seen that the sample contains a considerable number of voids with submilimeter sizes, for which induced gradients are diminished. One should be aware that in the very small pores in the sample, a significant part of the signal can be lost, but taking into account the current technical possibilities in MRI, and particularly DWI or DTI, this barrier is currently insurmountable.

At present, the simplest development path in this area seems to be the use of the existing imaging sequences in magnetic fields of 0.1–0.2 T (~10–20 MHz for ^{1}H), which will allow the use of very short TE echo times. Natural candidates here are the SPI or SPRITE (Adair et al., 2021) sequences, or the relatively new ZTE (Weiger & Pruessmann, 2019; Weglarz et al., 2016, 2018), which currently do not have a diffusion-weighted versions. Therefore, traditional SE or STE sequences with the use of strong gradient amplifiers might be an option (Cotts et al., 1989). However, the technological limitations here are considerable, since an increase of the rate of the gradients' rise causes the induction of strong eddy currents, which strongly distort the image (Chan et al., 2014). As a consequence, we have to use longer rise times, and therefore increase the echo time. Thus, the problem of short T_2 times limits the number of practical, petrophysical applications.

To summarize, the currently available technical solutions enable DTI imaging primarily for weakly doped rocks, characterized by the presence of relatively large pores, often met in the case of carbonate rocks. Extending the application of DTI to a wider range of rock cores (sandstones, shales, etc.) requires technological development. It seems possible in the light of theoretical works (Borkowski & Krzyzak, 2018) and the current state of the art, sequences of the SPI (Adair et al., 2021) and ZTE (Pheed et al., 2018; Weiger & Pruessmann, 2019; Weglarz et al., 2016, 2018) types. However, it requires further theoretical and experimental efforts. Advances in the field of widening the applications of DTI will be associated with the involvement of the geoscientific community and finding the answer to the question of whether, for example, the distributions of anisotropy based on the diffusion tensor proposed by DTI will be of a sufficient importance from the perspective of petrophysical research and related, industrial applications.

5. Conclusions

The imaging of the diffusion tensor of ^{1}H-containing fluids is currently possible primarily for carbonate rock cores, lightly doped with paramagnetic and ferromagnetic minerals, and with relatively large pore spaces. In classic D-T_2 or DWI experiments, the distribution of the projection of the diffusion tensor on a given axis is observed in practice. The projection is defined by the direction of the magnetic field gradient vector used in a given MR sequence. The obtained result for an anisotropic sample is equivocal. By changing the direction of the gradient, or rotating the sample in a MR scanner, different distributions of diffusion coefficients (D_{app}) are obtained. The solution is to introduce a full diffusion tensor and analyze the parameters based on its components, such as *FA* or *MD*, which are dependent only on the microstructure of a sample. After moving to the principal axis system, the problem of the ambiguity of results based on the diffusion phenomenon disappears. In this case, spatial distributions of the anisotropy of the system (*FA*), the mean value of the diffusion tensor (*MD*), or the main diffusion tracts (*PDT*), can now be analyzed in an unambiguous manner, which is a significant step toward the more detailed characterization of reservoir rocks, and carbonates in particular.

The proposed term of *PDT* is an analogy to the existing fiber tracking technique known from biomedical research, especially regarding the visualization of neural tracts in brain. In the case of rock cores, it is reasonable to refer to the spatial distribution of *PDT*, meaning that for each voxel the direction of the greatest probability of a fluid diffusion in the tested object can be determined. If we add the *MD* and *FA* values to this, which provide us with information about the total value of diffusion and the degree of anisotropy of a given area (voxel, or distribution for the entire sample), as well as the recorded *PD* images showing the spatial distribution of porosity, a very valuable set of quantitative data describing the local pore microstructure appears. The whole set can also be distributed for the entire rock core sample, while the distributions will reflect the average properties of a corresponding pore system.

Importantly, it seems that μCT and DTI data can be successfully combined to enhance insights into the interior of a sample. The quantitative data derived from DTI appears to have many geological applications. These include deciphering the distribution of fissures, assessing the geometry of pores, or drawing preliminary conclusions on the potential permeability of reservoir rocks. Generally, such parameters are crucial for the precise determination and exploitation of energy resources related to crude oil, natural gas and geothermal water. The use of sandstone

or shale rock cores and samples with pore distributions of nanometric diameters for analogous research, however, requires further technological progress in the field of MRI.

Conflict of Interest

The authors declare no conflicts of interest relevant to this study.

Data Availability Statement

The DTI data used for characterization of the sample based on diffusion properties in the study are available at Mendeley Data repository via https://doi.org/10.17632/sg488k8jrt.1 with CC BY 4.0 license.

Acknowledgments
The research was mainly financed by the Polish Ministry of Science and Higher Education (AGH-UST statutory funds no. 16.16.140.315/05). Diffusion tensor analysis was financially supported by the National Centre for Research and Development (contract no. STRATEGMED2/265761/10/NCBR/2015). WM has been partly supported by the EU Project POWR.03.02.00-00-I004/16. AF was also financially supported by the Polish National Science Centre (Grant No. UMO-2016/23/N/ST10/00350). We thank Hani Salman Al Mukainah from King Fahd University of Petroleum and Minerals and other KFUPM faculty members for providing access to μCT hardware and software. The authors are also grateful to Krzysztof Jaśkiński for conducting the experiments.

References

Adair, A., Richard, S., & Newling, B. (2021). Gas and liquid phase imaging of foam flow using pure phase encode magnetic resonance imaging. *Molecules*, *26*(1), 28. https://doi.org/10.3390/molecules26010028

Ale, W. M., Allen, D., Boyd, A., Bachman, H. N., Smithson, T., Clerke, E. A., et al. (2005). Confronting the carbonate conundrum. *Oilfield Review*, *17*(1), 18–29.

Ajayi, T., Gomes, J. S., & Bera, A. (2019). A review of CO2 storage in geological formations emphasizing modeling, monitoring and capacity estimation approaches. *Petroleum Science*, *16*(5), 1028–1063. https://doi.org/10.1007/s12182-019-0340-8

Alexander, D. C. (2006). An introduction to computational diffusion mri: The diffusion tensor and beyond. In J. Weickert, & H. Hagen (Eds.), *Visualization and processing of tensor fields. Mathematics and visualization* (pp. 83–106). Springer. https://doi.org/10.1007/3-540-31272-2_5

Allen, R., & Sun, S. (2017). Computing and comparing effective properties for flow and transport in computer-generated porous media. *Geofluids*, *2*, 1–24. https://doi.org/10.1155/2017/4517259

Arif, M., Lebedev, M., Barifcani, A., & Iglauer, S. (2017). CO2 storage in carbonates: Wettability of calcite. *International Journal of Greenhouse Gas Control*, *62*, 113–121. https://doi.org/10.1016/j.ijggc.2017.04.014

Borkowski, K., & Krzyżak, A. T. (2018). The generalized Stejskal-Tanner equation for non-uniform magnetic field gradients. *Journal of Magnetic Resonance*, *296*, 23–28. https://doi.org/10.1016/j.jmr.2018.08.010

Chen, R. W., von Deuster, C., Giese, D., Stoeck, C. T., Harmer, J., Aitken, A. P., et al. (2014). Characterization and correction of eddy-current artifacts in unipolar and bipolar diffusion sequences using magnetic field monitoring. *Journal of Magnetic Resonance*, *244*, 74–84. https://doi.org/10.1016/j.jmr.2014.04.018

Clavaud, J.-B., Maineult, A., Zamora, M., Rasolofosaon, P., & Schlitter, C. (2008). Permeability anisotropy and its relations with porous medium structure. *Journal of Geophysical Research*, *113*, B01202. https://doi.org/10.1029/2007JB005004

Coates, G. R., Xiao, L., & Prammer, M. G. (1999). *NMR logging: Principles and applications*. Halliburton Energy Services.

Cotts, R. M., Hoch, M. J. R., Sun, T., & Markert, J. T. (1989). Pulsed field gradient stimulated echo methods for improved NMR diffusion measurements in heterogeneous systems. *Journal of Magnetic Resonance*, *83*(2), 252–266. https://doi.org/10.1016/0022-2364(89)90189-3

Daigle, H., & Dugan, B. (2011). An improved technique for computing permeability from NMR measurements in mudstones. *Journal of Geophysical Research*, *116*, B08101. https://doi.org/10.1029/2011JB008355

Dale, B. M., Brown, M. A., & Semelka, R. C. (2015). *MRI: Basic principles and applications*. Wiley-Blackwell. (5th ed.).

Delgado, J. M. P. Q. (2006). A simple experimental technique to measure tortuosity in packed beds. *Canadian Journal of Chemical Engineering*, *84*(6), 651–655. https://doi.org/10.1002/cjce.5450840603

De Swiet, T. M., & Sen, P. N. (1996). Time dependent diffusion coefficient in a disordered medium. The *Journal of Chemical Physics*, *104*(1), 206–209. https://doi.org/10.1063/1.470890

Fheed, A. (2019). The impact of fossils on diagenetically controlled reservoir quality: The Zechstein Brońsko Reef (Upper Permian, W Poland). *Annales Societatis Geologorum Poloniae*, *89*(1), 47–81. https://doi.org/10.14241/asgp.2019.07

Fheed, A., Kłodowski, K., & Krzyżak, A. (2020). Fracture orientation and fluid flow direction recognition in carbonates using diffusion-weighted nuclear magnetic resonance imaging: An example from Permian. *Journal of Applied Geophysics*, *174*, 103964. https://doi.org/10.1016/j.jappgeo.2020.103964

Fheed, A., Krzyżak, A., & Świerczewska, A. (2018). Exploring a carbonate reef reservoir – Nuclear magnetic resonance and computed microtomography confronted with narrow channel and fracture porosity. *Journal of Applied Geophysics*, *151*, 343–358. https://doi.org/10.1016/j.jappgeo.2018.03.004

Fheed, A., Świerczewska, A., Strzelecki, P. J., Radzik-Hotlos, N., & Gebus-Czupyt, B. (2022). Influence of substrate morphology on reef diagenesis: Examples from the Zechstein Limestone formation (SE Wolsztyn Ridge, W Poland). *Marine and Petroleum Geology*, *136*, 105442. https://doi.org/10.1016/j.marpetgeo.2021.105442

Flügel, E. (2004). *Microfacies of carbonate rocks. Analysis, interpretation and application*. Springer-Verlag. https://doi.org/10.1007/978-3-662-08726-8

Hürlimann, M. D. (1998). Effective gradients in porous media due to susceptibility differences. *Journal of Magnetic Resonance*, *131*(2), 232–240. https://doi.org/10.1006/jmre.1998.1364

Hürlimann, M. D., & Venkataramanan, L. (2002). Quantitative measurement of two-dimensional distribution functions of diffusion and relaxation in grossly inhomogeneous fields. *Journal of Magnetic Resonance*, *157*(1), 31–42. https://doi.org/10.1006/jmre.2002.2567

Isakov, E., Ogilvie, S. R., Taylor, C. W., & Glover, P. W. J. (2001). Fluid flow through rough fractures in rocks I: High resolution aperture determinations. *Earth and Planetary Science Letters*, *191*(3), 267–282. https://doi.org/10.1016/S0012-821X(01)00424-1

Islam, M. A. (2004). Einstein-Smoluchowski diffusion equation: A discussion. *Physica Scripta*, *70*(2–3), 120–125. https://doi.org/10.1088/0031-8949/70/2-3/008

Jin, G., Xie, R., Liu, M., Guo, J., & Gao, L. (2019). A new method for permeability estimation using integral transforms based on NMR echo data in tight sandstone. *Journal of Petroleum Science and Engineering*, *180*, 424–434. https://doi.org/10.1016/j.petrol.2019.05.056

Katoch, N., Choi, B.-K., Park, J.-A., Ko, I.-O., & Kim, H.-J. (2021). Comparison of five conductivity tensor models and image reconstruction methods using MRI. *Molecules*, *26*(18), 5499. https://doi.org/10.3390/molecules26185499

Kingsley, P. B. (2006). Introduction to diffusion tensor imaging mathematics : Part II. Anisotropy , diffusion-weighting factors , and gradient encoding schemes. *Concepts in Magnetic Resonance*, *28A*(2), 123–154. https://doi.org/10.1002/cmr.a

Kleinberg, R. L., & Horsfield, M. A. (1990). Transverse relaxation processes in porous sedimentary rock. *Journal of Magnetic Resonance*, *88*(1), 9–19. https://doi.org/10.1016/0022-2364(90)90104-h

Klodowski, K., & Krzyżak, A. T. (2016). Innovative anisotropic phantoms for calibration of diffusion tensor imaging sequences. *Magnetic Resonance Imaging*, *34*(4), 404–409. https://doi.org/10.1016/j.mri.2015.12.010

Krzyżak, A. T., & Habina, I. (2016). Low field 1H NMR characterization of mesoporous silica MCM-41 and SBA-15 filled with different amount of water. *Microporous and Mesoporous Materials*, *231*, 230–239. https://doi.org/10.1016/j.micromeso.2016.05.032

Krzyżak, A. T., Habina-Skrzyniarz, I., Maschowski, G., & Mazur, W. (2020). Overcoming the barriers to the exploration of nanoporous shales porosity. *Microporous and Mesoporous Materials*, *298*, 110069. https://doi.org/10.1016/j.micromeso.2020.110069

Krzyżak, A. T., Mazur, W., Matyszkiewicz, J., & Kochman, A. (2020). Identification of proton populations in cherts as natural analogues of pure silica materials by means of low field NMR. *Journal of Physical Chemistry C*, *124*(9), 5225–5240. https://doi.org/10.1021/acs.jpcc.9b11790

Lang, P. S., Paluszny, A., & Zimmerman, R. W. (2014). Permeability tensor of three-dimensional fractured porous rock and a comparison to trace map predictions. *Journal of Geophysical Research*, *119*(8), 6288–6307. https://doi.org/10.1002/2014JB011027.Received

Latour, L. L., Svoboda, K., Mitra, P. P., & Sotak, C. H. (1994). Time-dependent diffusion of water in a biological model system. *Proceedings of the National Academy of Sciences of the United States of America*, *91*(4), 1229–1233. https://doi.org/10.1073/pnas.91.4.1229

Li, J. X., Rezaee, R., Miller, T. M., & Sarmadivaleh, M. (2020). Pore size distribution controls dynamic permeability. *Geophysical Research Letters*, *47*(5), e2020GL090558. https://doi.org/10.1029/2020GL090558

Luo, Z. X., Paulsen, J., Venkatasubramanian, M., & Song, Y. Q. (2015). Restricted diffusion effects on nuclear magnetic resonance DT2 maps. *Geophysics*, *80*(2), E41–E47. https://doi.org/10.1190/GEO2014-0206.1

Maerki, M., Wehrli, B., Dinkel, C., & Müller, B. (2004). The influence of tortuosity on molecular diffusion in freshwater sediments of high porosity. *Geochimica et Cosmochimica Acta*, *68*(7), 1519–1528. https://doi.org/10.1016/j.gca.2003.09.019

Materoglou, G., Kelessidis, V. C., Garcia, A. P., Heidari, Z., Fardis, M., Karayanni, M., & Maris, T. G. (2016). Evaluation of wettability and the petrophysical properties of carbonate reservoirs by advanced NMR and MRI techniques. In *Abu Dhabi International Petroleum Exhibition and Conference* (pp. 7–10). United Arab Emirates. (SPE-183531-MS).

Mazur, W., Krzyżak, A. T., & Ruszewski, Z. (2019). Towards the precise microstructural mapping. Testing new anisotropic phantoms with layered and capillary geometries. *41st Annual International Conference of the IEEE Engineering in Medicine and Biology Society (EMBC)*, 2835–2839. https://doi.org/10.1109/EMBC.2019.8857065

Méheust, Y., & Schmittbuhl, J. (2001). Geometrical heterogeneities and permeability anisotropy of rough fractures. *Journal of Geophysical Research: Solid Earth*, *106*(B2), 2089–2102. https://doi.org/10.1029/2000JB900306

Mitchell, J., Howe, A. M., & Clarke, A. (2015). Real-time oil-saturation monitoring in rock cores with low-field NMR. *Journal of Magnetic Resonance*, *256*, 34–42. https://doi.org/10.1016/j.jmr.2015.04.011

Mitra, P. P., Sen, M. P. N., Schwartz, L. M., & Doussal, P. L. (1992). Diffusion propagator as a probe of the structure of porous media. *Physical Review Letters*, *68*(24), 3555–3558. https://doi.org/10.1103/physrevlett.68.3555

Montanari, D., Minissale, A., Doveri, M., Gola, G., Trumpy, E., Santilano, A., & Manzella, A. (2017). Geothermal resources within carbonate reservoirs in western Sicily (Italy): A review. *Earth-Science Reviews*, *169*, 180–201. https://doi.org/10.1016/j.earscirev.2017.04.016

Mori, S., Crain, B. J., Chacko, V. P., & van Zijl, P. C. (1999). Three-dimensional tracking of axonal projections in the brain by magnetic resonance imaging. *Annals of Neurology*, *45*(2), 265–269. https://doi.org/10.1002/1531-8249(199902)45:2<265::aid-ana21>3.0.co

Mukhametdinova, A., Habina-Skrzyniarz, I., Kazak, A., & Krzyżak, A. T. (2021). NMR relaxometry interpretation of source rock liquid saturation - a holistic approach. *Marine and Petroleum Geology*, *132*, 105165. https://doi.org/10.1016/j.marpetgeo.2021.105165

Mutina, A. R., & Hürlimann, M. D. (2008). Correlation of transverse and rotational diffusion coefficient: A probe of chemical composition in hydrocarbon oils. *The Journal of Physical Chemistry A*, *112*(15), 3291–3301. https://doi.org/10.1021/jp710254d

Peryt, T. M., Raczyński, P., Peryt, D., & Chłódek, K. (2012). Upper Permian reef complex in the basinal facies of the Zechstein Limestone (Ca1), western Poland. *Geological Journal*, *47*(5), 537–552. https://doi.org/10.1002/gj.2440

Pomerantz, A. E., Sigmund, E. E., & Song, Y.-Q. (2007). Characterization of carbonate rock by MRI relaxometry. *Magnetic Resonance Imaging*, *25*(4), 580. https://doi.org/10.1016/j.mri.2007.01.091

Porion, P., Ferrage, E., Hubert, F., Tertre, E., Dubot, T., Faugère, A. M., et al. (2018). Water mobility within compacted clay samples: Multi-scale Analysis exploiting 1H NMR pulsed gradient spin echo and magnetic resonance imaging of water density profiles. *American Chemical Society (ACS) Omega*, *3*(7), 7399–7406. https://doi.org/10.1021/acsomega.8b01083

Raczyński, P., Peryt, T. M., & Strobel, W. (2017). Sedimentary and environmental history of the Late Permian Bonikowo reef (Zechstein limestone, Wuchiapingian), western Poland. *Journal of Palaeogeography*, *6*(3), 183–205. https://doi.org/10.1016/j.jop.2017.05.001

Raza, A., Gholami, R., Rezaee, R., Han Bing, C., Nagarajan, R., & Ali Hamid, M. (2017). Preliminary assessments of CO2 storage in carbonate formations: A case study from Malaysia. *Journal of Geophysics and Engineering*, *14*(3), 533–554. https://doi.org/10.1088/1742-2140/aa5e71

Saif, T., Lin, Q., Butcher, A. R., Bijeljic, B., & Blunt, M. J. (2017). Multi-scale multi-dimensional microstructure imaging of oil shale pyrolysis using X-ray micro-tomography, automated ultra-high resolution SEM, MAPS Mineralogy and FIB-SEM. *Applied Energy*, *202*, 628–647. https://doi.org/10.1016/j.apenergy.2017.05.039

Sen, A. K., & Torquato, S. (1989). Effective conductivity of anisotropic two-phase composite media. *Physical Review B*, *39*(7), 4504–4515. https://doi.org/10.1103/PhysRevB.39.4504

Tuch, D. S., Wedeen, V. J., Dale, A. M., George, J. S., & Belliveau, J. W. (2001). Conductivity tensor mapping of the human brain using diffusion tensor MRI. *Proceedings of the National Academy of Sciences of the United States of America*, *98*(20), 11697–11701. https://doi.org/10.1073/pnas.171473898

van Schadewijk, R., van Den Berg, T. E., Sol Sankar Gupta, K. B., Rozen, I., De Groot, H. J. M., & Alia, A. (2018). Non-invasive magnetic resonance imaging of oils in botryococcus braunii green algae: Chemical shift selective and diffusion-weighted imaging. *Plos One*, *13*(8), 1–17. https://doi.org/10.1371/journal.pone.0203217

Wang, H., Alvarado, V., McLaughlin, J. F., Bagdonas, D. A., Kaszuba, J. P., Campbell, E., & Grana, D. (2018). Low-field nuclear magnetic resonance characterization of carbonate and sandstone reservoirs from rock spring uplift of Wyoming. *Journal of Geophysical Research: Solid Earth*, *123*(9), 7444–7460. https://doi.org/10.1029/2018JB015779

Watanabe, N., Saito, K., Okamoto, A., Nakamura, K., Ishibashi, T., Sakaki, H., et al. (2020). Stabilizing and enhancing permeability for sustainable and profitable energy extraction from superhot geothermal environments. *Applied Energy*, *260*, 114306. https://doi.org/10.1016/j.apenergy.2019.114306

Węglarz, W., Krzyżak, A. T., Machowski, G., & Stefaniuk, M. (2018). ZTE MRI in high magnetic field as a time effective 3D imaging technique for monitoring water ingress in porous rocks at sub-millimetre resolution. *Magnetic Resonance Imaging*, *47*, 54–59. https://doi.org/10.1016/j.mri.2017.11.015

Węglarz, W., Krzyżak, A. T., & Stefaniuk, M. (2016). ZTE imaging of tight sandstone rocks at 9.4T - Comparison with standard NMR analysis at 0.05 T. *Magnetic Resonance Imaging*, *34*(4), 492–495. https://doi.org/10.1016/j.mri.2015.12.001

Weiger, M., & Pruessmann, K. P. (2019). Short-T2 MRI: Principles and recent advances. *Progress in Nuclear Magnetic Resonance Spectroscopy*, *114–115*, 237–270. https://doi.org/10.1016/j.pnmrs.2019.07.001

Yasuhara, H., Polak, A., Mitani, Y., Grader, A. S., Halleck, P. M., & Elsworth, D. (2006). Evolution of fracture permeability through fluid–rock reaction under hydrothermal conditions. *Earth and Planetary Science Letters*, *244*(1), 186–200. https://doi.org/10.1016/j.epsl.2006.01.046

Zhang, Z., Liu, Z., Pan, Z., Baena-Moreno, F. M., & Soltanian, M. R. (2020). Effect of porous media and its distribution on methane hydrate formation in the presence of surfactant. *Applied Energy*, *261*, 114373. https://doi.org/10.1016/j.apenergy.2019.114373

References From the Supporting Information

Arns, C. H., Bougt, F., Limaye, A., Sakellariou, A., Senden, T. J., Sheppard, A. P., et al. (2005). Pore-scale characterization of carbonates using x-ray microtomography. *SPE Journal*, *735 10*(4), 475–484. https://doi.org/10.2118/90368-PA

Legland, D., Arganda-Carreras, I., & Andrey, P. (2016). MorphoLibJ: Integrated library and plugins for mathematical morphology with ImageJ. *Bioinformatics*, *32*(22), 3532–3534. https://doi.org/10.1093/bioinformatics/btw413

Seyyedi, M., Mahmud, H. K., Ben, V. M., Giwelli, A., Esteban, L., Ghasemiziarani, M., & Clennell, B. (2020). Pore structure changes occur during CO2 injection into carbonate reservoirs. *Scientific Reports*, *10*(1), 1–14. https://doi.org/10.1038/s41598-020-60247-4

Strzelecki, P. J., Prasad, A., & Raczyński, P. (2020). 3D geometric evaluation of porosity types in carbonates. *AIP Conference Proceedings*, *2209*, 030002-1–030002-7. https://doi.org/10.1063/5.0000006

Vinegar, H. J. (1986). X-ray CT and NMR Imaging of Rocks. *Journal of Petroleum Technology*, *38*(3), 257–259. https://doi.org/10.2118/15277-PA